Universidad de Málaga
Escuela Técnica Superior de Ingeniería de Telecomunicación
(Programa de doctorado en Ingeniería de Telecomunicación)

TESIS DOCTORAL

Breakthrough silicon photonics devices using subwavelength grating metamaterials

Autor:

José Manuel Luque González

Directores:

Alejandro Ortega Moñux
Robert Halir

15 de julio de 2022

AUTOR: José Manuel Luque González

https://orcid.org/0000-0002-6838-8641

EDITA: Publicaciones y Divulgación Científica. Universidad de Málaga

DECLARACIÓN DE AUTORÍA Y ORIGINALIDAD DE LA TESIS PRESENTADA PARA OBTENER EL TÍTULO DE DOCTOR

D. JOSÉ MANUEL LUQUE GONZÁLEZ
Estudiante del programa de doctorado EN INGENIERÍA DE TELECOMUNICACIÓN de la Universidad de Málaga, autor/a de la tesis, presentada para la obtención del título de doctor por la Universidad de Málaga, titulada: BREAKTHROUGH SILICON PHOTONICS DEVICES USING SUBWAVELENGTH GRATING METAMATERIALS

Realizada bajo la tutorización de ALEJANDRO ORTEGA MOÑUX y dirección de ALEJANDRO ORTEGA MOÑUX Y ROBERT HALIR.

DECLARO QUE:

La tesis presentada es una obra original que no infringe los derechos de propiedad intelectual ni los derechos de propiedad industrial u otros, conforme al ordenamiento jurídico vigente (Real Decreto Legislativo 1/1996, de 12 de abril, por el que se aprueba el texto refundido de la Ley de Propiedad Intelectual, regularizando, aclarando y armonizando las disposiciones legales vigentes sobre la materia), modificado por la Ley 2/2019, de 1 de marzo.

Igualmente asumo, ante a la Universidad de Málaga y ante cualquier otra instancia, la responsabilidad que pudiera derivarse en caso de plagio de contenidos en la tesis presentada, conforme al ordenamiento jurídico vigente.

En Málaga, a 12 de MAYO de 2022

Fdo.: JOSE MANUEL LUQUE GONZÁLEZ
Doctorando

Directores de tesis

Yo, ALEJANDRO ORTEGA MOÑUX, tutor y director de la tesis titulada "*Breakthrough silicon photonics devices using subwavelength grating metamaterials*", realizada por el estudiante del programa de doctorado en Ingeniería de Telecomunicación JOSÉ MANUEL LUQUE GONZÁLEZ, autorizo la lectura de dicha tesis doctoral.

De igual forma, confirmo que las publicaciones que avalan esta tesis no han sido utilizadas en tesis anteriores.

En Málaga, a 12 de mayo de 2022.

Fdo. Alejandro Ortega Moñux
Director y tutor de tesis

Edificio Pabellón de Gobierno. Campus El Ejido. 29071
Tel.: 952 13 10 28 / 952 13 14 61 / 952 13 71 10
E-mail: doctorado@uma.es

Breakthrough silicon photonics devices using subwavelength grating metamaterials

José Manuel Luque González

Acknowledgements

Tiempo atrás, en mi primer día de clase de grado, muchos estudiantes llegamos 1 hora antes del inicio de la clase. Aquel día, fui el único en sentarme en primera fila y no hablé con nadie. En aquel momento, me convencí de que no necesitaba entablar conversación o amistad alguna, que la carrera es algo que iba a hacer yo solo. Nunca olvidaré dicho día, pues poco tiempo después me di cuenta de la estupidez de dicha mentalidad y cambié de actitud, pues toda buena aventura, como la realización de esta tesis doctoral, se realiza mucho mejor acompañado. Y por suerte, aun siendo como soy, mucha gente ha decidido acompañarme. Esta sección es justo para agradecer a todas estas personas.

Empezando por la familia, me faltarían palabras para describir todo el apoyo recibido. He sido siempre el consentido, no solo en mi casa, sino en la de toda mi familia. Todos me han facilitado todo desde que tengo memoria. Por supuesto, tengo que hacer mención especial a mis padres, hermano, mi abuela, mi tía y mi Tata, que me han dado todo lo que les ha sido posible y un poco más siempre que lo he necesitado. Mamá, gracias por consentirme. Papa y Pedro, gracias por guiarme. Dentro de la familia por supuesto incluyo a Miriam, mi apoyo en la sombra, siempre ahí para ayudarme en lo que me haga falta, complementándome en mis defectos y para orientarme en todos los temas no relativos a la interpretación de mapas.

Por supuesto, esta sección continúa agradeciendo como se debe a mis directores de tesis, Alejandro Ortega y Robert Halir. Con su trabajo y paciencia han conseguido que me aproxime a ser una persona de provecho para la ciencia. Dos grandes directores que se complementa extraordinariamente bien, ayudándome a crecer en cada aspecto laboral/personal. Por supuesto, extiendo los agradecimientos al resto de profesores del grupo de investigación de Photonics & RF, pues cada uno ha ido añadiendo su granito de arena en mi formación, especialmente Gonzalo e Iñigo, que con el ejemplo demuestran que trabajando duro es como se consiguen buenos resultados.

Durante la realización de la tesis, hay 3 meses que recuerdo con especial cariño, y son aquellos vividos en Montreal. La estrecha relación del tema que atañe esta tesis con Canadá me ha hecho, y me hará, viajar a dicho país con cierta frecuencia. Por suerte, tanto mis supervisores en Montreal, José Azaña y Luis Romero como mi supervisor en Ottawa, Pavel Cheben, han logrado que no me sienta extranjero, incómodo ni abandonado aun estando a miles de kilómetros de mi hogar y familia.

Para finalizar, me gustaría realizar un agradecimiento a mis amigos, los cuales descuido continuamente por el trabajo o los videojuegos. Aquí incluyo a mis compañeros de la carrera, los cuales me hicieron ver que las aventuras son mejores acompañado. Mis compañeros de laboratorio, tanto los presentes como los pasados, con los cuales he compartido infinito tiempo haciendo de todo menos trabajar. Mis amigos del pueblo, que me siguen recibiendo con cariño, aunque pase meses sin ir por allí. A todos ellos, gracias por haber estado ahí, tanto en los buenos momentos, como en los no tan buenos.

Contents

Acknowledgements

1. Silicon photonics metamaterials 1
   1.1. Integrated photonics . . . 1
      1.1.1. Fabrication of silicon-on-insulator devices . . . 5
      1.1.2. Light handling in silicon-on-insulator platform . . . 6
   1.2. Subwavelength grating metamaterials . . . 9
   1.3. Goals and contributions of this Thesis . . . 14
   1.4. Organization of this Thesis . . . 17

2. From ideas to silicon photonic devices 19
   2.1. Modeling and simulation of photonic devices . . . 19
      2.1.1. Numerical electromagnetic software tools . . . 19
      2.1.2. Simulation of the mode solutions in SWG periodic structures . . . 21
   2.2. Prototyping cycle of photonic devices on SOI . . . 23
   2.3. Conclusions . . . 33

3. Wave propagation in periodic dielectric structures 35
   3.1. Wave propagation in periodic media and homogenization theory . . . 35
   3.2. Laminar periodic structures . . . 37
      3.2.1. Wave propagation through LPS . . . 38
      3.2.2. Homogeneous metamaterial equivalent to a LPS . . . 42
      3.2.3. Conclusions on the homogenization theory of LPS . . . 46
   3.3. Silicon photonic SWG waveguides . . . 47
      3.3.1. Basic homogenization model of SWG waveguides: The LPS model . . . 48
      3.3.2. Advanced homogenization model of SWG waveguides: The PSS model . 50
   3.4. Conclusions . . . 53

4. Advanced subwavelength grating metamaterial topologies 55
   4.1. Limitations of conventional SWG metamaterial topologies . . . 55
   4.2. Tilted SWG metamaterials . . . 56
      4.2.1. Homogenization model of tilted SWG metamaterials . . . 57
      4.2.2. Waveguiding properties of tilted SWG metamaterials . . . 60
      4.2.3. Proof of concept of tilted SWG metamaterials . . . 61
      4.2.4. Design of a directional coupler polarization beam splitter . . . 63
      4.2.5. Additional contributions using tilted SWG metamaterials . . . 70
   4.3. Bricked SWG periodic structures . . . 71
      4.3.1. Homogenization model of the bricked SWG metamaterial . . . 71
      4.3.2. Waveguiding properties of bricked SWG metamaterials . . . 73
      4.3.3. Design of a broadband bricked SWG multimode interferometer . . . 75
   4.4. Conclusions . . . 80

5. Gradual Index subwavelength grating metamaterials **81**
5.1. Light propagation through GRIN media 81
5.2. GRIN metamaterials through duty-cycle modulated SWG structures 83
5.2.1. Topology proposal, design algorithm and homogenization 83
5.2.2. Validation of the gradual anisotropy homogenization model 85
5.3. Demonstration of a GRIN lens spot size converter implemented with a duty cycle modulated SWG metamaterial 86
5.3.1. Design of the GRIN lens spot size converter 87
5.3.2. Experimental demonstration 90
5.4. Conclusions 92

6. Conclusions, outlook and future research lines **95**
6.1. Conclusions and outlook 95
6.2. Future work 97
6.2.1. Design and experimental demonstration of photonic devices with improved performance using the proposed SWG metamaterial topologies. 97
6.2.2. Development of novel alternatives to implement GRIN metamaterial . . 97
6.2.3. Combination of the SWG metamaterials with inverse design / transformation optics design techniques 98

A. Curriculum Vitae **99**

B. Resumen en Español **105**
B.1. Introducción 105
B.1.1. Fotónica integrada 105
B.1.2. Metamateriales SWG 106
B.1.3. Objetivos y aportaciones de esta Tesis 107
B.2. Propagación de ondas en medios periodicos 108
B.2.1. Estructura periódica laminar 109
B.2.2. Homogeneización de la estructura laminar periódica 110
B.2.3. Guías de onda SWG 111
B.3. Topologías SWG avanzadas 117
B.3.1. Topología SWG inclinada 118
B.3.2. Modelo de homogeneización de metamateriales SWG inclinados 118
B.3.3. Propiedades de guía de ondas de los metamateriales SWG inclinados . . 119
B.3.4. Topología SWG enladrillada 120
B.3.5. Modelo de homogeneización del metamaterial SWG enladrillado 120
B.3.6. Propiedades de guía de ondas de los metamateriales SWG enladrilladas 122
B.4. Metamateriales SWG graduales 124
B.4.1. Propuesta de topología, algoritmo de diseño y homogeneización 124
B.5. Conclusiones y líneas futuras 126

Bibliography **129**

1. Silicon photonics metamaterials

This Thesis is devoted to the study of subwavelength grating (SWG) structures: extremely versatile optical metamaterials that have become a fundamental tool for the design of ultra high-performance photonic devices. The importance of SWG structures arises from their capability to synthesize artificial materials with tailorable optical properties, including refractive index, dispersion or anisotropy. A complete framework for SWG metamaterials is provided along the Thesis, including a revision of the different procedures and electromagnetic tools used along this Thesis to demonstrate proposed SWG topologies and devices (chapter 2), a theoretical study of wave propagation through SWG structures and the models predicting their homogeneous behavior (chapter 3), and the proposal, design and experimental characterization of various SWG topologies and devices (chapters 4 and 5). But prior to such discussions, this opening chapter starts by contextualizing the use of SWG metamaterials. For this purpose, the applications of integrated photonics and some of the most important fabrication platforms of photonics chips are discussed in section 1.1. Then, the emergence of SWG metamaterials in silicon photonic platforms is discussed in section 1.2. Finally, the objectives, contributions and organization of the Thesis are detailed in sections 1.3 and 1.4 respectively.

1.1. Integrated photonics

The term photonics defines the science and technologies in charge of generating, controlling, and detecting photons, which are particles of light. The applications of photonics range from its main driver, optical communications [1–4], to many others such as organic optoelectronic devices [5–7], photovoltaics [8, 9], X-ray science [10, 11], biomedical optics [12–14], sensing [15–17], spectroscopy [18, 19] or quantum photonics [20, 21] among many others. Historically, photonic applications have been addressed with discrete optical components connected via fiber optics or free space propagation. However, discrete optical systems are difficult to scale, expensive, and tend to suffer from mechanical instabilities. These drawbacks turned the market to integrated photonics (IPh) in the applications that allow it. IPh deals with the fabrication of several photonic components on a common planar substrate, including light sources, couplers, beam splitters, filters, polarization management devices, detectors or interferometers among others, which are used as building blocks for photonic integrated circuits (PICs). Some promising market applications of IPh are tele/datacom, aerospace, automotive, biosensing, and industrial internet of things (IoT) [22].

Many fabrication platforms of photonic chips have been proposed, analyzed and experimentally validated since the first proposal of integrated optics, conducted by Miller in 1969 [23], seeking the optimum solution for on-chip integration. Some of the most important platforms are:

- **Lithium niobate platforms:** Since mid-1970s, lithium niobate ($LiNbO_3$, LN) was recognized as a promising alternative for on-chip integration [24]. The interest surrounding LN arose from the large electro-optic coefficient of LN crystals, enabling the design of efficient active components such as modulators [25, 26]. Some further interesting properties of LN are: low loss propagation, wide transparency window, high acousto-optic effects and good temperature stability [27, 28]. The fabrication of conventional LN waveguides is done by sputtering and annealing a metal titanium strip on a LN crystal, creating an index contrast between the doped zone and the surrounding LN (Fig. 1.1, first row). However, the low index contrast obtained through this process $\Delta n \sim 0.01 - 0.03$ RIU results in large optical mode sizes, $\sim 5\,\mu$m and bent radii in the order of dozens of centimeters, impeding its large-scale photonic integration and lowering electro-optic efficiency as the electrodes are spaced far from the waveguide. For these reasons, the early dominance of LN platform vanished in favor of more compact fabrication platforms in most applications but for design of optical modulators where the good optical properties of LN are still prevailing.
- **III-V semiconductor platforms:** Semiconductor alloys of group III and V elements such as Gallium Arsenide (GaAs), Indium phosphide (InP) or Indium Gallium Arsenide (InGaAs) among others have been historically exploited in photonics chips. Interest in III-V compounds arose from the relative ease of fabricating lasers with them, the GaAs laser was demonstrated as early as 1962 [29], and the prospect of optical amplification and electronic integration. Group III-V materials allow almost all optical functionalities including light emission [29–31], transmission [32, 33], modulation [34, 35] and detection [36]. InP and its ternary and quaternary alloys have received most of the attention as they are widely utilized in optical transceivers [37] and for efficient scaling of optical networks [38]. There are many different types of InP waveguides, but they all usually have a thick InP substrate in which a InP/InPGaAs/InPGaAsP core is defined (Fig. 1.1, second row). The index contrast between these materials is about $\Delta n \sim 0.2 - 0.4$ RIU, resulting in optical mode sizes and bend radii in the order of 1 µm and 0.5 mm respectively, allowing a higher integration density than LN platforms. Numerous barriers associated with InP processing are slowing their success, such as difficulties on the required uniformity and reproducibility on manufacturing scale [39], the fragility and expensiveness of Indium substrates [40], the small size of InP wafers [41] or the sensitivity of modulators to the temperature [42].
- **Silicon photonics platforms:** Silicon photonics (SiPh) platforms started in mid-1980s with a series of seminal papers by R. A. Soref and coworkers [43–48] were they discussed the advantages of silicon over other materials. SiPh platforms comprises many different fabrication platforms including Silicon-On-Insulator (SOI), Silicon Nitride (SiN), silica-on-silicon, germanium-on-insulator, germanium-on-silicon (GOS) or silicon oxynitride (hydex). SOI platform, composed of silicon waveguides over silicon dioxide layer (Fig. 1.1, third row), is currently the benchmark SiPh platform in terms of both technological maturity and commercial use [49] with several devices and photonic integrated circuits implemented on it [50]. One of the most important features of silicon photonics platforms is the compatibility of their fabrication process with CMOS fabrication process, allowing to leverage the billions of dollars of investments and decades of research in this field [51]. Moreover, the high index contrast between SOI materials, $\Delta n \sim 2$ RIU, allows a sub-micron confinement and extremely short bending radii,

~ 5 µm. Apart from SOI, another silicon photonic platforms which is gaining attention in the last decade is SiN. Interest in SiN mainly comes from its potential ultra-low loss propagation losses (<1 dB/m), large transparency window and enhanced non-linear properties compared with SOI, such as the absence of two photon absorption effect enabling high power applications regime [52, 53]. In general, the applications that benefit most from the different silicon platform are those that require many devices to be strung together into a complex system. On the other hand, the main drawback associated with SiPh are the indirect bandgap of group IV materials, which hinders the efficient generation of light and the lack of different CMOS compatible materials, hampering the design of high-performance devices.

Each of discussed fabrication platforms have their unique advantages and disadvantages, measured in many different terms such as integration capacity, transparency bands, propagation losses, integrability of active components, etc. A summary of the three discussed platforms is shown in Fig. 1.1.

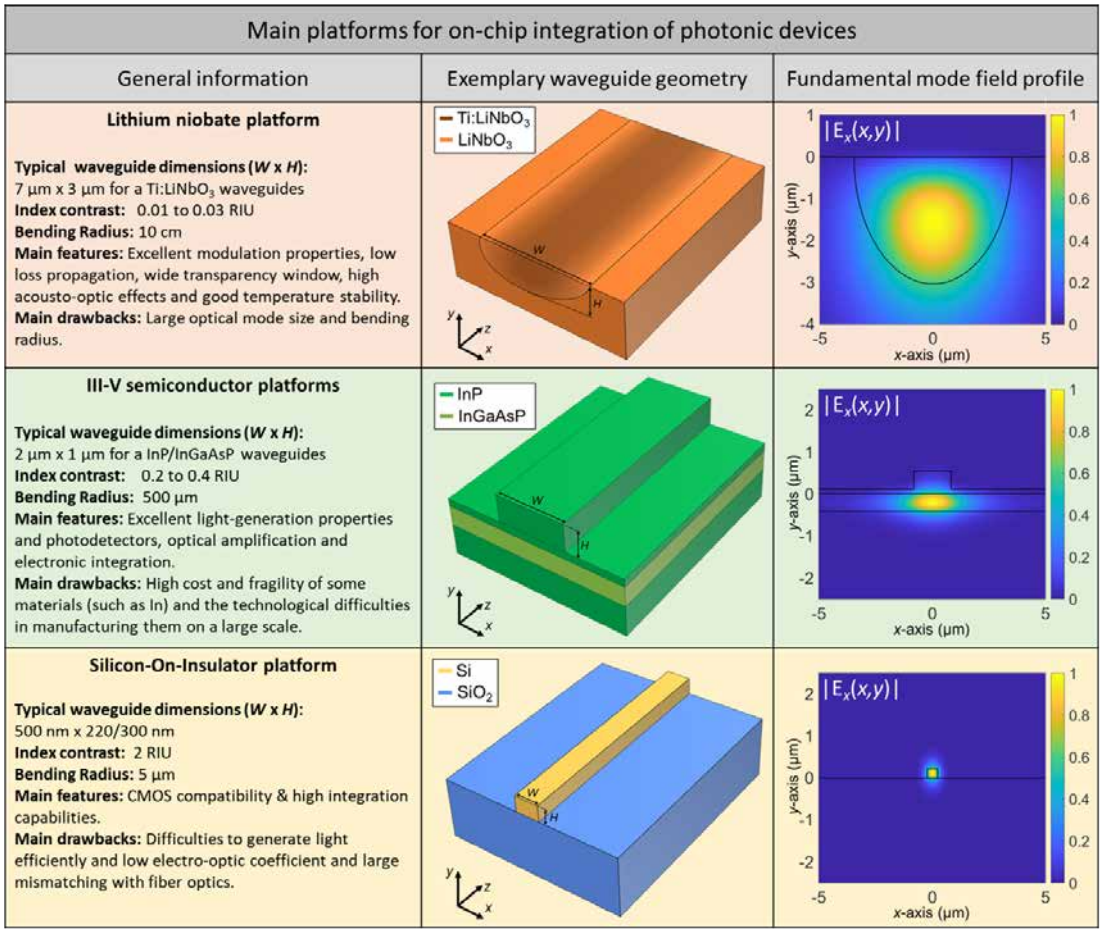

Figure 1.1: Summary of some of the main platforms for on-chip integration of photonic devices, including lithium niobate platform, III-V semiconductor platforms and Silicon photonics platforms. The summary includes the main properties, features and drawbacks of each platform, a schematic example of a waveguide and the field distribution of the fundamental mode in a typical interconnecting waveguide.

From the discussed platforms, SiPh platforms are becoming the prominent solution for on-chip integration, with SOI being the most advanced SiPh technology. The main reasons for the advantage of SiPh platforms are their CMOS compatible fabrication process and the huge integration capability at a low manufacturing cost of chips, allowing to integrate up to $2 \cdot 10^5$ components in a single chip (see Fig. 1.2). Indeed, some of the largest technology companies have already bet in silicon photonics such as Apple [54], Huawei [55], Nvidia [56], Intel [57] or Cisco [58] among others, with some of them already commercializing silicon photonic solutions such as Intel's 400-gigabit optical transceiver [59].

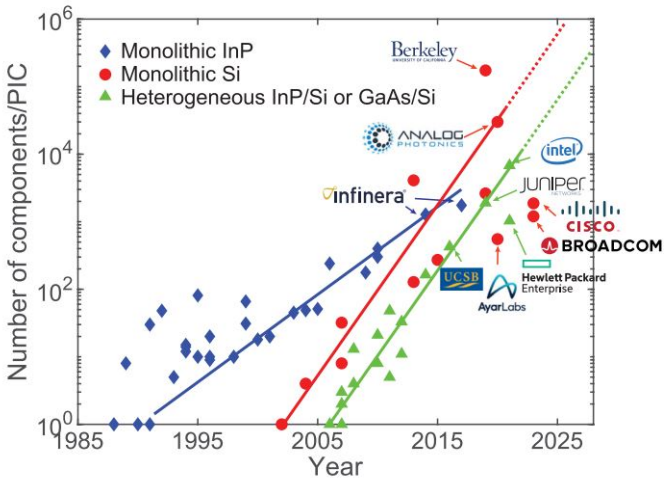

Figure 1.2: Number of photonic components integrated on a chip over time for three photonic integration platforms: InP with integrated lasers (blue), Si without integrated lasers (red), and Si with integrated lasers (green). Reproduced from [60] with permission.

Moreover, current trends aim to combine SiPh with other platforms to complement their weaknesses. Some of the most notorious hybrid platforms are:

- **LN+SiPh platforms:** The combination of these two platforms brings together the integrating capabilities of SiPh with the modulation capabilities of LN. The two main approaches to combine them are i) LN-on-insulator (LNOI), that is a LN waveguide over a silicon dioxide insulator layer [61] and ii) hybrid integration of LN membranes onto SOI PICs [62]. LN+SiPh platforms have demonstrate optical waveguides with propagation losses as low as 2.7 dB/m [63] and electro-optics modulator with CMOS compatible voltages [64] or with modulation bandwidths beyond 100 Ghz [65].
- **Group III-V materials+SiPh platforms**. Group III-V materials easily complement the lack of lasers and the difficulties to implement electro-absorption modulators (EAM) of SiPh platforms. Many different devices have been implemented by growing InP layers over SOI chips such as semiconductor optical amplifiers [66], lasers [67–70] or optical EAM modulators [71].
- **LN+SIPh+group III-V materials platforms:** Recent works propose to join together the LN, III-V and SIPh fabrication platforms. In Ref. [72] the authors butt-couple a InP laser on a LNOI platform. This combination of platforms is very promising as it allows to integrate simple InP lasers on LNOI, a fabrication platform with an impressive potential for light modulation.

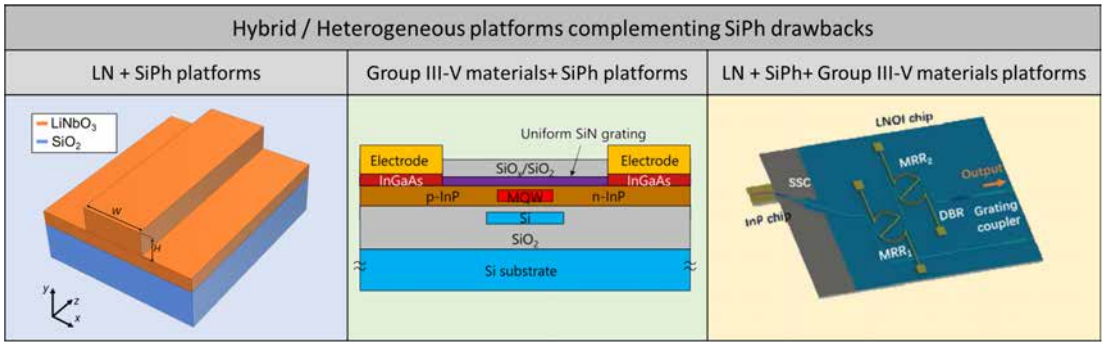

Figure 1.3: Example of some of the hybrid/heterogeneous platforms for complementing SiPh drawbacks, including the heterogeneous integration of LN with silicon dioxide (LNOI), the hybrid integration of InP laser with SOI waveguides (image replicated from [69]) and the butt-coupling a InP laser on a LNOI chip (image replicated from [72]).

Most of the success of these platforms will probably depends on making their fabrication compatible with the existing CMOS facilities and processes to fabricate SOI devices.

1.1.1. Fabrication of silicon-on-insulator devices

Silicon-on-insulator technologies were originally proposed in the context of microelectronic transistors to reduce the parasite capacitance between the source/drain terminals with the silicon substrate by introducing an insulator layer in between [73]. However, they soon proved suitable for the purpose of guided-wave optics [47]. Among the different SOI technologies, silicon on its native oxide (silicon dioxide, SiO_2), is the predominant and most mature platform for on-chip integration. The transparency bands of silicon and silicon dioxide start at wavelengths $\lambda_0 \sim 1.1\,\mu m$ and $\lambda_0 \sim 0.2\,\mu m$ respectively up to $\lambda_0 \sim 8\,\mu m$ and $\lambda_0 \sim 3.5\,\mu m$, thus they are extensively used in near infrared, and short wavelengths of the mid-Infrared bands. SOI chips are manufactured on SOI wafers with a three layer structure (from top to bottom): A thin silicon layer (220-300 nm) where the light travels, a silicon dioxide layer and a thick silicon layer acting as a substrate (Fig. 1.4a). To define the photonic devices, a photoresist is deposited on top of the wafer which protects the areas where the devices will be placed (Fig. 1.4b). There are two main alternatives to write the devices into the photoresist: i) Electron-beam (E-Beam) lithography and ii) optical lithography. In E-beam, an electron beam writes the structures in the resist pixel after pixel in a serial way (Fig. 1.4c), being capable of defining extremely small features. The minimum feature size (MFS) obtained in standard e-beam processes is in the order of MFS ~ 50 nm. This is the most used technique for research purposes and prototyping as it ensures the best fabrication possible. However, the process is very slow, and it is not suitable for large volumes. On the other hand, in optical lithography techniques the photoresist is illuminated through a mask which defines the devices (Fig. 1.4d). This process is limited by the optical diffraction of the illumination which dictates the minimum features as the illumination wavelength divided by the optical aperture of the lens system. Typical deep-ultraviolet (DUV) lasers work with wavelengths of 248 and 193 nm and typical lenses systems have an optical aperture around 0.6. Features of the order of the wavelength divided by the optical aperture become fuzzy or are not printed at all. There are many different techniques to improve the MFS, such as the immersion lithography techniques which submerge the process in water to obtain better resolutions as the optical

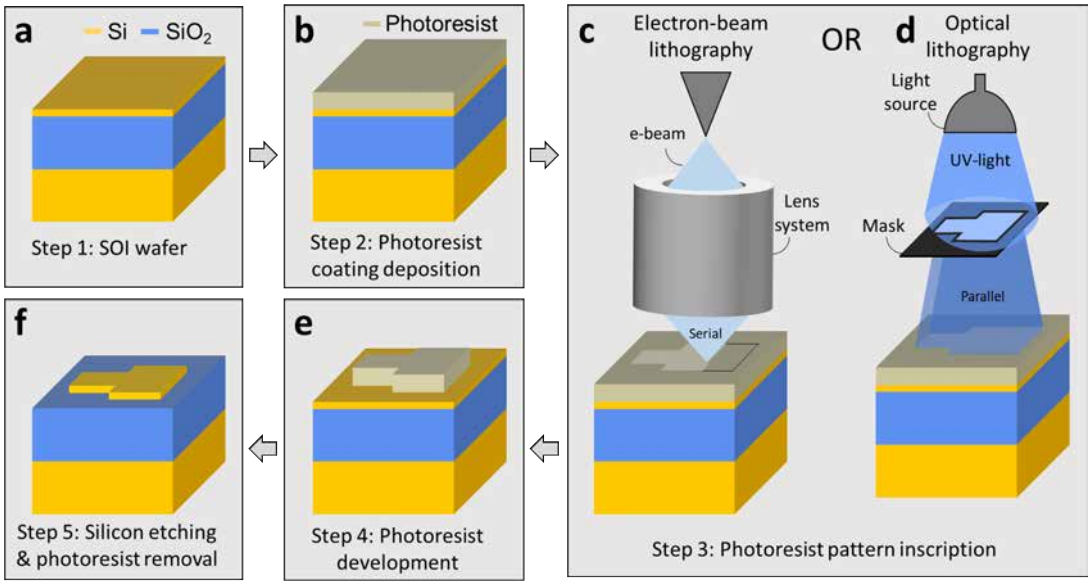

Figure 1.4: Typical fabrication process of SOI devices. The process starts with a SOI wafer (a), on top of which a photoresist is deposited (b). Then, the photonic devices are written into the photoresist by using either e-beam lithography (c) or (d) optical lithography. Once the photoresist has been written with the pattern, the non-written areas are removed (e). Finally, the uncovered silicon areas are etched, and the remaining photoresist is removed (f).

aperture is increased, obtaining MFS in the order of 100-200 nm [50]. Opposed to e-beam, optical lithography is widely adopted for commercial CMOS fabrication at the expense of a lower fabrication resolution. When the pattern is already written into the photoresist, the unexposed photoresist is removed (Fig. 1.4e). Finally, the silicon areas that are non-protected by the photoresist are etched, and the remaining photoresist is removed (Fig. 1.4f). A frequent etching process is reactive-ion etching (RIE), a dry etching process where high-energy ions attack the non-protected wafer surface. In many cases, after all this fabrication process, a silicon dioxide cladding is grown with plasma-enhanced chemical vapor deposition (PECVD) to protect the guiding silicon layer.

1.1.2. Light handling in silicon-on-insulator platform

The geometry of an SOI interconnecting waveguide was shown in Fig. 1.1, with typical dimensions being $W = 0.5\,\mu m$ and $H = 0.22\,\mu m$ for interconnecting waveguides. This kind of structures support two independent types of orthogonal solutions, known as polarizations, differing in the direction of the electric field main component: the quasi-TE and the quasi-TM polarization. The quasi-TE modes have most of the electric field in the component parallel to the chip surface (E_x) while the quasi-TM modes have the majority of the electric field in the component perpendicular to the chip surface (E_y). Each polarization allows a set of different field distributions called modes. For the sake of brevity, they are usually known as TE and TM modes. Figures 1.5a and 1.5b show the electric field profile of the fundamental TE and TM modes of the interconnecting waveguide, that is, the modes with a single oscillation in the core in both transversal dimensions. These modes travel along the z-axis with a propagation wavelength $\lambda_0/n_{\text{neff}}$ with λ_0 being the wavelength in the vacuum

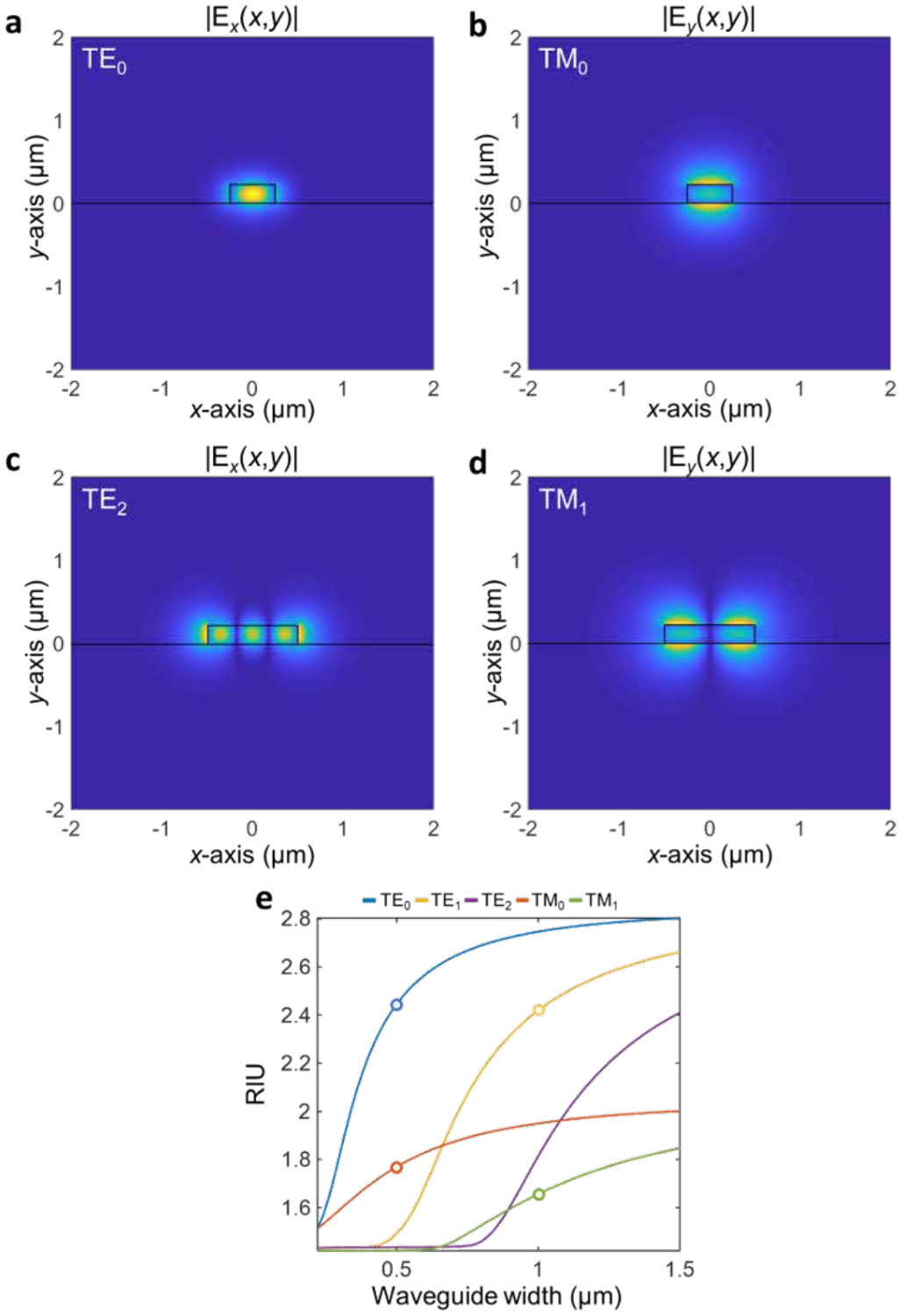

Figure 1.5: Transverse field distribution, $E(x,y)$, of the a) fundamental TE, b) fundamental TM, c) third order TE, and d) second order TM modes at a wavelength $\lambda_0 = 1.55\,\mu$m. The waveguide thickness (H) is 220 nm and the width (W) is 500 nm, in (a),(b) and 1000 nm, in (c),(d). e) Effective indices of the different modes supported by a silicon waveguide as a function of the width.

and n_{eff} a scalar number between the core and the cladding/substrate refractive indices. If the dimensions of the waveguide are incremented, higher order modes are allowed, i.e., field solutions with multiple oscillations in the core. In conventional SOI with silicon thickness of 220 nm, multiple modes are only allowed in the horizontal dimension, as only the modes with one vertical oscillation are supported. Figures 1.5c and 1.5d show the third TE mode and the second TM mode assuming a 1 µm wide waveguide. Figure 1.5e shows the effective index of the different modes supported by the proposed waveguide for different widths.

A wide variety of light handling passive devices have been demonstrated in SOI (see Fig. 1.6), including power splitters [74–76], polarization management devices [77–80], off-chip couplers [81, 82], or wavelength (de)multiplexers [83–85], etc. However, the design of SOI devices is tightly limited by the CMOS compatibility constrains which imposes a restriction on the usable materials: silicon, silicon dioxide and silicon nitride with refractive indices $n_{\text{Si}} = 3.476$, $n_{\text{SiO}_2} = 1.444$ and $n_{\text{SiN}} = 2$ at $\lambda_0 = 1.55$ µm. Under this limitation, the use of dielectric subwavelength metamaterials emerged in SOI as a design tool to optimize the performance of multiple devices. Such metamaterials emulate the behavior of homogeneous materials but with tailorable optical properties, opening a new world of possibilities for the designers.

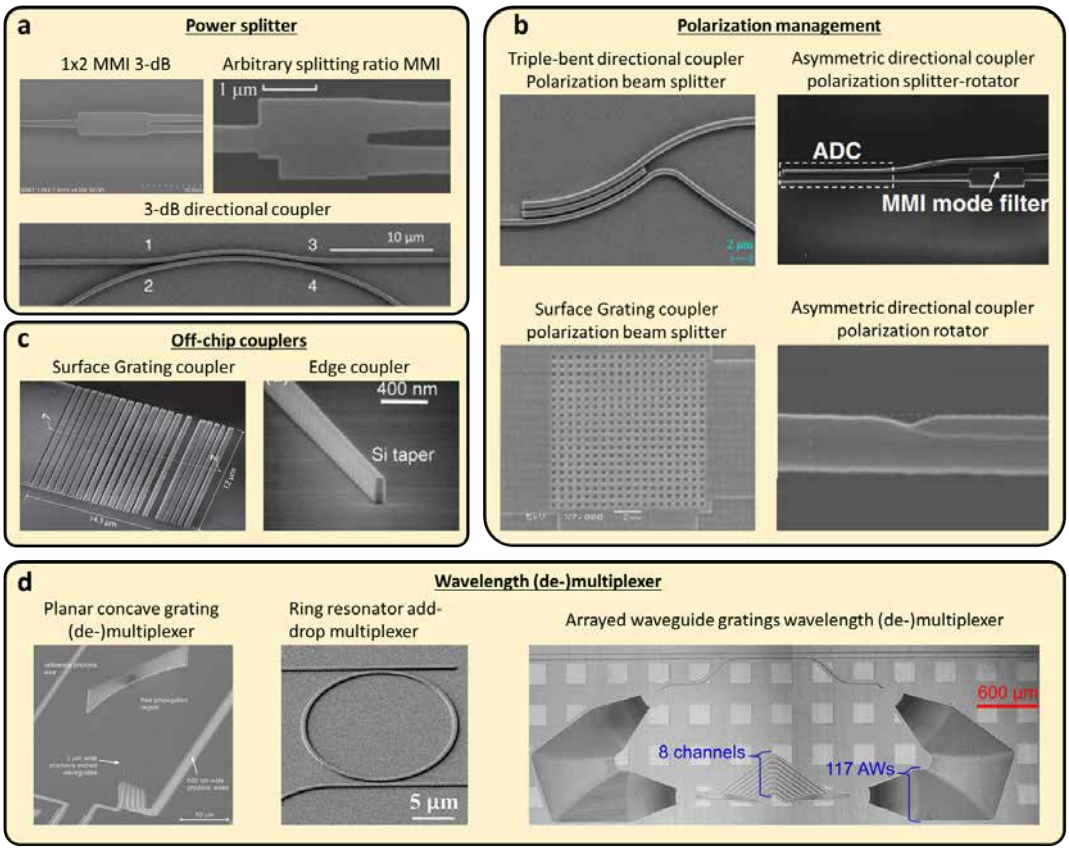

Figure 1.6: Scanning electron microscope images of some light handling devices fabricated in SOI platform, including a) Power splitter [74–76], b) Polarization management devices [77–80], c) Off-chip couplers [81, 82] and d) Wavelength (de-)multiplexers [83–85].

1.2. Subwavelength grating metamaterials

In 1967 the Russian physicist Victor Veselago theorized about the wave propagation along materials with electromagnetic properties beyond what can be found in nature [86]. They had simultaneously negative electric permittivity and magnetic permeability. These materials, first known as left-handed materials, possess many interesting and counter-intuitive behaviors such as negative refraction, inverse Doppler effect, perfect focusing properties, etc. However, just like Veselago noted, they cannot exist in nature because they contradict some fundamental physic laws, therefore, Veselago's study fell into oblivion. This paradigm changed in mid-1990s, when a British company called Marconi Materials Technology manufactured a radiation-absorbing carbon material to hide battleships from radar detection. At the beginning, they did not know the physics of how it worked, so they consulted with John B. Pendry and he concluded that the electrical properties allowing the material to absorb radiation came not from the carbon but from the fine periodic structure on a similar scale as the wavelength of the radars. These periodic patterning of specific materials emulated the behavior described by Veseleago. From that moment, a novel approach to control the electromagnetic propagation emerged: the science of metamaterials [87–89].

A decade before Veselago's proposal of the left-handed materials, Rytov was already studying the propagation of electromagnetic waves along periodic arrangements of dielectric materials at a subwavelength scale [90]. He theoretically demonstrated the equivalence between dielectric periodic structures at the subwavelength scale and homogeneous anisotropic uniaxial crystals. The periodic structures as analyzed by Rytov, from now refereed as subwavelength grating structures, do not have a negative permittivity or permeability, so they do not have most of the exotic properties described by Veselago. However, their unique optical properties circumvent the fundamentally limited choice of CMOS compatible materials enabling novel devices with unprecedented performance.

Subwavelength grating are periodic structures comprising two different dielectrics, typically silicon segments and silicon dioxide/air, arranged with a periodicity, Λ, much shorter than the wavelength, λ, of the propagating wave (Fig. 1.7a). Each material has a length a and b per period respectively, with the duty cycle DC=a/Λ measuring the amount of silicon per period. The interest surrounding SWG metamaterials relies on their capability to behave as homogeneous structures (Fig. 1.7b). That is to say, a wave propagating along an SWG waveguide will not be diffracted by the periodic interfaces, as waves normally do, but it will propagate similarly as it would do along a homogeneous waveguide. This type of SWG waveguides have been extensively used in SiPh since their demonstration in integrated platforms in 2006 by Cheben et al [91]. From that year until mid-2010s, most of the SWG works in integrated photonics used simple models where the SWG structure was homogenized as an isotropic material defined by an equivalent refractive index, n_{eq}. However, from 2016 this paradigm changed when it was demonstrated that anisotropic models, defined by an equivalent permittivity tensor $\boldsymbol{\varepsilon}_{\text{eq}}$, represent more accurately the actual behavior of SWG metamaterials [92] and predicts unique properties of the SWG devices. The equivalence between SWG metamaterials and anisotropic materials, sometimes knows as form birefringence [93], implies that the actual behavior of periodic structure strongly depends on the orientation of the SWG structure with respect to the polarization and propagation direction. In the exemplar SWG waveguide shown in Fig. 1.7a the wave propagation direction is the same as the direction along which the periodic segments are repeated, which is the most

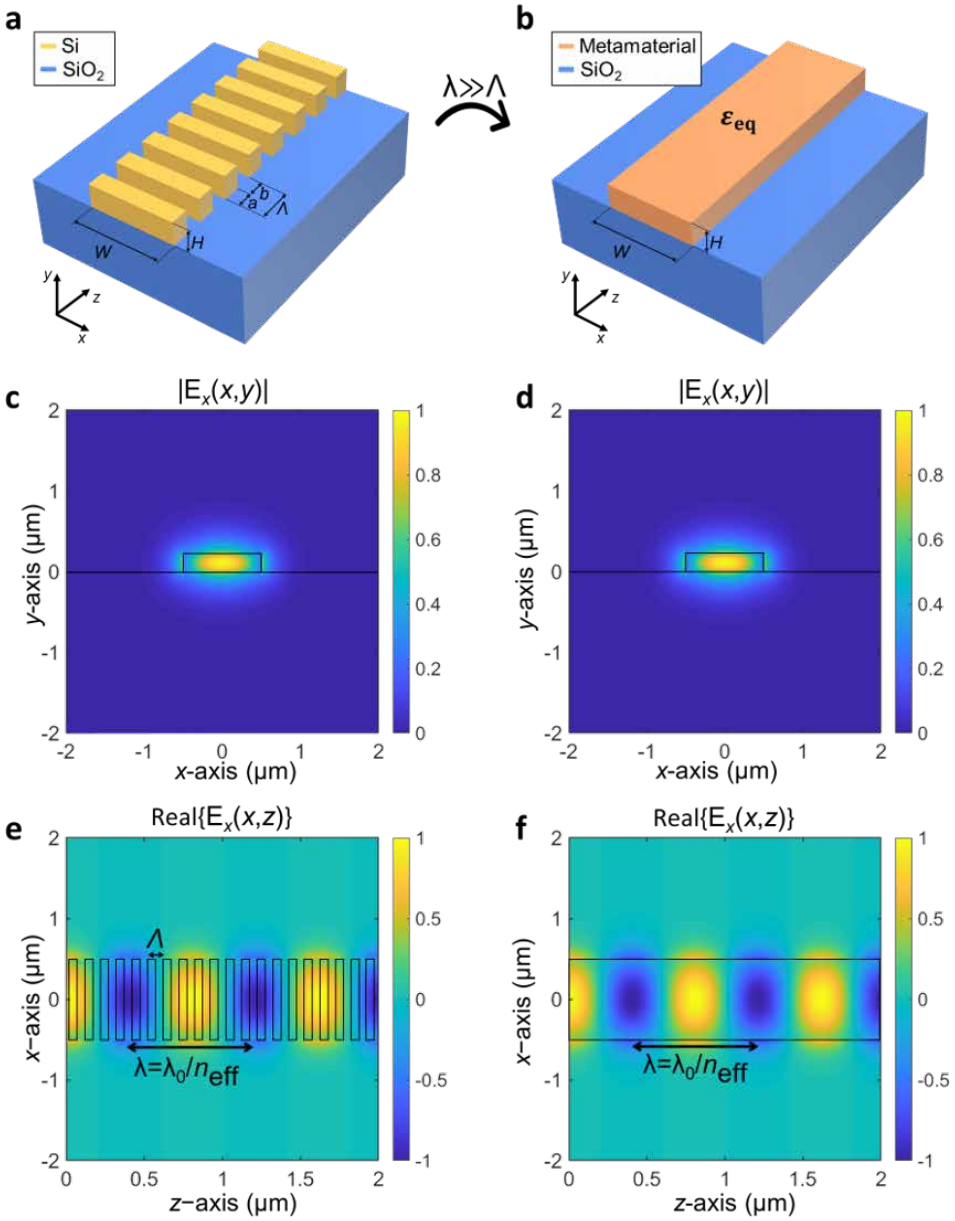

Figure 1.7: Schematic representation of a) an SWG waveguide in SOI and b) its corresponding equivalent homogeneous waveguide. c,d,e,f) Electromagnetic simulation of the (c),(d) cross section profiles and (e),(f) propagation profiles in the SWG waveguide and in the equivalent homogeneous waveguide. TE polarization and a free-space wavelength of $\lambda_0 = 1.55$ µm are considered. The geometry of the waveguide core are outlined in black in the field simulations. The waveguide layer is $H = 220$ nm thick and $W = 1$ µm wide. In (a), $\Lambda = 100$ nm, DC=0.5 and the refractive indices of the silicon and silicon dioxide are $n_{Si} = 3.476$ and $n_{SiO_2} = 1.444$. In (b) the metamaterial is defined by a diagonal permittivity tensor $\boldsymbol{\varepsilon}_{eq} = \text{diag}[2.68^2, 2.68^2, 1.89^2]$.

usual SWG topology, known as longitudinal SWG or z-periodic SWG. The field profile of the fundamental TE mode and the field propagation along the periodic structure are shown in Fig. 1.7c and Fig. 1.7e. This exemplar waveguide is modeled as a homogeneous anisotropic waveguides (Fig. 1.7b). The accuracy of the anisotropic homogenization of a SWG metama-

terial is shown in Figs. 1.7d and 1.7f, where the electromagnetic field profile and the field propagation in the equivalent homogeneous anisotropic waveguide are shown, obtaining virtually the same result in both cases when they are compared with the solutions of the periodic structure. The algorithm to calculate the permittivity tensor components of the homogenized structure are proposed and discussed in chapter 3.

The capability of subwavelength grating metamaterials to behave as homogeneous materials places them in a crucial spot in SiPh. They complement the lack of different material refractive index derived from the CMOS fabrication process. Moreover, the unique optical properties of SWG metamaterial and the capability to engineer them by properly tuning the periodic structure opens a myriad of possibilities for the photonic designers. For these reasons, they have been extensively used to optimize the performance of almost every passive device. Figure 1.10 shows a summary of the different applications were SWG metamaterials have been used. In these designs, there are three main approaches to engineer the SWG metamaterial, depending on the designed optical property:

1. **Refractive index engineering:** This is arguably the simplest type of SWG engineering. The SWG metamaterial is tuned to control the effective index of the TE or TM modes propagating through the periodic structure. This is typically achieved by tuning the duty cycle of the periodic pattern. As intuition predicts, high duty cycles imply higher effective indices while low duty cycles imply lower effective indices. This behavior is shown in Fig. 1.8a where the effective index of the fundamental TE and TM modes of an SWG waveguide for different duty cycles are shown. The tuning of the effective index has been used in several applications such as power/mode splitters where SWG refractive index engineering is used to control the phase matching or coupling strength [94–102], in grating couplers where the SWG enhances the coupling efficiency [103–108] or in gradual refractive index devices to implement the gradualness of the material [109–111], among other applications. The two insets in Fig. 1.8 show how the confinement of the field distribution follows the effective index, with high indices implying high confinements and vice versa. Therefore, refractive index engineering has been also used to control field profile for example in edge couplers, allowing to match the field

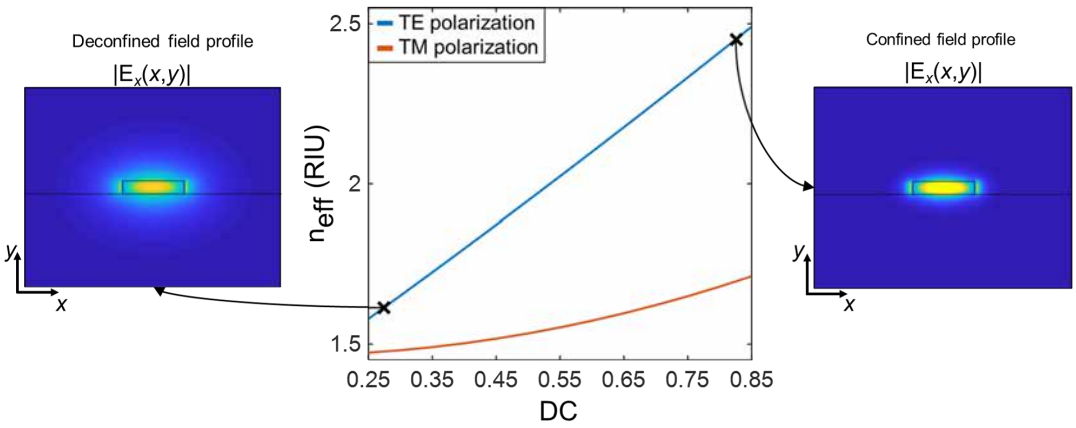

Figure 1.8: Effective index of the fundamental TE and TM modes of a SWG waveguide with height H = 220 nm, width W = 1 µm, period Λ = 100 nm, and duty cycle DC ranging from DC=0.25 to DC=0.85 at λ_0 = 1.55 µm. Insets: Main component of the traversal field profile $|E_x(x,y)|$ for a low and a high duty cycle. The confinement increased with the duty cycle.

profile at the edge of the chip with the field profile of the fibers [91, 112, 113], in waveguide crossing, decreasing the crosstalk by delocalizing the field profile [114, 115], in waveguide bends compensating the effect of the bend [116–118], in filters/antennas, weakening the interaction between the light and the reflective/diffractive elements [119, 120] or in biological sensing, increasing the light-matter interaction by placing as much field as possible in the sensing area [121–126].

2. **Birefringence/Anisotropy engineering:** The high-index contrast in SOI chips and the non-square cross sections of SOI waveguides cause TE and TM polarizations to propagate differently. This behavior is known as birefringence and it is defined as $B = n_{\text{eff}}^{\text{TE}} - n_{\text{eff}}^{\text{TM}}$, where $n_{\text{eff}}^{\text{TE}}$ and $n_{\text{eff}}^{\text{TM}}$ are the effective indices of the TE and TM modes respectively. The refractive index engineering can be used to reduce index contrast, allowing birefringence control as shown in Fig. 1.9a, where the birefringence between the fundamental TE and TM modes in the waveguide studied in Fig. 1.8 is shown for different duty cycles. Therefore, SWG metamaterials are ideal structures to design polarization management devices, including polarization beam splitters [133, 136–138], rotators [139, 140], splitter-rotators [130, 141, 142], or polarization filters [131, 143, 144]. Moreover, SWG structures are intrinsically anisotropic, that is, waves propagating along them change their characteristics, namely field profile and effective index, depending on the propagation direction. The anisotropy could be used to further engineer the birefringence, but the current SWG topologies do not provide a direct control over the metamaterial birefringence. This problem is solved in this Thesis by proposing different techniques to control the metamaterial birefringence. Moreover, the anisotropy can be also used to optimize multimode devices with reduced lengths [92, 118] or to modify the field confinement [145], by controlling the coupling between adjacent devices [133, 146].

3. **Dispersion engineering:** Large bandwidth is a frequent desirable feature for photonic devices. SWG metamaterials enable increased bandwidths as their optical properties depends on the wavelength, so the intrinsic dispersion of photonic devices can be par-

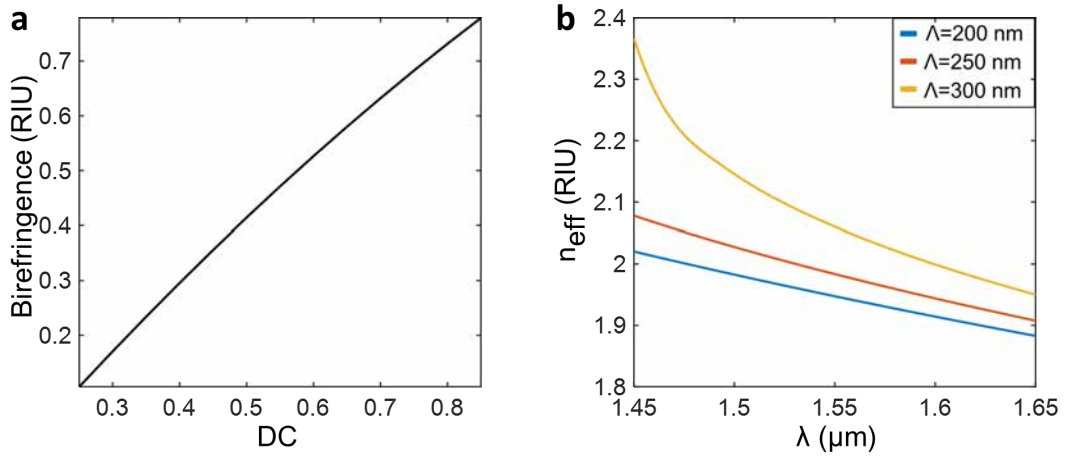

Figure 1.9: a) Birefringence in an SWG waveguide with height $H = 220$ nm, width $W = 1$ µm, period $\Lambda = 200$ nm, and duty cycle DC ranging from DC=0.25 to DC=0.85 at $\lambda_0 = 1.55$ µm. b) Variation of the effective index with wavelength for the fundamental TE for different periods for an SWG waveguide with height $H = 220$ nm, width $W = 1$ µm and duty cycle DC=0.5.

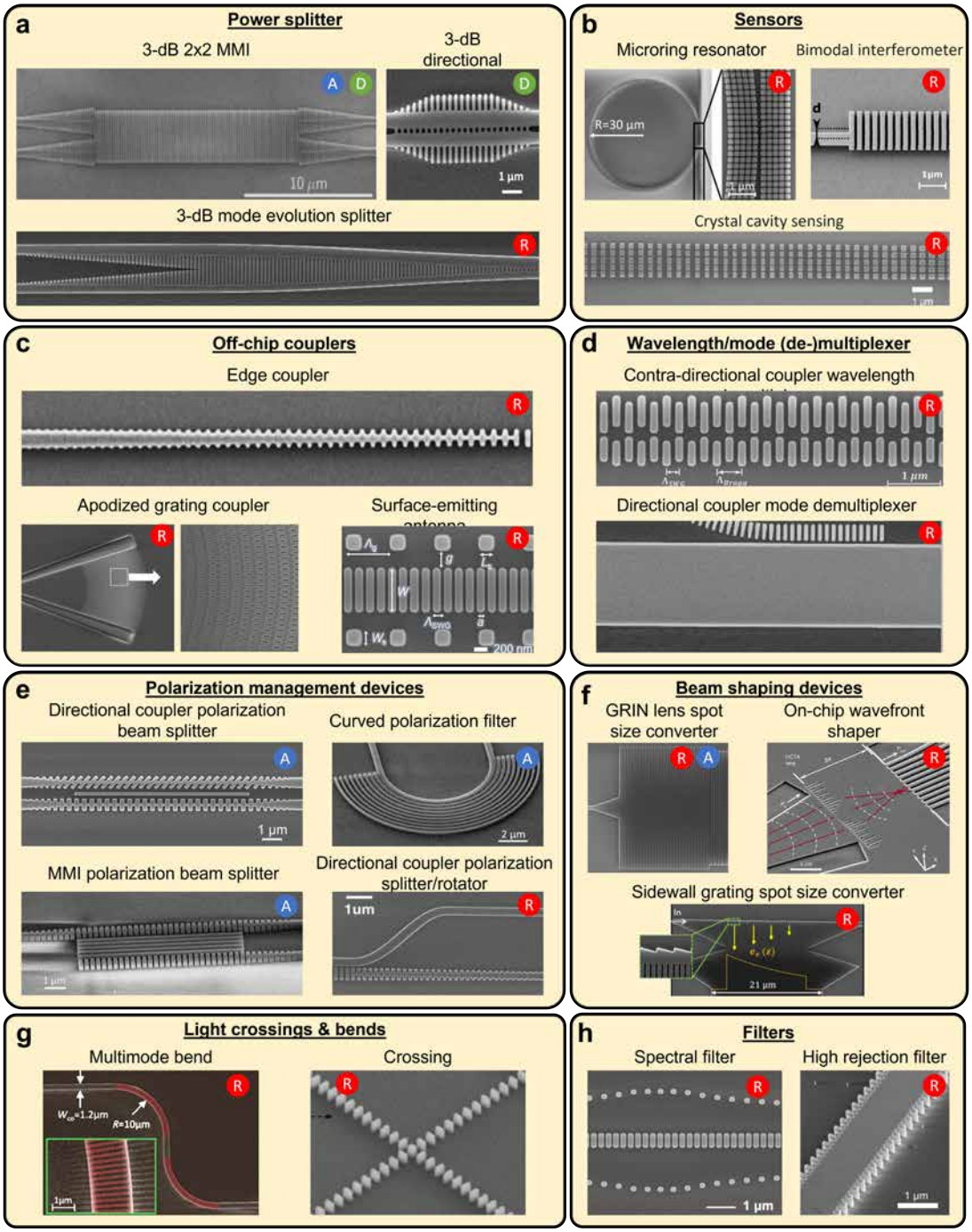

Figure 1.10: Scanning electron microscope images of some SWG enhanced devices fabricated in SOI platform, including a) power splitter [92, 96, 127], b) photonic biosensors [125, 126, 128], c) efficient off-chip couplers [107, 120, 129], d) wavelength/mode (de-)multiplexers [97, 100], e) polarization management devices [130–133], f) beam shaping devices [111, 118, 134], g) light crossing and bends [114, 117] and h) filters [119, 135]. The main engineering technique used in each device is noted in each image: R=Refractive index engineering. A=Anisotropy/birefringence engineering. D=Dispersion engineering.

tially compensated. Figure 1.9b shows the wavelength behavior of the effective index of the fundamental TE mode of the same SWG waveguide studied in the previous points for different periods, the most common method to engineer the dispersion, showing how the wavelength dependence of the modes can be modified. This dispersion engineering has been exploited to increase the bandwidth of multimode interferometers [92], directional couplers [127, 147] or phase shifters [148].

A detailed revision of the state-of-the-art of SWG devices in silicon photonics can be found in the many different reviews about the topic [149–153].

1.3. Goals and contributions of this Thesis

The main objective of this Thesis is to make progress towards the use of subwavelength grating metamaterials in both a fundamental and an applied level. On the fundamental level, novel SWG metamaterial topologies to achieve enhanced control over metamaterial anisotropy, implement gradual refractive index profiles, and increase feature sizes facilitating the device fabrication have been proposed and validated. On the application level, these novel topologies are leveraged to demonstrate high-performance devices, including beam splitters and polarization splitters and beam expanders. Finally, based on the developed experience, a set of universal modelling and simulation techniques that can dramatically accelerate the development of novel metamaterial-based devices are established. A description of the proposed SWG topologies and devices is further detailed below.

Two main SWG topologies were used in the literature when this Thesis started in 2017, longitudinal (Fig. 1.11a) and transversal SWGs (Fig. 1.11c). As discussed in section 1.2, these

Chapter 3: Wave propagation in periodic dielectric structures

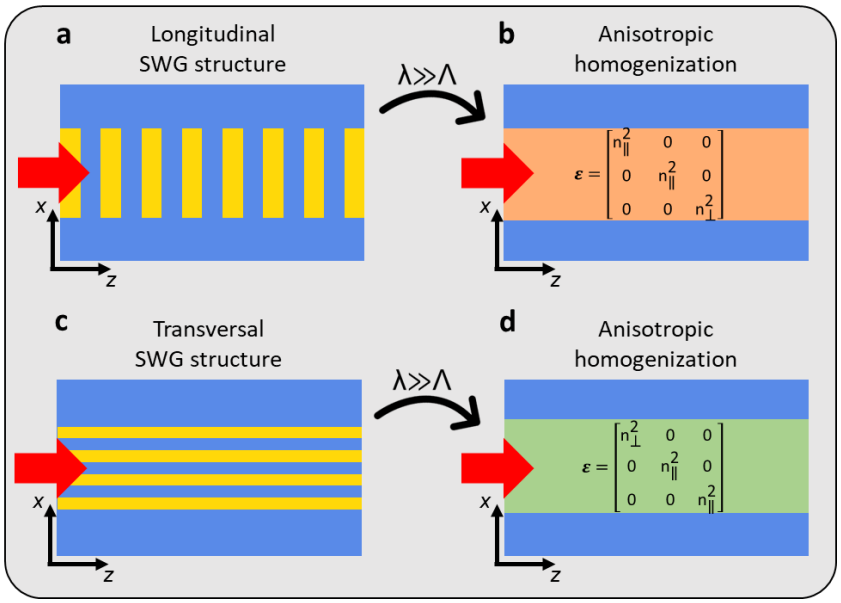

Figure 1.11: Conventional SWG topologies used in the literature, including a) a longitudinal and c) a transversal SWG structure and their equivalent homogeneous anisotropic metamaterials b) and d) respectively, defined by their permittivity tensor components.

SWG structures, known as conventional SWG topologies, have enabled the design of multiple high-performance devices. The first contribution of this Thesis has been to develop a set of homogenization models to predict the behavior in such conventional SWGs. In the invited review paper [153] the developed homogenization models are unified and consolidated, so that they are easier to understand and apply, easing the design of SWG based device. This work also critically analyzes the state-of-the-art on SWG devices in the years 2018 to 2021.

After studying the conventional SWG structures, three novel SWG topologies have been proposed for the first time and experimentally demonstrated to further expand the design space of silicon photonic devices: tilted SWG [154], bricked SWG [155] and duty cycle modulated longitudinal SWG [118]:

- **Tilted SWG structures:** In this SWG topology the silicon segments are tilted at an angle θ (Fig. 1.12a), providing a new degree of freedom to control the light propagation. Specifically, the tilt angle modifies the birefringence as only TE polarized waves are affected by the tilting. This means tilted SWG are ideal to engineer the polarization. The proposal of tilted SWG metamaterials is accompanied by the theoretical background required to predict their behavior and the model to homogenize them. To demonstrate tilted SWG structures in a more applied level, several works leveraging this topology to manage the on-chip polarization, such as the beam splitter shown in Fig. 1.12b, have been carried out in collaboration with the Spanish national research council (*Consejo superior de Investigaciones Científicas*, CSIC) [132, 156–158]. It is important to note that multiple polarization management devices building on our work have been already reported by other research groups [159–161], showing the great versatility of the topology. A patent comprising tilted SWG metamaterials and some of the devices

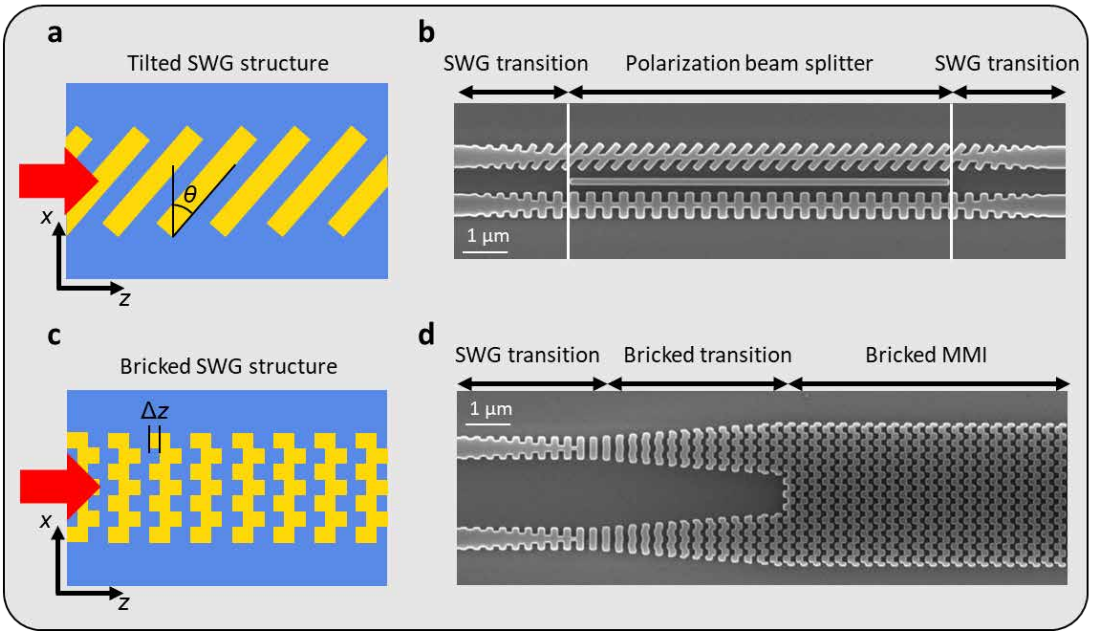

Figure 1.12: Advanced SWG topologies proposed in this Thesis to control the chip birefringence, including, a) tilted and c) bricked SWG structures . b,d) SEM images of the devices using the topologies shown in (a) and (c), including b) a polarization beam splitter and d) a 2×2 multimode interferometer.

arising from its use was published. Tilted SWG metamaterials were patented in the Spanish patent and trademark office, then was internationalized to the European patent office and it is now registered in the US and Singapore patent offices. This topology is discussed in chapter 4.

- **Bricked SWG structures:** In this topology a longitudinal SWG waveguide is periodically partitioned along the transversal direction, alternately shifting the resulting silicon blocks along the longitudinal direction a length Δz (Fig. 1.12e). Similar to tilted SWG, the TE polarization is affected by the shifting but the TM is not. This behavior can be used to design polarization management devices or to decrease the effective index of TE modes, enabling longer periods and thus facilitating the fabrication of this type of structures. This feature has been exploited to design and experimentally demonstrate an ultra-broadband SWG based multimode interferometer (MMI) with the largest reported gap size in the near infrared (Fig. 1.12d) [155]. A model to homogenized bricked SWG metamaterials has been also proposed. The polarization management properties of bricked SWG are being exploited also to design polarization insensitive devices [162]. This SWG topology is also being reused by others research groups for their devices [163]. A patent comprising bricked SWG metamaterials and some of the devices arising from its use was also published. Bricked SWG metamaterials were patented in the Spanish patent and trademark office, and it is currently in the European internationalization step. This topology is discussed in chapter 4.
- **DC-modulated longitudinal SWG structures:** In this SWG topology the duty cycle of a longitudinal SWG is modulated along the transversal direction (see Fig. 1.13a) enabling the implementation of gradual index materials with a single etch step and a CMOS compatible fabrication process. A gradual index (GRIN) lens spot size converter using the longitudinal gradual SWG topology (Fig. 1.13b) [118]. This topology has been also reused by other research groups for their designs of spot size converters [164, 165]. This topology is discussed in chapter 5.

Chapter 5: Gradual Index subwavelength grating metamaterials

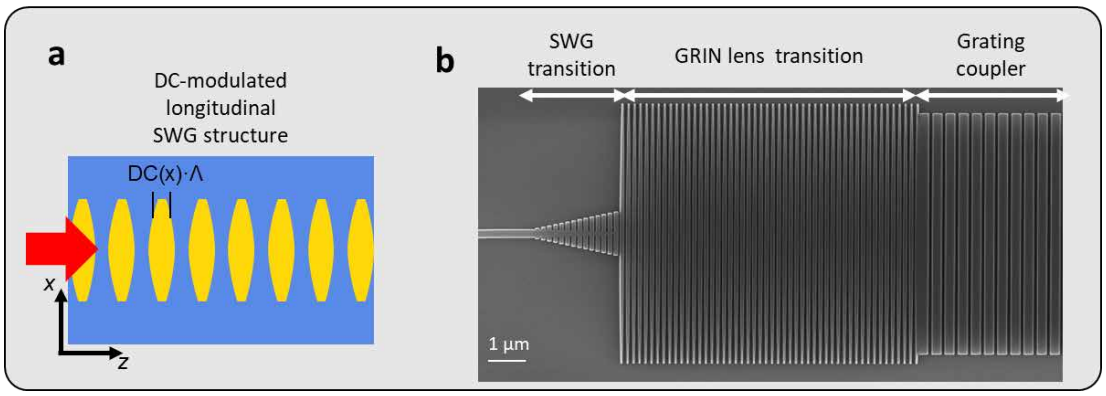

Figure 1.13: a) DC-modulated longitudinal SWG topologies proposed in this Thesis to control implement GRIN metamaterials. b) Spot size converter based proposed topology to adapt the field profile from a 500 nm wide waveguide to a grating coupler

1.4. Organization of this Thesis

This Thesis is organized as follows:

Chapter 1 is the current introduction.

Chapter 2 summarizes the typical workflow followed along the Thesis, describing the steps from the inception of a new idea to the experimental demonstration in the laboratory. This chapter provides an overview of the different electromagnetic simulation tools and procedures used along the Thesis to characterize periodic structures, the steps followed to draw the fabrication masks and a description of the experimental setup used to characterize the fabricated photonic devices.

Chapter 3 provides the theoretical background about the wave propagation along periodic dielectric structures. This study includes the proposal and development of the mathematical models to calculate the homogeneous anisotropic material of conventional SWG metamaterial topologies.

Chapter 4 presents the tilted and bricked SWG topologies. These advanced SWG topologies are both very interesting given the new degree of freedoms that they provide. This chapter also includes the mathematical models to characterize these two topologies and the designs carried out as a part of this Thesis.

Chapter 5 is devoted to the analysis of the longitudinal gradual index topology. This chapter overviews the basic theory about the wave propagation along gradual media, the methodology to include the gradualness on the developed mathematical models and the design and experimental validation of a gradual index lens.

Chapter 6 draws the conclusions and proposes future research lines.

2. From ideas to silicon photonic devices

This chapter outlines the working methods followed in this Thesis to demonstrate novel SWG metamaterial topologies and devices. This analysis is divided in two parts. In section 2.1, the main electromagnetic software tools used to model and simulate photonic devices are described. Special emphasis is placed on the simulation procedures to compute the electromagnetic solutions in periodic media. Then, in section 2.2, the prototyping cycle followed in this Thesis is discussed: from the inception of the idea to its experimental demonstration. This prototyping cycle does not pretend to be a guide or tutorial on the design process of photonic devices but just a panoramic vision on the working methodologies and experimental procedures used along this Thesis. Finally, the main conclusions of the developed process are drawn in section 2.3.

2.1. Modeling and simulation of photonic devices

The modeling and simulation of photonic devices and SWG metamaterials constitutes a fundamental part of this Thesis. Many different simulation software tools have been used in this process depending on the type of structure and the metric under study. This section summarizes the main electromagnetic software tools used along this work and some of the most important simulation procedures developed to analyze SWG periodic structures.

2.1.1. Numerical electromagnetic software tools

FEXEN: The Fourier EXpansion simulation ENvironment (FEXEN) is a 2D electromagnetic simulator developed by researchers at the Photonics & RF Lab of the University of Malaga. It is especially optimized for the simulation of periodic structures [166]. The three main modules of FEXEN used during this Thesis are:

- **Slab mode solver module:** This module computes the electromagnetic mode solutions of 1D dielectric structures (multilayer slabs) invariant along the propagation dimension (also known as longitudinal axis or z-axis). For that purpose, it uses the Fourier Decomposition Method (FDM). This module is mostly an auxiliary tool for the following modules.
- **Propagation module:** The 1D modes calculated using the Slab mode solver module are propagated along any z-variant structure with this module. For that purpose, FEXEN combines the Fourier eigenmode mode expansion (F-EME) and mode matching methods. It is a simple and fast simulation software tool to study the electromagnetic propagation along 1D dielectric structures, but it is limited by the lack of the second transversal dimension.

- **Floquet mode solver module:** The Floquet mode solver computes the electromagnetic mode solution of multilayer slabs with a periodicity along the longitudinal direction. For that purpose, it combines the slab mode solver and the propagation solver module algorithms. It is a powerful software for the mode calculation in 2D periodic structures, but once again it is limited by the lack of the second transversal dimension.

PhotonDesign is a commercial photonics CAD tool with many different products related with the design of photonic devices. In this Thesis, two PhotonDesign modules have been used:

- **FIMMWAVE**: A fully vectorial mode solver for computing the electromagnetic mode solutions in 2D photonic waveguides invariant along the longitudinal direction. It supports many different numerical algorithms to compute the mode solutions (FMM, FDM, FEM) and it allows isotropic, diagonal anisotropic and non-diagonal anisotropic materials. It is a powerful tool for the computation of the modes of z-invariant dielectric waveguides.
- **FIMMPROP**: The modes calculated with FIMMWAVE can be propagated along the concatenation of different z-invariant structures by using FIMMPROP. This software works very similar to FEXEN propagation module, using mode expansion and mode matching methods but with the modes including both transversal dimensions. It is a very powerful tool to study the wave propagation on isotropic and anisotropic photonic devices. However, unlike FEXEN propagation solver, it is not optimized for simulating the wave propagation along certain periodic structures such as SWG waveguides.

Synapsys RSoft is a photonics CAD tool with many different products related with the design of photonic devices. In this Thesis, four RSoft tools have been used:

- **FemSIM**: A fully vectorial mode solver for computing the electromagnetic mode solutions in 2D waveguides invariant along the longitudinal direction. It uses finite element method for the computation. FemSIM is very similar to FIMMWAVE but it does not support anisotropic materials. However, it is interesting to use it as it shares the same simulation framework with other used simulator such as BeamPROP or FullWAVE.
- **BandSOLVE**: A photonic band calculator software suited for the computation of the electromagnetic solutions in 3D periodic structures. It uses a plane wave expansion (PWE) algorithm very similar to the Fourier expansion method used by FEXEN but it supports 3D structures.
- **BeamPROP**: BeamPROP is a 3D simulation software based on the beam propagation method (BPM). It provides accurate results in a very short time, but it only works under the paraxial approximation with the light traveling in the forward direction.
- **FullWAVE**: A 3D finite-difference time-domain (FDTD) simulation method which performs fully vectorial simulations of the electromagnetic propagation through photonic devices composed of isotropic or anisotropic materials. It gives the most accurate possible solution at the expense of a high computational cost.

A summary of the electromagnetic software tools discussed above is shown in Fig. 2.1.

Numerical electromagnetic simulators				
Simulation software	Module	Simulation type	# of dimensions	Use cases
FEXEN	Slab mode solver	Modal (FDM)	1 transversal	▪ Mode calculation in 1D slab waveguides.
	Propagator	Propagation (F-EME)	1 transversal + 1 longitudinal	▪ Wave propagation calculation along 2D structures (3D with EIM).
	Floquet mode solver	Modal (FDM+F-EME)	1 transversal + 1 longitudinal (periodic)	▪ Floquet mode calculation in 2D periodic slabs waveguides (3D with EIM).
Photon design	FIMMWAVE	Modal (FDM/FEM)	2 transversals	▪ Mode calculation in *z*-invariant waveguides and bends composed of isotropic and/or anisotropic materials.
	FIMMPROP	Propagation (EME)	2 transversals + 1 longitudinal	▪ Wave propagation calculation along 3D structures.
Synopsys RSoft	FemSIM	Modal (FEM)	2 transversals	▪ Mode calculation in *z*-invariant waveguides and bends composed of isotropic materials.
	BandSOLVE	Modal (PWE)	2 transversals (periodics) + 1 longitudinal (periodic)	▪ Floquet mode calculation in 3D periodic structures.
	BeamPROP	Propagation (BPM)	2 transversal + 1 longitudinal	▪ Wave propagation along 3D structures under paraxial approximation.
	FullWAVE	Propagation (FDTD)	2 transversal + 1 longitudinal	▪ Wave propagation along 3D structures. ▪ Floquet mode calculation in 3D periodic structures.

Figure 2.1: Summary of the main numerical electromagnetic simulator used along this Thesis for the design of photonic devices. The summary includes a short description on the use cases for each module of each simulator.

2.1.2. Simulation of the mode solutions in SWG periodic structures

The analysis of the electromagnetic solutions in periodic structures has been fundamental in most of the proposed devices. The mode solutions in periodic structures are known as Bloch-Floquet modes and commercial electromagnetic simulators do not typically support their calculation. From the aforementioned electromagnetic modal simulators, only FEXEN and BandSOLVE allows the modal calculation in periodic structures. Many 3D-FDTD simulators such as FullWAVE can be also transformed into modal simulators allowing periodic structures. This section discusses how these software tools have been used to calculate the Bloch-Floquet modes of the SWG structures studied along the Thesis:

- **FEXEN Floquet mode solver module:** As already depicted in the previous section, FEXEN can calculate the mode solutions in periodic structures comprising 1 transversal and 1 longitudinal dimension in a simple and fast way. The simulator gives the effective index and field profile of periodic structures in just a few seconds. The main problem is the lack of the second transversal direction, which can be alleviated by using the effective index method (EIM) [167]. This mathematical tool simplifies 3D dielectric structures into 2D problems, enabling the resolution of 3D SWG periodic structures with 2D simulations. Of course, FEXEN can be also used to study the mode solutions in wide 3D periodic structures, as they can be approximated as 2D periodic structures with an infinite width. Grating couplers are typical devices where this approximation can be done with almost no error, so all the grating couplers used along this Thesis have been designed with FEXEN.
- **BandSOLVE:** Photonic bands calculator such as BandSOLVE are specialized in the resolution of periodic structures, therefore, the calculation of the mode solutions of 3D SWG periodic is possible. However, this kind of simulators are usually oriented to compute the bandgaps of photonic crystals. For this reason, they fix a wavevector, $\vec{k} = k_x\hat{x} + k_y\hat{y} + k_z\hat{z}$ and they calculate the field profile and the wavelength of the

mode solution with this wavevector. Therefore, to calculate the mode solution at a fixed wavelength, an iterative process should be run using different wavevector $\vec{k}$ until the simulation result is the working wavelength. This process usually takes, 3 or 4 simulation steps if the first wavevector guess is close enough to the final result. It is also important to note that BandSOLVE imposes a periodicity in all the directions of the structure, when typical SWG metamaterials are periodic in one or two dimensions. This problem is circumvented by using large simulation windows or the FDTD solver of BandSOLVE which allows PML conditions. Both methods imply longer simulations.

- **FullWAVE:** FDTD software simulators such as FullWAVE usually allow setting periodic conditions between its different opposed boundaries. Periodic boundary conditions emulate the behavior of photonic band solvers such as BandSOLVE, therefore, the modes in periodic structures can be calculated by following the same iterative process used in BandSOLVE but with the periodic boundary condition only set in the desired axes.

FEXEN Floquet mode solver has been used for preliminary/fast simulations of the periodic structures and BandSOLVE/FullWAVE for accurate solutions. The use cases of BandSOLVE and FullWAVE are mostly indistinguishable, but the slightly different interfaces of both software make BandSOLVE more suitable to study periodic structures with the light propagating along different angles, and FullWAVE for mode calculation in photonic devices with a defined propagation direction. The iterative process followed in both cases to calculate the mode solution in periodic structures at specific wavelengths requires some foundations on how the simulator works and scripting, but it provides accurate results.

Another interesting approach to simulate the mode solutions in SWG periodic waveguides is by means of the homogenization process. As it is discussed in chapter 3, SWG structures can be modeled as homogeneous anisotropic materials which can be easily solved by some modal simulators. Therefore, homogenizing the SWG periodic structure and then using a modal solver such as FIMMWAVE is an interesting alternative to calculate the mode solution in SWG periodic structures. The main problem with this method is that homogenization of integrated SWG structures has received little attention in the literature. This Thesis solves this problem by proposing and studying the feasibility of different homogenization models. Therefore, this approach is now fully feasible.

For the sake of illustration, Fig. 2.2 exemplifies the resulting fundamental TE Bloch-Floquet mode of the same SWG waveguide studied in section 1.2, that is, a 1 µm wide and 220 nm thick SWG waveguide with a period of 100 nm and a 50% duty cycle. This waveguide is solved by using the three proposed approaches. i) FEXEN, ii) FullWAVE/BandSOLVE and iii) FIMMWAVE. To use FEXEN, the effective index method is used first, obtaining in a periodic slab (see Fig. 2.2a). This slab can be understood as the top view of the SWG waveguide under study where the vertical confinement has been taken into account by reducing the refractive index of the core from $n_{\mathrm{Si}} = 3.476$ to $n_{\mathrm{SiEIM}} = 2.84$. The mode field profile and the effective index of this structure are shown in Fig. 2.2d. The calculation of this mode with FEXEN is quite straightforward as FEXEN is optimized for periodic structure, so the simulation assuming a 10 nm mesh in both directions has been performed in ~3 sec. The training time to solve this kind of problems with FEXEN is also short as the software allow it directly in his basic interface. Then, the same structure is analyzed by using FullWAVE, which solves the 3D periodic structure. The mode field profile and the effective index of this structure are shown

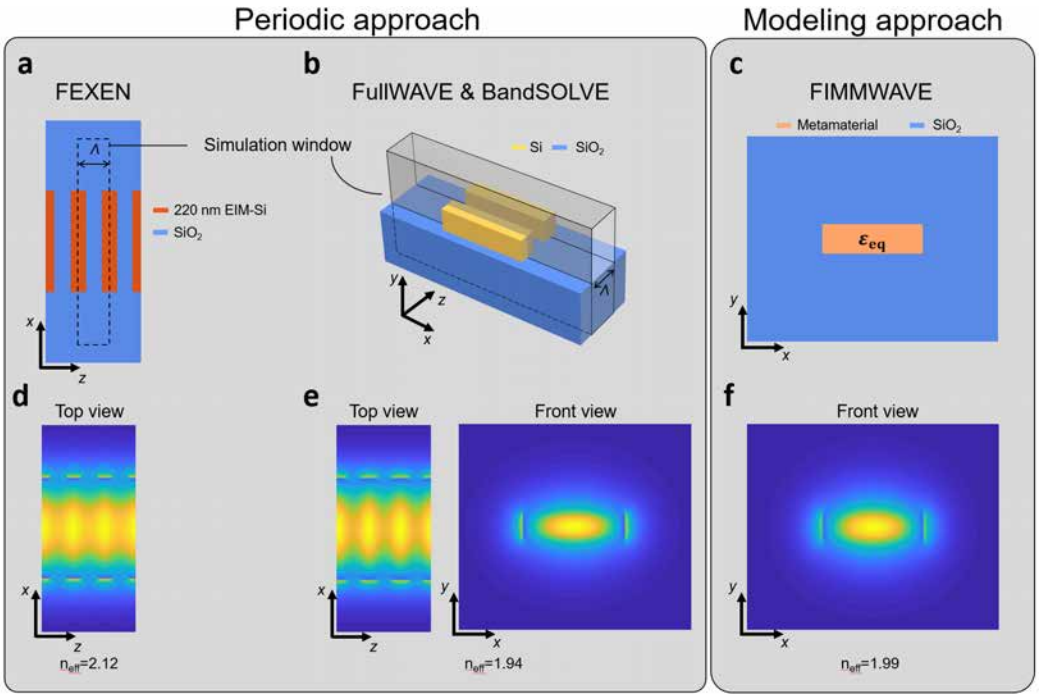

Figure 2.2: Three main alternatives used in this Thesis to solve the mode solutions in SWG structures by using a) FEXEN, b) FullWAVE/BandSOLVE c) FIMMWAVE. Fundamental TE mode of a 1 µm wide and 220 nm thick SWG waveguide with a period of 100 nm and a 50% duty cycle at $\lambda_0 = 1.55$ µm solved by using d) FEXEN e) FullWAVE/BandSOLVE, f) and FIMMWAVE.

in Fig. 2.2e. This calculation is quite more difficult to perform, as it needs some knowledge on simulation theory and it is also more time consuming, requiring about 10 minutes with the same 10 nm mesh. Finally, the structure is solved by using the homogenization approach. The SWG metamaterial is homogenized as an anisotropic metamaterial defined by its permittivity tensor $\varepsilon_{eq} = \text{diag}[2.66^2, 2.66^2, 1.88^2]$. The resulting structure is a simple waveguide but with an anisotropic core, requiring a mode solver allowing this kind of materials such as FIMMWAVE. The simulation time in this case has been about 20 second with the same 10 nm mesh grid. These calculations clearly show that: i) FEXEN can be used for quick explorations, allowing fast examination of the behavior of the periodic structures. ii) FIMMWAVE provides accurate results in short times. The homogenization also provides a physical understanding on the physics of the problem. iii) FULLWAVE/BandSOLVE gives the best results but at the expense of a high expertise on simulation techniques and long time consuming process.

2.2. Prototyping cycle of photonic devices on SOI

This section describes the prototyping cycle followed in this Thesis to experimentally demonstrate the proposed SWG topologies and photonic devices. Such a cycle is divided as follows: inception and development of the idea, preliminary design by using homogenization models, device design and refinement, mask layout preparation for the chip fabrication in an external foundry, experimental characterization and data processing and finally results dissemination. A summary diagram of the cycle is shown in Fig. 2.3.

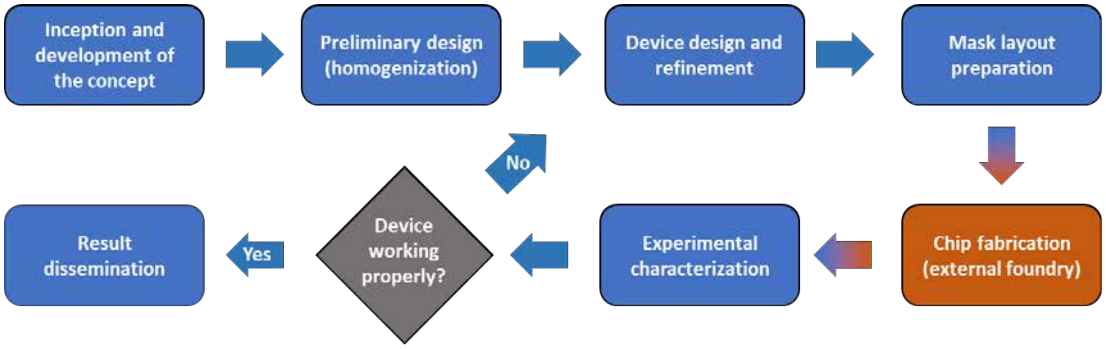

Figure 2.3: Schematic diagram of the prototyping cycle followed in this Thesis.

Inception and development of ideas

The unique optical properties of SWG metamaterials have been used to enhance the performance of many different photonic devices. Year after year, novel ideas still emerge to further improve the performance of silicon photonic devices by using SWG. Some good approaches to finding new design concepts and ideas are:

1. **Research on the foundations of wave propagation through SWG periodic structures:** The wave propagation through periodic structures, and specifically in SWG periodic structures, have been deeply analyzed in the last 50 years. The understanding of this knowledge is essential to propose new SWG optimized devices. Some interesting seminal articles to carefully study the wave propagation in periodic media are found in Refs. [90, 168], where laminar periodic dielectric structures are studied. This theory can be complemented with some reading about the homogenization of SWG structures, a common topic in the field of metasurfaces [169–172]. Finally, it is also highly recommended to study some of the review articles about SWG metamaterials in silicon photonics as they show how SWG engineering is used to optimize photonic devices [149–153]. In this thesis, chapter 3 summarizes most of the required foundations on the wave propagation in SWG structures.
2. **Choose an SWG metamaterial property to exploit:** The optical properties of SWG metamaterials such as refractive index, anisotropy or dispersion can be engineered by tuning the geometry of the periodic structure. Refractive index engineering provides control over the phase matching and field profiles, anisotropy/birefringence engineering controls the polarization behavior of the material and dispersion engineering can enlarge the operational bandwidth. Choosing specific properties to engineer can lead to the proposal of new devices.
3. **Choose a device to optimize:** Current silicon photonics technologies address many light handling functionalities, including power splitting, polarization management, wavelength or mode (de-)multiplexing, filtering, etc. A myriad of devices performing these functionalities have been optimized by using SWG metamaterials, but new approaches can still emerge. By choosing a specific device to optimize gives a starting point. Typically, this device is studied, theoretically or with simulations, to analyze how its performance can be enhanced knowing what material properties can be tailored. From this analysis, a possible idea to use SWG could emerge.

FEXEN is an auspicious simulator software tool in this stage as it provides fast results which predicts most of the phenomena related with the wave propagating through SWG metamaterials. This stage ends when an interesting idea to use the SWG metamaterial finally arises.

Preliminary design with homogenization model

The second step of the prototyping cycle is the modeling of the periodic SWG structures as a homogeneous anisotropic metamaterial. This process reduces the complexity of the problem as homogeneous mode solvers are much simpler and more time efficient than periodic mode solver. Moreover, the homogenization also provides the intuition about how the structure is working. FIMMWAVE and FIMMPROP enable the mode calculation and propagation in the resulting homogenized structures, yielding preliminary designs very close to the final design but in much less computation time. To be able to perform this step, a set of homogenization models which accurately predicts the behavior of the different SWG structures are required. For this reason, in this Thesis various homogenization models of SWG are demonstrated and every SWG metamaterial topology proposed is accompanied by its own homogenization model.

Device design and refinement

The design process of photonic devices frequently requires time consuming numerical electromagnetic simulations to optimize their performance. The preliminary design performed with the homogeneous model potentially saves much time by providing geometrical parameters close to the optimum values. Knowing about different simulator software tools can also save a lot of time, by choosing the right simulator for each scenario, and money, by reducing the necessary fabrication steps. To mention some examples, MMIs and directional coupler can be almost entirely designed with fast FIMMPROP simulations, long adiabatic tapers with BeamPROP, bends with FIMMWAVE/FEMSIM and grating couplers with FEXEN. In any case, the final device is always double-checked by using 3D-FDTD simulations of the full structure with FullWAVE. These are time domain simulations with a broadband temporal source covering the device bandwidth. Each simulation of the full device requires from 1 to 20 hours depending on its size.

The design and refinement step does not only consider the first device design, but it is also the step where the prototyping cycle resets if a fabricated device does not work properly. The measured data are carefully studied, mostly with electromagnetic simulations emulating different fabrication imperfections, to find out the reason for the device malfunction. Then, the device is corrected taking into account the inferred conclusions and the prototyping cycle continues.

Mask layout preparation

The proposed photonic devices have been fabricated in commercial foundries as this Thesis has been developed in a fabless research group. Specifically, Applied Nanotools (ANT) is the

commercial foundry used in most of the proposed devices [173]. ANT schedules a multi-project wafer (MPW) fabrication run of SOI chips every two months, with a delivery time of 2-3 months. They offer 9 mm x 9 mm chips fabricated in a 220 nm thick silicon layer over a 2 µm silicon dioxide buried oxide (BOX), optionally covered by a silicon dioxide upper cladding. The chips are fabricated with e-beam lithography and the minimum feature size reported by the foundry is 60 nm, which is enough for our SWG designs. To fabricate the chips, a mask layout defining the devices must be drawn and submitted to the foundry previous to the deadline of each MPW run, including not only the proposed photonic devices but also all the auxiliary elements required to measure their performance (light coupling devices, testing devices). The chip drawing is a very important step and it should be carefully done. This section summarizes the typical questions addressed in this Thesis to draw the masks.

1. **How is the light coupled into the chip?** The mismatching between the size of the modes in optical fibers, with a mode diameter about 10 µm and the modes in typical SOI waveguides, with mode field diameters about 1 µm makes the light coupling into the chip a non-trivial problem. There are two typical methods in SOI to inject the light into the chip: surface grating couplers and edge couplers.

    - **Grating couplers:** A simple way to get the light in/out of a chip is by using a surface grating coupler and a fiber optics placed above of the grating. Grating couplers are diffractive devices which radiate/collect light beams (see Fig. 2.4a and Fig.2.4b). Grating couplers are highly polarization sensitive devices and their main advantages are the chip area efficiency, the freedom to place them at any point of the chip and their tolerance to misalignment errors. The main drawbacks are the moderate efficiency and its narrow bandwidth. An exemplary grating coupler drawn in the mask layout is shown in Fig. 2.4c, including the transition

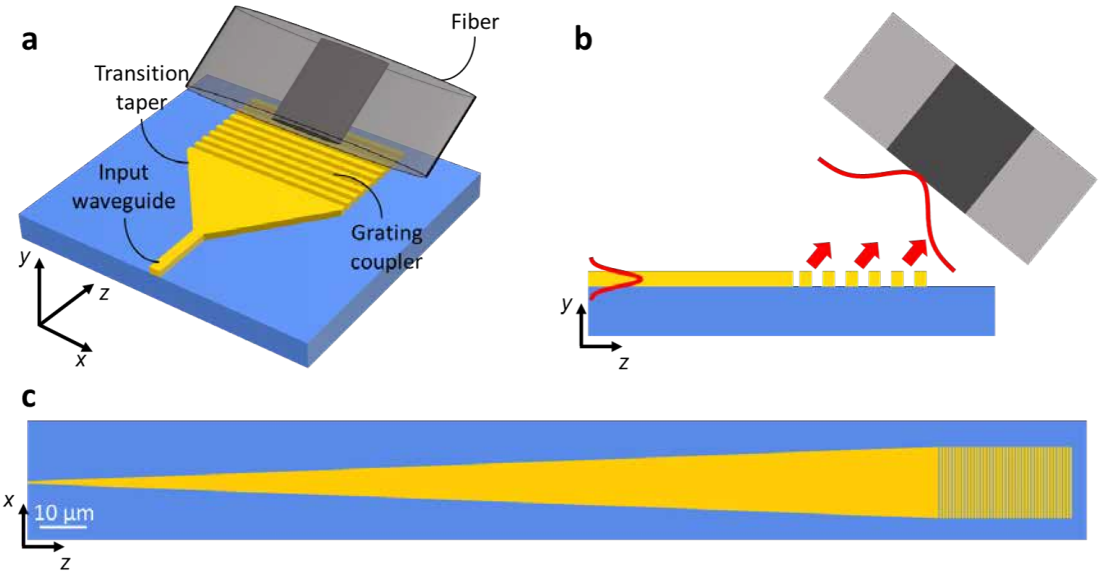

Figure 2.4: a) 3D-view and b) 2D lateral view of the of a grating coupler device. The periodic structure is working in the radiation regime, so it radiates the light upward being collected by a fiber placed with the radiation angle of the grating. c) Exemplary drawing in the mask layout of a grating coupler and its corresponding transition taper.

taper to adapt the field profile coming from the interconnecting waveguide.

- **Edge couplers:** Another way to get the light in/out of the chip is by placing a fiber at the chip facet in front of a chip waveguide. However, because of the size mismatching between modes in SOI waveguides, edge couplers are used to adiabatically transform the light confined into the chip waveguides into expanded beams with a spot size similar to the optical fibers placed in the chip facet (see Fig. 2.5a and Fig.2.5b). Edge couplers exhibit reduced polarization dependent loss and their main advantages are their ultra-low coupling loss and large bandwidths. The main drawback of edge couplers is the low area efficiency, as the amount of devices which can be measured in a chip by using edge couplers is limited by the separation of the edge couplers which should be at least 20-30 µm to avoid cross-talk between adjacent edge couplers. An exemplary grating coupler drawn in the mask layout is shown in Fig. 2.5c.

In this Thesis, both types of couplers have been used, with edge couplers predominating when measuring high bandwidth devices and grating couplers when high polarization extinction ratios are required.

2. **What calibration devices are included in the mask?** Reliable experimental results are fundamental when working in almost any research topic, and the accurate experimental characterization of photonic devices is arguably a complex problem. A good set of calibration devices integrated in the chips helps to accurately measure the performance of the fabricated devices, thus they are always included in the chips. Some typical calibration parameters are setup loss, propagation losses, grating/edge coupler loss, polarization extinction ratio or bending loss. Calibration devices also help with the alignment process, therefore, it is highly recommended to add reference calibration waveguides every 200-300 µm to ease the experimental characterization.

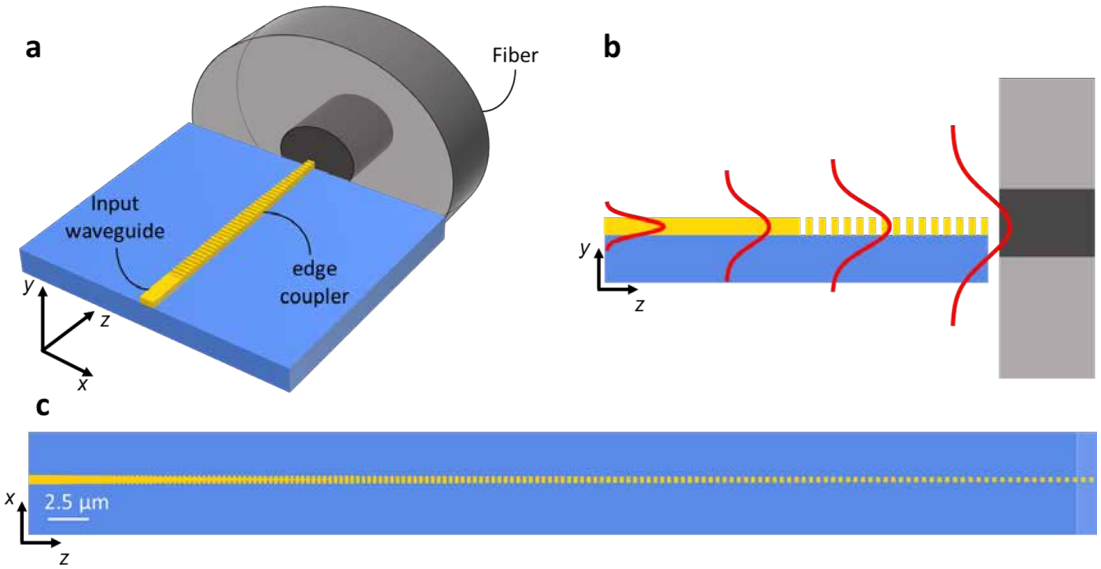

Figure 2.5: a) 3D-view and b) 2D lateral view of the of an edge coupler device. The periodic structure is working in the subwavelength regime, so it behaves as a homogeneous metamaterial delocalizing the field profile to match with the fiber placed in the chip facet. c) Exemplary drawing in the mask layout of an edge coupler.

3. **Which configurations measures the DUT performance?** The performance of photonic devices is measured in many different metrics such as excess loss, imbalance, extinction ratio, phase error or cross-talk, among many others. Specific configurations such as cut-back, back-to-back or Mach-Zehnder interferometers configurations are required to measure these parameters. The metrics of the device under test are obtained from the systemic models derived from the specific configuration. The simplest way to choose the required configuration is to imitate those found in the literature used for similar purposes.
4. **What fabrication compensations are applied?** Fabrication errors are expected when fabricating photonic devices. The most typical errors are the under-etching or over-etching of the silicon segments. These errors are especially important in SWG devices as their width and duty cycle are affected. To compensate them, the designed devices are replicated, slightly widening or narrowing the silicon segments to compensate the over/under-etching. These replicas are commonly known as flavors. Some simulations assuming typical deviations are performed previous to the fabrication to predict typical deviations on the device response, thus helping to choose the fabricated flavors. A typical procedure along this Thesis has been to fabricate the SWG devices with their nominal dimensions, 20 nm wider and 20 nm narrower, triplicating the required chip area. Moreover, some device flavors shortening/enlarging the device length are also typically fabricated.
5. **What SEM images are taken?** Prior to the deposition of the silicon dioxide cladding, the foundry can optionally take some SEM images of the fabricated devices. A good set of SEM images helps to quantify the fabrication error which can be fundamental to understand the measurements of the devices. Therefore, a good procedure here is to take some SEM images of the most critical parts of the devices.

After taking these decisions, the fabrication mask with the proposed devices is drawn. There are many different options to generate the mask, such as directly drawing by using AutoCAD® software, use commercial/open-source software tools as Nazca or by using in-house scripts. In this Thesis a set of in-house codes running on Visual Basic have been used to draw the gds file on AutoCAD®. These codes are object-oriented programs where some typical structures are already defined as classes, including waveguides, periodic waveguides, bends, tapers, etc. However, the specific SWG devices developed along this Thesis have to be programmed, including the tilted and bricked SWG topologies and the gradual SWG metamaterial overviewed described in chapters 4 and 5 respectively. After the required classes are programmed, the main code including the specific devices, flavours, configuration and testing device are programmed. This process has to be done very carefully as any little error can ruin the whole mask. Therefore, the mask layout has to be revised thoroughly while developing the mask and once again when it is complete. It is mandatory to check the layer labeling rules of the foundry to ensure that the devices are fabricated in the correct layer. An example of a fabrication mask drawn with this method is shown in Fig. 2.6. This mask includes edge couplers and grating couplers. Note that all the devices in the mask have the same color as they all are in same layer (silicon layer). Once the mask is ready, it is submitted to the foundry and it is time to wait until the chip is fabricated and received.

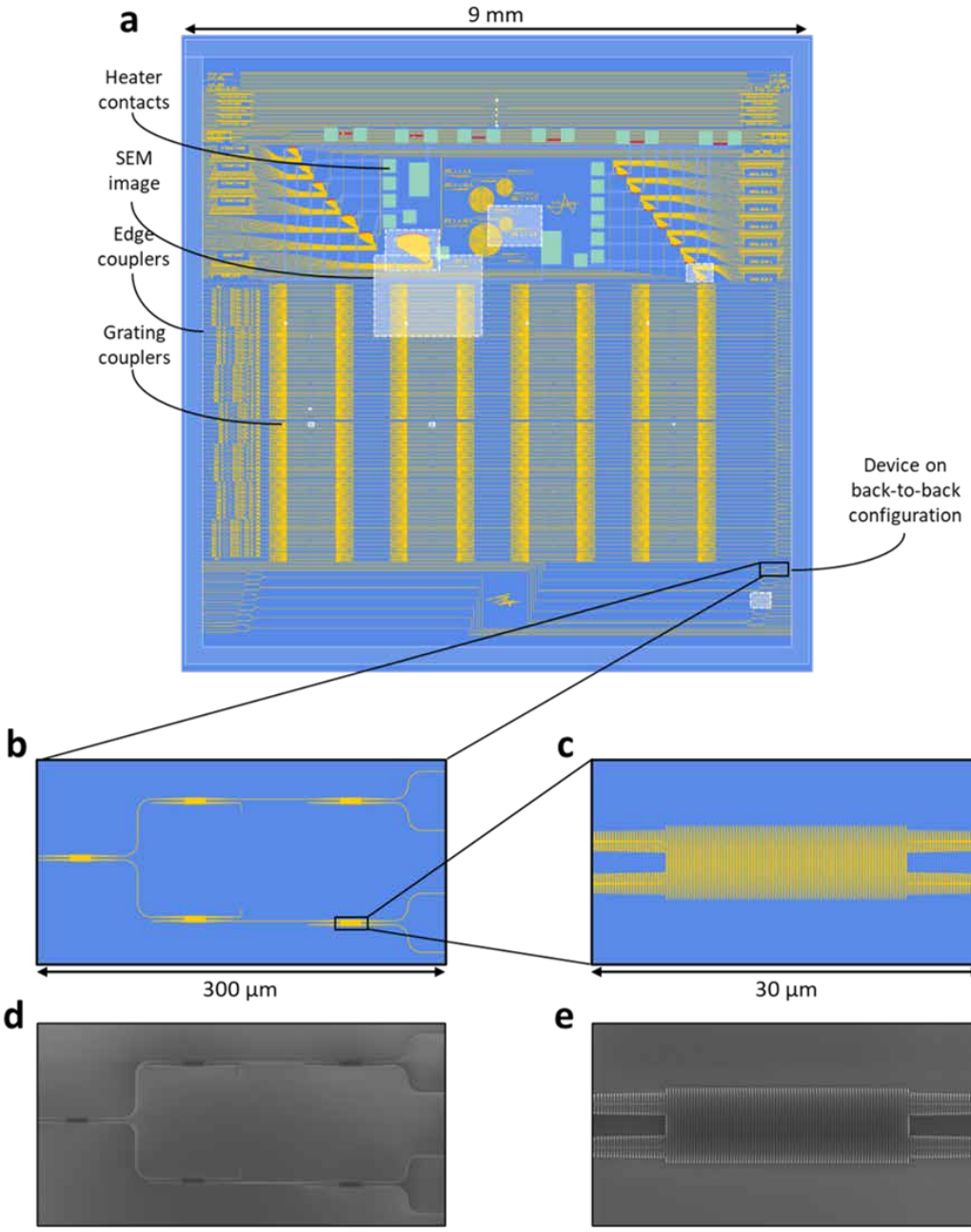

Figure 2.6: a) Exemplary mask layout. The yellow/blue colors represent the written and non-written areas. The green/red colors indicate the heater contacts and heater metals. The white color set the SEM image areas. b) Zoom in into a back-to-back configuration of a device under test. c) Zoom in into a device under test in the configuration shown in (b). d,e) SEM image of the mask layout zooms shown in (b) and (c) respectively.

Experimental characterization

The experimental characterization of photonic devices is the final stage of the prototyping cycle followed in this Thesis. This section discusses the steps followed to characterize the performance of the SWG photonic devices.

1. **SEM examination:** The foundry typically sends the taken SEM images some weeks before the chip reception. These images are carefully examined to estimate the fabrication deviations. Two exemplary SEM images superposed to the mask layout (yellow lines) are shown in Fig. 2.7. The minimum feature size in Fig. 2.7a is 100 nm, much longer than the 60 nm feasible by the fabrication process, so the structure is well fabricated. The minimum feature size in Fig. 2.7b is around 45 nm, so the structure exhibits significant fabrication errors. The performance of the device with the estimated error is carefully studied by means of electromagnetic simulations to try to predict the behavior of the fabricated devices.

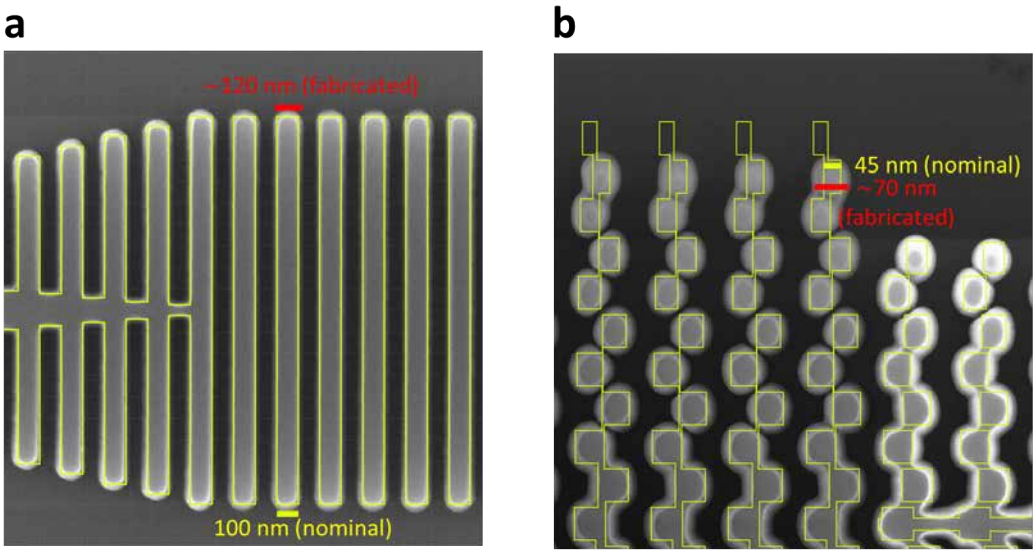

Figure 2.7: a,b) SEM image of a) a simple and b) a complex SWG waveguide superposed with the fabrication mask layout in that region (yellow line).

2. **Experimental characterization:** The majority of the photonic devices presented in this Thesis have been measured in the laboratories of the Malaga University. The experimental setup is divided in three differentiated stages: i) The input stage, where the light is guided from the laser to the chip. ii) The chip stage, in charge of coupling light into and out of the chip. iii) The output stage, collecting the output light onto a power meter. Depending on the coupling scheme used in the device under test (grating coupling or edge coupling) the chip stage changes, requiring fibers placed on top of the chip or at the chip facets. The input/output stage could be independent of the chip stage, but in the setup used in this Thesis, the output stage changes while the input is the same in both cases.

    a) **Input stage:** A tunable laser (Agilent 81600B) injects the light into a conventional SMF-28 fiber. A polarization controller is then used to align the almost linearly polarized output light of the laser with a well characterized linear polarization filter. The output of the linear polarization filter is then connected with another SMF-28 fiber which guides the light to another polarization controller which aligns the polarization of the fiber with the on-chip polarization. This SMF-28 is connected to an optical circulator whose outputs are a fiber injecting the light into the chip and a photodiode to measure the reflections coming from the chip. (See Fig. 2.8).

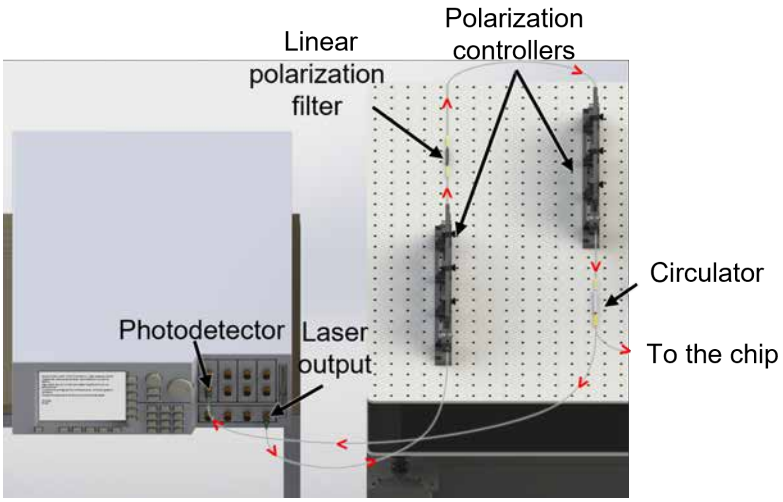

Figure 2.8: 3D Modeling of the input stage used to get the light from the laser to the chip stage.

b) **Chip stage:** The chip stage depends on the coupling scheme used in the DUT. In grating coupling, the fiber coming from the circulator is mounted on a goniometer to inject the light into the chip with the radiation angle of the grating. Another optical fiber mounted on a second goniometer get the light out of the chip (Fig. 2.9a). In edge coupling, a lens fiber coming from the circulator at the input stage is placed on the facet while a microscope objective is placed at the output chip facet to collect the light (Fig. 2.9b).

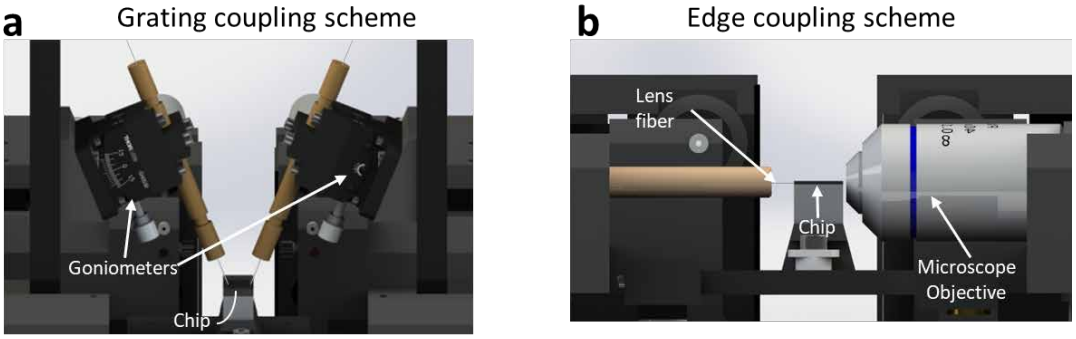

Figure 2.9: 3D Modeling of the two stages used to inject the light into the chips, including the a)grating coupling scheme and b) edge coupling scheme.

c) **Output stage:** The output stage used in this Thesis depends on the light coupling scheme. In grating coupling, the output light from the chip is injected in a fiber which is directly connected to a power meter connected to the PC. In edge coupling, a free space setup is used. The output light from the chip is collimated by the microscope objective, focusing the light beam through a Glan-Thompson polarizer and then onto a photodetector (818-IR). A folding mirror can be used to focus the light into a camera. This second case is shown in Fig. 2.10b.

By using the corresponding setup, the calibration devices are first measured to verify light guiding in basic structures. Propagation loss of the waveguides, insertion loss of

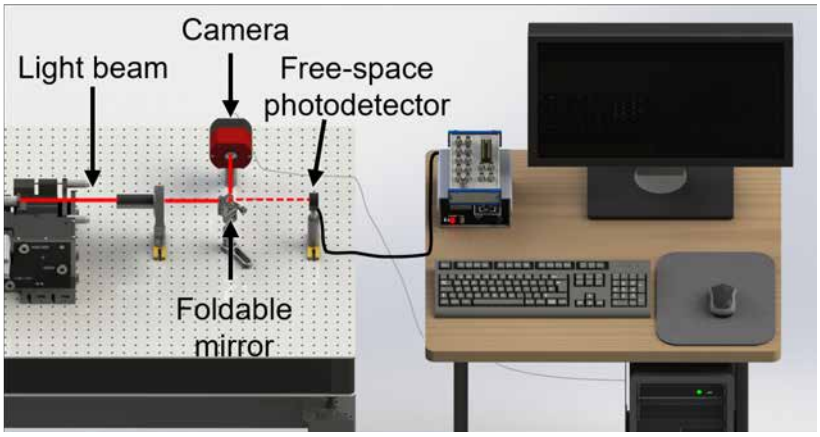

Figure 2.10: 3D Modeling of the output stage to measure the light from the chip in the case of the edge coupling setup.

the grating/edge coupler and bending couplers are typical characterized. Then, the different DUTs are characterized by using the corresponding setup for each device. The measured power is stored in the computer for future processing of the data.

3. **Processing of the measured data:** The measured data are processed to extract the performance of the fabricated devices. While some data processing algorithms are general from almost any measurement, many others are device specific. In this section some of the methods used along this Thesis to process the measured data are discussed:

   - **Power referencing:** This is arguably the simplest and most usual algorithm to process the data. The measured power in the DUT is referenced (divided) by the measured power in a reference circuit. The reference circuit must be as equal as possible to the DUT circuit but without the DUT. This algorithm provide the power loss introduced by your DUT.

   - **Cut-back algorithm:** A usual method to measure the insertion loss of low-loss devices is the cut-back configuration. A set of independent circuits with the DUT replicated a different number of times are measured. By interpolating the different measurement, the insertion loss per device is easily and accurately obtained. The same methodology is applied to calculate the propagation loss in straight waveguides, where the replication is done by using different lengths.

   - **Minimum phase algorithm:** A typical problem when measuring photonic chips is the formation of microcavities in between different interfaces, such as for example the cavity formed by the Fresnel reflections when the light is injected in and out of the chip by the chip facets or the microcavity formed for the reflections at the input of the grating couplers, etc. These cavities perturb the measurement of the DUT by adding additional oscillations. The minimum phase algorithms [174] characterize, under certain assumptions, the different cavities found on the measurement data and to cancel them, cleaning the data from the perturbation to obtain the device response. There are two main differences between the minimum phase algorithm and a simple smooth of the curve: 1) The minimum phase algorithms gives a reflectogram, identifying the reflections coming from the device and those that not. 2) The minimum phase algorithms can be used to

cancel specific oscillations, similar to a band suppression filter.

- **Mach-Zehnder interferogram analysis:** MZIs are well-known devices in optics whose output is governed by the phase delay difference between the light traveling along its two arms. By placing the DUT in the arms of the MZI and measuring the output power spectra multiple parameters can be deduced such as the effective/group indices or the phase delay.

By using these processing algorithms, the measured data from the fabricated devices along the Thesis have been analyzed, obtaining the different results shown along this document. If the processing data matches the expected results, the prototyping cycle moves into his final step where the results are disseminated. If they not, the measured data should be properly analyzed to find the problem, getting back to the design and refinement step of the prototyping cycle.

Results dissemination

After the successfully experimental characterization of the proposed devices, the dissemination of the results is a fundamental step in research. For each successful device, in this Thesis it has been sought to publish at least one journal publication and one or two conferences to help disseminating the results. As the last part of this Thesis has been carried out during the COVID pandemic, some of these conferences have been virtual. The results dissemination has been accompanied in some cases with the publication of a patent.

2.3. Conclusions

In this chapter, the main electromagnetic software tools used along the Thesis have been discussed. The electromagnetic simulation of the modes in SWG periodic structures is a non-trivial problem as most of the software tools do not support it. The three alternatives to perform such a calculation have been presented contextualizing the use cases of each of them. On the other hand, the prototyping cycle to design photonic devices followed along this Thesis has been discussed; the main novelty here is the homogenization step when designing SWG devices to reduce the computational complexity of the designs. The discussion of the prototyping cycle has been also useful to introduce some interesting topic such as how the fabrication layout mask has been drawn, what is the experimental setup and how the measured data have been processed. In short, this chapter have helped to contextualize the workflow followed along the different designs performed along this Thesis.

3. Wave propagation in periodic dielectric structures

Periodic dielectric structures are a fundamental building block in integrated photonics, enabling the implementation of optical metamaterials, reflectors or antennas depending on the wavelength to period ratio. This Thesis mainly focuses on the first situation, dielectric periodic structures working as non-resonant optical metamaterials, known as subwavelength grating (SWG) metamaterials. These structures have tailorable optical properties so they are ideal for the design of photonic devices, especially in fabrication platforms limited by the amount of different materials such as SOI as they circumvent the restriction on the available refractive indices, enabling the optimization of device performance.

This chapter thoughtfully studies the foundations on wave propagation in dielectric periodic structures. It starts by setting the basic theoretical background of waves propagating along periodic structures in section 3.1. This theory is then applied to the simplest periodic structure, the laminar periodic structure in section 3.2, deriving multiple interesting conclusions about periodic structures working as homogeneous materials. The developed knowledge is then applied to study silicon photonics scenarios in section 3.3, proposing different homogenization models to calculate the metamaterial which mimics the behavior of the periodic structure. Finally, the chapter ends by summarizing the most important conclusions in section 3.4.

3.1. Wave propagation in periodic media and homogenization theory

The interesting phenomena related to light propagation through periodic structures captivated to the scientific community even before the light was consider a wave [175]. Gaston Floquet [176], Lord Rayleigh [177] or Felix Bloch [178], among many others scientists set the foundations on wave propagation in periodic structures. They used different approaches, notations and even different languages in their studies, explaining why still nowadays the nomenclature in this topic is often confusing. They obtained that the general solution of a monochromatic electromagnetic wave propagating along a periodic medium is given by:

$$\vec{E}(\vec{r}) = \vec{E}_{\mathrm{F}}(\vec{r}) e^{-j\vec{k}\cdot\vec{r}}. \tag{3.1}$$

where $\vec{E}_{\mathrm{F}}(\vec{r})$ and $\vec{k}$ are the periodic field profile and the wavevector of the wave. The Bloch-Floquet theorem claims that the periodic field profile, $\vec{E}_{\mathrm{F}}(\vec{r})$, has the same periodicity as the structure [179]. This simple statement has many interesting consequences which are discussed along this chapter. For this purpose, a unidimensional periodicity, Λ, along the longitudinal z-axis and a Cartesian coordinate system is assumed $\vec{r} = x\hat{x} + y\hat{y} + z\hat{z}$. Moreover,

propagation along the vertical y-axis is omitted ($\vec{k} = k_x\hat{x} + k_z\hat{z}$) as this Thesis focuses on planar guided devices. In this situation, Eq. (3.1) can be rewritten in the Fourier domain as a sum of weighted complex exponential functions:

$$\vec{E}(x,y.z) = \underbrace{\left[\sum_{m=-\infty}^{\infty} \vec{E}_{F,m}(x,y)e^{-j\frac{2\pi}{\Lambda}mz}\right]}_{\text{Fourier series of } \vec{E}_{\mathrm{F}}(x,y,z)} e^{-j(k_x x + k_z z)}. \tag{3.2}$$

where both exponential can be combined as:

$$\vec{E}(x,y.z) = \sum_{m=-\infty}^{\infty} \vec{E}_{F,m}(x,y)e^{-j(k_x x + (k_z + \frac{2\pi}{\Lambda}m)z)} = \sum_{m=-\infty}^{\infty} \vec{E}_{F,m}(x,y)e^{-j\vec{k}_{\mathrm{F},m}\vec{r}} \tag{3.3}$$

This new expression decomposes the solution of a wave propagating along a periodic structure as the summation of infinite plane waves, $\vec{E}_{F,m}(x,y)$, usually called harmonics, each with a wavevector $\vec{k}_{\mathrm{F},m} = k_x\hat{x} + (k_z + \frac{2\pi}{\Lambda}m)\hat{z}$. The behavior of multiple devices, such as grating couplers [180] or contradirectional couplers [181], arise from the decomposition of the field profile in multiple harmonics. However, the implementation of homogeneous metamaterials with desirable optical properties comes from the opposite situation. That is, when only the fundamental harmonic of the Fourier decomposition stands, $m = 0$. In this situation, the wave propagates as:

$$\vec{E}(x,y.z) \approx \vec{E}_0(x,y)e^{-j\vec{k}_{\mathrm{F},0}\vec{r}}. \tag{3.4}$$

This equation is the wave solution in a z-periodic medium if only the fundamental harmonic stands, but it is also the wave solution in a z-invariant medium. That is to say, both problems have the same electromagnetic solution, they are equivalent problems. Intuitively, this situation is achieved when the waves traveling along the periodic structure do not appreciate the division of the structure in different materials. For that purpose, the wavelength of the propagating wave must be much larger than period of the structure, $\lambda \gg \Lambda$. This condition is often known as the long wave or deep subwavelength regime. An example of the wave propagation along a periodic SWG waveguide in the long wave regime and its corresponding equivalent metamaterial was shown in Fig. 1.7. A deep understanding on the foundations of this equivalence potentially opens new designs approaches to design photonics devices. For that purpose, this chapters aims to answer the following questions:

1. Under what circumstances does a periodic structure behave as a homogeneous metamaterial?
2. How is the equivalent homogeneous metamaterial of a periodic structure calculated?
3. Is the homogenization an exact equivalence or just an approximation?
4. How are the optical properties of the synthesized material engineered?

To answer these questions the simplest periodic dielectric structure is analyzed in detail, the laminar periodic structure (LPS). This study provides physical insight into the wave propagation along a periodic structure with a simple mathematics.

3.2. Laminar periodic structures

A laminar periodic structure is composed of a set of transversely infinite lossless dielectric laminae arranged with a periodicity Λ (see Fig. 3.1). The laminae have refractive indices n_1 and n_2, and lengths a and b respectively and the length of each material per period is frequently given with the duty cycle, defined as the amount of the n_1 material in a period: DC $= a/\Lambda$. From the Bloch-Floquet theorem, Eq. (3.1), the wave solution of a monochromatic plane wave propagating along any direction of the x-z plane of the LPS is derived as:

$$\vec{E}(x,z) = \vec{E}_F(z)e^{-j(k_x x + k_z z)}. \tag{3.5}$$

Analytic formulae for both the periodic wave profile, $\vec{E}_F(z)$, and the wavevector, $\vec{k}$, were derived by Yeh et al in 1976 [168]. For that purpose, Yeh assumed that the electric field within each homogeneous layer can be expressed as a sum of an incident and a reflected plane wave propagating along the periodic structure:

$$\vec{E}(x,z) = \vec{E}_F(z)e^{-jk_z z}e^{-jk_x x} = [\underbrace{\vec{a}_m^i e^{-jk_{iz}(z-m\Lambda)}}_{\text{Forward}} + \underbrace{\vec{b}_m^i e^{jk_{iz}(z-m\Lambda)}}_{\text{Backward}}]e^{-jk_x x} \tag{3.6}$$

were $\vec{a}_m^i$ and $\vec{b}_m^i$ denotes the complex amplitudes of such forward and backward waves in the i-th material of the m-th period. By properly solving the values of such amplitudes, the wavevector equation of any plane wave propagating through an LPS is obtained [168]:

$$\cos(k_z\Lambda) = \cos(k_{1z}a)\cos(k_{2z}b) - \Delta\sin(k_{1z}a)\sin(k_{2z}b), \tag{3.7}$$

where $k_{iz} = \sqrt{(k_0 n_i)^2 - k_x^2}$, $k_0 = 2\pi/\lambda_0$, with λ_0 being the wavelength of the propagating wave in the vacuum and Δ is a polarization-dependent factor:

$$\Delta_{\text{TE}} = \frac{1}{2}\left(\frac{n_2^2}{n_1^2}\frac{k_{1z}}{k_{2z}} + \frac{n_1^2}{n_2^2}\frac{k_{2z}}{k_{1z}}\right) \text{ and } \Delta_{\text{TM}} = \frac{1}{2}\left(\frac{k_{1z}}{k_{2z}} + \frac{k_{2z}}{k_{1z}}\right), \tag{3.8}$$

defining as TE polarization the waves with electric field polarized in the x-z plane, and TM polarization as the y-polarized waves. The effective index of the wave is calculated with Eq.

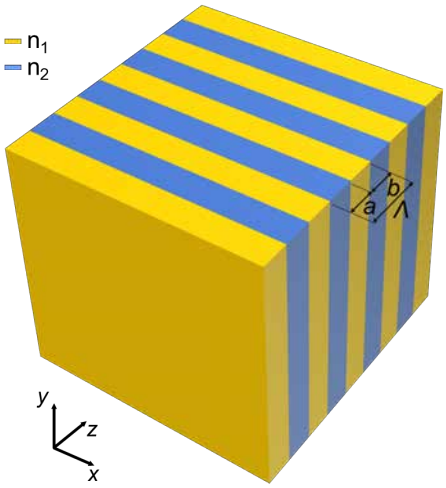

Figure 3.1: Schematic representation of a laminar periodic structure composed by the periodic concatenation of infinitely wide and high dielectric laminae.

(3.7) as the wavevector is normalized by wavevector in the vacuum: $n_{\text{eff}} = |\vec{k}|/k_0$. Equations (3.6) and (3.7) are thoroughly analyzed to study the wave propagation along the LPS.

3.2.1. Wave propagation through LPS

This section thoroughly studies the field propagation along the LPS. For this purpose, the wave propagation along the periodic direction (z-axis), along the non-periodic direction (x-axis) and along any arbitrary direction in the x-z plane is studied. In each case, the analysis focuses on the behavior of the structure for different periods, seeking under what condition the structure behaves as a homogeneous structure. In these analyses the following typical SOI parameters are assumed unless specified otherwise:

1. The refractive indices of the laminae are set to $n_1 = n_{\text{Si}} = 3.476$ and $n_2 = n_{\text{SiO}_2} = 1.444$.
2. The length of both laminae is assumed equal $a = b \rightarrow \text{DC} = 0.5$.
3. The wavelength is set to $\lambda_0 = 1.55\,\mu\text{m}$.

Wave propagation along the z-axis of the LPS

Figure 3.2a schematically shows the orientation of a TE and a TM polarized wave propagating along the z-axis of the LPS. As the structure is invariant to rotations in the x-y plane, the propagation of these two polarizations is indistinguishable in this case. The effective indices of the TE/TM plane waves traveling along the periodic axis are shown in Fig. 3.2b. They are calculated as $n_{\text{eff}} = k_z/k_0$, where k_z is obtained by solving Eq. (3.7) with $k_x = 0$. Both polarizations have the same effective index because they are both parallel to the periodic interfaces. Two different working regime are observed in Fig. 3.2b: the regimes where the effective index increases with the period and the regimes where the effective index decreases with the period. In the former regimes, known as propagation regimes, the effective index is a real number so the plane waves propagate along the periodic structure with a phase velocity $\vec{k} = k_z\hat{z}$. In the latter regimes, known as forbidden bands or band gaps, the effective index is a complex number, and the plane waves cannot propagate forwards because the reflections in each interface are interfering constructively, so that the wave is reflected back. Indeed, this constructive interference is the condition for a structure to work in the Bragg regime:

$$k_z\Lambda = \frac{2\pi}{\lambda_0} n_{\text{eff}}\Lambda = l\pi \tag{3.9}$$

with l being any natural number. Each band gap is identified by its l number, starting with the first band gap ($l = 1$) and so on. The propagation regime below the first Bragg it is frequently known as subwavelength regime, and it is defined from the above condition as the propagation regime with a phase delay over a period lower than π:

$$\frac{2\pi}{\lambda_0} n_{\text{eff}}\Lambda < \pi \quad \text{or} \quad \Lambda < \frac{\lambda_0}{2n_{\text{eff}}} = \frac{\lambda_{\text{eff}}}{2} \tag{3.10}$$

It is important to note that the propagation regimes different from the subwavelength regime are known as radiation regimes in periodic structure which allow radiation.

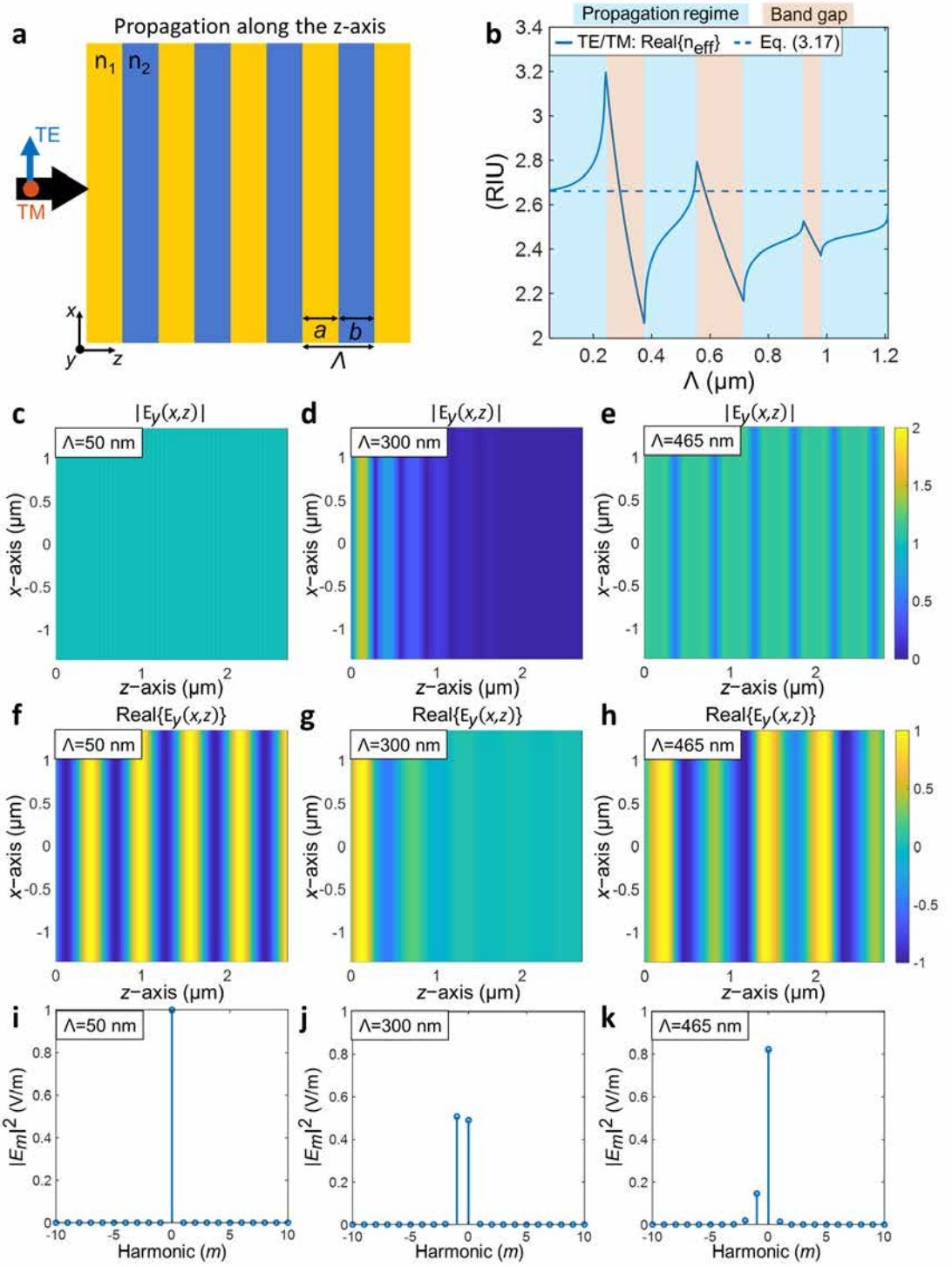

Figure 3.2: a) Schematic of the direction and polarization orientation of a wave propagating along the z-axis of the LPS. b) Real part of the effective index of the TE or TM polarized plane wave propagating as shown in (a). c-k) Magnitude, f-h) real part and i-k) harmonic decomposition of the electric field of a TE/TM polarized plane wave propagating along the LPS shown in (a) for a period in the c,f,i) deep subwavelength regime, $\Lambda = 50$ nm, d,g,j) center of the first Band gap $\Lambda = 300$ nm and e,h,k) center of the second propagation regime, $\Lambda = 465$ nm.

Figures 3.2c-h show the magnitude and the real part of the field profile of a TM plane wave propagating through the z-axis of the LPS for three different periods, calculated with Eq. (3.6). The first period, $\Lambda = 50$ nm, is inside of the subwavelength regime, the second period, $\Lambda = 300$ nm, is on the center of the first forbidden band, and the third period, $\Lambda = 465$ nm, is on the center of the second propagation regime. In the subwavelength regime (Figs. 3.2c, 3.2f and 3.2i), the magnitude of the field propagation is almost constant, with the real part of the wave showing a sinusoidal propagation of the phase fronts. Moreover, the harmonic decomposition of the field profile in this case shows that in the only the fundamental term, $m = 0$ stands. Therefore, this solution is indistinguishable from the solution of a plane wave propagating through a homogeneous medium. In the forbidden band (Figs. 3.2d, 3.2g and 3.2j), the magnitude of the electric field propagation decays to zero, no propagation is allowed in this regime. The harmonic decomposition in this case shows that there are two harmonics, $m = -1$ and $m = 0$, with almost the same power. They correspond with the wavevector of the forward and backward waves, which are propagating at the same speed but in opposed directions. Finally, in the second propagation regime (Figs. 3.2e, 3.2h and 3.2k) the structure again allows propagation. In this case, the periodicity of the structure clearly seen in the magnitude of the field profile, therefore, the propagation of the real part is highly modulated. The harmonic decomposition for this period shows multiple components, so the homogeneous behavior is not found in this regime.

Wave propagation along the x-axis of the LPS

Figure 3.3a schematically shows the orientation of a TE and a TM polarized wave propagating along the x-axis of the LPS. The effective indices of the TE/TM plane waves propagating along this direction are shown in Fig. 3.3b. They are calculated as $n_{\text{eff}} = k_x / k_0$, where k_x is obtained by solving Eq. (3.7) with $k_z = 0$. Both polarizations have different effective indices because the different relative position between their electric field main component and the periodic discontinuities. TE polarized waves are perpendicular to the discontinuities while the TM polarized waves are parallel to the discontinuities. Moreover, both polarizations have a real effective index increasing with the period. There are no forbidden bands in this direction.

Figures 3.3c-h show the magnitude and the real part of the field profile of a TM plane wave propagating through the x-axis of the LPS for the three same periods studied in the previous section: $\Lambda = 50$ nm, $\Lambda = 300$ nm, $\Lambda = 465$ nm. As this structure has no forbidden gap, wave propagation is allowed in all three cases. For the first period, $\Lambda = 50$ nm, the field propagation is indistinguishable from the propagation along a homogeneous structure (Figs. 3.3c and 3.3f), and all the power of the harmonic decomposition in the fundamental term (Fig. 3.3i). For the second period, $\Lambda = 300$ nm, the field profile is slightly modulated (Fig. 3.2d and Fig. 3.2g), however, observing the harmonic decomposition it is clear that almost all the power is still in the $m = 0$ component. Therefore, this structure is very close to the propagation through a homogeneous structure. Finally, for the period $\Lambda = 465$ nm the modulation of the field profile along the z-axis has increased, however, observing the field harmonic decomposition almost the 85% of the power remains in the fundamental component of the decomposition. From this study it is seen that periodic structures with the periodicity in the transversal direction allow longer periods while still behaving as homogeneous materials.

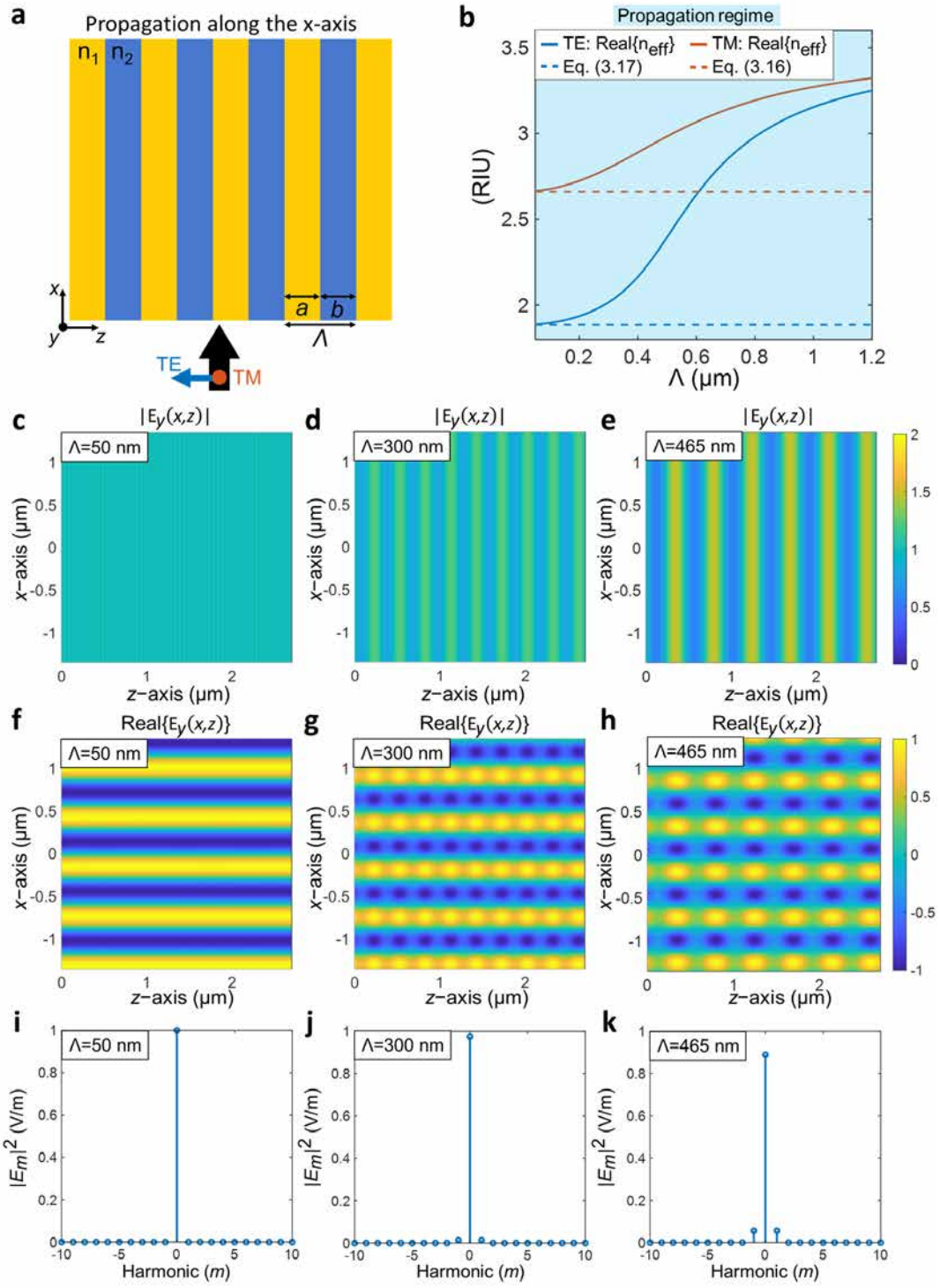

Figure 3.3: a) Schematic of the direction and polarization orientation of a wave propagating along the x-axis of the LPS. b) Real part of the effective index of the TE (blue) and TM (red) polarized plane waves propagating as shown in (a). c-k) Magnitude, f-h) real part and i-k) harmonic decomposition of the electric field of a TM polarized plane wave propagating along the LPS shown in (a) for the same three periods studied in Fig. 3.2: c,f,i) $\Lambda = 50$ nm, d,g,j) $\Lambda = 300$ nm and e,h,k) $\Lambda = 465$ nm.

Wave propagation along any arbitrary angle in the x-z plane of the LPS

Figure 3.4a schematically shows the orientation of the TE and TM polarizations when a wave is propagating along an arbitrary angle ϕ in the x-z-plane of the LPS. The real part of effective index of the TE/TM plane waves traveling along any angle ϕ is shown in Figures 3.4b, 3.4c and 3.4d for three different periods: $\Lambda = 50$ nm, $\Lambda = 300$ nm, and $\Lambda = 465$ nm. They are calculated as $n_{\text{eff}} = (k_x^2 + k_z^2)^{1/2}/k_0$ with the pairs (k_x, k_z) obtained by giving suitable values to k_x in Eq. (3.7) and getting the corresponding k_z. The propagation angle is then calculated as $\phi = \arctan(k_x/k_z)$. The areas shaded as blue in the dispersion diagrams are the propagation angles allowing TE and TM propagation, the areas shaded as yellow are the propagation angles with the TM polarization inside of the bandgap, the areas shaded as brown are the propagation angles with both polarizations inside of the bandgap. For the first period, $\Lambda = 50$ nm, the structure always works in the first propagation regime for any propagation angle, obtaining an elliptical shape for the TE polarization and a circle for the TM. For the second period, $\Lambda = 300$ nm, the structure works in the first propagation regime for any propagation angle $\phi > 40°$ for the TM polarization and $\phi > 20°$ for the TE polarization. The wave propagation with a rotation angle from 20 to 0 degrees is forbidden for both polarizations. For the third period, $\Lambda = 465$ nm, the structure works in the first propagation regime for any angle $\phi > 55°$ for the TM polarization and $\phi > 50$ for the TE polarization. Then, the TM polarization gets inside of the bandgap for the angles $35° < \phi < 55°$ and the TE polarization for the angles $36° \leq \phi \leq 50°$. The wave propagation with a rotation angle from 35 to 0 degrees is allowed for both polarizations as the structure is working in the second propagation regime.

The magnitude and the real part of the electromagnetic field profile of a plane wave propagating through a propagation angle of $\phi = 50°$ is shown for the three periods in Figs. 3.4e-j. For the first period, $\Lambda = 50$ nm, (Fig. 3.4e and Fig. 3.4h) any propagation angle is allowed. This short period allows wave propagation in a similar way as it would propagate in a homogeneous structure. For the period $\Lambda = 300$ (Fig. 3.4f and Fig. 3.4i) the structure is working in the first propagation regime for an angle of $\phi = 50°$ (Fig. 3.4b). A remarkable modulation on the real part and magnitude of the field propagation is observed, but the structure is still working in the subwavelength regime. Finally, for the period $\Lambda = 465$ (Fig. 3.4g and Fig. 3.4j) the structure is working in the first band gap for an angle of $\phi = 50°$ (Fig. 3.4d), so the wave propagation is not allowed.

3.2.2. Homogeneous metamaterial equivalent to a LPS

The condition for periodic structures to behave as homogeneous metamaterials is that only the fundamental harmonic of the Fourier series of its electromagnetic solutions stands [see Eq. (3.4)]. Figures 3.2i and 3.3i clearly show that the wave propagating along the LPS satisfy the aforementioned condition for short periods. Therefore, the next step is to find the equivalent homogeneous material which mimics the electromagnetic behavior of the periodic structures in this situation. For the case of the LPS, the analytical formulae to calculate the equivalent homogeneous material were deduced by Rytov in 1956 assuming that the structure is working in the long wave regime [90] ($\lambda \gg \Lambda$). Twenty years later, Yeh et al obtained the same results by studying the dispersion equation of the LPS under the long wave condition. By doing so, the dispersion equation [Eq. (3.7)] collapses into the equations

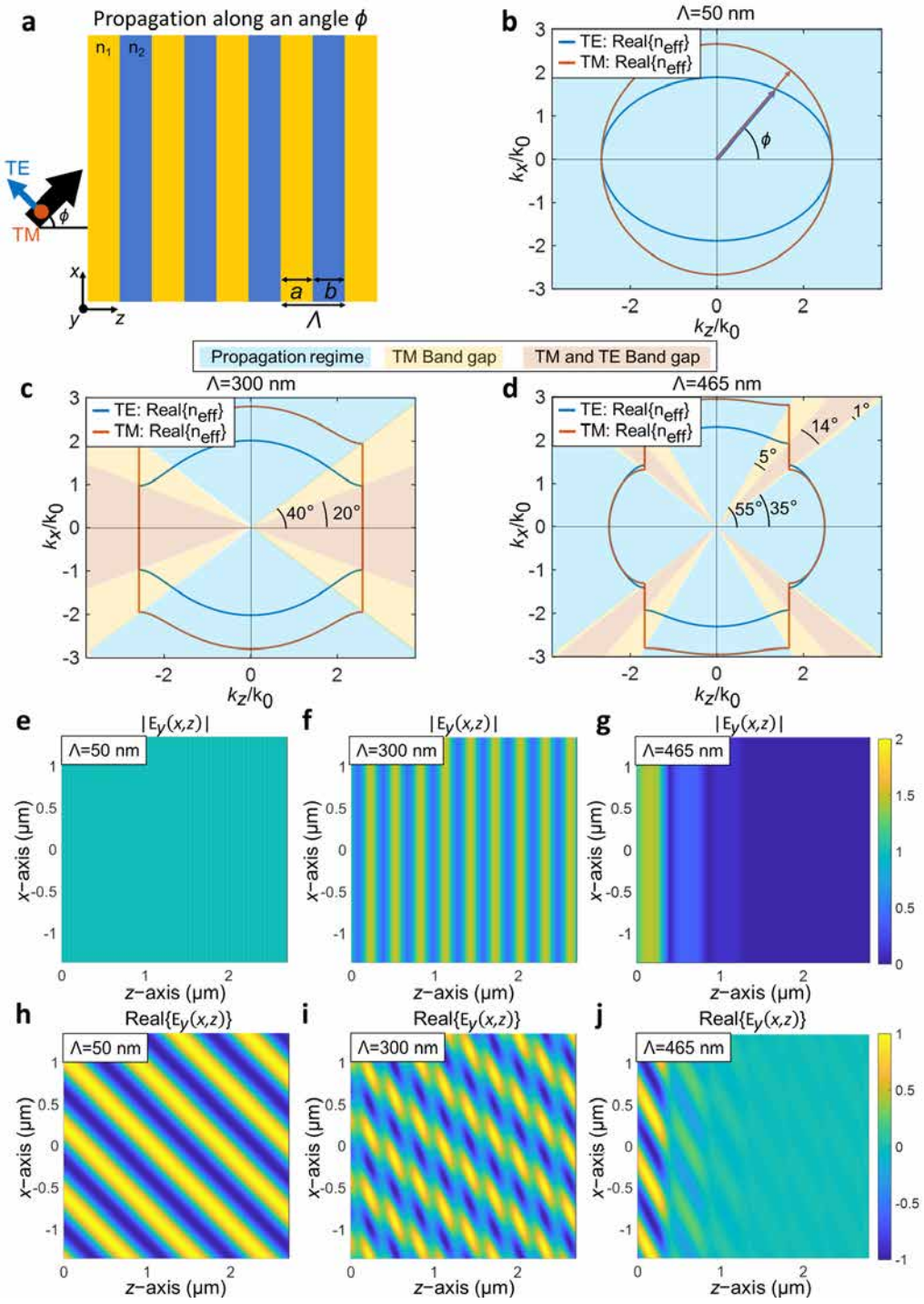

Figure 3.4: a) Schematic of the direction and polarization orientation of a wave propagating along an arbitrary angle ϕ on the x-z plane of the LPS. b-d) Dispersion diagrams of a TE/TM plane wave propagating along any angle ϕ of the x-z plane of the LPS for a period of b) $\Lambda = 50$ nm, c) $\Lambda = 300$ nm and d) $\Lambda = 465$ nm. The colors on the diagrams show the propagation angles allowing propagation for: both polarization (blue), only TE (yellow) or neither TE or TM (brown). e-g) Magnitude and h-j) Real part of the electric field of a TM polarized plane wave propagating with a rotation angle of $\phi = 50°$ for a period of e,h) $\Lambda = 50$ nm, f,i) $\Lambda = 300$ nm and g,j) $\Lambda = 465$ nm.

of an ellipse and a circle for the TE and TM polarizations respectively [182]:

$$\text{TE waves}: \frac{k_x^2}{n_\perp^2} + \frac{k_z^2}{n_\parallel^2} = k_0^2, \tag{3.11}$$

$$\text{TM waves}: \frac{k_x^2}{n_\parallel^2} + \frac{k_z^2}{n_\parallel^2} = k_0^2. \tag{3.12}$$

These two equations are then the dispersion equations of TE and TM plane waves propagating along the x-z plane of a LPS in the deep subwavelength regime. Interestingly, they are also the dispersion equations of TE and TM planes waves propagating through the x-z plane of a homogeneous uniaxial crystal, with $n_\parallel$ and $n_\perp$ being the ordinary and extraordinary indices of refraction respectively [93]. Therefore, from an electromagnetic point of view, the periodic structure is mimicking the behavior of a uniaxial crystal. In other words, the homogeneous metamaterial equivalent to a LPS working in deep subwavelength regime is a uniaxial crystal: an anisotropic medium where the wave propagates at the same speed in two of the three axes, but different in the third one. The wave propagation along a uniaxial crystal is characterized by its permittivity tensor:

$$\boldsymbol{\varepsilon}_{\text{LPS}} = \begin{bmatrix} n_\parallel^2 & 0 & 0 \\ 0 & n_\parallel^2 & 0 \\ 0 & 0 & n_\perp^2 \end{bmatrix}. \tag{3.13}$$

This tensor imposes a phase velocity $k_0 n_\parallel$ for the x-polarized and y-polarized waves and a phase velocity $k_0 n_\perp$ for the z-polarized waves propagating. As LPSs and uniaxial crystals have the same dispersion equations in the deep subwavelength regime, the permittivity tensor given by Eq. (3.13) can be used to model the behavior of the LPS. This kind of anisotropic homogenization of LPS has been used in the field of free-space optics and metasurfaces [169–172], but it is usually substituted by simplest isotropic homogenization because of the small difference between the isotropic and the anisotropic approaches in the free space problem. This Thesis overviews this homogenization in integrated periodic structures, demonstrating how in certain cases the anisotropy is essential to properly model the actual behavior of SWG based devices. But prior to that, the homogenization of LPS working as uniaxial crystal is studied by comparing the dispersion equations of plane waves propagating along LPSs and their equivalent homogeneous anisotropic metamaterial. The former calculated with Eq. (3.7) while the latter uses Eq. (3.11) and Eq. (3.12). For that calculation, the first step is to define how the tensor index components are obtained:

$$n_\parallel = \frac{k_z}{k_0} \text{ (when } k_x = 0), \tag{3.14}$$

$$n_\perp = \frac{k_x}{k_0} \text{ (when } k_z = 0). \tag{3.15}$$

Note that these equations are the effective indices of a plane wave propagating along the z-axis and the x-axis of the LPS respectively, obtained with Eq. (3.7) and shown in Figs. 3.2b and 3.3b for different periods. The wave propagating along the z-axis can be calculated either assuming TE or TM polarization, as both x and y polarized plane waves provide the same result. The wave propagating along the x-axis has to be calculated assuming TE polarization to ensure that the polarization direction is along the z-axis. A MATLAB and a Python script which makes the calculation of Eq. (3.14) and Eq. (3.15) has been developed during this Thesis and it can be downloaded from the supplementary material of Ref. [153].

The proposed definitions to calculate the permittivity tensor components $n_{\parallel}$ and $n_{\perp}$ are in a good agreement with the well-known Rytov's equations for the LPS in the deep subwavelength regime:

$$n_{\parallel} \approx [\mathrm{DC} \cdot n_1^2 + (1-\mathrm{DC}) \cdot n_2^2]^{0.5}, \tag{3.16}$$

$$n_{\perp} \approx [\mathrm{DC} \cdot n_1^{-2} + (1-\mathrm{DC}) \cdot n_2^{-2}]^{-0.5}. \tag{3.17}$$

Figure 3.5 compares the permittivity tensor components calculated with the proposed definition, Eqs. (3.14) and (3.15) and Rytov's definitions, Eq. (3.16) and Eq. (3.17) for a typical LPS with SOI materials at $\Lambda = 1.55$. Note that for periods up to ~ 100 nm, they both provide the same results, however, when the LPS approaches the Bragg regime the proposed model takes into account the dispersion of the periodic structure behavior predicting its behavior more accurately. On the other hand, Rytov's approximation is still useful as it is simple to use it provides a good physical insight on the dependence of the metamaterial material compositions, which, as intuition predicts, a high duty cycle implies permittivity tensor components close to n_1 and a low duty cycle implies tensor components close to n_2.

The accuracy of the homogenization of LPSs as uniaxial crystals is studied by comparing the dispersion equation of a plane wave propagating along an LPS, calculated with Eq. (3.7), and its equivalent homogeneous anisotropic metamaterial, calculated with Eqs. (3.11) and (3.12). The homogenization uses the proposed model to calculate the permittivity tensor components, based on solving Eq. (3.7). For illustration purposes, two comparisons between

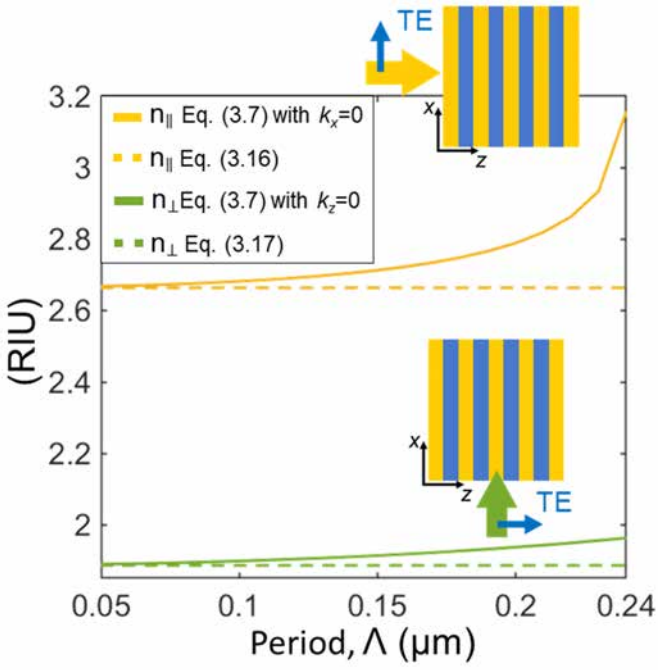

Figure 3.5: Permittivity tensor components of the homogeneous anisotropic material equivalent to a LPS with SOI materials at a wavelength $\lambda = 1.55$ μm for different periods. The solid lines are calculated with the proposed definition based on solving Eq. (3.7) twice. The dashed lines are calculated with Rytov's equations [Eq. (3.16) and Eq. (3.17)].

a LPS and its equivalent metamaterial have been made: 1) A LPS with a period much shorter thant the wavelength, $\Lambda = 50$ nm, and 2) A LPS with a period close to the Bragg regime, $\Lambda = 220$ nm. As expected, in the deep subwavelength regime, both structures exhibit the exact same behavior (Fig. 3.6a) for any propagation angle as both structures are totally equivalent from an electromagnetic point of view in this regime. On the other hand, when the structure is no longer working in the deep subwavelength regime, both solutions are not exactly equal (Fig. 3.6b), however, it still yields a remarkably similar result. Note that the proposed homogenization provides no error in the principal axes, as the model is constructed by using the propagation on the LPS in these axes. After this study, the main conclusions of the homogenization of the LPS are discussed.

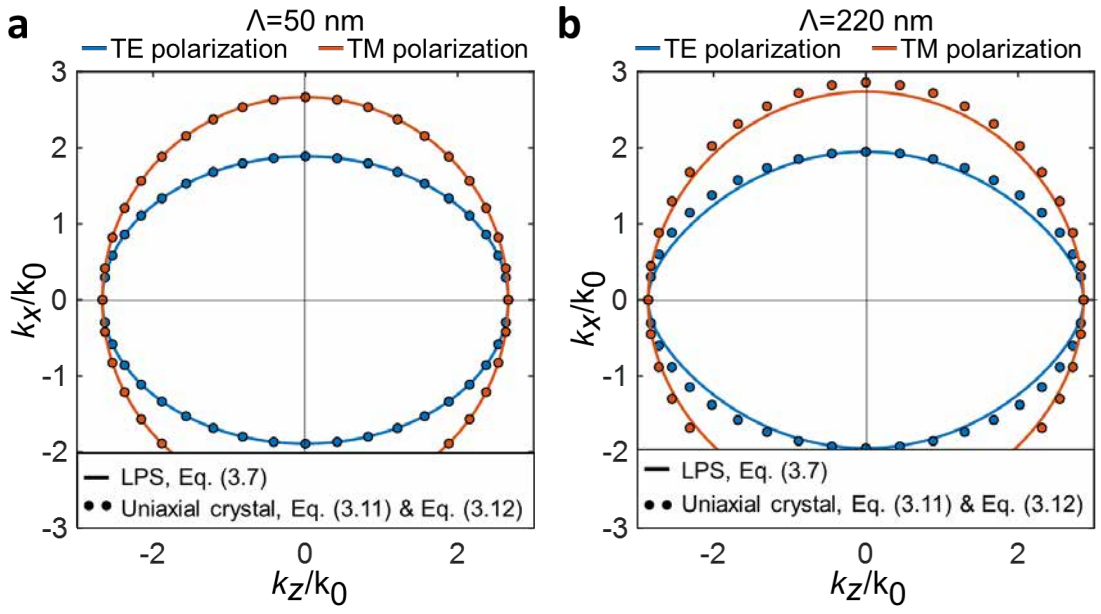

Figure 3.6: a) Normalized wave vector components, (k_x and k_z), of a plane wave propagating along any angle of the laminar periodic structure (DC = 0.5) and of its equivalent anisotropic homogeneous material for the structure

3.2.3. Conclusions on the homogenization theory of LPS

After the analysis of the laminar periodic structure, the four questions formulated at the end of section 3.1 can be answered for the LPS:

1. **Under what circumstances does an LPS behave as a homogeneous metamaterial?** Strictly speaking, an LPS only works as a homogeneous material when the subwavelength condition is taken to the limit $\Lambda/\lambda \to 0$ (long wave condition). In this case, the field profile and the dispersion equation of the LPS and the equivalent homogeneous structure are equal. However, the similarities between the periodic structures and its equivalent homogeneous structure are maintained out of the long wave regime, with the accuracy progressively deteriorating as the period approaches the wavelength. For light propagating along the x-axis there is no a strict limit for the structure to stop working as a homogeneous structure, but the accuracy slightly decreases as the period

increases. For the light propagating along the z-axis the homogenization ends when the Bragg condition is reached: $\Lambda = \lambda_0/(2n_{\text{eff}})$.

2. **How is the homogeneous metamaterial of the LPS calculated?** For the case of the LPS, the homogeneous material is a uniaxial crystal defined by its permittivity tensor. The components of the tensor are calculated as defined by Eqs. (3.14) and (3.15). The resolution of these two equations requires solving Eq. (3.7).

3. **Is the homogenization an exact equivalence or just an approximation?** The equivalence between the LPS and its corresponding homogeneous structure is exact in terms of electromagnetic wave propagation when the long wave condition is satisfied. A set of plane waves propagating along both materials would have the same wavevector and the same field profile. When the long wave condition is not satisfied, but the homogenization is still allowed, the wavevector of both the LPS and its corresponding homogeneous structure is similar, with little differences in the propagation angles in-between both main axes (see Fig. 3.11).

4. **How are the optical properties of the synthesized material engineered?** To control the optical properties of the implemented metamaterial means to control the tensor components of the uniaxial crystal. In the long wave regime these components only depends on the duty cycle (see Eq. (3.16) and (3.17)), so in this regime the optical properties are controlled by tuning the duty cycle. Out of the long wave regime, the tensor components also depend on the period to wavelength ratio (see Fig. 3.5), so the period can be used also to the tune of the implemented metamaterial.

3.3. Silicon photonic SWG waveguides

There is no a unique definition of what a silicon photonics SWG waveguide is. Many different SWG waveguide are possible, but the two most common types are longitudinal (Fig. 3.7a) and transversal (Fig. 3.7b) topologies. SWG waveguides have been widely used in silicon photonics to optimize the performance of multiple different devices (see section

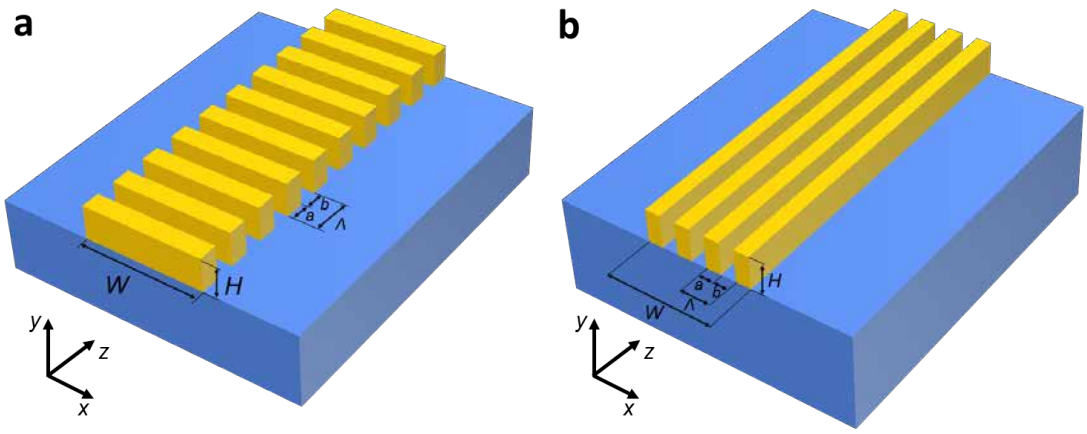

Figure 3.7: Schematic representation of an integrated SWG waveguide with the periodic segments arranged along a) the longitudinal direction and b) the transversal direction.

1.2) but little to none analysis on the homogenization of this kind of structures has been made in silicon photonics integrated platforms. One of the contributions of this Thesis has been to study the homogenization of this SWG waveguides as homogeneous structures, proposing and validating novel homogenization models to calculate the permittivity tensor $\varepsilon_w = \text{diag}[n_{xx}^2, n_{yy}^2, n_{zz}^2]$ of the equivalent homogeneous material to the SWG structures.

3.3.1. Basic homogenization model of SWG waveguides: The LPS model

A simple homogenization model of SWG waveguide is derived from the study of LPS. It consists in the three following steps, schematically summarized in Fig 3.8:

1. Extract the corresponding LPS of the SWG waveguide. That is, the LPS with the same materials, duty cycle, period as the SWG waveguide. The periodic axis of the SWG waveguide and the LPS has to be the same.
2. Calculate the equivalent homogeneous anisotropic metamaterial of the LPS. That is, the permittivity tensor components, $n_\parallel$ and $n_\perp$, of the permittivity tensor ε_{LPS} as shown in section 3.2.2.

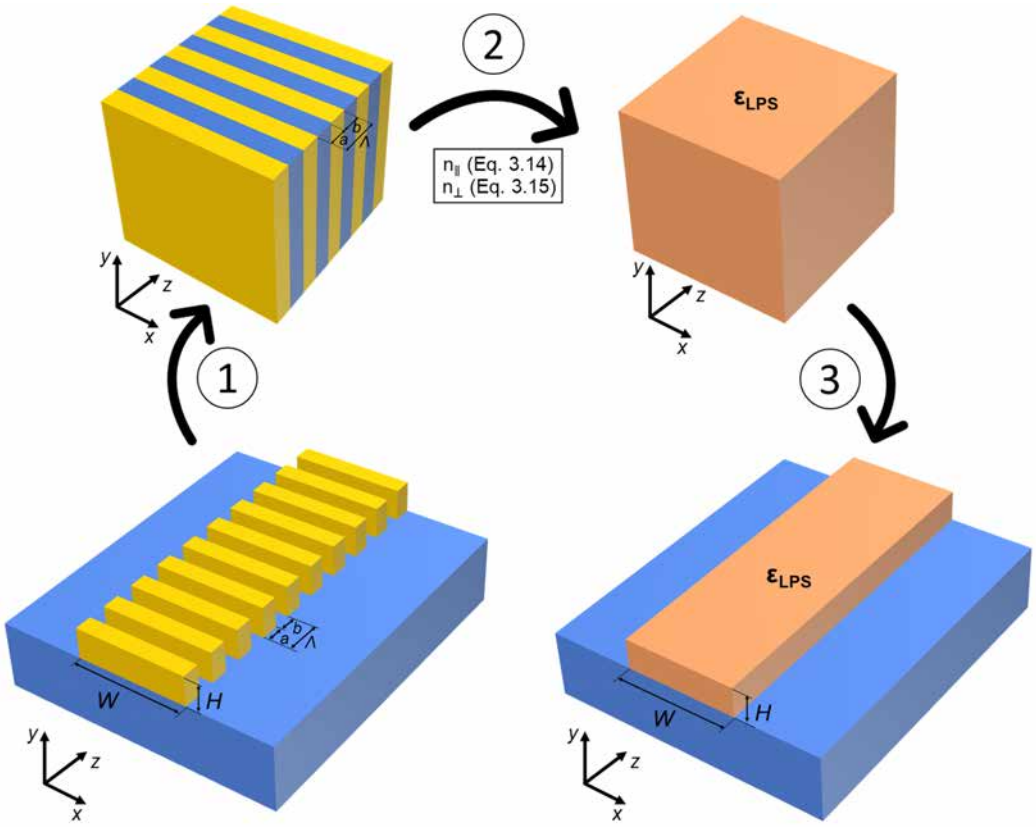

Figure 3.8: Algorithm to calculate the equivalent homogeneous material of a given SWG waveguide. The steps of the algorithm are: 1) Extract the corresponding LPS of a given SWG waveguide. That is, the LPS with the same materials, duty cycle, period. 2) Calculate the permittivity tensor components, $n_\parallel$ and $n_\perp$. 3) Impose the calculated permittivity tensor components of the LPS to the homogeneous anisotropic core.

3. Use the calculated permittivity tensor components of the LPS as the homogeneous anisotropic core. That is, $\varepsilon_{\mathrm{w}} = \mathrm{diag}[n_{xx}^2, n_{yy}^2, n_{zz}^2] = \varepsilon_{\mathrm{LPS}} = \mathrm{diag}[n_{\parallel}^2, n_{\parallel}^2, n_{\perp}^2]$.

To study the accuracy of the proposed model, a multimode waveguide with a width, $W = 3\,\mu$m, a height, $H = 220$ nm, and a duty cycle, DC = 0.5 is modeled and analyzed. Figure 3.9a shows the effective index of the fundamental TE and TM modes of the SWG waveguide (solid lines) and its corresponding homogeneous equivalent waveguide for different periods (circles). As discussed in section 2.1.2, the analysis of the periodic structure requires complex 3D-FDTD simulations while the simulation of the equivalent homogeneous anisotropic waveguide just requires a much more simpler 2D-FEM solver. From this figure is clear that the homogenization accurately predict the behavior of the waveguide for periods up to $\Lambda = 200$ nm. Beyond this period, the accuracy of the homogenization decreases because the LPS used to model the SWG structure approaches the Bragg regime while the SWG waveguide is still far from Bragg regime because of its lower modal confinement. Beyond the period where the LPS gets into the Bragg regime, $\Lambda = 240$ nm, the LPS homogenization is no longer possible. Figure 3.9b and 3.9c shows not only the fundamental but also the high order modes of both structures for two different periods. The first in the deep SWG regime, $\Lambda = 50$ nm and the second close to the Bragg regime of the LPS, $\Lambda = 220$ nm. Once again, in the deep-SWG

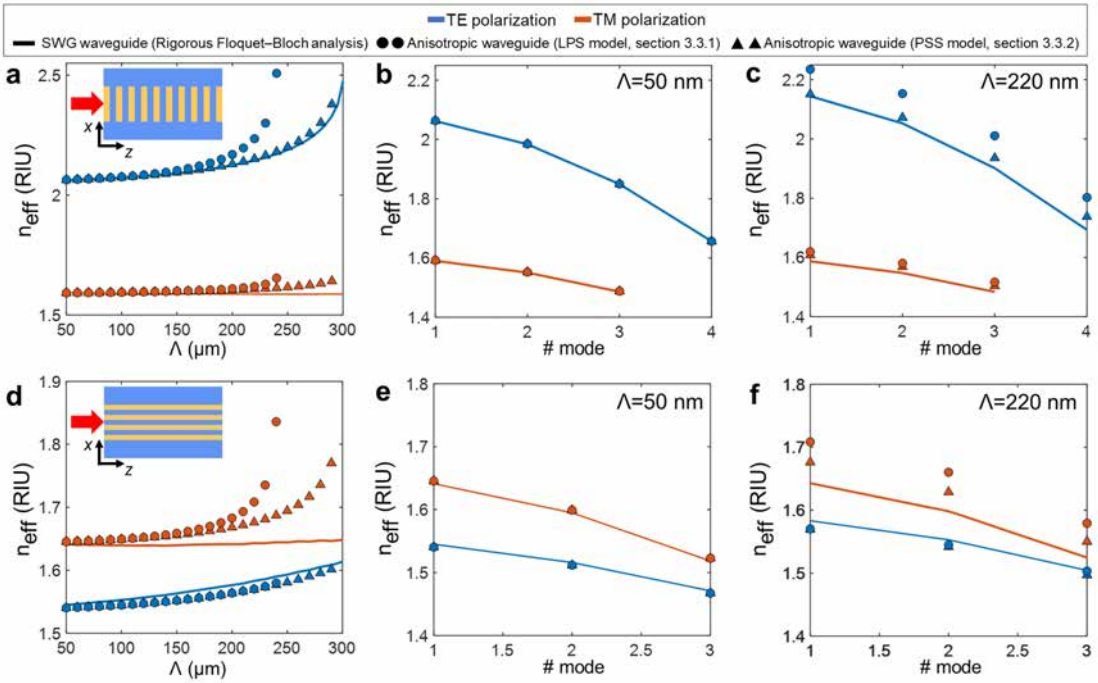

Figure 3.9: a-c) Effective indices of (a) the fundamental Floquet–Bloch mode and b),c) higher order Floquet–Bloch modes of a longitudinal SWG waveguide calculated by rigorous 3D full-vectorial simulations (TE: Blue solid lines, TM: Orange solid lines) compared with those of the corresponding anisotropic homogeneous-core waveguides obtained using the LPS (circles) and the PSS (triangles) models for a period b) $\Lambda = 50$ nm and c) $\Lambda = 220$ nm. d–f) Effective indices of (d) the fundamental Floquet–Bloch mode and e),f) higher order Floquet–Bloch modes of a transverse SWG waveguide calculated by rigorous 3D full-vectorial simulations (TE: Blue solid lines, TM: Orange solid lines) compared with those of the corresponding anisotropic homogeneous-core waveguides obtained using the laminar model (circles) and the slab model (triangles) for a period e) $\Lambda = 50$ nm and f) $\Lambda = 220$ nm.

regime both structures offer similar results and the accuracy decreases when the period get close to the Bragg regime of the LPS.

The same homogenization can be used for transversal SWG waveguides. This rotation is taken into account in the first step of the algorithm, as the LPS has the same periodicity of the SWG waveguide. Therefore, the LPS is analyzed with a 90º degree rotation on the x-z plane, being the x-axis the periodic dimension. Therefore, the permittivity tensor of the equivalent homogeneous waveguides in this case is given by $\varepsilon_{\mathrm{w}} = \mathrm{diag}[n_{xx}^2, n_{yy}^2, n_{zz}^2] = \mathrm{diag}[n_{\perp}^2, n_{\parallel}^2, n_{\parallel}^2]$. Figure 3.9d-f shows the homogenization study for transversal SWG waveguides, getting similar conclusions to the one done for the longitudinal SWG waveguide. The accuracy for the TM polarization modelling is decreased for periods close to the Bragg regime, especially in the transversal SWG waveguide. This problem comes from the difficulties to model both polarizations at the same time with the same anisotropic material. This problem could be alleviated by properly adjusting the n_{yy} component depending on the orientation of the SWG waveguide, but this solution is not commented to avoid confusions.

Therefore, in both longitudinal and transversal SWG waveguides, the LPS homogenization model accurately works for periods up to $\Lambda = 200$ nm assuming typical SOI values. From that point, the precision decreases until the Bragg period, $\Lambda = 240$ nm from which the homogenization is no longer possible. This unavailability comes from a simple issue: The laminar periodic structure gets into the Bragg regime, so no solution is available. However, light in integrated SWG waveguides still propagates for periods beyond 240 nm because the effective indices of the waves in SWG waveguides are lower than in the LPS, so the Bragg regime for the SWG waveguide is reached for a longer period. Therefore, the limitation of LPS model is given by the difference on the period in which the LPS structure and the modelled SWG waveguide get into the Bragg regime. In this context, sub-micrometric structures with a high-index contrast are one of the worst-case scenarios, and even do, the demonstrated results are satisfactory. To partially compensate this issue, the next section proposed an advanced homogenization model in which the sum-micrometic thickness is introduced as a part of the model.

3.3.2. Advanced homogenization model of SWG waveguides: The PSS model

The previous model is limited because the LPS get into the Bragg regime for a period shorter than the SWG waveguides which are being modeled. This difference in the Bragg regime period comes from the low refractive indices of the cladding and substrate materials of the SWG waveguides which reduce the effective index of the mode compared with the effective index of a plane wave propagating along the LPS. To alleviate this problem, the finite thickness of the waveguide can be taken into account as a property of the material. For that purpose, the periodic slab structure (PSS) is introduced (see Fig. 3.10a). This new structure can be understood as a LPS with a finite thickness, H, embedded between a substrate and a cladding. Following a similar argument as in the LPS, the periodic core of the PSS can be homogenized as a uniaxial crystal defined by its permittivity tensor $\varepsilon_{\mathrm{PSS}}$. Analogously, the tensor components of this new metamaterial are calculated from the TE wave propagation along the x- and the z-axis of this structure. The plane waves propagating along these two axes have effective refractive indices $n_{\mathrm{eff}x}$ and $n_{\mathrm{eff}z}$ (see Fig. 3.10b). In order to convert these effective indices into refractive indices, the homogeneous slab which results in these modes

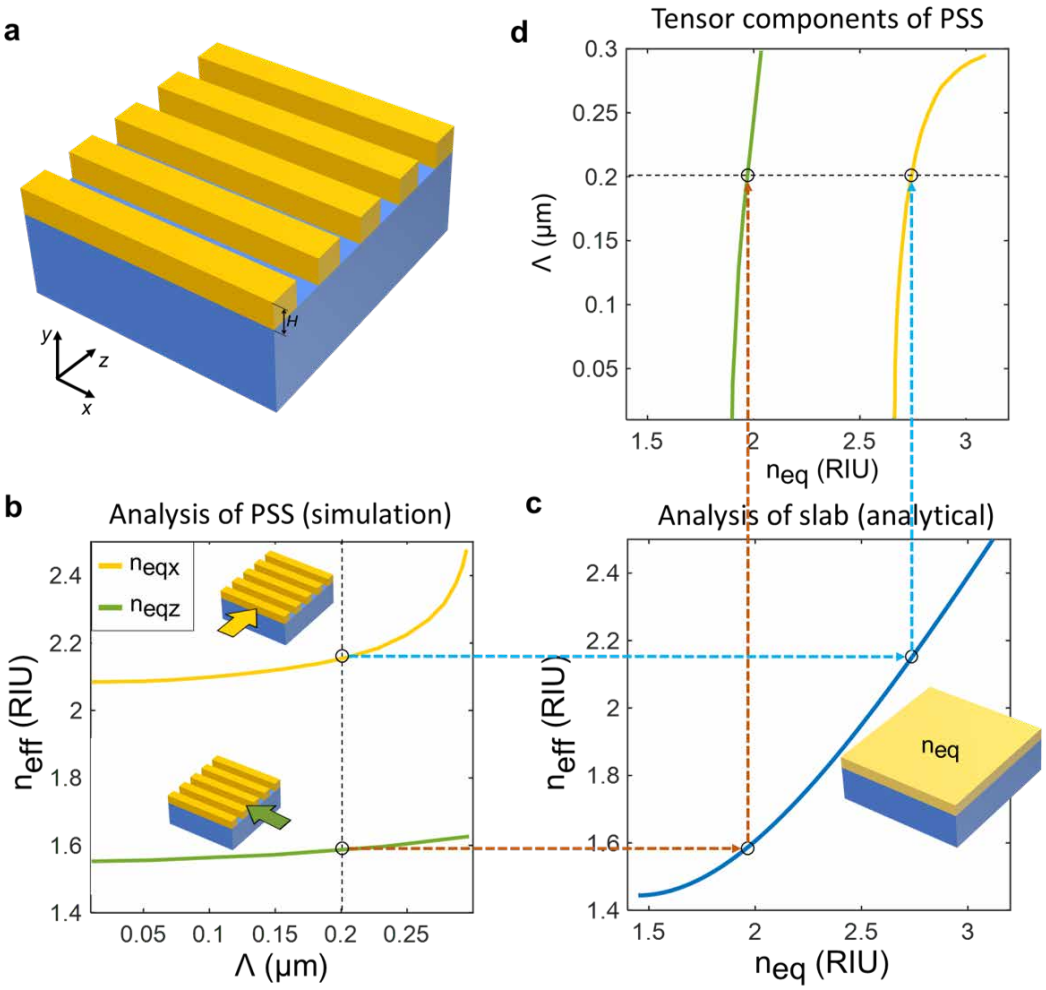

Figure 3.10: a) Schematic representation of a periodic slab structure. b) Effective index of the fundamental TE mode propagating along the z-axis (n_{effx}) and x-axis (n_{effz}) of the periodic slab. c) Mapping function between the effective index of the fundamental TE mode of an isotropic slab and the corresponding core material refractive index. d) Synthesized refractive index tensor components for a periodic-core slab with period Λ.

has to be calculated. For this purpose, an isotropic slab with the same height, cladding and substrate is solved with different core materials n_{eq} (see Fig. 3.10c), calculating the mapping function which relates the tensor components $n_{\text{eq}x}$ and $n_{\text{eq}z}$ from $n_{\text{eff}x}$ and $n_{\text{eff}z}$. It is important to note that the resolution of the effective indices of PSS requires to solve a 2D periodic problem, which in this Thesis is easily done with FEXEN just in a few seconds.

Based on this procedure, the PSS homogenization model is performed by following the next three steps, schematically summarized in Fig 3.11:

1. Extract the corresponding PSS of a given SWG waveguide. That is, the PSS with the same materials, duty cycle, period, thickness. The periodic axis of the SWG waveguide and the PSS has to be the same.
2. Calculate the permittivity tensor components, $n_{\text{eq}x}$ and $n_{\text{eq}z}$, of the extracted PSS by solving the PSS and mapping the resulted effective indices as shown in Fig. 3.10.

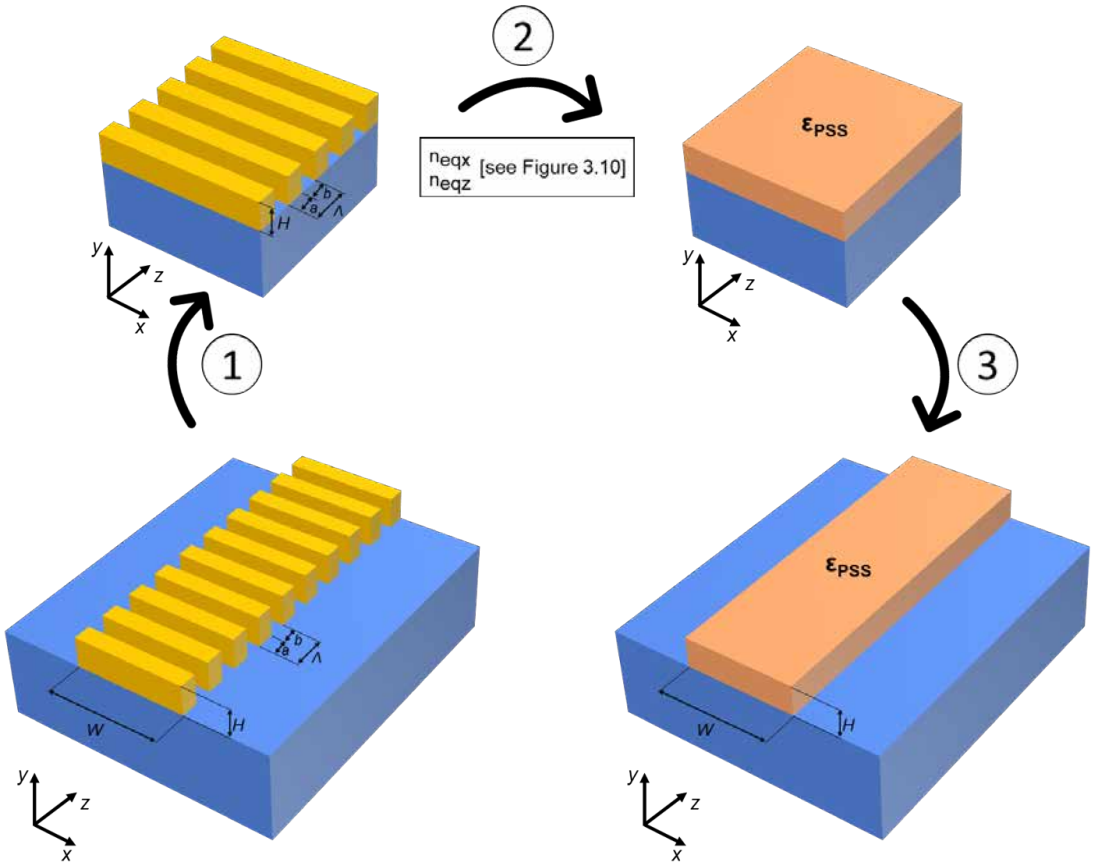

Figure 3.11: Algorithm to calculate the equivalent homogeneous material of a given SWG waveguide with the PSS model. The steps of the algorithm are: 1) Extract the corresponding PSS of a given SWG waveguide. That is, the PSS with the same materials, duty cycle, period, height and orientation. 2) Calculate the permittivity tensor components, n_{eqx} and n_{eqz}. 3) Impose the calculated permittivity tensor components of the PSS to the homogeneous anisotropic core.

3. Use the calculated permittivity tensor components of the PSS as the homogeneous anisotropic core, that is, $\varepsilon_{\mathrm{w}} = \mathrm{diag}[n_{xx}^2, n_{yy}^2, n_{zz}^2] = \varepsilon_{\mathrm{PSS}} = \mathrm{diag}[n_{\mathrm{eq}x}^2, n_{\mathrm{eq}x}^2, n_{\mathrm{eq}z}^2]$.

To study the accuracy of the PSS model, the same SWG waveguide studied in section 3.3.1 is model and solved. Figure 3.9a compares the effective indices of the fundamental TE and TM modes of the waveguide solved by using 3D-FDTD Floquet simulations (solid lines), the LPS model (circles) and the PSS model (triangles). It is clearly shown that the PSS model is indeed more accurate than the laminar model in the vicinity of the Bragg threshold, yet at the expense of a higher complexity in the modeling stage. This improvement is also noted for higher-order modes: while for the 50-nm pitch both laminar and slab models give virtually exact results (see Fig. 3.9b), for the 220-nm pitch the error in the effective indices is below 3% for the PSS model, compared to 6% for the laminar approximation (see Fig. 3.9c). The same study has been done for the transverse subwavelength waveguide, the PSS model does also provide benefits compared to the laminar model in this case (see Fig. 3.9d-f). However, the homogenization of transversal SWG structures is less frequent as they are easily solved with conventional mode solvers. In any case, both proposed homogenization models provides quick but accurate results, helping in the analysis of SWG waveguides.

3.4. Conclusions

In this chapter, the basic foundations of the wave propagation through dielectric periodic structures have been discussed. For that purpose, the wave propagation along the laminar periodic structure has been revised in detail, providing the basic knowledge about wave propagation in periodic media. Special emphasis has been placed in the conditions in which a periodic structure behaves as homogeneous material, known as subwavelength condition. The equivalent metamaterial of an SWG structure is a uniaxial crystal defined by a permittivity tensor $\varepsilon = \text{diag}[n_{xx}^2, n_{yy}^2, n_{zz}^2]$. A set of equations to calculate the permittivity tensor components of an LPS in the subwavelength regime have been proposed and validated. This equivalence between SWG structures and uniaxial crystal is a key element in this Thesis.

The homogenization theory of periodic SWG structures has been then extended to SWG waveguides. Two models to calculate the equivalent homogeneous metamaterial of an SWG waveguide have been proposed and validated: the LPS model and the PSS model. The LPS model is easier as it only requires solving Eq. (3.7). This model can be used to homogenize periodic structure with a period up to $\Lambda = 240\,\text{nm}$. For longer periods, the PSS model is required. This model is slightly more complex as it is based on 2D simulations. However, it is still more simple than 3D-FDTD simulations of the real periodic problem. This model can be used until a period up to $\Lambda = 300\,\text{nm}$. A study of the accuracy of the homogenization of SWG waveguide have been done in section 3.3 with Fig. 3.9 being a good summary of the obtained results.

4. Advanced subwavelength grating metamaterial topologies

Longitudinal and transversal SWG waveguides are the two most common SWG topologies. They have been extensively used in the last decade to optimize the performance of a myriad of silicon photonics devices. However, as discussed in section 4.1, the limited set of degrees of freedom of these conventional SWG hampers the synthesis of complex metamaterials requiring a fine tuning of the tensor components. To overcome this problem, two advanced SWG topologies have been proposed in this Thesis: the tilted (section 4.2) and the bricked SWG metamaterial topologies (section 4.3). These topologies are a fundamental contribution of this Thesis, so they are carefully examined along this chapter, including the proposal of their homogenization model, the study of their waveguiding properties and the design and experimental characterization of some photonic devices which leverages them.

4.1. Limitations of conventional SWG metamaterial topologies

Conventional SWG topologies are used in silicon photonics platform to optimize the performance of the integrated devices. This optimization mostly relies on design of the metamaterial with the right optical properties for the specific application. Therefore, the capability to accurately control the implemented metamaterial is fundamental to design high-performance SWG based photonic devices. In conventional SWG topologies, the available degrees of freedom to engineer the synthesized metamaterial are the period and the duty cycle of the structure. For the sake of illustration, the available set of permittivity tensor components synthesizable in a standard 220 nm SOI thick platform with a longitudinal SWG structure is calculated assuming 80 nm feature size. For that purpose, the PSS model (Fig. 4.1a) is used, calculating the synthesizable component tensors $n_{xx} = n_{yy}$, n_{zz} and the anisotropy $A = n_{xx} - n_{zz}$ for each pitch/duty cycle pair (Figs. 4.1b, 4.1c and 4.1d). These figures shows that conventional SWG topologies provides a good range of different metamaterials, however, they have two important limitations:

1. The engineering of the period and duty cycle both affect all permittivity tensor components, not allowing to tune some components while maintain other unaltered.
2. The period and duty cycle are restricted by the fabrication constraints, limiting the range of different available metamaterials.

To break these restriction, two SWG metamaterial topologies have been proposed in this Thesis: the tilted and bricked SWG metamaterials. Figure 4.2 shows an exemplar tilted and a bricked SWG waveguide. The tilted SWG waveguide is based on tilting the silicon segments of a conventional longitudinal SWG waveguide. In order to maintain the MFS, the period

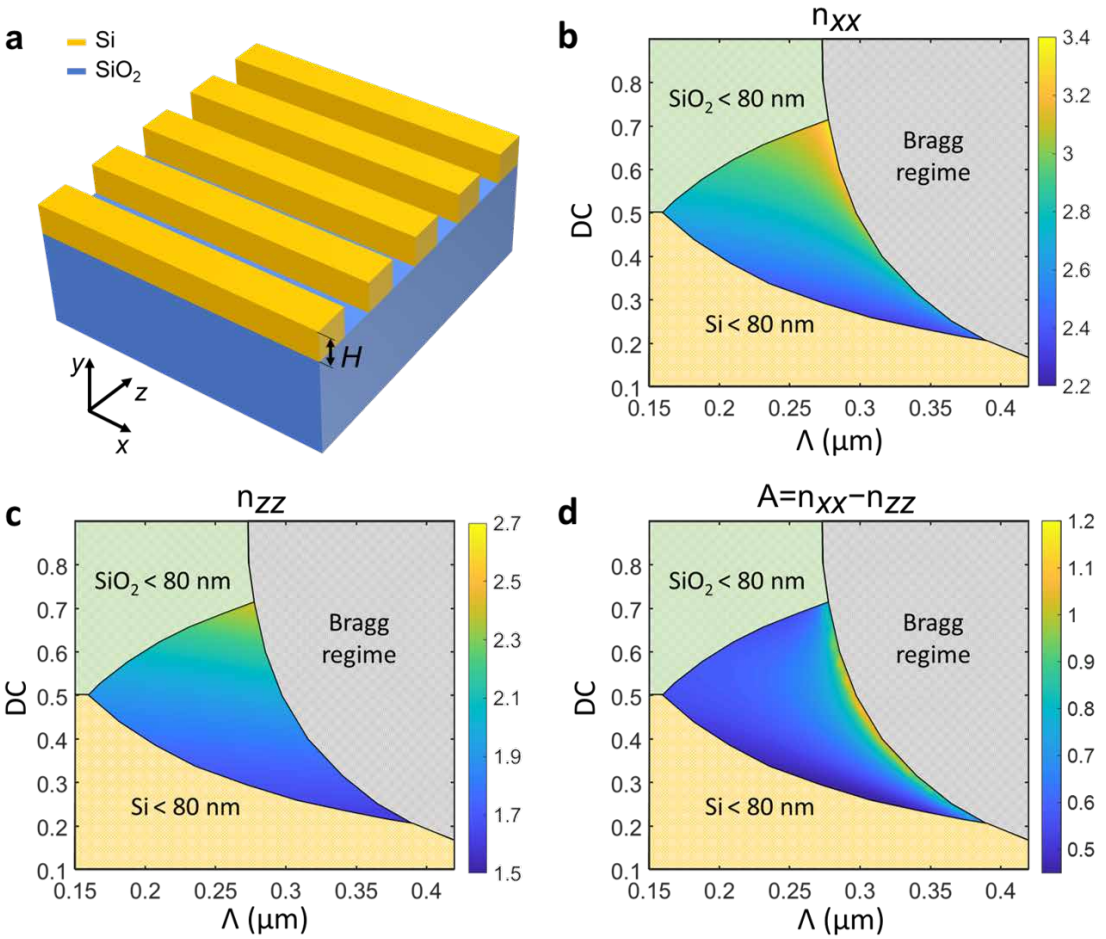

Figure 4.1: a) Schematic illustration of the periodic slab structure used to study the range of synthesizable tensor components in a 220 nm thick SOI platform longitudinal SWG waveguide for different periods an duty cycles. b,c,d) Permittivity tensor components of the equivalent metamaterial achievable in 220 nm thick SOI. including the b) n_{xx} c) n_{zz} and d) anisotropy, $A = n_{xx} - n_{zz}$.

is increased with the tilting angle as $\Lambda = \Lambda_0 / \cos\theta$, where Λ_0 is the period of the non-tilted SWG waveguide and θ is the rotation angle. On the other hand, the bricked SWG waveguide relies on the periodic segmentation of the longitudinal SWG waveguide along the transversal direction, alternatively shifting the resulting blocks a distance Δz. They both provide novel degrees of freedom: the tilting angle, θ and the block shifting Δz increasing the design space. Moreover, as discussed in their corresponding section, they both provide control over specific permittivity tensor components, enabling the design of a new set of photonic devices with non-equal tensor components, $n_{xx} \neq n_{yy} \neq n_{zz}$, while staying inside of the fabricable region.

4.2. Tilted SWG metamaterials

In anisotropic materials, the behavior of light waves depends on the orientation of the electric field components with respect to the optical axis of the material. Therefore, the idea of tilting the subwavelength structure to control the light propagation naturally emerges. The study of

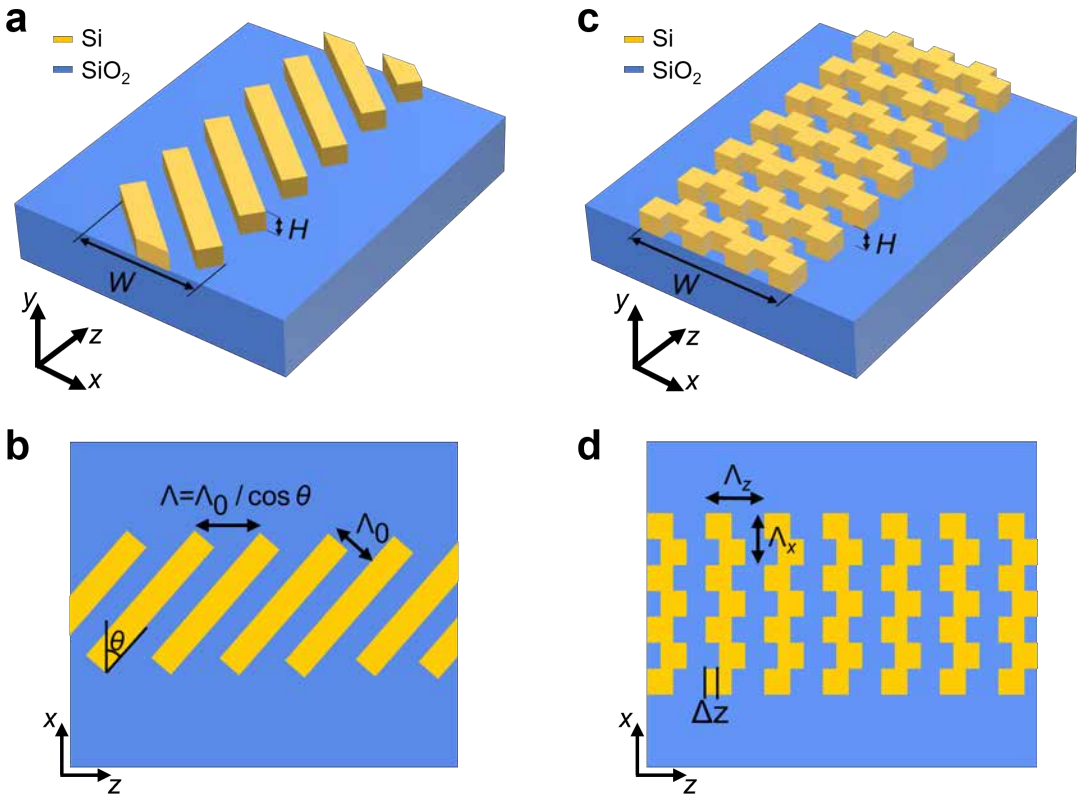

Figure 4.2: a,b) Schematic illustration of the proposed tilted SWG topology, including the a) 3D-schematic and b) top view schematic. c,d) Schematic illustration of the proposed bricked SWG topology, including the c) 3D-schematic and d) top view schematic.

this structure, known as tilted SWG metamaterial, has been a main research line of this Thesis, resulting in several journal publications [132, 154, 156–158]. The unique optical properties of tilted SWG metamaterials are discussed along this section.

4.2.1. Homogenization model of tilted SWG metamaterials

The development of an analytical model to homogenize tilted SWG metamaterials starts by considering a simple LPS in SOI platform (Fig. 4.3a). For the sake of simplicity, the deep SWG regime and a 50% duty cycle is assumed, so the behavior of the structure is just given by the material refractive indices, $n_{Si} = 3.476$ and $n_{SiO_2} = 1.444$. As discussed in section 3.2, such an LPS is homogenized as an anisotropic uniaxial crystal with permittivity tensor calculated with the well-known Rytov's theory as $\varepsilon_{LPS} = \text{diag}[n_{\parallel}^2, n_{\parallel}^2, n_{\perp}^2] = [2.66^2, 2.66^2, 1.89^2]$ where $n_{\parallel}$ and $n_{\perp}$ have been calculated by using Eqs. (3.16) and (3.17). Any TE/TM plane wave propagating along this homogeneous anisotropic medium has a wavevector $\vec{k}$ following the dispersion relation shown in Fig. 4.3c. The accuracy of the homogenization of this structure was discussed in section 3.2.2, concluding that the homogenization has no error in the deep SWG regime and the error increases as the structure approaches the Bragg regime. Now, to analyze the tilted LPS, the structure is tilted at an angle θ with respect to the z-axis as shown in Fig. 4.3d, maintaining the coordinate system unaltered. The permittivity tensor of the

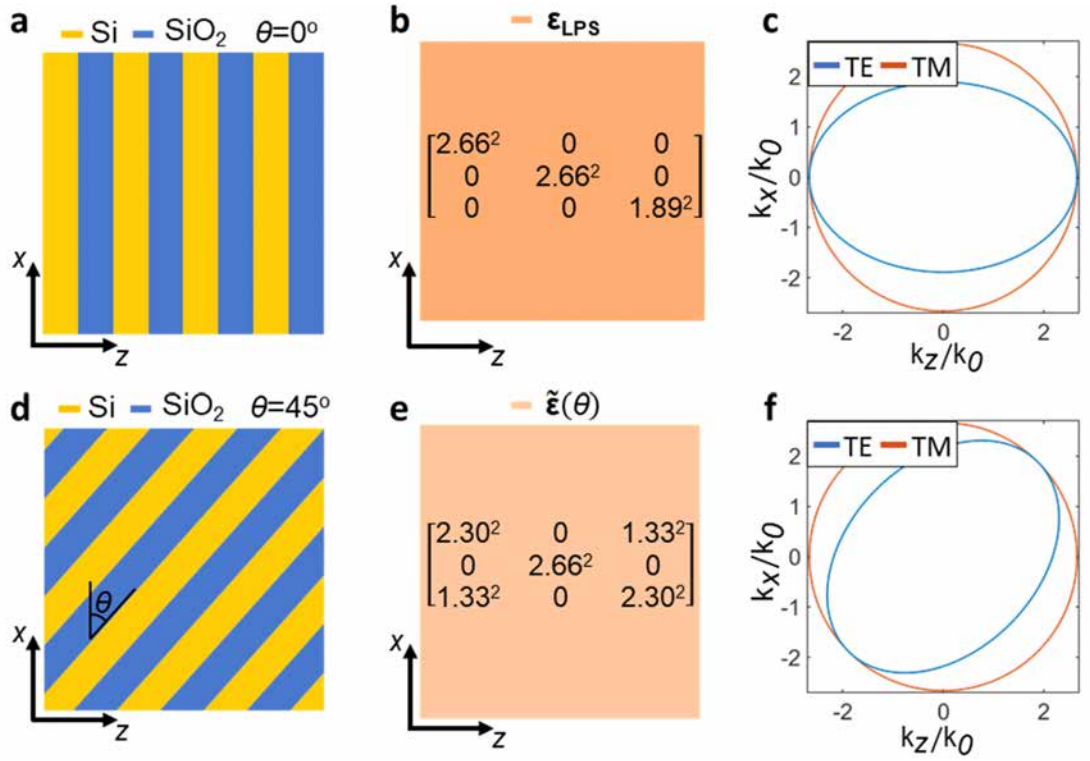

Figure 4.3: a,d) Schematic representation of a) a non-tilted and d) a 45° tilted LPS. b,e) Schematic representation and permittivity tensor of the metamaterial equivalent to the LPS shown in a) and d) respectively assuming deep subwavelength regime and refractive indices $n_1 = 3.476$ and $n_2 = 1.444$. c,f) Dispersion diagrams for the TE (blue) and TM (red) plane wave propagating along the anisotropic medium shown in b) and e) respectively.

tilted LPS is calculated by properly rotating the tensor of the non-tilted structure as [183]:

$$\tilde{\varepsilon}(\theta) = \mathbf{T}^{-1}(\theta)\varepsilon_{\mathrm{LPS}}\mathbf{T}(\theta) = \begin{bmatrix} \tilde{n}^2_{xx}(\theta) & 0 & \tilde{n}^2_{xz}(\theta) \\ 0 & \tilde{n}^2_{yy} & 0 \\ \tilde{n}^2_{xz}(\theta) & 0 & \tilde{n}^2_{zz}(\theta) \end{bmatrix}, \tag{4.1}$$

where $\mathbf{T}$ is the rotation matrix around the y-axis. The elements of the tensor $\tilde{\varepsilon}(\theta)$ are calculated from the tensor components of the non-tilted SWG as:

$$\begin{aligned} \tilde{n}^2_{xx}(\theta) &= n^2_{\parallel}\cos^2(\theta) + n^2_{\perp}\sin^2(\theta), \\ \tilde{n}^2_{yy} &= n^2_{\parallel}, \\ \tilde{n}^2_{zz}(\theta) &= n^2_{\parallel}\sin^2(\theta) + n^2_{\perp}\cos^2(\theta), \\ \tilde{n}^2_{xz}(\theta) &= (n^2_{\perp} - n^2_{\parallel})\cos(\theta)\sin(\theta). \end{aligned} \tag{4.2}$$

This set of equations is used to calculate the permittivity tensor components of the equivalent metamaterial to a tilted LPS from the tensor components of the non-tilted LPS. Therefore, the simplicity and limitations of the LPS model in non tilted SWG structures are shared with the model of tilted SWG metamaterials. For the sake of illustration, the range of synthesizable components obtained by tilting the LPS under study is shown in Fig. 4.4, ranging from $\theta = 0°$ where the structure is a longitudinal LPS to $\theta = 90°$, where the structure is as a transversal LPS. Moreover, in the in-between angles the structure behaves as a biaxial crystal: $n_{xx} \neq n_{yy} \neq n_{zz}$,

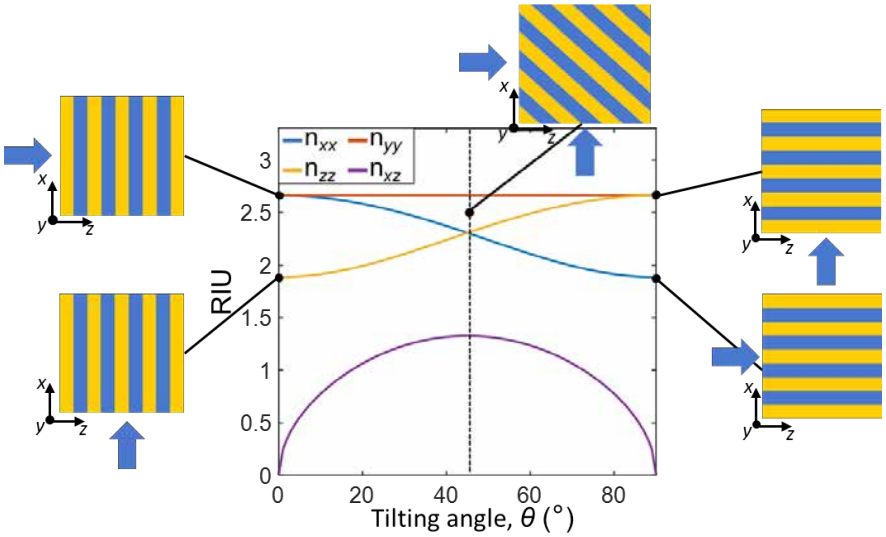

Figure 4.4: Available set of permittivity tensor components synthesized by tilting the silicon segments of an SOI LPS in the deep subwavelength regime.

enabling to control the birefringence as the n_{yy} is not affected by the tilting. Figure 4.3e shows the resulting permittivity tensor components assuming an exemplary rotation of $\theta = 45°$. An interesting property of the tilted permittivity tensor, $\tilde{\varepsilon}(\theta)$, is the independence of its determinant with the tilting angle, that is: $|\tilde{\varepsilon}(\theta)| = n_{\parallel}^4 n_{\perp}^2$. This property, derived from the index conservation law [184], is also satisfied by the bricked SWG topology discussed in section 4.3.

To calculate the dispersion relations for the TE/TM waves propagating along this tilted uniaxial crystal, the wavevector components of the equations of a wave propagating along a non-tilted LPS, $k_x^{'}$ and $k_z^{'}$ [Eq. (3.11) and Eq. (3.12)] are rotated as $k_x = k_x^{'}\cos(\theta) + k_z^{'}\sin(\theta)$ and $k_x = k_x^{'}\sin(\theta) - k_z^{'}\cos(\theta)$, obtaining the dispersion relations:

$$\text{TE waves}: k_x^2\left(\frac{\tilde{n}_{xx}(\theta)}{n_{\parallel}n_{\perp}}\right)^2 + k_z^2\left(\frac{\tilde{n}_{zz}(\theta)}{n_{\parallel}n_{\perp}}\right)^2 + 2k_xk_z\left(\frac{\tilde{n}_{xz}(\theta)}{n_{\parallel}n_{\perp}}\right)^2 = k_0^2, \tag{4.3}$$

$$\text{TM waves}: \frac{k_x^2}{\tilde{n}_{yy}^2} + \frac{k_z^2}{\tilde{n}_{yy}^2} = k_0^2. \tag{4.4}$$

These dispersion relations are an ellipse with a rotation angle θ for TE polarized waves and a circle for TM polarized waves, as shown in Fig. 4.3f for the exemplar $\theta = 45°$ LPS.

Finally, once the homogenization of tilted LPS has been discussed, the algorithm to homogenize on-chip tilted SWG structures is proposed (see Fig. 4.5): First, the corresponding LPS or PSS of the tilted SWG waveguide under study is extracted. That is, the LPS/PSS with the same period, duty cycle, materials and silicon thickness for the case of the PSS. The period of the extracted LPS/PSS must be from the non-rotated structure (Λ_0). Second, the permittivity tensor of the equivalent homogeneous anisotropic metamaterial of the extracted LPS/PSS is calculated as shown in section 3.3. Third, the permittivity tensor $\varepsilon_{\text{LPS/PSS}}$ calculated in the previous step is rotated by using Eq. (4.2) and it is introduced into the core of the homogeneous waveguide. The accuracy of this model is studied in next section together with the waveguiding properties of tilted SWG metamaterials.

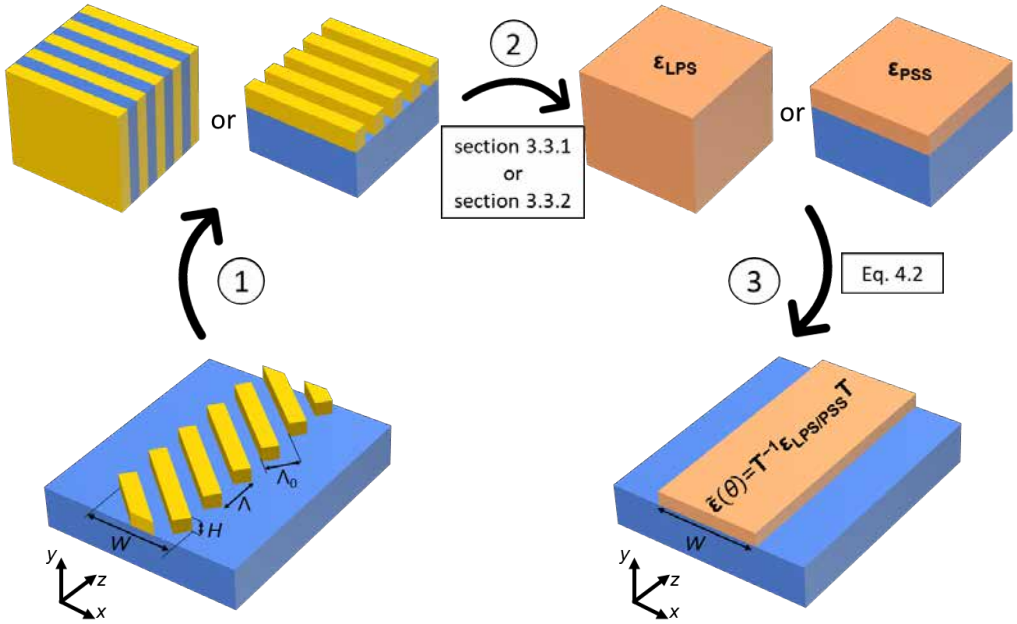

Figure 4.5: Algorithm to calculate the equivalent homogeneous material of a tilted SWG waveguide: 1) Extract the corresponding LPS or PSS of the SWG waveguide under study. That is, the LPS/PSS with the same period, duty cycle, materials and silicon thickness for the case of the PSS. It is important to note that the LPS/PSS is considered with the non-tilted period Λ_0. 2) Homogenize the LPS/PSS by using the theory detailed in section 3.3. 3) Rotate the permittivity tensor $\varepsilon_{\text{LPS/PSS}}$ by using Eq. (4.2) and introduced the resulting permittivity tensor into the core of the homogeneous waveguide.

4.2.2. Waveguiding properties of tilted SWG metamaterials

To study the waveguiding properties of tilted SWG metamaterials, the wave propagation along a tilted multimode SWG waveguide ($W = 3.25\,\mu$m, $\Lambda_0 = 0.25\,\mu$m and DC = 0.5) in a standard 220 nm thick silicon platform is studied. The analysis starts by calculating the fundamental TE and TM modes supported by the tilted SWG waveguide under study and its equivalent homogeneous anisotropic waveguide for different tilting angles. While the modes in the periodic waveguide are calculated with time consuming 3D-FDTD modal simulations (FullWAVE), the solutions in the homogeneous waveguide are calculated with fast FEM anisotropic simulations (FIMMWAVE). In this case, the PSS homogenization has been used as the period is larger than $\Lambda_0 = 0.24\,\mu$m, which is the maximum period for the LPS model with SOI materials at $\lambda = 1.55\,\mu$m. Figure 4.6a compares the effective indices of the TE and TM modes for both waveguides, providing similar results thus validating the proposed homogenization model of tilted SWG metamaterials. Moreover, it is also shown that the effective index of the TE polarized modes is strongly affected by the tilting angle, while the TM mode effective index barely changes. This behavior is expected as the TE modes mainly depends on the n_{xx} component of the tensor while the TM modes depends on the n_{yy} component. Then, the wavelength dispersion of the fundamental TE and TM modes in the tilted SWG is analyzed (see Fig. 4.6b), showing again how the TE modes are much more affected by the tilting angle than TM modes. Moreover, it also shown how the dispersion of the effective index of the TE polarized modes is also notably reduced by tilting the silicon segments. Therefore, tilted SWG metamaterials are ideal structures for polarization management by controlling the birefringence and dispersion of the devices.

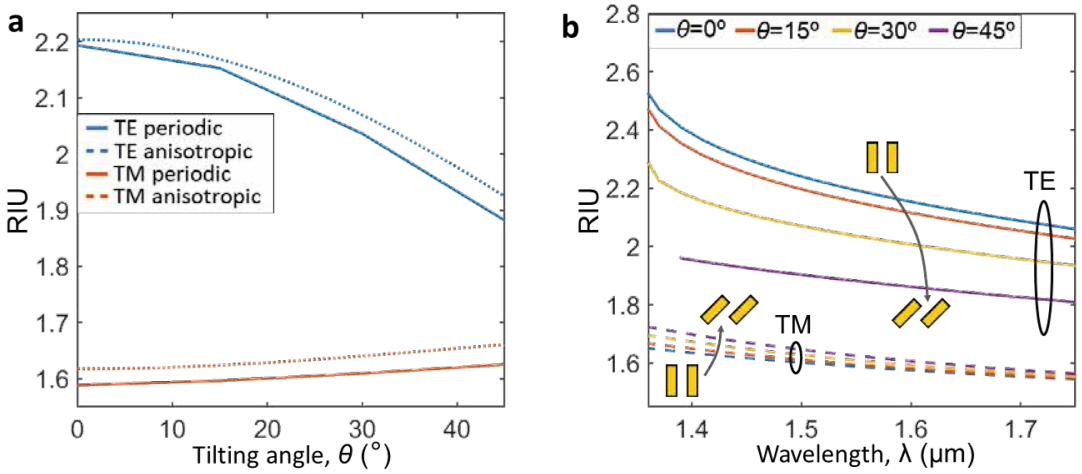

Figure 4.6: a) Effective indices of the fundamental TE and TM modes of a tilted SWG waveguide and its equivalent homogeneous anisotropic waveguide with a silicon thickness $H = 220$ nm, a width $W = 3.25$ µm, a non-tilted period $\Lambda_0 = 0.25$ µm and duty cycle DC = 0.5 for different tilting angles ranging from $\theta = 0°$ to $\theta = 45°$ at $\lambda = 1.55$ µm. b) Wavelength dependence of the effective index for the fundamental TE and TM modes of the tilted SWG waveguide described in (a) calculated using the periodic approach.

4.2.3. Proof of concept of tilted SWG metamaterials

To experimentally validate the tuning properties of tilted SWG metamaterials, a set of tilted SWG waveguide are fabricated and characterized. For that purpose, a fabrication mask including the input/output light scheme, the specific configuration enabling to measure the desired behavior and the proposed devices under test is drawn. For the input/output light scheme, edge couplers are used as the tilted SWG waveguides need to be characterized for both polarizations. The configuration used to measure the tuning properties of tilted SWG metamaterials is a Mach-Zehnder Interferometer (MZI) configuration where a tilted SWG waveguide is placed in one arm of the MZI while a reference non-tilted SWG waveguide is placed in the other arm (Fig. 4.7a). This architecture estimates the difference of the group indices between the waveguides placed in both arms by studying the resulting interferogram at the output of the MZI. Figure 4.7b shows three MZI architectures already drawn in the mask layout with three different tilting angles. The fabricated tilting angles ranges from $\theta = 0°$ to $\theta = 45°$ with a 7.5° step. The tapers between the homogeneous and SWG waveguides in the MZI arms are 30 µm long to avoid transition losses, and the SWG waveguides are 600 µm long to accurately characterize the group index variation. Figures 4.7c and 4.7e show a zoom into the MZI arms where the non-tilted SWG waveguide and the tilted SWG waveguide are placed. A period of $\Lambda_0 = 0.25$ µm has been used to ease the fabrication while working far from the Bragg regime. To reduce the influence of fabrication jitter, narrow single-mode SWG waveguides are preferred, so a width of $W = 1$ µm is chosen [185]. Once the fabrication mask has been finished, it is submitted to the foundry which fabricates the mask layout in a 220 nm SOI platform with 3 µm buried oxide (BOX) and deposits a 3 µm thick upper SiO_2 cladding by plasma enhanced chemical vapor deposition (PECVD). A set of SEM images of the fabricated non-tilted and tilted SWG waveguide prior to the cladding deposition are shown in Figs. 4.7d and 4.7f respectively.

To characterize the tilted SWG waveguides, the output interferogram of the MZI in any of the output ports is measured. Figure 4.8a shows an exemplar interferogram for the MZI with a tilted SWG with an angle $\theta = 37.5°$. The fringe separation, known as free spectral range (FSR), is used to calculate the difference between the group indices of both waveguides as:

$$\Delta n_g = n_{g1} - n_{g2} = \frac{\lambda_0^2}{L \cdot FSR}, \tag{4.5}$$

where L is the length of the interferometer arms. Figure 4.8b shows the estimated group index difference obtained from the FSR analysis of the different fabricated structures. An excellent agreement with the simulated group index difference is noted for both polarization. By simulating the relation between the group index and effective index in both SWG waveguides, the effective index difference can be estimated from the measured group index difference. In particular, for the 45° tilt SWG waveguide an effective index variation of $\Delta n_{eff}^{TE} \sim 0.23$ RIU for the TE mode and only $\Delta n_{eff}^{TM} \sim 0.01$ RIU for the TM mode is found. These results confirm birefringence engineering of tilted SWG metamaterials, and they were published in Ref.

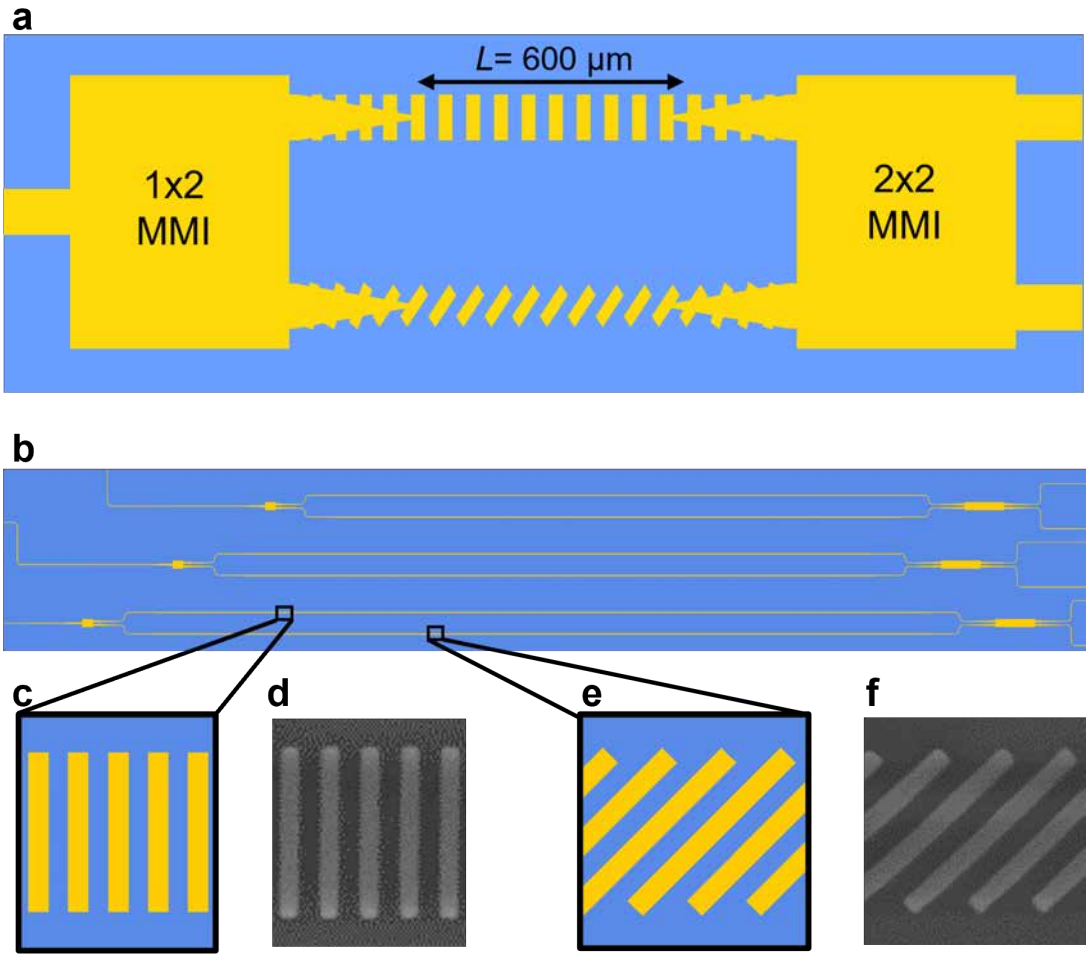

Figure 4.7: a) Schematic representation of the Mach-Zehnder interferometer configuration used to measure the group index difference. b) Three exemplary MZIs drawn in the mask layout with different rotation angles. c,e) Zoom-in into the arms of a MZI where a non-tilted and a tilted SWG waveguide have been drawn. d,f) SEM image of a fabricated non-tilted and tilted SWG waveguides.

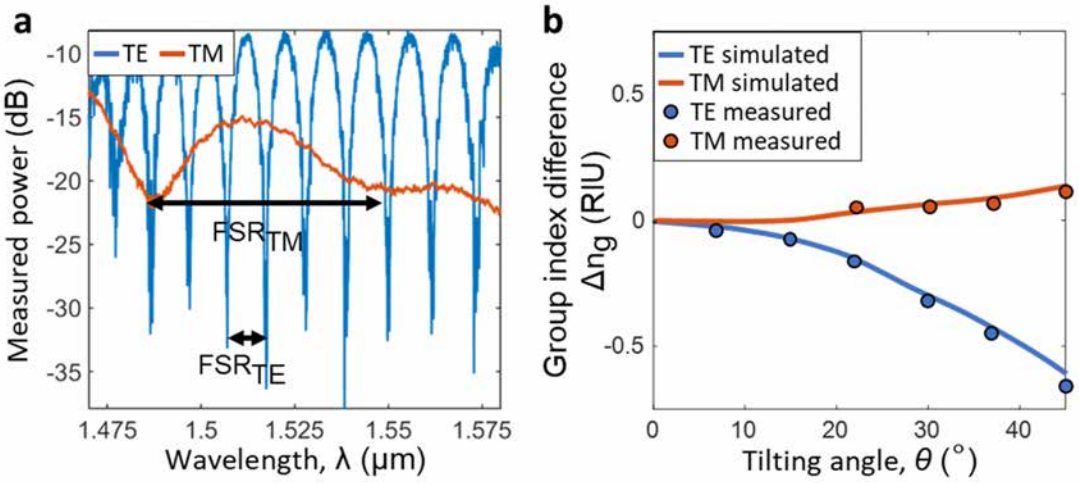

Figure 4.8: a) Measured interferogram for MZI with a tilted SWG waveguide with a titlting angle $\theta = 37.5°$. b) Group index difference of the measured (dots) and simulated (solid lines) tilted SWG waveguide for different tilting angles.

[154] as they pave the way for the design of polarization management devices such as the polarization beam splitter discussed in the next section.

4.2.4. Design of a directional coupler polarization beam splitter

The control over the birefringence offered by tilted SWG metamaterials is leveraged to design a high-performance asymmetric directional coupler polarization beam splitter (DC-PBS). The basic idea exploited in this design is to control the coupling of the TE polarization by tilting the segments of one of the waveguides without affecting the cross-coupling for TM polarization. This section describes the demonstration of the proposed device, from its theoretical validation to the design and experimental characterization.

Working principle of an asymmetrical directional coupler polarization beam splitter

Directional coupling is arguably the most widely used mechanism for polarization splitting in integrated photonic chips. A conventional directional coupler is composed of two parallel waveguides placed in close proximity, allowing power transfer between them. At the distance known as coupling length, L_c all the transferable power from one waveguide travels to the other waveguide and, then, it comes back to the original waveguide in the same distance. According to coupled mode theory [167], the maximum power transferred between both waveguides is inversely proportional to the detuning, δ, between the waveguides, $\delta = (n_{\text{eff}_u} - n_{\text{eff}_b})\pi/\lambda$, where $n_{\text{eff}_{u,b}}$ are the effective indices of modes of the upper and bottom waveguides of the directional coupler. When both waveguides are equal, they support the same modes so the detuning is zero. In this situation, the input light in the directional coupler is completely exchanged between both arms for both polarizations. To design a polarization beam splitter in the symmetric case, the coupling lengths of the TE and TM polarizations, L_c^{TE} and L_c^{TM} have to satisfy the splitting condition, that is: $L_{\text{device}} = mL_c^{TE} = nL_c^{TM}$, where L is the device length and m and n are integers with $|m-n|$ being an odd number. This device, known as

symmetric DC-PBS, is schematised in Fig. 4.9a for m=2, n=1. The operational bandwidth and robustness of symmetric DC-PBSs are limited because they exhibit a wavelength-dependent behavior for both polarizations caused by the narrow-band phase matching conditions. To overcome this problem, asymmetrical DC-PBS are preferred. In these devices, the phase matching condition is satisfied by only one of the polarizations, which couples to the bottom arm of the directional coupler, while the other polarization cannot be transferred as it does not satisfy the phase matching condition. This behavior is schematised in Fig. 4.9b. This configuration frequently presents a better performance thus it is more used in the literature. However, the techniques to break the symmetry usually make the fabrication processes more complex, requiring multiple etch steps or the deposition of additional materials [186–189]. In the proposed device, the asymmetry is achieved just by tilting the segments of the top SWG waveguide (see Fig. 4.9c), which do not increment the complexity of the fabrication process.

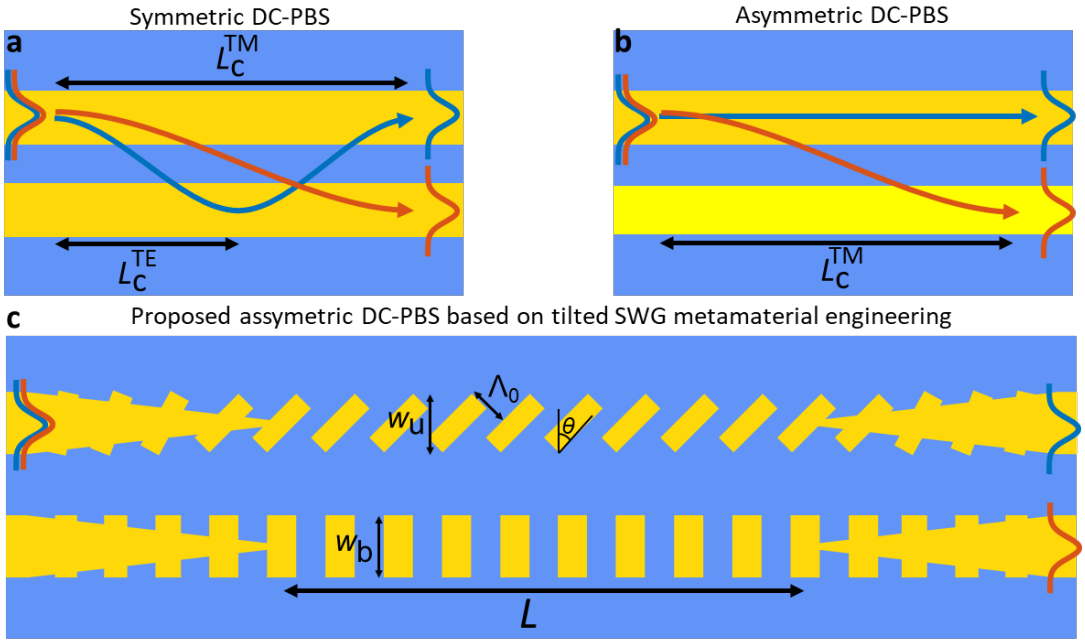

Figure 4.9: Schematic representation (top view) of a) a symmetric directional coupler polarization beam splitter and b) an asymmetric directional coupler polarization beam splitter. The blue/red lines represent TE/TM polarizations. In the symmetric case, as both waveguides are equal, both polarizations couple between both waveguides. In the asymmetric case, only the polarization satisfying the phase matching condition. c) Schematic representation (top view) of the proposed asymmetric DC-PBS where the asymmetry is achieved just by tilting the silicon segments of the upper waveguide an angle θ.

Breaking the phase matching condition with a tilted SWG metamaterial

To demonstrate the breaking of the phase matching condition, the device shown in Fig. 4.9c is analyzed. A 100 nm wide silicon strip has been included inside of both SWG waveguides to smooth the transition between the input/output homogeneous waveguides and the SWG structures, shortening the transitions. The electromagnetic field propagation along the proposed directional coupler is studied. First, it is assumed that both waveguides are non-tilted, (see Fig. 4.10a). In this case, as both waveguides are equal, both polarizations satisfy

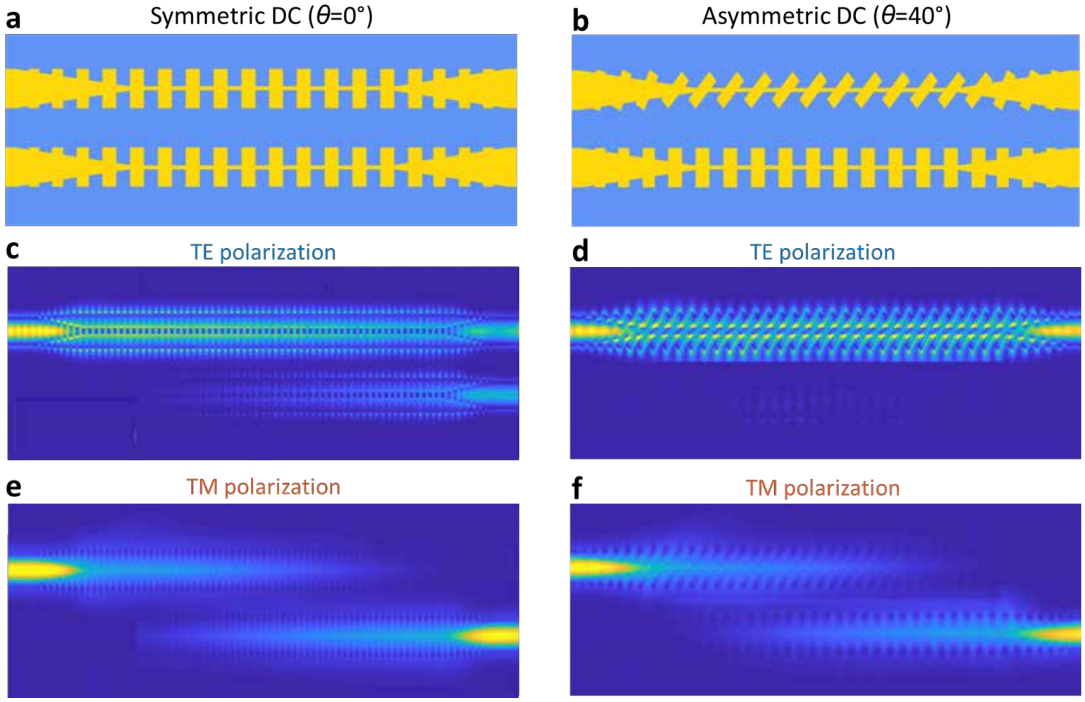

Figure 4.10: a,b) Schematic representation of a directional coupler polarization beam splitter composed of two SWG waveguides when a) both waveguides are equal and b) when the upper waveguide is tilted. c,d) TE polarized wave propagating along the c) symmetric DC and d) asymmetric directional couplers. e,f) TM polarized wave propagating along the e) symmetric DC and f) asymmetric directional couplers.

the phase matching condition, traveling from one waveguide to the other but with a different rate as the coupling length of both polarizations are different, $L_\pi^{\mathrm{TE}} \neq L_\pi^{\mathrm{TM}}$ (see Fig. 4.10c and Fig. 4.10e). In the proposed device (see Fig. 4.10b), the silicon segments of the upper waveguides are tilted. In this case, the tilting angle changes the n_{xx} and n_{zz} components of the equivalent homogeneous material, but the n_{yy} component of both waveguides is the same. Therefore, TM modes of the individual waveguides barely changes while the TE modes are affected. This behavior is easily observed by studying the propagation of both polarizations. Only the TM polarization can travel from one waveguide to the other while the TE stays in the same waveguide (see Fig. 4.10f and Fig. 4.10h). It is clear that the phase matching condition is effectively broken for the TE polarization while the TM polarization can be totally transferred from one waveguide to the other, allowing the design of an asymmetrical directional coupler. In this design, the waveguide widths have been set to $w_u = w_b = 0.6\,\mu\mathrm{m}$ to sufficiently confine the field avoiding leakage losses [190]. The period of the structure is $\Lambda_0 = 0.275\,\mu\mathrm{m}$, with a duty cycle DC = 0.5 to facilitate fabrication.

Device design and optimization

Figure 4.11a shows an schematic representation of the proposed tilted SWG directional coupler with the upper arm tilted an angle of 40° and with both waveguides having a period $\Lambda = 0.275/\cos(40°)$. A silicon strip has been included in-between both waveguides. The width of this strip, w_s, will be used to optimize the device bandwidth. To evaluate the

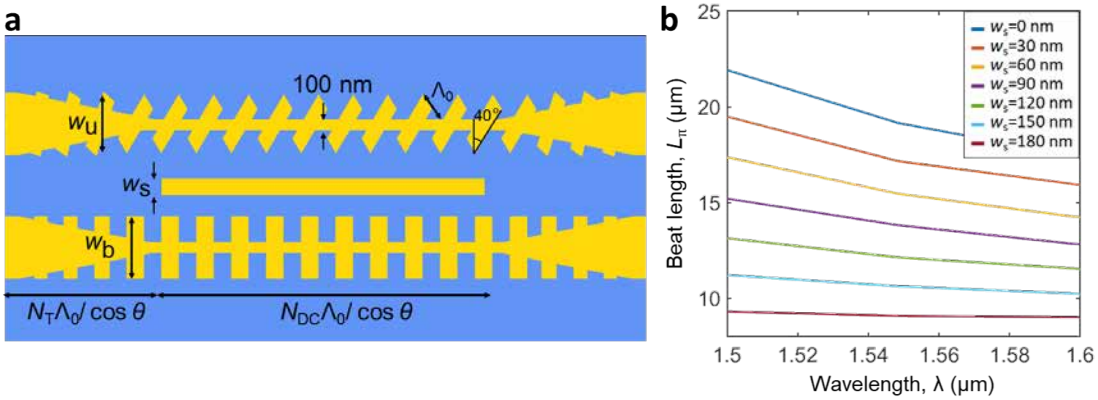

Figure 4.11: a) Schematic representation of the proposed asymmetric directional coupler polarization beam splitter. b) Beat length of the proposed directional coupler for different widths of the central silicon strip.

performance of the preliminary directional coupler, the insertion loss (IL) and the extinction ratio (ER) are used, defined as:

$$\begin{aligned} \mathrm{IL}^{\mathrm{TE}} &= \mathrm{P}_{\mathrm{bar}}^{\mathrm{TE}}/\mathrm{P}_{\mathrm{in}}^{\mathrm{TE}}, \qquad \mathrm{ER}^{\mathrm{TE}} = \mathrm{P}_{\mathrm{cross}}^{\mathrm{TE}}/\mathrm{P}_{\mathrm{bar}}^{\mathrm{TE}}, \\ \mathrm{IL}^{\mathrm{TM}} &= \mathrm{P}_{\mathrm{cross}}^{\mathrm{TM}}/\mathrm{P}_{\mathrm{in}}^{\mathrm{TM}}, \qquad \mathrm{ER}^{\mathrm{TM}} = \mathrm{P}_{\mathrm{bar}}^{\mathrm{TM}}/\mathrm{P}_{\mathrm{cross}}^{\mathrm{TM}}, \end{aligned} \tag{4.6}$$

where $\mathrm{P}_{\mathrm{bar}}^{\mathrm{TE/TM}}$ and $\mathrm{P}_{\mathrm{cross}}^{\mathrm{TE}}$ are the power in the fundamental TE/TM mode in the bar and cross ports and $\mathrm{P}_{\mathrm{in}}^{\mathrm{TE/TM}}$ is the power of the fundamental TE/TM mode at the input port. To calculate these parameters, the proposed device is analyzed with 3D-FDTD simulations for different wavelengths with FullWAVE. The dashed lines in Fig. 4.12 show the simulated IL and ER of the width of the silicon strip is zero, $w_s = 0$, achieving an ER > 20 dB over a 40 nm bandwidth with negligible IL, being limited mainly by the wavelength-dependent phase matching condition for TM polarization. To optimize the bandwidth of the device, the silicon strip in between both SWG waveguides is included, obtaining a bridged directional coupler. From an intuitive point of view, this central strip affects only the even TM supermode, allowing to engineer the coupling length, defined as:

$$L_\pi^{\mathrm{TM}} = \frac{\lambda_0}{2[n_e(\lambda) - n_o(\lambda)]} \tag{4.7}$$

where λ_0 is the free-space wavelength, and $n_{e,o}$ are the effective indices of the even and the odd TM polarized supermodes. The coupling lengths for TM polarization for the proposed directional coupler are shown in Fig. 4.11b for different central silicon strip widths. It is observed that as the strip is widened the coupling length is reduced. Moreover, the device also becomes less wavelength dependent as the variation of the beat length with wavelength is, to first order, proportional to the square of the beat length. Increasing the width over 150 nm has an undesired influence on the losses of the device, which is why a 150-nm-wide silicon strip is chosen, yielding an almost flat wavelength response with a small penalty in IL. Solid lines in Fig. 4.12 show the performance of the optimized PBS design with a tilt angle $\theta = 40°$ and a silicon strip width $w_s = 150$ nm, obtaining an ER higher than 20 dB over an 86 nm bandwidth for both polarizations, with IL lower than 1 dB. The input tapers and the coupling region are $N_T = 8$ periods and $N_{DC} = 27$ periods long, respectively, resulting in a device length of only 14 μm.

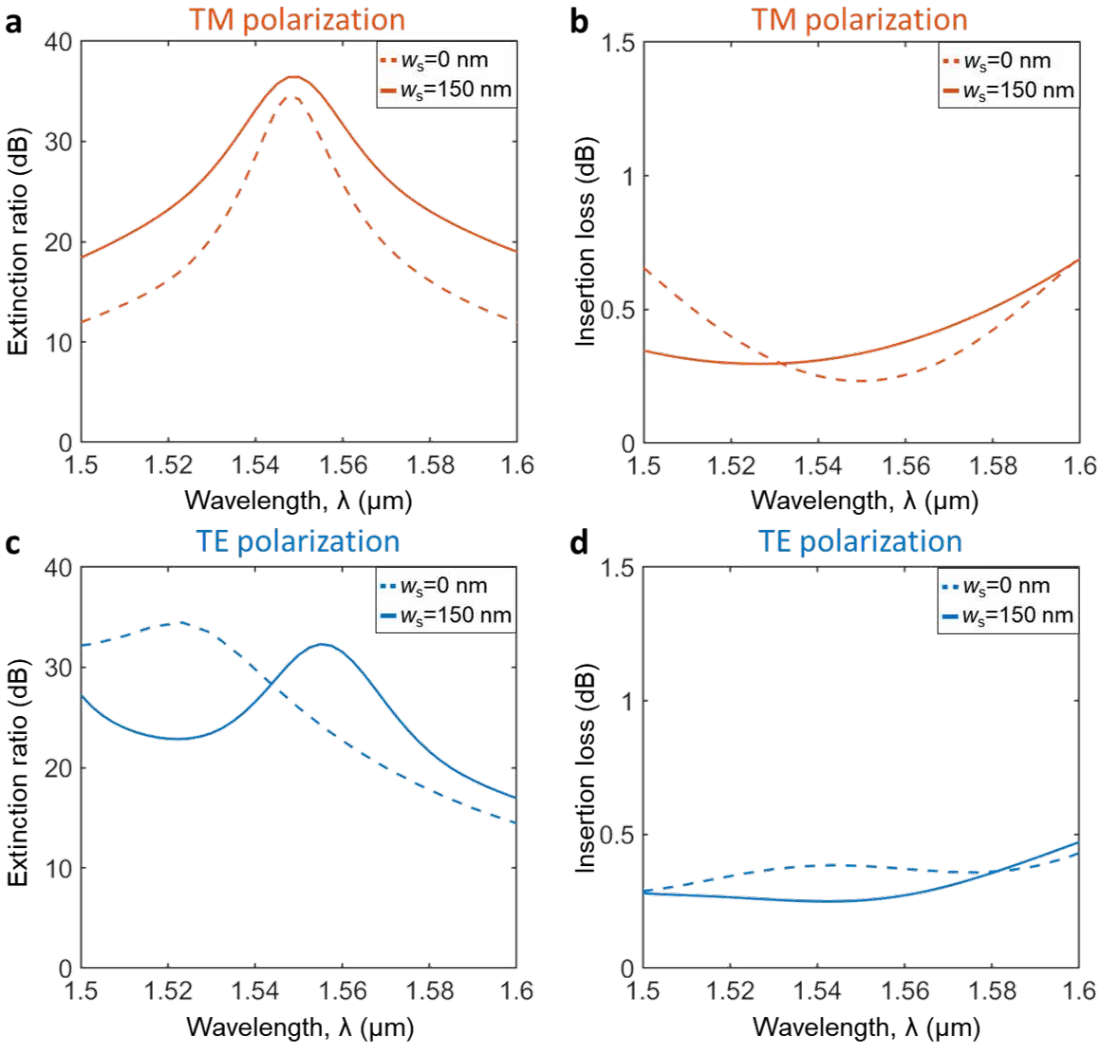

Figure 4.12: Simulated extinction ratio for the a) TE and b) TM polarizations, and insertion loss for the c) TE and d) TM polarizations, of the tilted SWG directional coupler with (solid line) and without (dashed lines) the central silicon strip.

Experimental validation

The proposed device is prepared for fabrication in a MPW of ANT foundry [173]. Figure 4.13a shows the full fabrication mask submitted for the MPW run where the DC-PBS devices occupy the red outlined area. Figure 4.13b shows a zoom into the area where the DC-PBS are drawn. Both light injecting schemes have been used to measure the device performance. Figure 4.13c shows the drawn configuration used to measure the devices with grating coupler, including the input grating, the device under test and both output grating couplers. Figure 4.13d shows the drawn configuration used to measure the device with edge coupler, including the input edge coupler, the device under test and the two output arms which go directly to the opposed chip facet. A comparison between the drawn device in the mask and a SEM image is shown in Figs. 4.13e and 4.13f.

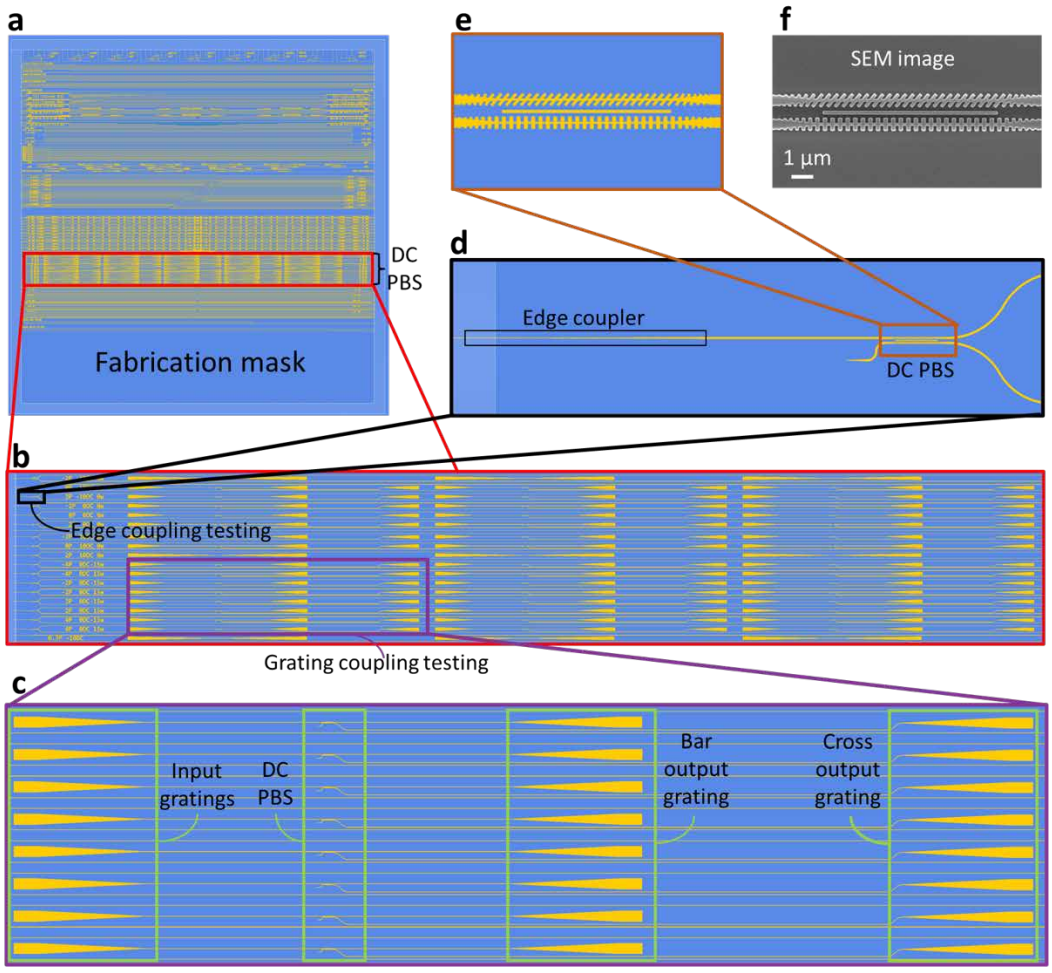

Figure 4.13: a) Full fabrication mask including many different designs. b) Zoom-in into the red zone outlined in (a) where the DC-PBS are drawn. This zone includes devices measured by injecting the light with edge coupler and by grating couplers. c) Zoom-in into the purple zone outlined in (b) where the DC-PBS measured with the grating coupler setup are drawn. d) Zoom-in into the black zone outlined in (b) where the DC-PBS measured with edge coupler are drawn. e) Zoom-in into a DC-PBS. f) SEM image of a fabricated DC-PBS.

The fabricated devices are characterized by measuring the power in both output ports (bar and cross) when the device is excited through the input port using the corresponding setup depending on the chip access method. A reference waveguide is used to calibrate the setup and fiber-to-chip coupling losses for both polarizations. The polarization ER is calculated by dividing the power in both output ports. The measured ER and IL of the fabricated device for both polarizations are shown in Figs. 4.14a and 4.14b after applying the minimum phase technique to filter spurious oscillations [174] not related with the device behaviour as they only appeared when measuring with the edge coupling setup. The fabricated nominal device achieves an ER in excess of 15 dB and an IL below 1 dB for both polarizations over a 72 nm bandwidth (1505–1577 nm). Figure 4.14a indicates that for long wavelengths, the device performance is limited by the ER for TE polarization. Operation at longer wavelengths can be achieved by increasing the duty cycle of the SWG structure, to enhance the modal confinement, which in turn suppresses the coupling of the TE mode to the cross port. Note

that, for TM polarization, the increasing in duty cycle will only result in a minor detuning of the phase matching condition. In Figs. 4.14c and 4.14d, the measured device performance when the duty cycle is increased from 50% to 60%, i.e., the silicon blocks are 28 nm longer, and the overall device length is enlarged two periods. This biased device yields IL below 1 dB and ER in excess of 15 dB at longer wavelengths over a 67 nm bandwidth. The reduction on the duty cycle from 20 dB to 15 dB with this variation of the block size shows the resiliency of the device to fabrication errors. Note that, for TM polarization, the increasing in duty cycle will only result in a minor detuning of the phase matching condition. In Figs. 4.14c and 4.14d, the measured device performance when the duty cycle is increased from 50% to 60%, i.e., the silicon blocks are 28 nm longer, and the overall device length is enlarged two periods. This biased device yields IL below 1 dB and ER in excess of 15 dB at longer wavelengths over a 67 nm bandwidth. Table 4.1 compares the proposed device with some similar directional coupler devices in 220 nm SOI. This comparison shows that the proposed structure stands out for its low insertion loss and small footprint.

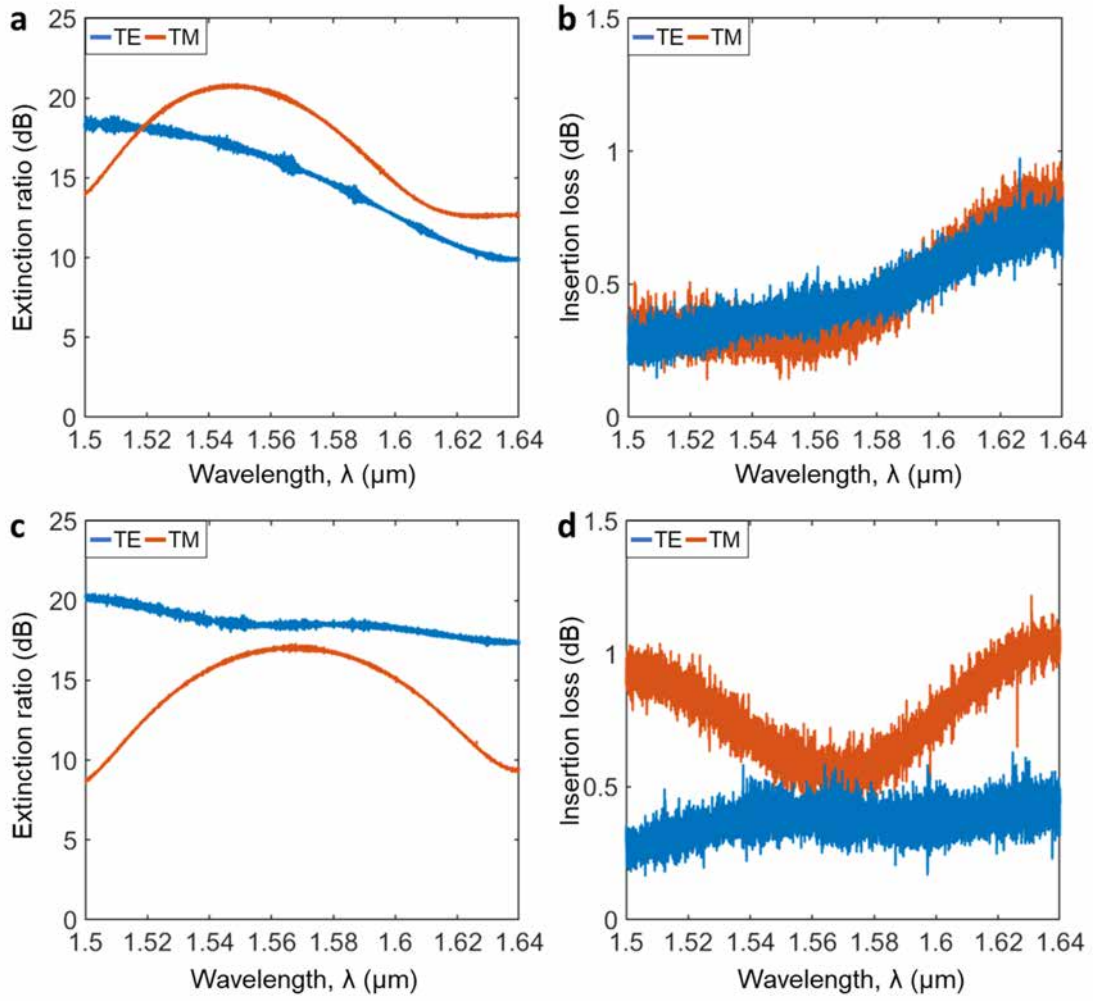

Figure 4.14: Measured a) extinction ratio and b) insertion loss of the nominal device. The IL is below 1 dB, and the ER is better than 15 dB in a bandwidth of 72 nm. Measured c) extinction ratio and d) insertion loss for a device with a duty cycle increased by 10%. The IL are <1 dB, and the extinction ratio is >15 dB in a bandwidth of 67 nm.

Ref	Device	Length (μm)	Simulation		Experimental	
			Max. IL (dB) @ BW (nm)	Min. EL (dB) @ BW (nm)	Max. IL (dB) @ BW (nm)	Min. EL (dB) @ BW (nm)
[191]	Conventional SWG DC	7.2	1@180	10@170	2.5@150	10@150
[192]	Cascaded skin-depth engineered DC	130	0.4@250	20@250	-	-
[138]	Conventional SWG MMI	133	1.15@95	20@110	2.5@84	11.7@84
[158]	Tilted SWG MMI	118	1.6@130	20@130	1@120	13@120
[132]	This work	14	0.6@100	20@86	1@143	15@72

Table 4.1.: Performance comparison of recently demonstrated subwavelength-enhanced polarization beam splitters.

4.2.5. Additional contributions using tilted SWG metamaterials

After the proposal of Tilted SWG metamaterials, they have been applied to design some polarization management devices in collaboration with the Spanish national research council (Consejo superior de Investigaciones científicas, CSIC). From this collaboration, some notorious contributions have been made, including:

- **Multimode interferometer polarization beam splitter based on tilted SWG metamaterial:** Multimode interferometers can be used to splits the input polarizations by following a similar philosophy to the one discussed in symmetric directional couplers. If the beat lengths for the TE and TM polarizations satisfy the aforementioned splitting condition, the input polarizations are split. However, this condition is not easily achievable in high-index contrast platforms such as SOI. To solve that problem, a tilted SWG metamaterial has been used as the core of the MMI, enabling to engineer the beat lengths to satisfy the splitting condition. This device has been designed [156] and experimentally validated [158], showing an excellent performance.
- **Non-birefringence SOI waveguides:** Submicron SOI waveguides are highly birefringent because of the high-index contrast of SOI materials and the usual non-square cross sections of the waveguides. Tilted SWG metamaterials have been used to cancel out the birefringence by reducing the n_{xx} component of the tensor below the n_{yy}. This engineering has enabled the design of a non-birefringence waveguide with a non-square cross section (550 nm × 300 nm) [157].
- **Patent:** Tilted SWG metamaterials have been patented, including the geometry, the homogenization method and the proposed devices discussed in this Thesis. This patent has been awarded by Spanish Patent and Trademark Office in the category of best young inventor and it has been licensed by the company Alcyon Photonics S.L for its industrial exploitation.

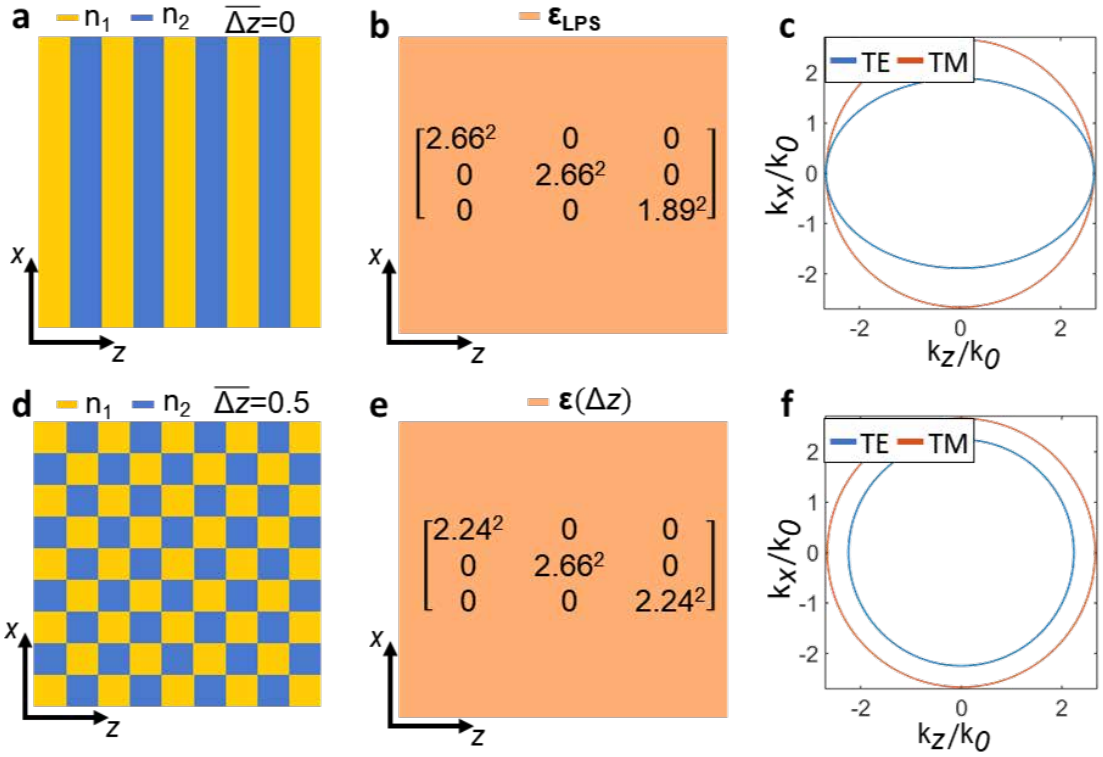

Figure 4.15: a,d) Schematic representation of a) a non-bricked and d) a $\Delta z = 0.5$ bricked LPS. b,e) Schematic representation and permittivity tensor of the metamaterial equivalent to the LPS shown in a) and d) respectively assuming deep subwavelength regime and refractive indices $n_1 = 3.476$ and $n_2 = 1.444$. c,f) Dispersion diagram for the TE (blue) and TM (red) plane wave propagating along the anisotropic medium shown in b) and e) respectively.

4.3. Bricked SWG periodic structures

The bricked SWG structure is the second SWG metamaterial topology proposed in this chapter. This topology is also an important contribution of this Thesis which is being exploited in recent articles [155, 162]. This section discusses the unique optical properties of bricked SWG topology.

4.3.1. Homogenization model of the bricked SWG metamaterial

To obtain an analytical model of bricked SWG metamaterial, a simple LPS in SOI platform is again studied (see Fig. 4.15a). For the sake of simplicity, deep SWG regime and a 50% duty cycle is also chosen in this case. The permittivity tensor of the equivalent homogeneous anisotropic metamaterial is then calculated with the well known Rytov equations $\varepsilon_{\text{LPS}} = \text{diag}[n_{\parallel}^2, n_{\parallel}^2, n_{\perp}^2] = [2.66^2, 2.66^2, 1.89^2]$ (see Fig. 4.15b). Any TE/TM plane wave propagating along this homogeneous anisotropic medium has a wavevector $\vec{k}$ following the dispersion relation shown in Fig. 4.15c as discussed in section 3.2. Then, the LPS is transformed into a bricked LPS by periodically partitioning the structure along the transversal direction and shifting the resulting blocks as shown in Fig. 4.15d for the exemplary case where the blocks

are shifted half of the period. To obtain the permittivity tensor of the metamaterial equivalent to the bricked LPS, $\varepsilon(\Delta z)$, the boundary cases $\Delta z = 0$ and $\Delta z = \Lambda_z/2$ are first analyzed. The shifting will be always given normalized to the period in the z-axis: $\overline{\Delta z} = \Delta z/\Lambda_z$, so the cases under study are $\overline{\Delta z} = 0$ and $\overline{\Delta z} = 0.5$. When there is not shifting, the structure becomes the conventional LPS shown in Fig. 4.15a, so this case is straightforward and it is already solved. For the second case, $\overline{\Delta z} = 0.5$, four considerations are made based on the homogenization of tilted SWG structures:

1. The permittivity tensor of the bricked LPS is a diagonal permittivity tensor:

$$\varepsilon(\overline{\Delta z}) = \begin{bmatrix} \hat{n}_{xx}^2(\overline{\Delta z}) & 0 & 0 \\ 0 & \hat{n}_{yy}^2 & 0 \\ 0 & 0 & \hat{n}_{zz}^2(\overline{\Delta z}) \end{bmatrix}, \tag{4.8}$$

   so its determinant is given by the product: $|\varepsilon(\overline{\Delta z})| = \hat{n}_{xx}^2\,\hat{n}_{yy}^2\,\hat{n}_{zz}^2$.

2. The determinant of the permittivity tensor is invariant with the shifting (index conservation law [184]), so it can be calculated from the non-shifted structured as $|\varepsilon(\overline{\Delta z})| = |\varepsilon(0)| = n_{\parallel}^4 n_{\perp}^2$,

3. The shifting does not affect to y-polarized (TM) waves: $\hat{n}_{yy}(\Delta z) = n_{\parallel}$, because y-polarized waves are always parallel to the all the periodic discontinuities independently of the shifting.

4. The light propagation along the x and z axes of TE waves is identical when the shifting is half of the period: $\hat{n}_{xx}(0.5) = \hat{n}_{zz}(0.5)$

By combining the first three assumptions the following condition for the permittivity tensor components of the bricked LPS is obtained: $\hat{n}_{xx}(\overline{\Delta z}) \cdot \hat{n}_{zz}(\overline{\Delta z}) = n_{\parallel}^2 n_{\perp}^2$. By combining this equation, with the last condition, the permittivity tensor for $\overline{\Delta z} = 0.5$ is derived as: $\varepsilon(0.5) = \mathrm{diag}[n_{\parallel} n_{\perp}, n_{\parallel}^2, n_{\parallel} n_{\perp}]$. Figure 4.15e shows the calculated permittivity tensor for the exemplary bricked LPS under study. These two boundary cases, $\overline{\Delta z} = 0$ and $\overline{\Delta z} = 0.5$ have been calculated directly from the symmetry considerations and the index conservation law. For the intermediate values a periodic and smooth solution is assumed:

$$\hat{n}_{xx}(\overline{\Delta z}) = A + B\cos(2\pi\overline{\Delta z}) \tag{4.9}$$

Then, the n_{zz} component can be calculated as:

$$\hat{n}_{zz}(\overline{\Delta z}) = n_{\parallel} n_{\perp} / \hat{n}_{xx}(\overline{\Delta z}) \tag{4.10}$$

with $A = 0.5(n_{\parallel} + \sqrt{n_{\parallel} n_{\perp}})$ and $B = 0.5(n_{\parallel} - \sqrt{n_{\parallel} n_{\perp}})$ obtained from the boundary cases $\overline{\Delta z} = 0$ and $\overline{\Delta z} = 0.5$. It is important to note that these tensor components of the bricked SWG metamaterial are calculated from the permittivity tensor components of the conventional LPS, $n_{\parallel}$ and $n_{\perp}$. Figure 4.16 shows the range of synthesizable permittivity tensor components with the proposed bricked metamaterial calculated for any shifting from $\overline{\Delta z}$ to $\overline{\Delta z} = 0.5$. Similar as happen in tilted SWG metamaterials, a wide range of birefringences is achieved for a fixed period and duty cycle by properly shifting the structure. The main difference here is that bricked SWG metamaterials maintain a rectangular, Manhattan-like geometry. With the permittivity tensor components, the dispersion relation of the plane waves propagating along

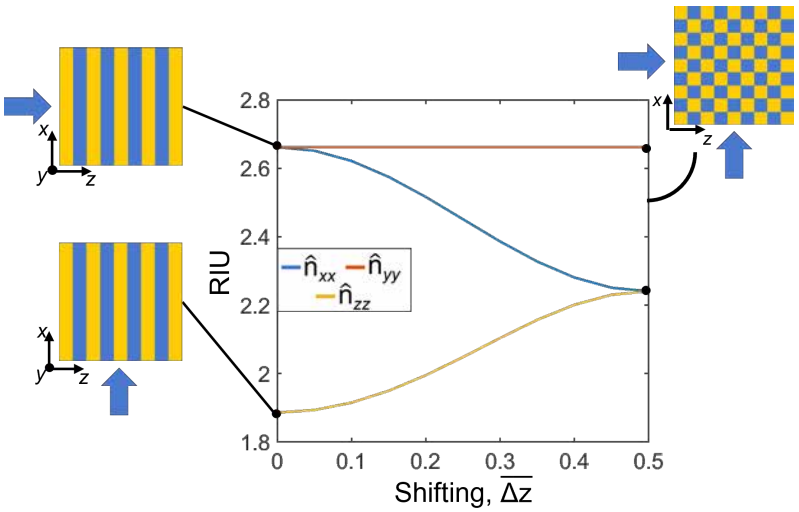

Figure 4.16: Available set of permittivity tensor components synthesized by shifting the segments of a bricked SWG structure in the deep subwavelength regime.

the equivalent homogeneous anisotropic metamaterial to a bricked anisotropic materials can be calculated as:

$$\text{TE waves}: \frac{k_x^2}{n_{zz}^2(\overline{\Delta z})} + \frac{k_z^2}{n_{xx}^2(\overline{\Delta z})} = k_0^2, \tag{4.11}$$

$$\text{TM waves}: \frac{k_x^2}{n_{\parallel}^2} + \frac{k_z^2}{n_{\parallel}^2} = k_0^2. \tag{4.12}$$

Note that, once again, for the TM polarization the dispersion relation is a circle for any shifting. On the other hand, the relation dispersion of the TE polarization is an ellipse which semi-axes depends on the shifting. For the sake of illustration, the dispersion relation for the $\overline{\Delta z} = 0.5$ LPS is shown in Fig. 4.15f. Interestingly, in this case the relation dispersion of the TE polarization degenerates into another circle.

Finally, the homogenization algorithm for on-chip bricked SWG structures is proposed (see Fig. 4.17). The algorithm is the same proposed for the tilted SWG metamaterials. First, the corresponding LPS or PSS of the bricked SWG waveguide under study is extracted. That is, the LPS/PSS with the same period, duty cycle, materials and silicon thickness for the case of the PSS. Second, the permittivity tensor of the equivalent homogeneous anisotropic metamaterial of the extracted LPS/PSS is calculated as shown in section 3.3. Third, the permittivity tensor components of the conventional LPS or PSS are used to calculate the homogeneous anisotropic metamaterial equivalent to the bricked SWG waveguide by using Eq. (4.9) and Eq. (4.10). The calculated permittivity tensor $\varepsilon(\overline{\Delta z})$ is introduced into the core of the homogeneous waveguide.

4.3.2. Waveguiding properties of bricked SWG metamaterials

The waveguiding properties of bricked SWG metamaterial are examined in the same scenario as tilted SWG metamaterials. That is, a multimode bricked SWG waveguide ($W = 3.25\,\mu$m, $\Lambda = 0.25\,\mu$m and DC = 0.5) in a standard 220 nm thick silicon platform. The study starts

by validating the anisotropic model of bricked SWG waveguides. For that purpose, the fundamental TE and TM modes of the bricked SWG waveguide and its corresponding homogeneous anisotropic waveguide are calculated for different shiftings Δz by using FullWAVE and FIMMWAVE respectively. The effective indices of those fundamental modes are shown in Fig. 4.18a, providing similar results. As expected, the TE polarized mode is strongly affected by the shifting while the TM polarized mode barely changes. Next, the wavelength behavior response of the effective indices of the modes propagating along bricked SWG waveguide for different shifting is shown in Fig. 4.18b. These simulations clearly show that bricked SWG waveguides provides an accurate control over the effective index and the dispersion of the TE modes, while the fundamental TM mode is almost unaffected. Moreover, as the effective index of the TE modes is being reduced while the period of the periodic structure is kept constant, the Bragg condition [Eq. (3.9)] is satisfied for a shorter wavelength. To clearly show this effect, the study of the effective index dispersion of the bricked SWG structure is repeated for a period of 300 nm (see Fig. 4.18c). Without shifting, the SWG waveguide with the 300 nm period, cannot effectively guide the wavelengths near 1.55 µm because it operates in the bandgap. As the shifting increases, the Bragg wavelength is shortened, allowing to work with longer periods. The waveguiding properties of bricked SWG metamaterials are interesting to engineer the refractive index of TE modes in integrated optics and the modal birefringence while also allowing larger periods. These interesting properties are now exploited to design two broadband 2 × 2 multimode interferometers.

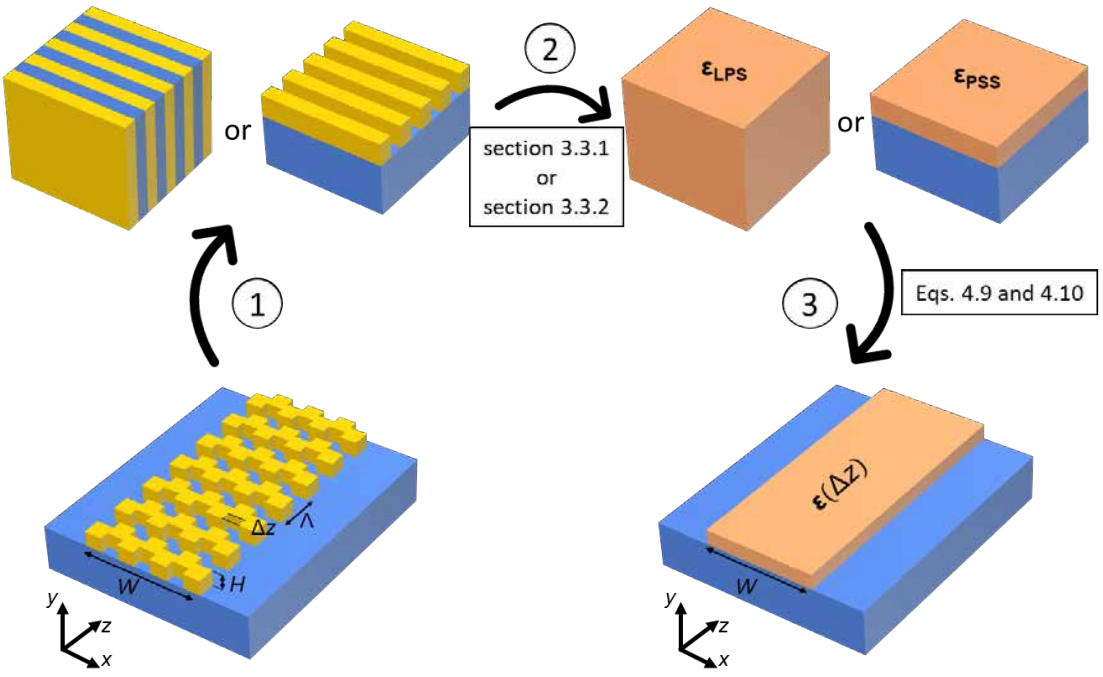

Figure 4.17: Algorithm to calculate the equivalent homogeneous material of a bricked SWG waveguide: 1) Extract the corresponding LPS or PSS of the SWG waveguide under study. That is, the LPS/PSS with the same period, duty cycle, materials and silicon thickness for the case of the PSS. 2) Homogenize the LPS/PSS by using the theory discussed in section 3.3. 3) Calculate the permittivity tensor $\varepsilon(\overline{\Delta z})$ of equivalent homogeneous material to the bricked SWG waveguide by using Eqs. (4.9) and (4.10) and introduce the resulting permittivity tensor into the core of the homogeneous waveguide.

4.3.3. Design of a broadband bricked SWG multimode interferometer

Conventional MMI couplers (i.e. with solid core) are robust and broadband beam splitter devices when compared with other alternatives as directional couplers. However, they still exhibit a limited bandwidth. The dispersion engineering of SWG structures alleviates this limitation by implementing a metamaterial core with a dispersion opposed to the intrinsic wavelength behavior of MMIs. The bricked topology is leveraged in this section to design ultra-broadband MMI couplers with a larger period compared with MMI based on conventional SWG topologies, making progress toward the viability of fabricating these devices with massive production fabrication process such as DUV.

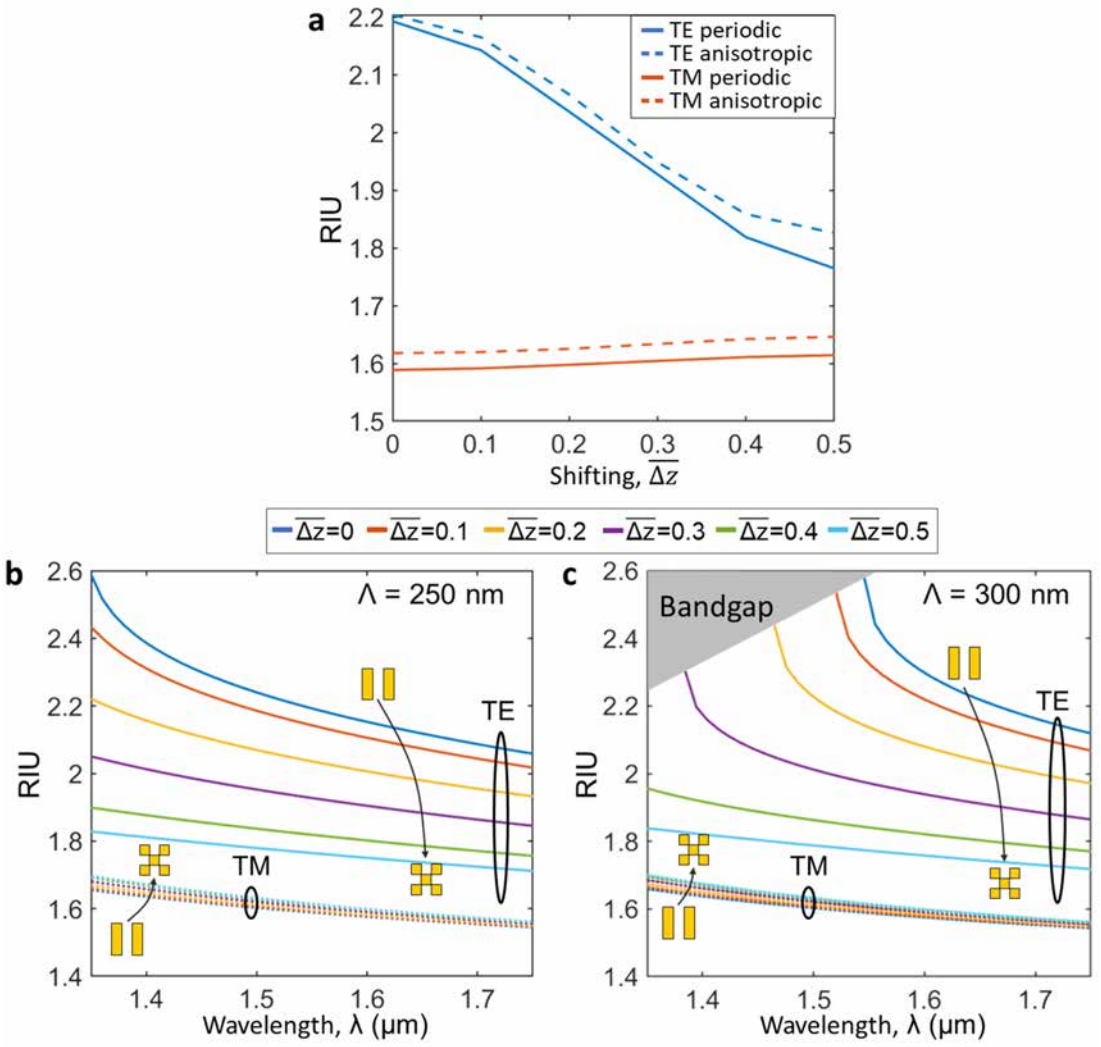

Figure 4.18: a) Effective indices of the fundamental TE and TM modes of a bricked SWG waveguide and its equivalent homogeneous anisotropic waveguide with a silicon thickness $H = 220$ nm, a width $W = 3.25\,\mu$m, a period $\Lambda = 0.25\,\mu$m and duty cycle DC = 0.5 for different shiftings ranging from $\overline{\Delta z} = 0$ to $\overline{\Delta z} = 0.5$ at $\lambda = 1.55\,\mu$m. b) Effective index dispersion of the fundamental TE and TM modes of the tilted SWG waveguide described in (a) c) The effective index dispersion of the fundamental TE and TM modes of the tilted SWG waveguide described in (a) with a period increased to $\Lambda = 300\,\mu$m.

Working principle of multimode interferometers

MMI devices have a remarkable practical interest, since they are widely used as a fundamental component in many photonic integrated devices, such as power splitters and combiners [193], Mach–Zehnder interferometers [194], or 90° hybrids for coherent optical receivers [195, 196]. MMI couplers are composed of a multimode waveguide of width W_{MMI} and length L_{MMI} and a set of input/output waveguides of widths W_{a}, as schematically shown in Fig. 4.19a. The operation of MMI devices is based on the self-image principle, which describes the formation of N-fold images (copies) of the input field at specific positions within the multimode waveguide [197]. For this purpose, the multimode region should support a set of guided modes capable of accurately representing the input field excitation as a linear combination of paraxial modes. The excited modes in the multimode region interfere with specific phases at the output of the device creating a number of self-images of the input excitation precisely at the location of the output ports. For a 2×2 MMI and considering general interference, the MMI length is given by $L_{\mathrm{MMI}} = (3/2)L_\pi$ where L_π is the beat length defined as:

$$L_\pi = \frac{\lambda_0}{2(n_{\mathrm{eff1}} - n_{\mathrm{eff2}})} \tag{4.13}$$

where n_{eff1} and n_{eff2} are the effective indices of the first and second modes. The optimum excitation of paraxial modes is controlled by properly choosing the width of the access ports, W_{a}. A linear taper is then required to adiabatically adapt the mode field distributions. The port-to-port separation, s, is chosen to be as small as possible while ensuring negligible crosstalk between the access waveguides. Therefore, the design process of conventional MMI devices require a good combination of multimode region width, W_{MMI}, access ports width W_{a} and separation s ensuring that the electromagnetic field profile at the input port excites a set of paraxial modes capable of represent such field with low loss while the output separation, s is enough to avoid the crosstalk between the output ports.

Device design and optimization

To optimize the bandwidth of conventional MMIs, the homogeneous multimode region is replaced by a bricked SWG metamaterial as shown in Fig. 4.19b. The metamaterial width is set to $W_{\mathrm{MMI}} = 3.3\,\mu\mathrm{m}$, the input/output port width and separation are set to $W_{\mathrm{a}} = 1.2\,\mu\mathrm{m}$ and $s = 0.9\,\mu\mathrm{m}$ respectively. With these parameters, two different MMI couplers are designed with periods $\Lambda = 250$ nm and $\Lambda = 300$ nm respectively. These periods are chosen to ensure a 125 and a 150 nm gap size. The wavelength behavior of the beat lengths of those bricked SWG waveguides for different shiftings are shown in Figure 4.20. These are calculated by solving the fundamental and first order Floquet modes of the periodic waveguide using 3D-FDTD simulations (FULLWAVE). It is observed that in both cases an almost flat beat length can be achieved for a shifting in-between the conventional, $\overline{\Delta z} = 0$ and totally shifted waveguides SWG $\overline{\Delta z} = 0.5$. Specifically, a $\overline{\Delta z} = 0.2$ and $\overline{\Delta z} = 0.35$ are the optimum shift for the $\Lambda = 250$ nm and $\Lambda = 300$ nm periods respectively. Once the multimode region has been designed, its length is optimized around the theoretical value of $3L_\pi/2$. For that purpose, 3D-FDTD simulations of the full device are performed also with FULLWAVE. These simulations include not only the wide SWG waveguide core but also the input/output tapers. Note that the tapers are divided in two sections: the first one is a conventional adiabatic taper from the Si-wire to a non-bricked SWG waveguide, $\overline{\Delta z} = 0$, of the same width ($W = 500$ nm). The second

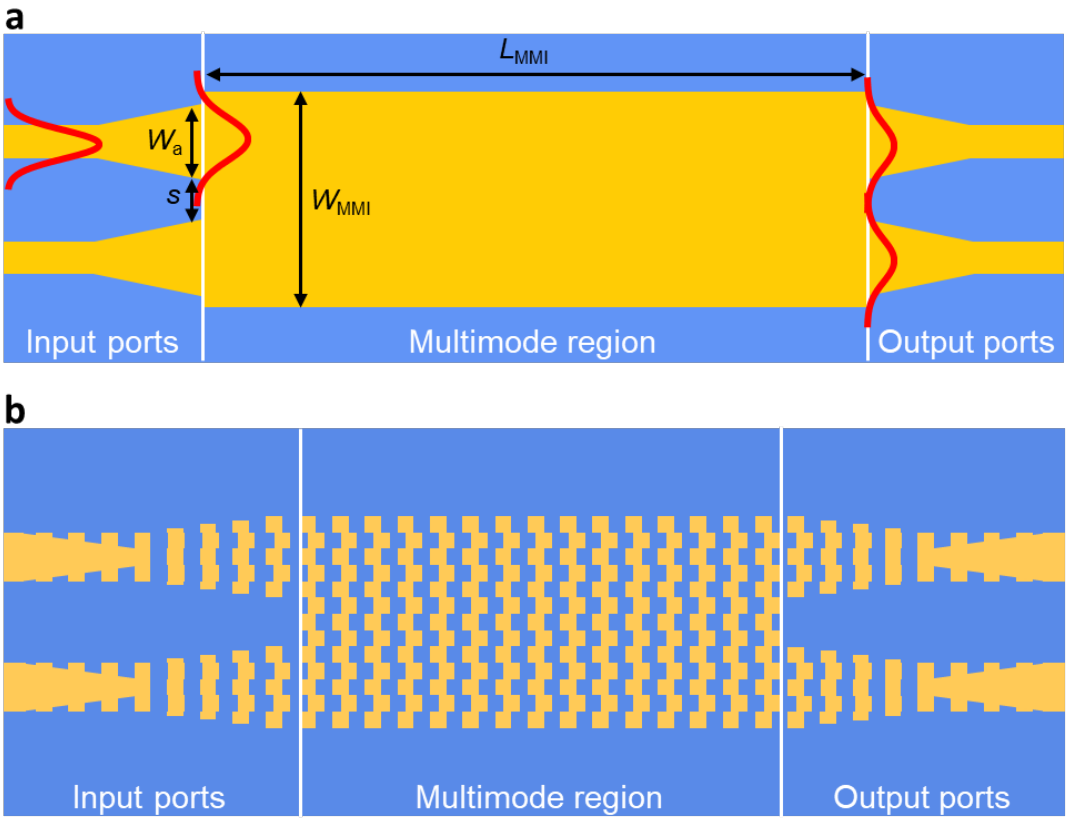

Figure 4.19: a) Schematic representation of a conventional MMI. The structure replicates the input field profile into N-images splitting the power between them. The input waveguides are widened to excite only the paraxial modes of the multimode region. b) Schematic representation of the proposed bricked SWG metamaterial based MMI. The multimode region is replaced by a wavelength optimized metamaterial to achieve the ultra-broadband behavior. The input/output ports not only widen the interconnecting waveguide but also adiabatically introduce the periodic pattern.

section gradually transforms the SWG waveguide into the wider bricked SWG input port, which is done by linearly increasing the waveguide width while progressively introducing the shifting. This two-section taper is preferred to a direct conversion from the single-mode Si-wire to the widened bricked SWG structure since it minimizes losses arising from localized Bragg reflections. With the taper included, 3D-FDTD simulations are performed to obtain the figures of merit of the devices, specifically, the Excess Loss (EL) and the Imbalance (IB):

$$\begin{aligned} \mathrm{EL} &= 10\log(|S_{41}|^2 + |S_{31}|^2), \\ \mathrm{IB} &= 10\log(|S_{41}|^2 / |S_{31}|^2), \end{aligned} \tag{4.14}$$

where S_{31} and S_{41} are the scattering parameters which relate the power in the fundamental mode of the output waveguides with the power in the fundamental mode of the input port. In Figure 4.21a the field propagation along the final design for the 300 nm pitch is shown. In Fig. 4.21b and Fig. 4.21c the calculated excess loss and imbalance of the optimized devices are shown for both designs, obtaining an ultra-broad bandwidth of 400 nm for an EL and IB lower than 1 dB.

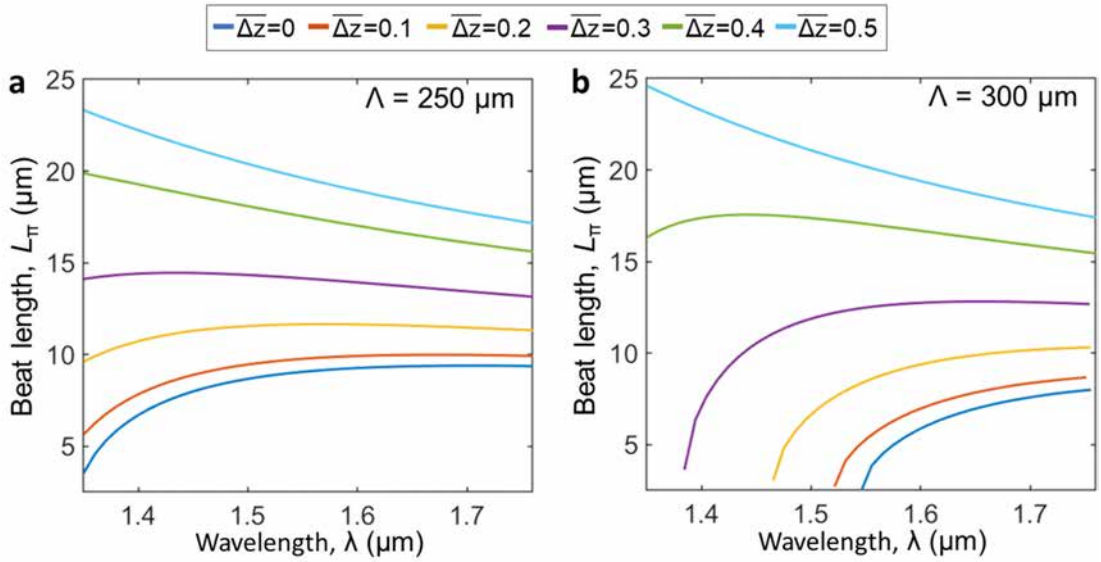

Figure 4.20: Beat lengths dispersion for TE polarization in the proposed bricked SWG waveguide with a period of a) $\Lambda = 250$ nm and b) $\Lambda = 300$ nm.

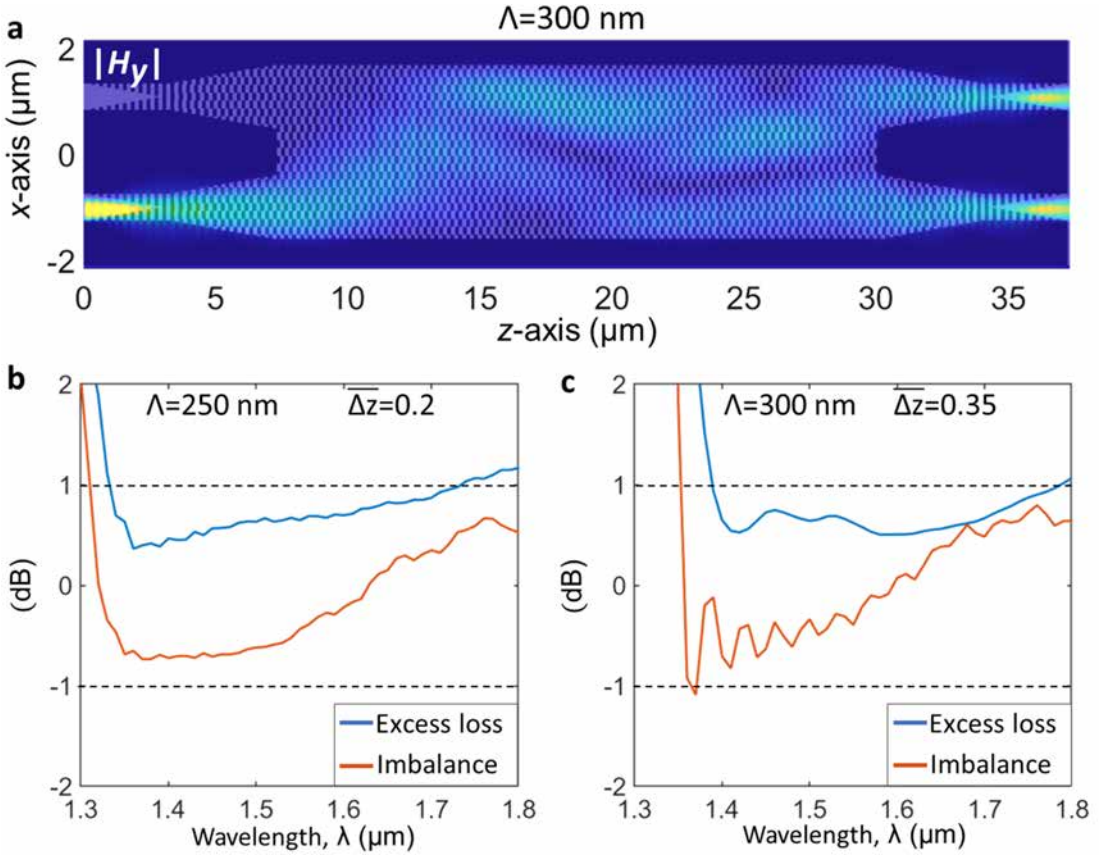

Figure 4.21: a) Simulated magnetic field propagation along the $\Lambda = 300$ nm bricked SWG based MMI design $|H_y|$. Simulated excess loss (blue line) and imbalance (red line) of the optimized bricked SWG MMIs with a period of b) $\Lambda = 250$ nm and c) $\Lambda = 300$ nm. In both cases a 400 nm 1-dB-bandwidth is covered, from 1330 to 1730 nm (b), and from 1380 to 1780 nm (c).

Experimental validation

To experimentally demonstrate the bricked SWG design strategy, both designed MMIs are fabricated in a MPW of ANT. Figure 4.22a shows the full fabrication mask submitted for the MPW run where the bricked MMI devices occupy the red outlined area. A set of edge couplers are used as to inject light into the chip as bricked MMI devices require large bandwidth measurements. Figure 4.22b shows a zoom into the area where the MMI splitters are drawn. A comparison between the device drawn in the mask and a SEM image is shown in Figs. 4.22c and 4.22d.

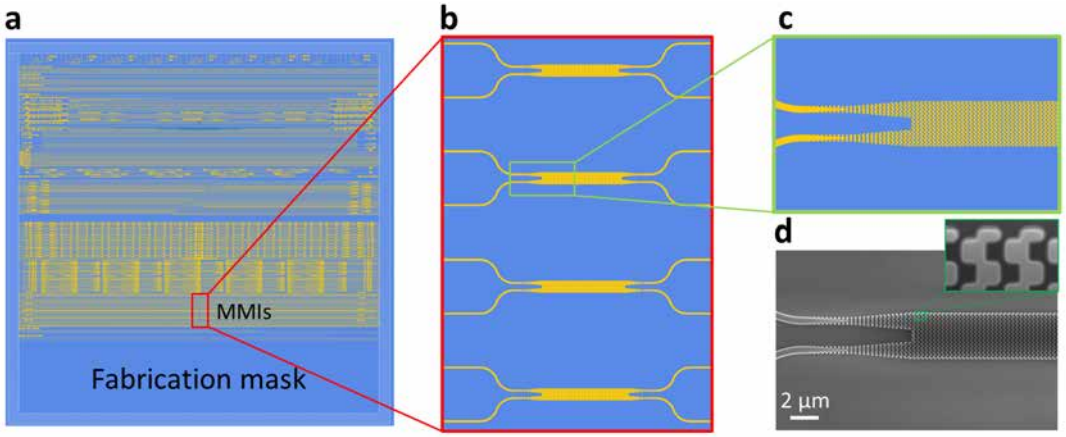

Figure 4.22: a) Full fabrication mask including many different designs. b) Zoom-in into the red zone outlined in (a) where the some bricked MMIs are drawn. c) Zoom-in into the input stage of an MMI and d) SEM image of the fabricated MMI.

The fabricated devices are characterized by measuring the power in both output ports when the device is excited through the input port using the corresponding edge coupling setup. A reference waveguide is used to calibrate the setup and fiber-to-chip coupling losses allowing to calculate the excess loss. The imbalance is calculated by dividing the measured power in both output ports. An EL and IB below 1 dB over the full 140 nm bandwidth of the

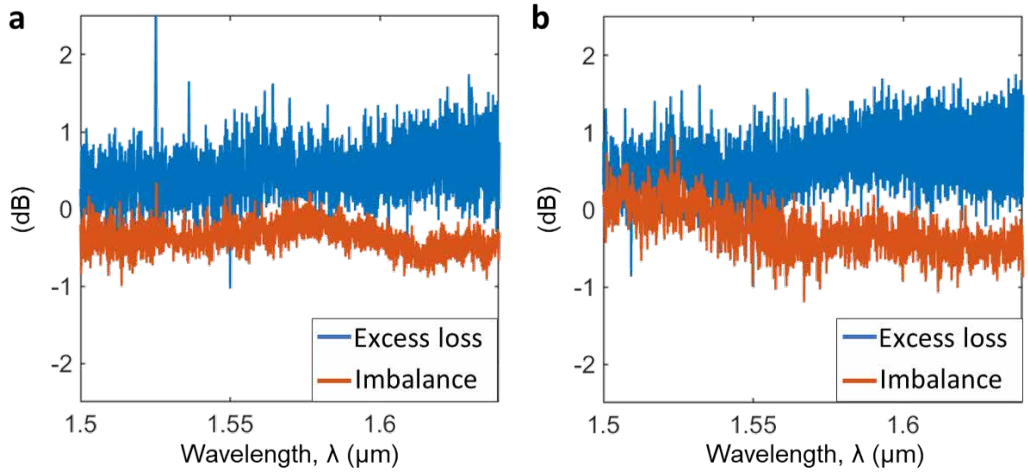

Figure 4.23: Measured excess loss and imbalance for the a) $\Lambda = 250$ nm and b) $\Lambda = 300$ nm structures. In both cases the measured 1 dB bandwidth is limited by the 140 nm bandwidth of our setup.

laser is obtained for both MMIs (see Fig. 4.23). Note that the noise in the measurements is not related with the device behavior, as it was also in the reference waveguide. This is, to the best of our knowledge, the first time such outstanding performance is achieved with these large periods.

4.4. Conclusions

In this chapter two advanced SWG topologies have been proposed and demonstrated: the tilted and the bricked SWG topologies. Both structures increase the range of optical properties synthesizable by using SWG periodic structures, while staying inside of the fabricable region, allowing the design of novel devices. Both SWG topologies are well poised to design polarization management devices, as they both allow to control the birefringence. Bricked SWG topology also relaxes the period limitation of conventional SWG topologies, opening a new path toward the exploitation of SWG metamaterial devices fabricated with DUV, allowing wafer-scale fabrication. These new SWG topologies potentially opens the way for the next generation of SWG optimized devices.

5. Gradual Index subwavelength grating metamaterials

Gradual Index (GRIN) optics is the branch of optics which proposes to control light propagation by designing the refractive index profile of the material where the light is propagating. The first researcher who proposed to handle light behavior with GRIN media was Maxwell in 1854 [198], proposing the Maxwell fisheye lens to collimate light rays. From that point, GRIN optics developed slowly, being followed by Wood in 1905 [199], Luneburg in 1944 [200] and the proposal of GRIN rods in 1954 [201]. The slow growth of this subject was mainly due to the limitations of manufacturing GRIN materials, which was not possible until the 1970s. [202–204]. From that point, GRIN optics reborn, being nowadays a well-established design methodology [205]. However, silicon photonics platforms still suffers the fabrication limitations to implement GRIN media, especially if CMOS compatibility is desired. In this chapter the viability of synthesizing GRIN metamaterials through SWG structures is discussed.

The chapter starts in section 5.1 discussing some basic foundations of light propagating in GRIN media. Then, in section 5.2, a topology to implement GRIN metamaterials with SWG structures is proposed, including a step-by-step algorithm to implement the desired index profile. Next, in section 5.3, a GRIN device is designed and experimentally demonstrated using the proposed SWG topology. Finally, the chapter ends in section 5.4 with the concluding remarks about the synthesis of GRIN metamaterials by using SWG structures.

5.1. Light propagation through GRIN media

Light propagating through gradual index (GRIN) has always attracted researchers' attention as it produces multiple fascinating effects in nature from conventional optical mirages to the apparent sunrise/sunset described by writings of Cleomedes [206] (first century, A.D) or the sun's disc flattening predicted by Alhazen [207] (1100 A.D). These effects are frequently analyzed from a ray optics point of view. Under this theory, the trajectory of a light ray propagating through a GRIN medium satisfies the ray equation:

$$\frac{\mathrm{d}}{\mathrm{d}s} n_{\mathrm{GRIN}}(\mathbf{r}) \frac{\mathrm{d}\mathbf{r}(s)}{\mathrm{d}s} = \nabla n_{\mathrm{GRIN}}, \tag{5.1}$$

where $n_{\mathrm{GRIN}}(\mathbf{r})$ describes the variation of the refractive index with the position, s is the ray trajectory and $\mathbf{r}(s)$ is a vector from any arbitrary point to the trajectory. This equation is derived from Fermat's principle, which states that light always takes the shortest minimum path. The ray equation is hard to solve in its general form, thus simplified GRIN materials with geometrical symmetries are common. For example, the ray equation for a 2D GRIN

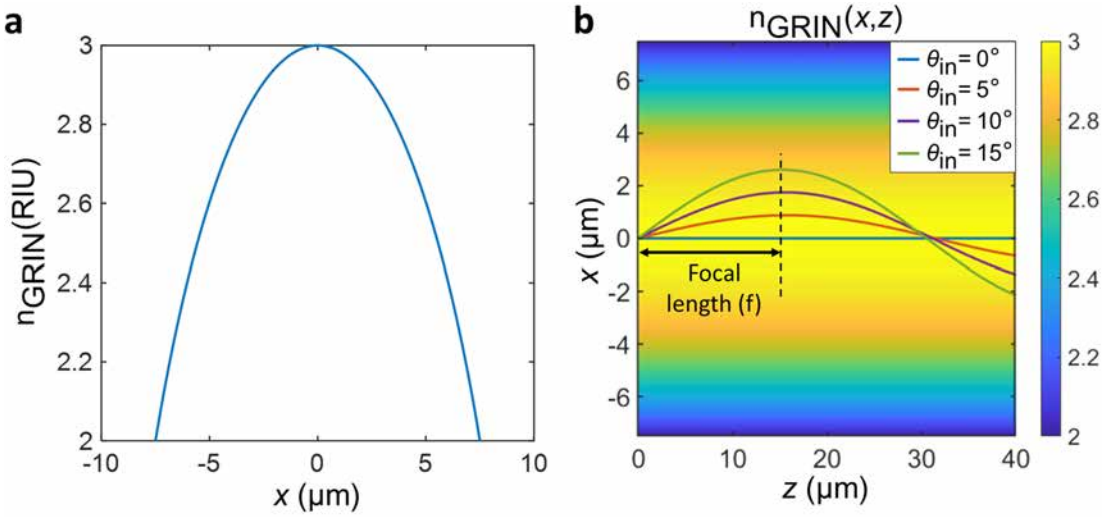

Figure 5.1: a) Parabolic refractive index defined by Eq. (5.3) with $n_{max} = 3$ and $\gamma = 0.3$. b) Trajectory of different rays along the GRIN medium shown in (a) for different input angles.

material with a gradualness along the transversal direction is given by the ray equation:

$$\frac{\partial x}{\partial z} = \sqrt{\frac{n_{GRIN}^2(x)}{\beta^2} - 1}, \tag{5.2}$$

where $\beta = n_{in}\cos\theta_{in}$, is known as the invariant of the ray, with n_{in} and θ_{in} being the refractive index and ray angle in the input point x_{in}. The trajectory function of a ray in a GRIN medium is calculated by integrating Eq. (5.2).

The most common GRIN profile is the parabolic medium (see Fig. 5.1a):

$$n_{GRIN}^2(x) = n_{max}^2 - \gamma^2 x^2, \tag{5.3}$$

where n_{max} is the refractive index at the center and γ measures the curvature of the parabola. An input ray at the center of this medium, $x = 0$, with an input angle angle θ_{in} will follow the trajectory obtained by integrating Eq. (5.2):

$$x = \frac{n_{max}\sin(\theta_{in})}{\gamma}\sin\left(\frac{\gamma}{\beta}z\right). \tag{5.4}$$

Figure 5.1(b) shows the trajectory of different input rays entering the parabolic GRIN medium with different input angles calculated with Eq. (5.4). This example shows the collimation properties of parabolic GRIN media. All the input rays reach their maximum expansion at a similar distance, known as focal length. Indeed, under the paraxial approximation this distance is independent of the input angle, $f = \pi/2\frac{n_{max}}{\gamma}$. Therefore, the parabolic profile synthesizes a GRIN lens which can expand, collimate and focus the paraxial input rays.

This example shows the potential of GRIN materials to control the light propagation. However, it also shows a typical problem of GRIN optics. You need to know the actual index profile that achieves a desired light behavior. Three typical solution to obtain the required GRIN profiles are:

1. **Use well-known index profiles**. Parabolic or secant hyperbolic profiles are for example typical solution of GRIN optics to focus the light. However, there are only a few different known profiles. Therefore, this methodology is very limited.

2. **Use inverse-design methods**. Inverse design can be used to obtain the GRIN material which achieves a desired light behavior [208]. This solution opens multiple new designs but requires a high computation effort.

3. **Use transformation optics profiles**. Transformation optics is a systematic method to calculate the GRIN profile which enforces the light to follow the desired trajectory [209, 210]. The main drawback of these techniques is that they result in complex materials with strong anisotropy and permeability tensors. Quasi-conformal transformation optics is a subset of transformations that minimize the required anisotropy [211], resulting in more feasible GRIN materials.

Based in these solutions, GRIN optics enable the design of high performance optical devices. The fabrication limitations of GRIN materials are still an issue in silicon platforms which offer a very limited set of different materials. Some previous works on this topic are transversal SWG GRIN materials [109], gray-scale lithography waveguides [212] or fish-eye-lenses based on GRIN rods [213].

In this chapter, a novel way to synthesize GRIN metamaterials by using SWG periodic structures is proposed. A mathematical model to analyze the proposed structure is also developed and validated. Finally, a device based on a GRIN metamaterial is designed, including the electromagnetic simulations, the layout of the fabrication mask and the characterization of the fabricated device. The resulting device is a GRIN lens which increases an input beam width by a ×30 factor (from 0.5 µm to 15 µm) in a length shorter than 15 µm.

5.2. GRIN metamaterials through duty-cycle modulated SWG structures

The capability of SWG periodic structures to synthesize anisotropic homogeneous metamaterials was described in chapter 3. In this section it is discussed how gradually modifying the duty cycle of the SWG structure synthesizes equivalent anisotropic metamaterials with a gradual refractive index. An implementation algorithm to design the gradualness of the duty cycle is proposed and validated through electromagnetic simulations.

5.2.1. Topology proposal, design algorithm and homogenization

The proposed structure is a periodic SWG waveguide with a width w_G, a height h and a period Λ (see Fig. 5.2). The duty cycle of the periodic structure, $DC_G(x) = a(x)/\Lambda$, is transversely modulated to achieve desired profile. The minimum gap between segments, MFS_G, and the minimum silicon tip, MFS_T, yields the maximum and minimum duty cycle. The two main assumptions made to analyze this structure are:

(i) The duty cycle modulated structure behaves as a GRIN metamaterial defined by a gradual permittivity tensor $\varepsilon(x) = \mathrm{diag}[n_{xx}^2(x), n_{yy}^2(x), n_{zz}^2(x)]$ (see Fig. 5.2b).

(ii) The permittivity tensor components at specific points, $n_{xx}^2(x_0)$, $n_{yy}^2(x_0)$, and $n_{zz}^2(x_0)$, are equal to the tensor components of a non-gradual SWG structure with the duty-cycle at that point, $DC(x_0)$. Therefore, the theory about non-graded SWG structures

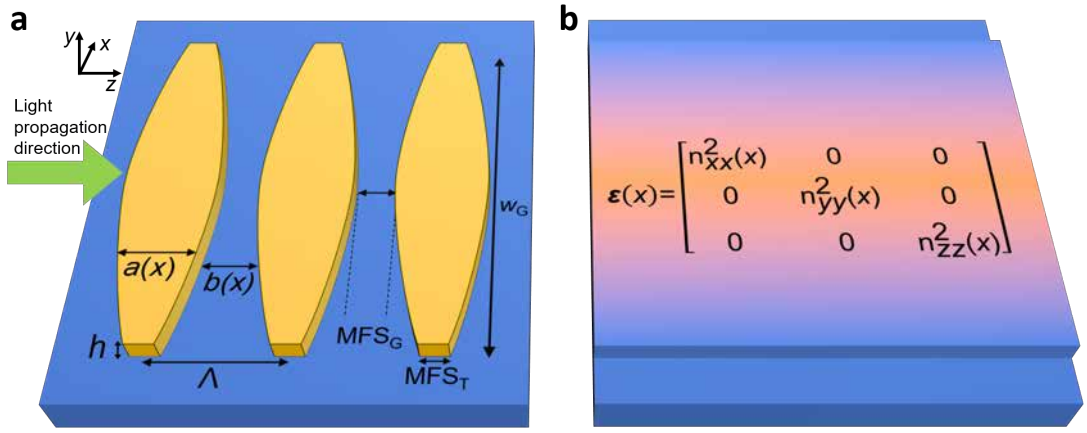

Figure 5.2: a) Schematic representation of the proposed duty cycle modulated SWG structure and b) its corresponding GRIN anisotropic homogeneous model.

discussed in chapter 3 can be locally applied in this structure. For example, $n_{xx}(x)$ is equal to $n_{yy}(x)$ as $n_{xx} = n_{yy}$ in non-graded SWG structures.

With these assumptions, the following algorithm to implement GRIN profiles, $n_{\mathrm{GRIN}}(x)$, is proposed. For illustration purposes the algorithm is applied to synthesize the parabolic index profile of Eq. (5.3).

1. Calculate the permittivity tensor component dependence with the duty cycle $n_{xx}(\mathrm{DC})$, $n_{yy}(\mathrm{DC})$, and $n_{zz}(\mathrm{DC})$ for a non-graded SWG waveguide following the procedure shown in chapter 3 (see Fig. 5.3b).
2. Invert the function $n_{xx}(\mathrm{DC})\rightarrow\mathrm{DC}(n_{xx})$. The inverted function gives the required duty cycle for a desired index.
3. Impose the desired GRIN profile goal function to the x component of the tensor, $n_{xx}(x) = n_{\mathrm{GRIN}}(x)$.
4. Use the inverted function, $\mathrm{DC}(n_{xx})$, to calculate the duty cycle, $\mathrm{DC_G}(x)$, such that achieves the imposition made. That is: $\mathrm{DC_G}(x) = \mathrm{DC}(n_{\mathrm{GRIN}}(x))$ (see Fig. 5.3c).
5. Complete the anisotropic metamaterial model by calculating the implemented $n_{zz}(x)$ given by the duty cycle $\mathrm{DC_G}(x)$ using the mapping function $n_{zz}(\mathrm{DC})$, that is: $n_{zz}(x) = n_{zz}(\mathrm{DC_G}(x))$ (see Fig. 5.3a, red line).

Note that, with this algorithm the desired gradual index is implemented in two out of three components of the tensor as $n_{\mathrm{GRIN}}(x) = n_{xx}(x) = n_{yy}(x)$. Typical silicon-on-insulator values have been considered in Fig. 5.3. That is: $n_1 = 3.476$, $n_2 = 1.444$, $\lambda_0 = 1.55\,\mu\mathrm{m}$, $h = 220\,\mathrm{nm}$ and $\Lambda = 200\,\mathrm{nm}$. The metamaterial width has been chosen to be $w_G = 16\,\mu\mathrm{m}$ and the maximum and minimum refractive indices, $n_{\max}$ and $n_{\min}$, are calculated by assuming minimum feature sizes $\mathrm{MFS_T} = \mathrm{MFS_G} = 50\,\mathrm{nm}$.

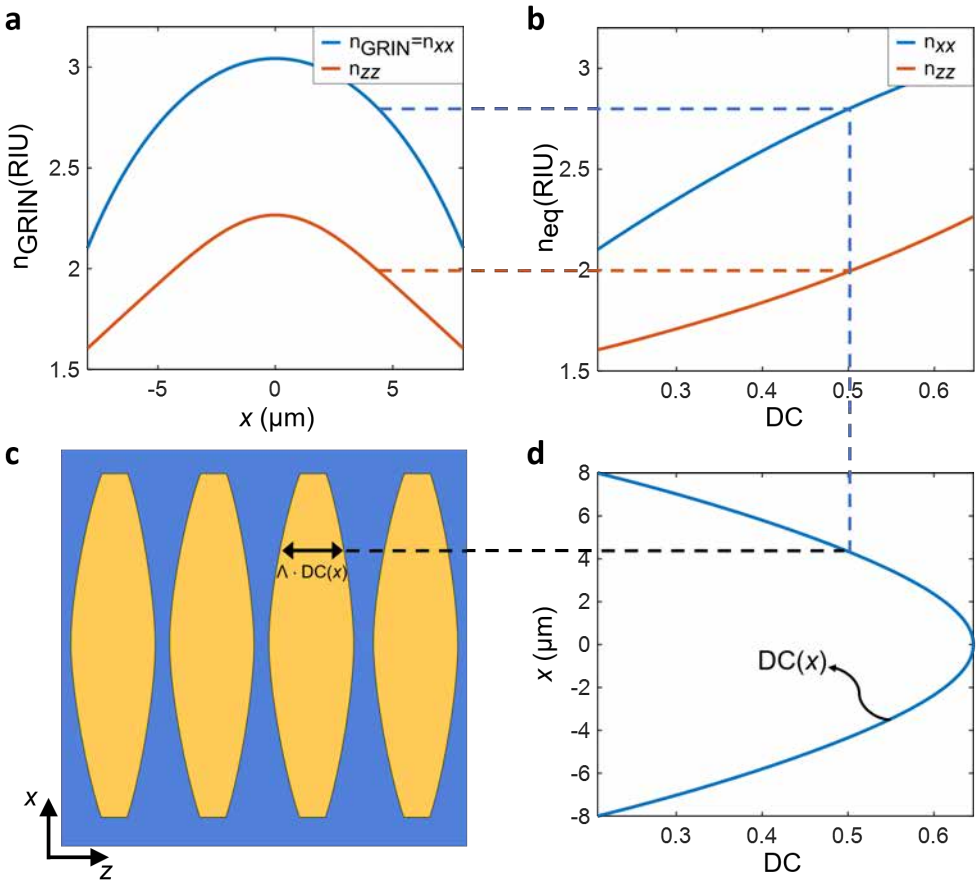

Figure 5.3: (a) Desired GRIN equivalent refractive index, $n_{\mathrm{GRIN}}(x)$ (blue line) and implemented $n_{zz}(x)$ component (red line). (b) Dependence of the implemented permittivity tensor components with the duty cycle, n_{xx}(DC) and n_{zz}(DC). (c) Schematic representation of the silicon segment shape modulation. d) Duty cycle along the transversal period required to implement the desired profile.

5.2.2. Validation of the gradual anisotropy homogenization model

In this section the proposed algorithm to synthesize GRIN metamaterials through SWG periodic structures is validated. For that purpose, the resulting SWG waveguide with duty cycle $\mathrm{DC_G}(x)$ shown in Fig. 5.3d is analyzed and compared with its corresponding anisotropic waveguide with the tensor components shown in Fig. 5.3a. The comparison is first done by studying the effective indices of the modes of both waveguides and then the electromagnetic field propagation.

1. **Effective index comparison.** The effective indices of the modes of both waveguides are shown in Fig. 5.4. An excellent agreement is found for the fundamental and most of the higher order modes. The modes of the periodic SWG waveguide are solved with 3D-FDTD Floquet simulations (FULLWAVE) while the anisotropic waveguide modes are calculated with 2D FEM simulations(FIMMWAVE). From these effective indices, the focal length of the parabolic GRIN waveguide is calculated as:

$$f = \frac{\lambda_0}{2(n_{\mathrm{eff1}} - n_{\mathrm{eff2}})} \tag{5.5}$$

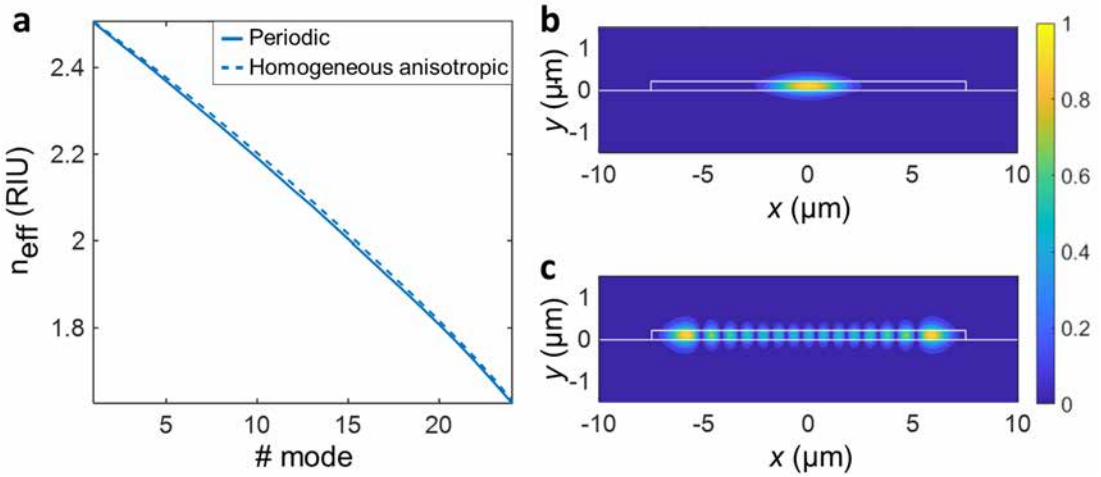

Figure 5.4: a) Comparison of the effective indices of the first 24 modes of SWG GRIN waveguide designed in section 5.2.1 and its corresponding anisotropic model. b), c) Electric field main component (E_x) of the b) fundamental and c) 15th mode of the anisotropic homogeneous GRIN waveguide.

where n_{eff1} and n_{eff2} are the effective indices of the fundamental and first order mode. The estimated focal length, f, in the period and modeled structures is ~ 12 μm. The mode field profiles of the fundamental and 15th modes calculated with the anisotropic model are shown in Fig. 5.4b and 5.4c. Interestingly, in this structure the fundamental mode only occupies the inner part of the waveguide, while high order modes use the whole waveguide.

2. **Field propagation comparison.** The electromagnetic field propagation along both waveguides is shown in Fig. 5.5a and Fig. 5.5b. Moreover, an isotropic GRIN material with the three components equal to n_{xx} is also shown in Fig. 5.5c. All three structures have been fed with the same TE polarized 2 μm wide Gaussian beam in the aforementioned silicon-on-insulator platform. Multiple interesting conclusions arise from these propagations. i) The focus length estimated with Eq. (5.5) accurately predicts the device behavior for the periodic and the anisotropic homogeneous structures. ii) Even with the anisotropy, the parabolic metamaterial still works as a lens, expanding and focusing the input beam but in a shortened length compared with the isotropic case. iii) The isotropic case simulation matches with the focus length given by the ray equation solved in Eq. (5.2), shown in Fig. 5.1.

Therefore, an SWG based parabolic GRIN metamaterial works as a GRIN lens with a shortened length compared to an isotropic implementation, being thus an auspicious structure to design compact spot size converters.

5.3. Demonstration of a GRIN lens spot size converter implemented with a duty cycle modulated SWG metamaterial

In this section, a compact spot size converter is demonstrated based on the parabolic GRIN metamaterial shown in section 5.2. Spot size converters are useful devices in SOI to couple

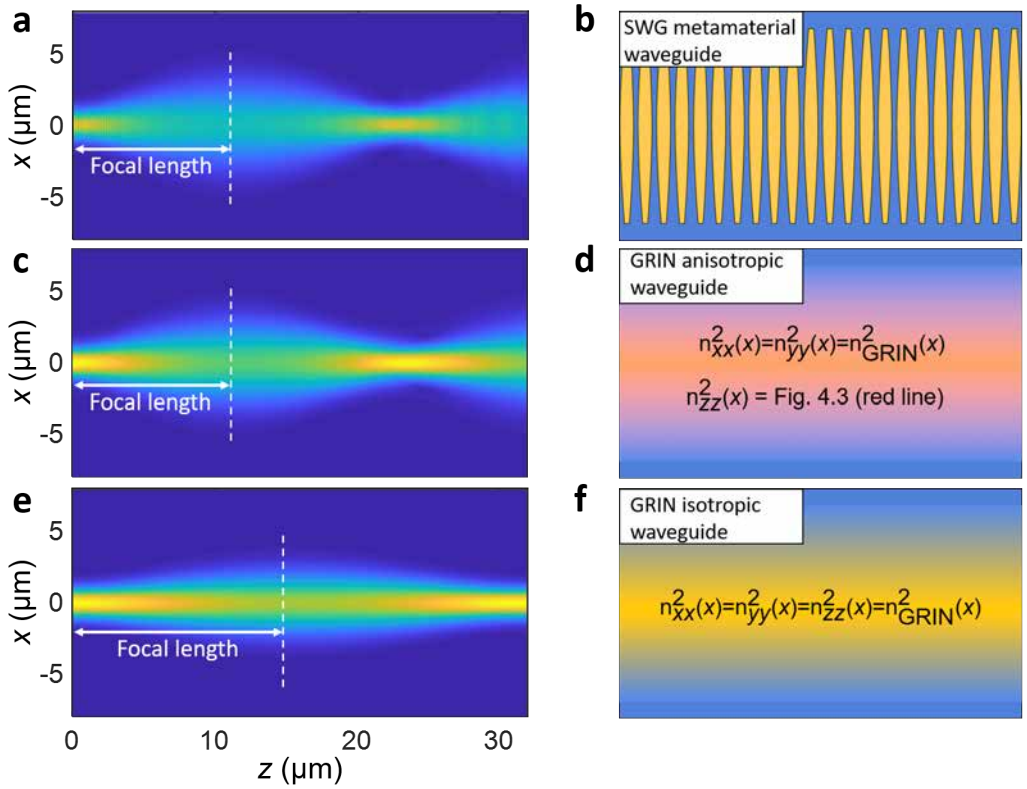

Figure 5.5: a), c), d) 3D-FDTD simulated Field amplitude main component of the TE polarized electric field propagation, $|E_x(x,z)|$, along a b) z-periodic SWG structure d) a gradual anisotropic material, and f) a gradual isotropic material.

the light from interconnecting waveguides to multiple devices such as multimode interferometers or grating couplers. The proposed device expands from a 0.5 µm interconnecting waveguide to a 15 µm wide waveguide with low loss, high bandwidth and high tolerance to fabrication errors. This section is divided in two parts. First, the design of the proposed device by means of electromagnetic simulations. Second, the experimental demonstration of the fabricated spot size converter.

5.3.1. Design of the GRIN lens spot size converter

The design process of the GRIN metamaterial spot size converter starts with the optimization of the GRIN region. In this step the modes of the parabolic GRIN waveguide are studied to achieve a focus length tolerant to fabrication errors and with a flat wavelength response. Then in a second step the electromagnetic propagation from the narrow input waveguide to the wide output waveguide is studied to minimize the power loss on the device.

Design and optimization of the GRIN metamaterial

The proposed SWG topology to implement GRIN metamaterials has 5 degrees of freedom: the metamaterial width, w_G, its period, Λ, the shape of the segments, $DC_G(x)$, the minimum

gap between segments, MFS_G and minimum tip of the segments, MFS_T (see Fig. 5.2a). To achieve the desired spot beam conversion, the metamaterial width is set to $w_G = 16\,\mu m$, slightly wider than the output waveguide. The other parameters are set as follows:

1. Choose a metamaterial period.
2. Choose a minimum gap between segments and a minimum silicon tip.

These elections set the maximum and minimum duty cycles, $DC_{max} = 1 - MFS_{gap}/\Lambda$ and $DC_{min} = MFS_{tip}/\Lambda$, thus fixing the maximum and minimum synthesizable indices imposed by the fabrication constrains: $n_{max} = n_{xx}(DC_{max})$ and $n_{min} = n_{xx}(DC_{min})$.

3. Calculate the parabolic GRIN profile:

$$n^2_{GRIN}(x) = n^2_{max} - \frac{4(n^2_{max} - n^2_{min})}{w^2_G} x^2, \tag{5.6}$$

4. Calculate the duty cycle function, $DC_G(x)$ which implements the GRIN profile by following the algorithm of section 5.2.1.

Therefore, with the width fixed by the desired expansion, the design of the parabolic GRIN region relies on the two first points: To choose the metamaterial period and both minimum feature sizes. To simplify this process, in this Thesis the minimum tip was set to $MFS_{tip} = 50$ nm. Therefore, the GRIN metamaterial was optimized by designing the minimum gap between silicon segments, MFS_G and the period, Λ. The anisotropic homogenization model was used in this optimization as it provides accurate results with a much lower computational effort.

The minimum gap size is one of the most critical dimensions in SWG periodic structures. Small gaps are not only hard to etch but also hard to fill with the cladding material. In the proposed parabolic GRIN profile the minimum gap is found at the center of the structure. Intuition says that this gap should be chosen as small as possible, maximizing the curvature of the parabola, thus minimizing the focus length. However, this intuition is based on isotropic materials. The intrinsic anisotropy of SWG structures changes this paradigm. The minimum focal length in SWG based parabolic GRIN materials is found for non-zero gap sizes. Figure 5.6a shows the focus length for different gap sizes and different periods. Note that for each period the optimum non-zero gap not only minimizes the focal length but it also is in a valley zone where the focal length remains unaltered for small changes on the gap size. This behavior is ideal as it facilitates the device fabrication. To choose the optimum period–gap pair, the focal length bandwidth is studied for each duo (see Fig. 5.6b). In this figure the wavelength behavior of the focal length is shown for each period–gap pair. From these two figures the $\Lambda = 240$ nm design is chosen because although it does not show the flattest bandwidth behavior, it has an easily affordable minimum gap size of ~ 80 nm. The design with a period $\Lambda = 220$ was also a very good candidate, however, it was discarded because of the challenging 60 nm MFS required for this design.

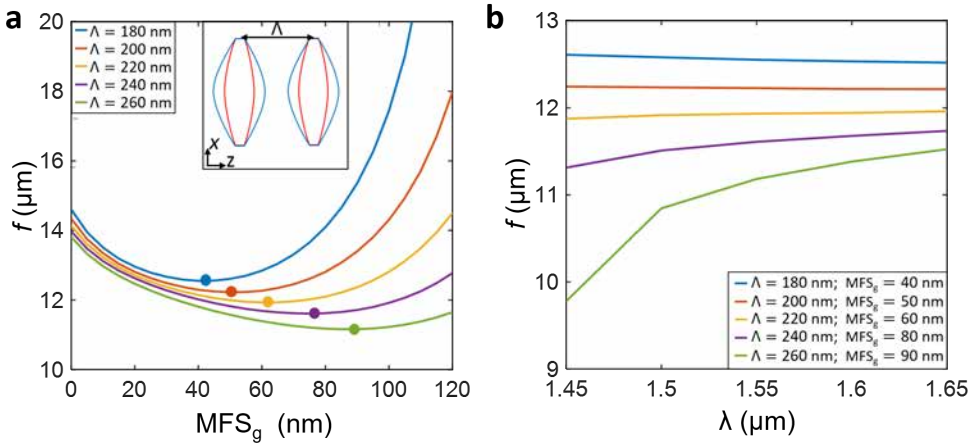

Figure 5.6: a) Focus length as a function of the gap size in the center of the lens obtained through modal analysis of the homogenized anisotropic structure. Inset: Schematic of the period shape variation when changing the gap size. b) Focus length dispersion assuming the optimum hole size for each period (marked with solid circles in (a)).

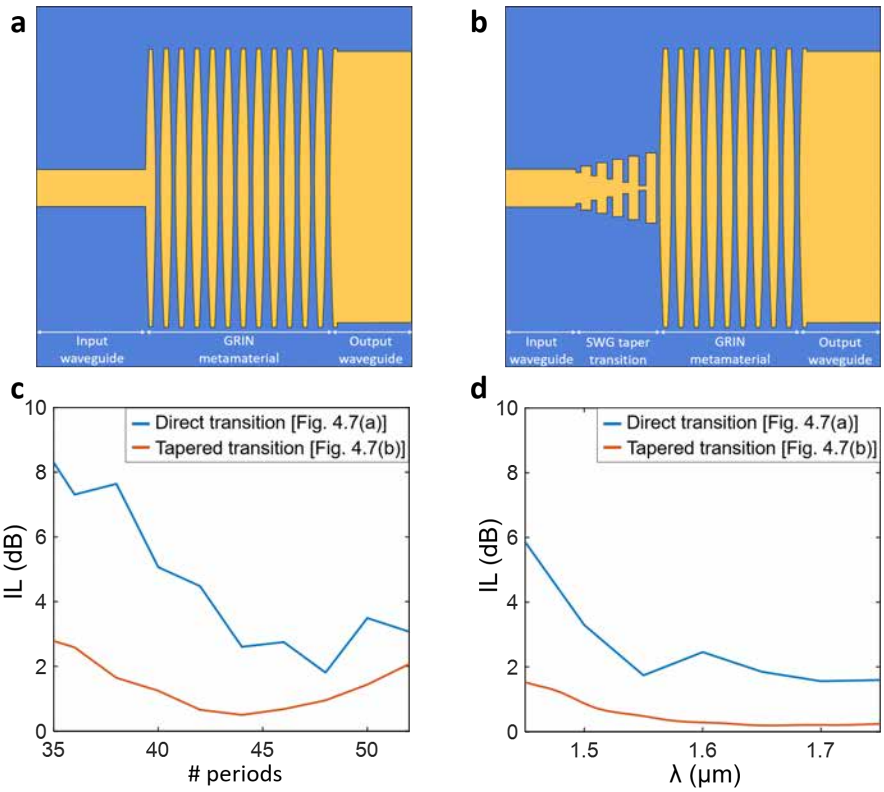

Figure 5.7: a),b) Schematic representation of the GRIN lens spot size converter, a) without and b) with an input transition. c) Insertion losses as a function of the number of periods of the lens with and without transition. d) Insertion losses as a function of wavelength with and without transition.

Device optimization

The second step to design the spot size converter is to minimize the insertion loss (IL) of the device, defined as:

$$\mathrm{IL} = \frac{P_{\mathrm{out}}}{P_{\mathrm{in}}} \tag{5.7}$$

where P_{in} and P_{out} are the power for the fundamental mode of the 500 nm wide input waveguide and the 15 µm wide output waveguide respectively. These two waveguides are connected through the GRIN metamaterial designed in the previous point (see Fig. 5.7a). The simulated IL for different number of periods of the GRIN metamaterial is shown in Fig. 5.7c (blue line). The optimum length is about 48 periods (~ 11.5 µm), matching the focus length predicted in Fig 5.6b (blue line). This structure achieves the desired transition with a power loss of ~ 2 dB. To further minimize the IL a smooth transition between the homogeneous input waveguide and the periodic SWG waveguide is added (see Fig. 5.7b). These kinds of transitions are frequently used to feed SWG based devices. They have two purposes: i) To adapt the electromagnetic field of the homogeneous waveguide to the periodic structure. ii) To widen the input field into the lens to ensure that only paraxial modes are excited. Figures 5.7c and 5.7d red lines show the improvement on the insertion loss when a 15 period long adaptation is inserted. The wavelength behavior of the designed device shows a simulated bandwidth exceeding 350 nm for insertion losses lower than 1 dB.

5.3.2. Experimental demonstration

The experimental demonstration of the designed spot size converters includes the drawing of the fabrication mask, the experimental characterization and the post-processing of the raw measurements. All these parts are essential elements in the prototyping as described in chapter 2.

Mask drawing

The proposed devices was fabricated in a open-access multi project wafer (MPW). A fabrication mask was submitted to the foundry including not only the devices but also specific photonic circuits to measure their performance. The full GDS file from the mask is shown in Fig. 5.8. Two different circuits were drawn to properly characterize the device behavior:

1. **Cut-back configuration circuits**: The proposed spot size converter was replicated 0, 2, 4 and 6 times in four different circuits (see Fig. 5.9a). This configuration allows us to obtain the power loss of a single device with a linear cut-back regression. Moreover, each set of 2 spot size converter has a wide waveguide in between forming a Fabry-Perot cavity , where the lenses are the partial mirrors. The cavity length (25 µm) was designed to be able to characterize the mismatching of the wide waveguide with the lenses. The light gets in and out of the chip in this configuration with a set of SWG edge coupler.
2. **Back to back configuration circuits**: The proposed spot size converter is used to transform the light beam from the grating couplers to the interconnection waveguides and vice versa (see Fig. 5.8c and Fig. 5.8d). This structure couples the light in and out

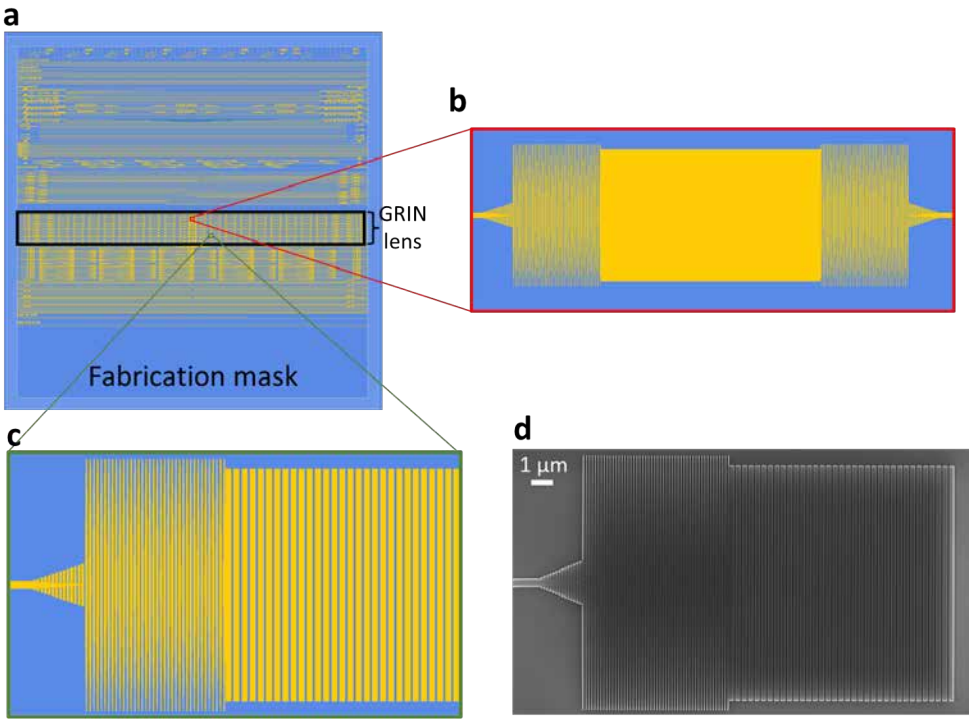

Figure 5.8: a) Full GDS mask with different projects. The mask dimensions are ~ 8.78 mm × 8.78 mm. b) Zoom in specific part of the spot size converter region. c) Zoom in a spot size converter in back-to-back configuration. d) Zoom in a spot size converter feeding a grating coupler.

of the chip occupying a minimal chip area. This configuration allows us to obtain the power loss of a single device in a realistic scenario. For comparison purposes, the same configuration but substituting the designed spot size converter by 150 µm long linear tapers was also fabricated.

Experimental characterization and post-processing of the raw data

Characterization of the edge coupler configuration circuits: The experimental characterization started by measuring the cut back configuration circuits. Figure 5.9b shows the measured output power of the back-to-back configurations with the spot size converter repeated 0 (reference), 2, 4 and 6 times. The ripples on the spectra appear because of the Fabry-Perot cavities formed by each set of two lenses and a wide waveguide in between. These ripples were analyzed using a minimum phase technique, their periodicity confirms that they come from the 25 µm cavity and their amplitude predicts a 3% desadaptation between the lenses and the wide waveguide. Figure 5.9c shows the IL of a single device calculated from the raw data shown in Fig. 5.9b. For that purpose, the output power of the 1 back-to-back circuit is normalized using the reference waveguide and divided by a factor of 2 (number of lenses in 1 back-to-back). Filtering the curve to erase the artificial ripples gives the performance of a single spot size converter (see Fig. 5.9c, blue line). Repeating this process for all the circuits and flavours the cut back linear regression shown in Fig. 5.9d is calculated. This figure shows the IL of the nominal lens and some flavours emulating over-etching and under-etching of 10% of the duty cycle. All of them have insertion loss lower

than 1 dB. Therefore, the proposed spot size converter shows low-loss, high bandwidth and high tolerance to fabrication errors.

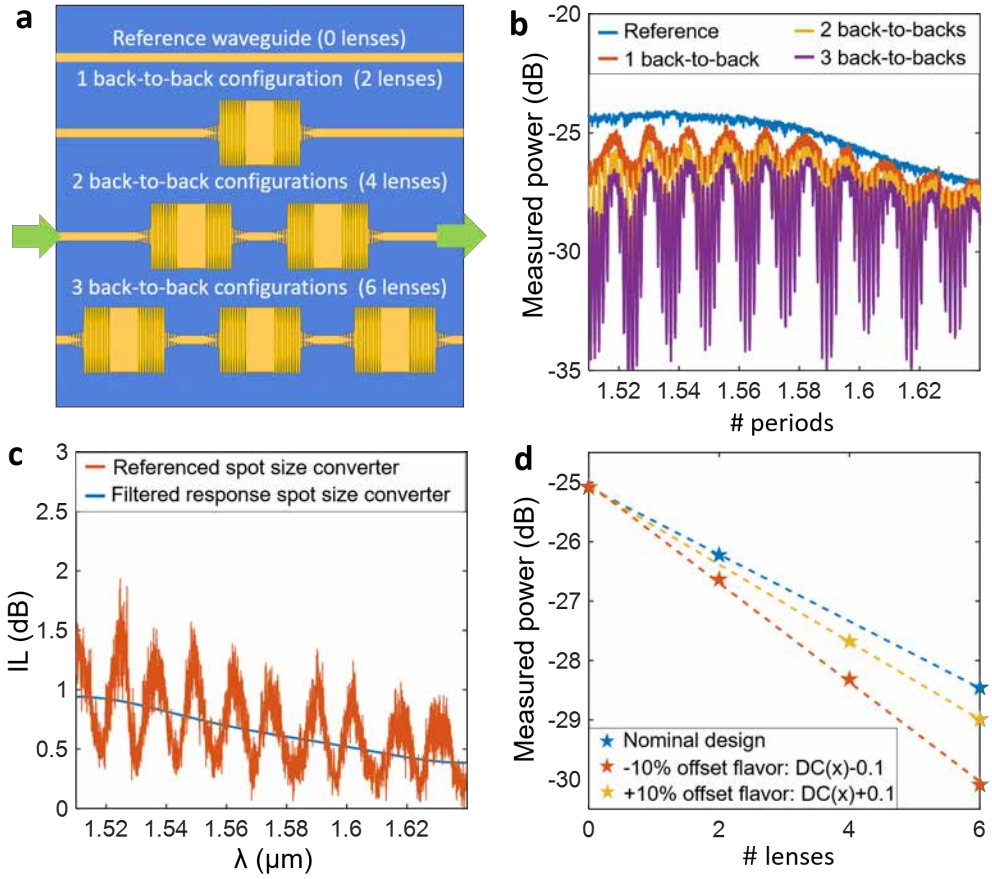

Figure 5.9: a) Schematic representation of the GRIN lens spot size converter cascaded 0, 2, 4 and 6 times. b) Raw measurement of the output power of each circuit shown in (a). c) Insertion losses of a single device with and without filtering the ripples generated in the Fabry-Perot cavity. d) Cut back regression of the insertion loss of the measured devices at the central wavelength of the laser, $\lambda = 1.58\,\mu m$.

Characterization of the grating coupler configuration circuits: Once the performance of a single device was characterized in the back-to-back configuration a realistic scenario of a grating coupler being fed by a GRIN lens spot size was measured. Figure 5.10 shows the raw measured power of a set of grating couplers fed by the designed GRIN spot size converter. For comparison purposes, the measured power for a set of grating couplers fed by 150 µm long is also shown. Both structures shows a similar behavior with the designed spot size converter occupying much less chip area.

5.4. Conclusions

In this chapter the implementation of gradual index metamaterials through SWG structures has been demonstrated. Such a demonstration includes the proposal of the SWG topology to implement gradual metamaterials, the implementation algorithm of the desired index profile,

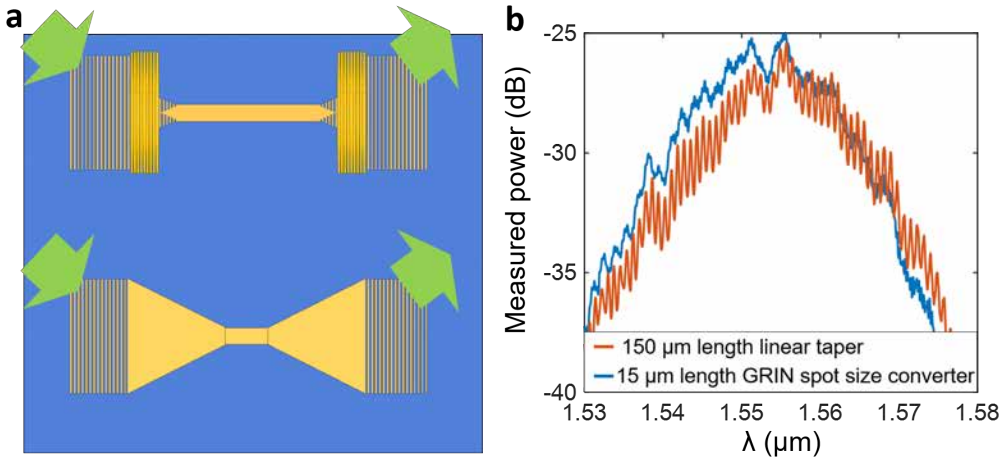

Figure 5.10: a) Schematic representation of a pair of grating coupler fed by a set of GRIN lens based spot size converter and 150 µm length grating coupler. b) Raw measurement of the output power of each circuit shown in (a).

and the validation of the design process through electromagnetic simulations. The proposed SWG topology allows us to implement anisotropic GRIN metamaterials with the desired index profile in two out of three elements of the diagonal tensor (n_{xx} and n_{yy}). The consequences of the detuning of the n_{zz} component with respect to the other two components will depend on the specific device. Such consequences can be easily studied with the provided model developed in section 5.2.1, as it accurately predicts the metamaterial behavior as was shown in Fig. 5.4 and Fig. 5.5.

Then, to experimentally validate the implementation of GRIN metamaterials, a parabolic GRIN waveguide was fabricated in a standard 220 nm-thick SOI platform. This metamaterial has been used to implement an ultra-compact spot size converter. In this application the detuning of the n_{zz} component reduces the device length (see Fig. 5.5) and increases the resilience to fabrication errors (see Fig. 5.6). The fabricated spot size converter has a total length of ~ 15 µm and it has a performance comparable with a 150 µm long linear taper.

Therefore, the proposed topology and implementation algorithm is a relatively easy method to implement GRIN metamaterial in standard silicon photonics platforms. This capability opens multiple avenues in the design of integrated photonic devices as GRIN materials that can be used to handle the flow of the light.

6. Conclusions, outlook and future research lines

This chapter summarizes the main conclusions and achievement of this Thesis (section 6.1), and then discusses the ongoing work and research activities that can be continued in the future (section 6.2).

6.1. Conclusions and outlook

The design of metamaterials with optimized optical properties by using of subwavelength structures (SWG) has become an essential tool in silicon photonics, and more specifically in the silicon on insulator (SOI) platform. SWG metamaterials enable improvements in the performance of integrated optical devices, as well as new functionalities, without increasing the complexity of the manufacturing processes. For this reason, today it is very common to find SWG metamaterials in high-performance integrated optical devices implemented on SOI platform.

In this Thesis several advances in fundamental aspects related to the design of SWG metamaterials have been proposed, such as the development of modeling and simulation tools, new topologies to implement SWG metamaterials and the design of high performance integrated photonic devices. In all cases, rigorous electromagnetic simulations of the proposed structures have been performed and prototypes have been developed and then experimentally characterized. The devices have been fabricated on multi-project wafers from a commercial foundry and have not required any additional process to the standard offered by the foundry. The most relevant contributions have been published in high impact peer-reviewed journals and international conferences.

As a result of the research work on SWG metamaterials developed in this Thesis, the following conclusions have been reached:

1. **It is essential to have modeling and simulation tools providing physical insight and reducing design times.** The simulation of SWG periodic structures frequently requires a high computational cost. The developed modeling tools of SWG periodic structures as equivalent homogeneous anisotropic metamaterials allow us to perform quick but accurate preliminary simulations, saving much time in the design process of photonic devices. Moreover, the homogenization of the SWG structures as anisotropic metamaterials eases the understanding of the underlying physics promoting the proposal of novel SWG based devices. Two homogenisation models to calculate the equivalent anisotropic structure of a given SWG have been demonstrated: The laminar periodic structure (LPS) model and periodic slab structure (PSS) models. The LPS is a very simple model, requiring just the resolution of a semi-analytical equation but it is very

limited by the Bragg regime. Assuming typical SOI platform, this model is limited to SWG with periods above ~ 240 nm at a wavelength of $\lambda = 1.55\,\mu m$ and a 50% duty cycle. On the other hand, the PSS model is a little more complex, requiring the simulation of 2D periodic slab, but it can be used for SWG structures with a period up to ~ 300 nm.

2. **The canonical SWG structure has a small number of degrees of freedom, which limits the design possibilities.** The control over the optical properties of the SWG metamaterials opens multiple new avenues for the design of high-performance photonic devices. In this Thesis, two novel SWG topologies to enhance the control over the synthesized metamaterial have been proposed: Tilted SWG metamaterials and bricked SWG metamaterials. These SWG topologies expand the design space of implemented metamaterials by offering new degrees of freedom to control the on-chip light propagation. Specifically, they both provide control over the effective index and dispersion of TE polarized modes without affecting the TM polarized or adding any additional difficulties to the fabrication process. Therefore, they are well poised for the design of polarization management devices. Tilted and bricked SWG metamaterials are interchangeable in most situations, with both providing a similar control over the metamaterial properties. However, bricked SWG metamaterials have two main advantages which make them a more interesting solution in many applications: 1) their Manhattan-like pattern. 2) their longer periods.

3. **Gradual index metamaterials can be synthesized with standard CMOS fabrication process.** Gradual index (GRIN) materials offers virtually complete control over light propagation. In this Thesis, a methodology to implement GRIN metamaterials in integrated chips by using SWG metamaterials have been proposed. It is based on gradually modify the duty cycle along the transversal direction. The proposal includes a mathematical model to incorporate the gradualness into the permittivity tensor component of the synthesized structure. The synthesis of GRIN metamaterials in SOI chips opens multiple design approaches such as those based on inverse design or transformation optics.

4. **The topologies proposed above can be incorporated in devices with practical applications, improving their performance or implementing new functionalities.** The final goal of SWG metamaterials is the design of high-performance devices. A set of devices using the developed models and SWG topologies have been demonstrated along this Thesis:

   a) Asymmetrical directional coupler polarization beam splitter: A tilted SWG metamaterial has been used to break the TE polarization phase matching condition of directional coupler. By doing so, the input polarizations are split at the output ports of the directional coupler with a measured bandwidth 70 nm with ER larger than 15 dB and 140 nm with IL lower than 1 dB.

   b) Ultra-broadband 2 × 2 multimode interferometer: The dispersion engineering of bricked SWG metamaterial has been used to optimize the bandwidth response of an MMI. This topology allow us to design the dispersion of the SWG metamaterial while setting a specific period, ensuring a minimum gap size between segments. The proposed MMI shows a measured insertion loss and imbalance lower than 1 dB in the 140 nm bandwidth of the laser.

c) Spot size converter GRIN lens: The proposed duty cycle modulated SWG GRIN metamaterials has been used to implement an integrated GRIN lens expanding the light from a narrow 0.5 μm wide input waveguide to a 15 μm wide grating coupler. The proposed device has demonstrated an impressive bandwidth, limited by the 140 nm bandwidth of the laser source.

These four conclusions are the end of this Thesis but they are also the beginning of multiple novel approaches to control the light on silicon photonic chips. As a proof of that, the work developed in this Thesis has been already reused by many different research groups [159–161, 163–165] and we believe that it paves the way towards ever increasing adoption of subwavelength engineered devices in mass scale fabrication processes. Of course, such a commercial success of SWG metamaterial is contingent upon other factors, such as the improvements on the fabrication techniques or the emergence of a killer application requiring the ultra-high performance enabled by SWG metamaterials. Deep-UV immersion lithography techniques with 80-100 nm resolution is being offered by several silicon photonics foundries and improved lithographic resolution achieved by extreme-ultraviolet [214] techniques facilitates the use of SWG structures even at visible wavelengths and opening up the long-wave limits in the near- and mid-infrared bands.

6.2. Future work

The main results of this Thesis set the basis for a series of attractive lines of investigation. Ongoing work and several possible directions for future research activities are listed here.

6.2.1. Design and experimental demonstration of photonic devices with improved performance using the proposed SWG metamaterial topologies.

There is a plethora of application where the proposed SWG topologies can be used to optimize the performance of integrated photonic devices, especially in the design of polarization management devices. Some devices which are currently under examination includes polarization management devices based on GRIN lenses, spot size converters based on bricked SWG metamaterials, MMIs with arbitrary splitting ratio or polarization agnostic devices such as multimode interferometers or grating couplers.

6.2.2. Development of novel alternatives to implement GRIN metamaterial

GRIN metamaterials have been demonstrated by using duty-cycle modulated SWG structures. An interesting alternative which is being currently under examination is the implementation of GRIN metamaterial with bricked modulated SWG structures. These structures allow us to work with longer periods compared with conventional SWG structures, a critical parameters to increase the range of gradualness. Moreover, the combination of both kind of GRIN metamaterials (duty-cycle and bricked modulated), would further increase synthesizable gradualness.

6.2.3. Combination of the SWG metamaterials with inverse design / transformation optics design techniques

Inverse design / transformation optics techniques are design strategies which have been extensively exploited in the last decade [208–211] to design photonic devices. These techniques frequently results in a refractive index maps which have to be synthesized. The combination of the bricked/tilted topologies with the engineering of the duty cycle and even the gradualness of those parameters opens a roadmap to implement the required index profiles.

A. Curriculum Vitae

José Manuel Luque González earned his BSc and MSc in Telecommunication Engineering from the Universidad de Málaga in 2015 and 2017 respectively. In 2017 he received a national scholarship from the Spanish Ministry of Science that funded his Ph.D. on the development of subwavelength grating metamaterials supervised by Dr. Alejandro Ortega Moñux and Dr. Robert Halir. The work developed in his PhD thesis was mostly done in the Photonics and Rf Lab at Málaga's University but in close collaboration with the National Research Council of Canada (NRC) and the National Research Council of Spain (CSIC).

A complete list of his publications is given below.

Articles in International Journals

1. C. Pérez-Armenta, A. Ortega-Moñux, **J. M. Luque-González**, et al., "Polarization independent multimode interference coupler with anisotropy-engineered bricked metamaterial," *Photon. Res.* vol. 10, A57-A65 (2022)
2. **J. M. Luque-González**, A. Sánchez-Postigo, A. Hadij-ElHouati et al., "A review of silicon subwavelength gratings: building break-through devices with anisotropic metamaterials," *Nanophotonics*, vol. 10, pp. 2765-2797 (2021).
3. D. González-Andrade, J. Vilas, I. Olivares, A. Dias, **J. M. Luque-González** et al., "Mode Converter and Multiplexer With a Subwavelength Phase Shifter for Extended Broadband Operation," *IEEE Photonics Technology Letters*, vol. 33, 1262-1265, (2021)
4. **J. M. Luque-González**, A. Ortega-Moñux, R. Halir, et al., "Bricked subwavelength gratings: a tailorable on-chip metamaterial topology," *Laser Photon. Rev.*, vol. 15, p. 2000478, (2021).
5. D. Pereira-Martín, **J. M. Luque-González**, J. Gonzalo Wangüemert-Pérez, et al., "Complex spectral filters in silicon waveguides based on cladding-modulated Bragg gratings," *Opt. Express,* vol. 29, pp. 15867–15881, (2021).
6. **J. M. Luque-González**, A. Herrero-Bermello, A. Ortega-Moñux, et al., "Polarization splitting directional coupler using tilted subwavelength gratings," *Opt. Lett.*, vol. 45, pp. 3398–3401, (2020).
7. D. González-Andrade, **J. M. Luque-González**, J. Gonzalo Wangüemert-Pérez, et al., "Ultra-broadband nanophotonic phase shifter based on subwavelength metamaterial waveguides," *Photonics Res.*, vol. 8, pp. 359–367, (2020).
8. A. Herrero-Bermello, A. Dias-Ponte, **J. M. Luque-González**, et al., "Experimental demonstration of metamaterial anisotropy engineering for broadband on-chip polarization beam splitting," *Opt. Express,* vol. 28, pp. 16385–16393, (2020).

9. **J. M. Luque-González**, R. Halir, J. G. Wangüemert-Pérez, et al., "An ultracompact GRIN-lens-based spot size converter using subwavelength grating metamaterials,"*Laser Photon. Rev.*, vol. 13, p. 1900172, (2019).
10. A. Herrero-Bermello, **J. M. Luque-González**, R. Halir, et al., "Zero-birefringence silicon waveguides based on tilted subwavelength metamaterials," *IEEE Photonics J.*, vol. 11, p. 2700308, (2019)
11. A. Herrero-Bermello, **J. M. Luque-González**, A. V. Velasco, et al.„ "Design of a broadband polarization splitter based on anisotropy engineered tilted subwavelength gratings," *IEEE Photonics J.*, vol. 11, p. 6601508, (2019).
12. **J. M. Luque-González**, A. Herrero-Bermello, A. Ortega-Moñux, et al., "Tilted subwavelength gratings: controlling anisotropy in metamaterial nanophotonic waveguides," *Opt. Lett.*, vol. 43, pp. 4691–4694, (2018).
13. R. Halir, P. Cheben, **J. M. Luque-González**, et al., "Ultrabroadband nanophotonic beamsplitter using an anisotropic sub-wavelength metamaterial," Laser Photon. Rev., vol. 10, pp. 1039–1046, (2016).
14. A. Sánchez-Postigo, J. Gonzalo Wangüemert-Pérez, **J. M. Luque-González**, et al., "Broadband fiber-chip zero-order surface grating coupler with 0.4 dB efficiency," *Opt. Lett.*, vol. 41, pp. 3013–3016, (2016).

International Conference Proceedings

1. **J. M. Luque-González**, A. Ortega-Moñux, J. G. Wangüemert-Pérez, et al., "Advanced subwavelength grating metamaterial topologies for light propagation tailoring," *Photonics North,* Niagara Falls, Canada, 24-26 May (2022) [Invited presentation].
2. **J. M. Luque-González**, R. Halir, J. G. Wangüemert-Pérez, et al., "Ultra-broadband polarization beam splitter with a gradual anisotropy engineered subwavelength metamaterial," *European Conference on Integrated Optics (ECIO),* Milan, Italy, 4-6 May (2022) [Poster presentation].
3. **J. M. Luque-González**, A. Ortega Moñux, Robert Halir et al., "Bricked subwavelength structures: a flexible metamaterial topology," *Photonics North,* Virtual Conference, 31 May - 2 June (2021) [Oral presentation].
4. **J. M. Luque-González**, A. Herrero-Bermello, A. Ortega-Moñux, et al., "A Broadband Polarization Splitter Directional Coupler Based on Tilted Subwavelength Grating Metamaterials," *IEEE Photonics Conference*, Virtual Conference, 28 September - 1 October (2020). [Oral presentation].
5. **J. M. Luque-González**, A. Herrero-Bermello, A. Ortega-Moñux, et al., "Independent phase matching for TE and TM polarization in directional couplers with tilted subwavelength structures," *European Conference on Integrated Optics (ECIO)*, Virtual Conference, 23-25 June (2020). [Oral presentation].
6. **J. M. Luque-González**, A. Herrero, A. Ortega-Moñux, et al., "Separador de polarización integrado de altas prestaciones basado en estructuras sub-longitud de onda," *XXXV Simposio Nacional de la Unión Científica Internacional de Radio (URSI)*, Virtual Con-

ference. 2-4 September (2020) [Oral presentation].

7. **J. M. Luque-González**, A. Herrero-Bermello, A. Ortega-Moñux, et al,. "Designing polarization management devices by tilting subwavelength grating structures," *SPIE Optics + Optoelectronics*, Prague, Czech Republic, 1-4 April (2019). [Oral presentation].

8. **J. M. Luque-González**, R. Halir, J. de-Oliva-Rubio, et al,. "Design of a Subwavelength grating metamaterial GRIN lens", *XXVII International Workshop on Optical Waveguide Theory and Numerical Modelling (OWTNM)*, Málaga, Spain, 10-11 May (2019). [Oral presentation].

9. **J. M. Luque-González**, Herrero-Bermello, A. Ortega-Moñux, et al., "Controlling birefringence in silicon photonics SWG waveguides," *XXVII International Workshop on Optical Waveguide Theory and Numerical Modelling (OWTNM)*, Málaga, Spain, 10-11 May (2019). [Oral presentation].

10. **J. M. Luque-González**, A. Ortega-Moñux, R. Halir, et al,. "High performance and small footprint spot size converters based on SWG metamaterial lenses ", *European Conference on Integrated Optics (ECIO),* Valencia, Spain, 28-31 May (2018). [Oral presentation].

Patents

1. **Tilted SWG metamaterials:** R. Halir, **J. M. Luque-González**, A. Herrero-Bermello, A. Ortega-Moñux, Í. Molina-Fernández, J. G. Wangüemert-Pérez, A. Villafranca-Velasco, "Guía de onda, método de fabricación de dicha guía de onda y divisor de polarización que hace uso de dicha guía de onda," P201830653.

2. **Bricked SWG metamaterials:** J. G. Wangüemert-Pérez, Í. Molina-Fernández, A. Ortega-Moñux, R. Halir, **J. M. Luque-González**, "Guía de onda periódica sub-longitud de onda enladrillada, adaptador modal, divisor modal y divisor de polarización que hacen uso de dicha guía de onda," P202030367.

Awards

1. **June 2022** Best young inventor patent (P201830653). Given by Spanish Patent and Trademark Office.

2. **May 2022** Finalist in the 3M Thesis-Talk at University of Málaga.

3. **December 2021** Best publication in Engineering/Architecture area. Given by the Universidad de Málaga, Kazuyo Sejima 11th Edition Award.

4. **June 2018** Best MSc Thesis. Given by the Spanish Official National Telecommunications Engineer Association (COIT).

5. **March 2018** Best MSc Thesis. Given by the Escuela Técnica superior de Ingeniería de Telecomunicación (ETSIT) de la Universidad de Málaga.

Stay at foreign centers

1. **May-June 2022** 3 weeks research stay at national research council (NRC) of Canada designing pump rejection filters under the supervision of Prof. Pavel Cheben.
2. **May-August 2019** 3 months research stay at institut national de la recherche scientifique (INRS) designing Bragg filters to implement delay lines under the supervision of Prof. José Azaña.

Courses

1. **June 2022** ePIXfab silicon photonics summer school at the Centre for Nanosciences and Nanotechnology (C2N) of Paris-Saclay.
2. **March 2022** Formation on the technology aspects fabricating photonic circuits at Institute of microelectronic of Barcelona (IMB-CNM).
3. **September 2019** Electronic-Photonic Integrated Systems Summer School at Universidad de Málaga.

Teaching

1. **Señales y sistemas (Signals and systems):** 70 lecture hours.
2. **Servicios de difusión audiovisual (Audiovisual broadcasting services)** 120 lecture hours.
3. **Fundamentos de propagación de ondas (Foundations on wave propagation)** 13 lecture hours.

Participation in invited/keynote conferences as co-author (Being one of the first three authors)

1. R. Halir, A. Sánchez-Postigo, **J. M. Luque-González**, et al., "Subwavelength Grating Metamaterial Structures for Integrated Photonics," *Optical Fiber Conference (OFC)*, San Francisco, California, United States, 6-10 June 2021 [Invited presentation].
2. R. Halir, **J. M. Luque-González**, A. Sánchez-Postigo, et al., "Subwavelength metamaterials: the path towards next-generation silicon photonic devices," *Integrated Optics Conference of the SPIE Optics and Optoelectronics Symposium*, Prague, Czech Republic, 19-22 April 2021 [Keynote presentation].
3. Í. Molina-Fernández, A. Hadij-ElHouati, **J. M. Luque-González**, et al., "Subwavelength grating silicon photonic devices," SPIE Photonics West, San Francisco, United States, 6-11 March 2021 [Invited presentation].
4. R. Halir, **J. M. Luque-González**, A. Sánchez-Postigo, et al., "Building high performance devices with silicon metamaterials," *Next generation Silicon Photonics Workshop at the Asia Communications and Photonics Conference (ACP)*, Virtual Conference, 24-27 October (2020), [Invited presentation].
5. R. Halir, A. Herrero-Bermello, **J. M. Luque-González**, et al., "Silicon Subwavelength

Structures: Practical Metamaterials for Communications and Sensing," *OSA Advanced Photonics Congress – Integrated Photonics Research, Silicon and Nanophotonics,* Virtual conference, 13-16 July, (2020) [Invited presentation].

6. R. Halir, **J. M. Luque-González**, A. Sánchez-Postigo, et al., "Subwavelength silicon photonics," *Photonics North,*, Virtual conference, 26-28 May (2020) [Keynote presentation].

7. R. Halir, **J. M. Luque-González**, A. Sánchez-Postigo, et al., "Practical metamaterial photonics," *IEEE Group IV Photonics*, Singapore, 28-30 August (2019) [Invited presentation].

8. R. Halir, **J. M. Luque-González**, A. Sánchez-Postigo, et al., "High performance silicon photonic devices based on practical metamaterials," *Optoelectronics and Communications Conference*, Fukuoka, Japan, 7-11 July (2019) [Invited presentation].

9. A. Ortega-Moñux, **J. M. Luque-González**, D. Pereira-Martín, et al., "Design of Subwavelength Grating Metamaterial Waveguides for Communications and Sensing Applications," *Photonics & Electromagnetics Research Symposium*, Rome, Italy, 17-20 June (2019) [Invited presentation].

10. R. Halir, A. Sánchez-Postigo, **J. M. Luque-González**, et al., "Subwavelength gratings: from basic physics to state-of-the-art-devices," XXVII International Workshop on Optical Waveguide Theory and Numerical Modelling (OWTNM), Málaga, Spain, 10-11 May (2019) [Invited presentation].

11. R. Halir, **J. M. Luque-González**, A. Herrero-Bermello, et al., "Designing high performance devices with silicon subwavelength structures," *European Optical Society Biennial Meeting (EOSAM)*, Delft, Netherlands, 8-12 October (2018) [Invited presentation].

12. A. Ortega-Moñux, **J. M. Luque-González**, A. Sánchez-Postigo, et al., "Subwavelength Grating Metamaterial Engineering: A New Tool for Silicon Photonics," *Integrated Photonics Research (IPR)*, Zurich, Switzerland, 2-5 July (2018) [Invited presentation].

13. R. Halir, A. Herrero-Bermello, **J. M. Luque-González**, A. Ortega-Moñux, G. Wangüemert-Pérez, A. V. Velasco, J. H. Schmid, P. Cheben, and Í. Molina-Fernández, "Designing Anisotropy with Waveguide Subwavelength Structures," *20th International Conference on Transparent Optical Networks (ICTON)*, Bucharest, Romania, 1-5 July (2018) [Invited presentation].

14. A. Ortega-Moñux, A. Sánchez-Postigo, **J. M. Luque-González**, et al., "Subwavelength grating metamaterial engineering in integrated optics," *Photonics North*, Montreal, Canada, 5-7 June (2018) [Invited presentation].

15. J. Gonzalo Wangüemert-Pérez, A. Sánchez-Postigo, **J. M. Luque-González**, et al., "Design of integrated photonic devices based on subwavelength structures for Near and Mid-Infrared applications", *Photonics North*, Ottawa, Canada, 6-8 June (2017) [Invited presentation].

B. Resumen en Español

Esta Tesis está dedicada al estudio de las estructuras de rejilla de sublongitud de onda (SWG, por sus siglas en inglés): metamateriales ópticos extremadamente versátiles que se han convertido en una herramienta fundamental para el diseño de dispositivos fotónicos de ultra alto rendimiento. La importancia de las estructuras SWG radica en su capacidad para sintetizar materiales artificiales con propiedades ópticas personalizables, como el índice de refracción, la dispersión o la anisotropía. A lo largo de la Tesis se proporciona un marco completo para los metamateriales SWG, incluyendo una revisión de los diferentes procedimientos y herramientas electromagnéticas utilizadas a lo largo de esta Tesis para demostrar las topologías y dispositivos SWG propuestos, un estudio teórico de la propagación de ondas a través de estructuras SWG, los modelos para predecir su comportamiento homogéneo, y la propuesta, diseño y caracterización experimental de varias topologías y dispositivos SWG. Pero antes de estas discusiones, se contextualiza el uso de los metamateriales SWG.

B.1. Introducción

B.1.1. Fotónica integrada

El término fotónica define la ciencia y las tecnologías encargadas de generar, controlar y detectar los fotones, que son partículas de luz. Las aplicaciones de la fotónica van desde su principal impulsor, las comunicaciones ópticas [1–4] a muchos otros, como los dispositivos optoelectrónicos orgánicos [5–7], la fotovoltaica [8, 9], ciencia de los rayos X [10, 11], óptica biomédica [12–14], detección [15–17] o espectroscopía [18, 19] entre muchas otras. Históricamente, las aplicaciones fotónicas se han abordado con componentes ópticos discretos conectados a través de la fibra óptica o la propagación en el espacio libre. Sin embargo, los sistemas ópticos discretos son difíciles de escalar, caros y tienden a sufrir inestabilidades mecánicas. Estos inconvenientes hicieron que el mercado se decantara por la fotónica integrada (IPh) en las aplicaciones que lo permiten. La IPh se ocupa de la fabricación de varios componentes fotónicos en un sustrato planar común, incluyendo fuentes de luz, acopladores, divisores de haz, filtros, dispositivos de gestión de la polarización, detectores o interferómetros, entre otros, que se utilizan como bloques de construcción para los circuitos integrados fotónicos (PIC). Algunas aplicaciones prometedoras del mercado de IPh son la comunicaciones de corta y larga distancia, la industria aeroespacial, la automoción, la biodetección y el Internet de las cosas (IoT) [22].

Entre las distintas plataformas de fotónica integrada, las plataformas de fotónica de silicio (SiPh) destacan actualmente como la solución prominente, sobre todo para la implementación de dispositivos pasivos. Las plataformas de silicio se iniciaron a mediados de la década de 1980 con una serie de artículos seminales de R. A. Soref y sus colaboradores [43–48] donde se discutieron las ventajas del silicio sobre otros materiales. Las plataformas de SiPh

comprenden muchas plataformas de fabricación diferentes, como la de silicio sobre aislante (SOI), la de nitruro de silicio (SiN), la de sílice sobre silicio, la de germanio sobre aislante, la de germanio sobre silicio (GOS) o la de oxinitruro de silicio (hydex). La plataforma SOI, compuesta por guías de onda de silicio sobre una capa de dióxido de silicio, es actualmente la plataforma SiPh de referencia tanto en términos de madurez tecnológica como de uso comercial [49] con multiples dispositivos y circuitos integrados implementados sobre ella [50]. Una de las características más importantes de las plataformas fotónicas de silicio es la compatibilidad de su proceso de fabricación con el proceso de fabricación CMOS, lo que permite aprovechar los miles de millones de dólares de inversión y las décadas de investigación en este campo [51]. Además, el alto contraste de índice entre los materiales SOI, $\Delta n \sim 2$, permite un confinamiento submicrométrico y radios de curvatura extremadamente pequeños, $\sim 5\,\mu$m. Aparte de SOI, otra plataforma fotónica de silicio que está ganando atención en la última década es el nitruro de silicio. El interés por el SiN proviene principalmente de sus potenciales pérdidas de propagación ultrabajas (<1 dB/m), su gran ventana de transparencia y sus propiedades no lineales mejoradas en comparación con el SOI, como la ausencia del efecto de absorción de dos fotones [52, 53]. En general, las aplicaciones que más se benefician de la plataforma de silicio son las que requieren que muchos dispositivos se encadenen en un sistema complejo. Por otro lado, el principal inconveniente asociado al SiPh es el bandgap indirecto de los materiales del grupo IV, que dificulta la generación eficiente de luz y la falta de diferentes materiales compatibles con el CMOS, lo que dificulta el diseño de dispositivos de alto rendimiento.

B.1.2. Metamateriales SWG

Para suplir el limitado número de materiales compatibles con el CMOS en fotónica integrada de silicio se propuso el uso de guías SWG. Este tipo estructuras periódicas comprenden dos dieléctricos diferentes, normalmente segmentos de silicio y dióxido de silicio/aire, dispuestos con una periodicidad, Λ, mucho más corta que la longitud de onda, λ, de la onda que se propaga (Véase Fig. B.1a). Cada material tiene una longitud a y b respectivamente, con el ciclo de trabajo DC=a/Λ que mide la cantidad de silicio por período. El interés de los metamateriales SWG radica en su capacidad para comportarse como estructuras

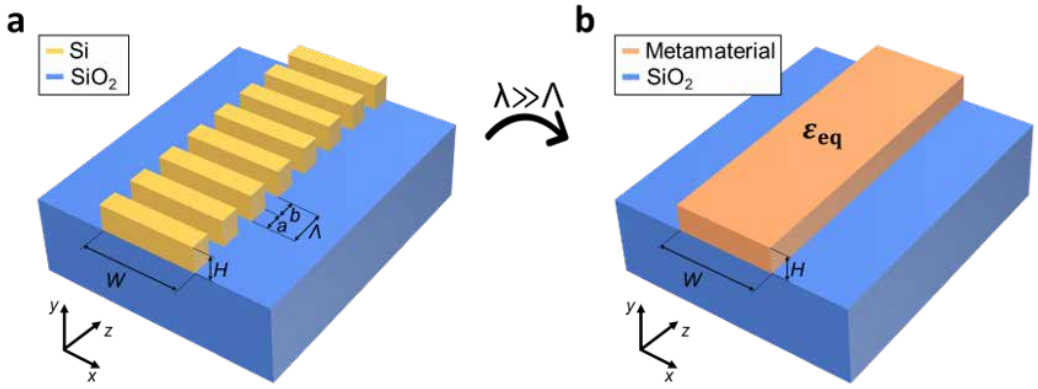

Figure B.1: Representación esquemática de a) una guía de onda SWG en SOI y b) su correspondiente guía de onda homogénea equivalente.

homogéneas (Véase Fig. B.1b). Es decir, una onda que se propague a lo largo de una guía de ondas SWG no se difractará por las interfaces periódicas, sino que se propagará de forma similar a como lo haría a lo largo de una guía de ondas homogénea. Este tipo de guías de onda SWG se han utilizado ampliamente en SiPh desde su demostración en plataformas integradas en 2006 por Cheben et al [91]. Desde ese año y hasta mediados de la década de 2010, la mayoría de los trabajos sobre SWG en fotónica integrada utilizaban modelos simples en los que la estructura del SWG se modelaba como un material isótropo definido por un índice de refracción equivalente, n_{eq}. Sin embargo, a partir de 2016 este paradigma cambió cuando se demostró que los modelos anisótropos, definidos por un tensor de permitividad equivalente $\boldsymbol{\varepsilon}_{\mathrm{eq}}$, representan con mayor precisión el comportamiento real de los metamateriales SWG. Hasta de inicio de esta tesis, los modelos matemáticos que permiten calcular las propiedades anisotropas de las estructuras SWG han sido poco estudiados. Dichos modelos son útiles para poder proponer nuevos dispositivos fotónicos que utilicen estructuras SWG, ayudando tanto al diseño como al entendimiento de las mismas.

B.1.3. Objetivos y aportaciones de esta Tesis

El objetivo principal de esta Tesis es avanzar en el uso de metamateriales de rejilla de sublongitud onda tanto a nivel fundamental como aplicado. A nivel fundamental, se han propuesto y validado novedosas topologías de metamateriales SWG para lograr un mayor control sobre la anisotropía del metamaterial, implementar perfiles graduales de índice de refracción y aumentar el tamaño de las características facilitando la fabricación de dispositivos. En un nivel aplicado, estas topologías novedosas se aprovechan para demostrar dispositivos de alto rendimiento, incluyendo divisores de haz y divisores de polarización y expansores de haz. Por último, basándose en la experiencia desarrollada, se establece un conjunto de técnicas universales de modelado y simulación que pueden acelerar drásticamente el desarrollo de nuevos dispositivos basados en metamateriales. A continuación se detalla una descripción de las topologías y dispositivos SWG propuestos.

Cuando se inició esta Tesis en 2017, en la literatura se utilizaban principalmente dos topologías SWG, los SWGs longitudinales y los transversales. Estas topologias de SWGs, denominadas como topologías convencionales, han permitido el diseño de múltiples dispositivos de alto rendimiento. La primera contribución de esta Tesis ha sido desarrollar un conjunto de modelos de homogeneización para predecir el comportamiento en dichas toplogias SWGs convencionales. En el articulo de revisión invitado [153] se unifican y consolidan los modelos de homogeneización desarrollados, de forma que sean más fáciles de entender y aplicar, facilitando el diseño de dispositivos basados en SWGs. Este trabajo también analiza de forma crítica el estado del arte de los dispositivos SWG en los años 2018 a 2021. Después de estudiar las estructuras SWG convencionales, se han propuesto por primera vez tres topologías SWG novedosas y se han demostrado experimentalmente para ampliar aún más el espacio de diseño de los dispositivos fotónicos de silicio: SWG inclinado [154], SWG bricked [155] y SWG longitudinal modulado por ciclo de trabajo [118].

B.2. Propagación de ondas en medios periodicos

La solución general de una onda electromagnética monocromática que se propaga por un medio periódico viene dada por:

$$\vec{E}(\mathbf{r}) = \vec{E}_{\mathrm{F}}(\mathbf{r}) e^{-j\vec{k}\cdot\vec{r}}. \tag{B.1}$$

donde $\vec{E}_{\mathrm{F}}(\mathbf{r})$ y $\vec{k}$ son el perfil de campo periódico y el vector de onda de la onda propagandose a través de la estructura periódica. El teorema de Bloch-Floquet afirma que el perfil de campo periódico, $\vec{E}_{\mathrm{F}}(\mathbf{r})$, tiene la misma periodicidad que la estructura [179]. Esta simple afirmación tiene muchas consecuencias interesantes. Para analizarlas, se asume una periodicidad unidimensional, Λ, a lo largo del eje longitudinal z y un sistema de coordenadas cartesianas. Además, se omite la propagación a lo largo del eje vertical y ($\vec{k} = k_x\hat{x} + k_z\hat{z}$) ya que esta Tesis se centra en dispositivos guiados planos. En esta situación, la Ec. (B.1) puede reescribirse en el dominio de Fourier como una suma de funciones exponenciales complejas ponderadas:

$$\vec{E}(x,y.z) = \underbrace{\left[\sum_{m=-\infty}^{\infty} \vec{E}_{F,m}(x,y) e^{-j\frac{2\pi}{\Lambda}mz}\right]}_{\text{Serie de Fourier de } \vec{E}_{\mathrm{F}}(x,y,z)} e^{-j(k_x x + k_z z)}. \tag{B.2}$$

donde ambas funciones exponenciales se pueden combinar como:

$$\vec{E}(x,y.z) = \sum_{m=-\infty}^{\infty} \vec{E}_{F,m}(x,y) e^{-j(k_x x + (k_z + \frac{2\pi}{\Lambda}m)z)} = \sum_{m=-\infty}^{\infty} \vec{E}_{F,m}(x,y) e^{-j\vec{k}_{\mathrm{F},m}\vec{r}} \tag{B.3}$$

Esta nueva expresión descompone la solución de una onda que se propaga a lo largo de una estructura periódica como la suma de infinitas ondas planas, $\vec{E}_{F,m}(x,y)$, normalmente llamadas armónicas, cada una con un vector de onda $\vec{k}_{\mathrm{F},m} = k_x\hat{x} + (k_z + \frac{2\pi}{\Lambda}m)\hat{z}$. El comportamiento de los dispositivos múltiples, como los acopladores de rejilla [180] o los acopladores contradireccionales [181], surge de la descomposición del perfil de campo en múltiples armónicos. Sin embargo, la realización de metamateriales homogéneos con propiedades ópticas deseables proviene de la situación contraria. Es decir, cuando sólo se mantiene el armónico fundamental de la descomposición de Fourier, $m = 0$. En esta situación, la onda se propaga como:

$$\vec{E}(x,y.z) \approx \vec{E}_0(x,y) e^{-j\vec{k}_{\mathrm{F},0}\vec{r}}. \tag{B.4}$$

Esta ecuación es la solución de onda en un medio z-periódico si sólo se mantiene el armónico fundamental, pero también es la solución de onda en un medio z-invariante. Es decir, ambos problemas tienen la misma solución electromagnética, son problemas equivalentes. Intuitivamente, esta situación se consigue cuando las ondas que viajan a lo largo de la estructura periódica no aprecian la división de la estructura en diferentes materiales. Para ello, la longitud de onda de la onda que se propaga debe ser mucho mayor que el período de la estructura, $\lambda \gg \Lambda$. Esta condición se conoce a menudo como el régimen de onda larga o sub-longitud de onda profunda. Una comprensión profunda de los fundamentos de esta equivalencia abre potencialmente nuevos enfoques de diseño de dispositivos fotónicos. Para ello, se analiza en detalle la estructura dieléctrica periódica más sencilla, la estructura periódica laminar (LPS). Este estudio proporciona una visión física de la propagación de ondas a lo largo de una estructura periódica con una matemática sencilla.

B.2.1. Estructura periódica laminar

Una estructura periódica laminar (LPS) se compone de un conjunto de láminas dieléctricas sin pérdidas transversalmente infinitas dispuestas con una periodicidad Λ (véase la Fig. B.2). Las láminas tienen índices de refracción n_1 y n_2, longitudes a y b respectivamente y la longitud de cada material por período se da frecuentemente con el ciclo de trabajo, definido como la cantidad del material n_1 en un período: DC = a/Λ. A partir del teorema de Bloch-Floquet [Ec. (B.1)], la solución de onda de una onda plana monocromática que se propaga a lo largo de cualquier dirección del plano x-z del LPS se deduce como:

$$\vec{E}(x,z) = \vec{E}_F(z)e^{-j(k_x x + k_z z)}. \tag{B.5}$$

Las fórmulas analíticas tanto para el perfil de onda periódica, $\vec{E}_F(z)$, como para el vector de onda, $\vec{k}$, fueron derivadas por Yeh et al en 1976 [168]. Para ello, Yeh supuso que el campo eléctrico dentro de cada capa homogénea puede expresarse como una suma de una onda plana incidente y otra reflejada que se propaga a lo largo de la estructura periódica:

$$\vec{E}(x,z) = \vec{E}_F(z)e^{-jk_z z}e^{-jk_x x} = [\underbrace{\vec{a}_m^i e^{-jk_{iz}(z-m\Lambda)}}_{\text{Incidente}} + \underbrace{\vec{b}_m^i e^{jk_{iz}(z-m\Lambda)}}_{\text{Reflejada}}]e^{-jk_x x} \tag{B.6}$$

donde $\vec{a}_m^i$ y $\vec{b}_m^i$ denotan las amplitudes complejas de dichas ondas hacia adelante y hacia atrás en el material i-ésimo del período m-ésimo. Resolviendo adecuadamente los valores de dichas amplitudes, se obtiene la ecuación vectorial de onda de cualquier onda plana que se propague a través de un LPS [168]:

$$\cos(k_z\Lambda) = \cos(k_{1z}a)\cos(k_{2z}b) - \Delta\sin(k_{1z}a)\sin(k_{2z}b), \tag{B.7}$$

donde $k_{iz} = \sqrt{(k_0 n_i)^2 - k_z^2}$, $k_0 = 2\pi/\lambda_0$ y Δ es un factor dependiente de la polarización:

$$\Delta_{\text{TE}} = \frac{1}{2}\left(\frac{n_2^2}{n_1^2}\frac{k_{1z}}{k_{2z}} + \frac{n_1^2}{n_2^2}\frac{k_{2z}}{k_{1z}}\right) \text{ and } \Delta_{\text{TM}} = \frac{1}{2}\left(\frac{k_{1z}}{k_{2z}} + \frac{k_{2z}}{k_{1z}}\right), \tag{B.8}$$

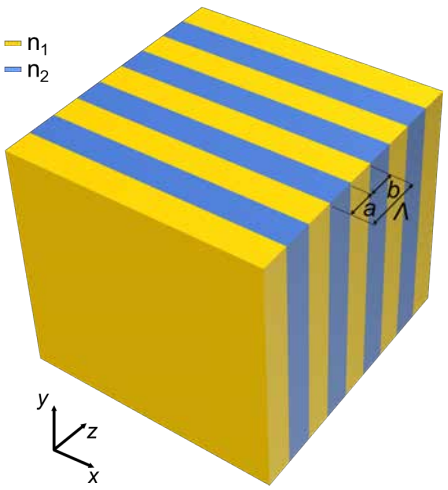

Figure B.2: Representación esquemática de una estructura periódica laminar compuesta por la concatenación periódica de láminas dieléctricas de anchura y altura infinitas.

definiendo como polarización TE las ondas con campo eléctrico polarizado en el plano x-z, y polarización TM como las ondas polarizadas en y. El índice efectivo de la onda se calcula con la Ec. (B.7) al normalizar el vector de onda por el vector de onda en el vacío: $n_{\text{eff}} = |\vec{k}|/k_0$.

B.2.2. Homogeneización de la estructura laminar periódica

La condición para que las estructuras periódicas se comporten como metamateriales homogéneos es que sólo se mantenga el armónico fundamental de la serie de Fourier de sus soluciones electromagnéticas [véase la Ec. (B.4)]. Esta condición ocurre cuando el período es mucho más corto que la longitud de onda. Por lo tanto, el siguiente paso es encontrar el material homogéneo equivalente que imita el comportamiento electromagnético de las estructuras periódicas en esta situación. Para el caso del LPS, las fórmulas analíticas para calcular el material homogéneo equivalente fueron deducidas por Rytov en 1956 suponiendo que la estructura trabaja en el régimen de onda larga [90] ($\lambda \gg \Lambda$). Veinte años más tarde, Yeh et al obtuvieron los mismos resultados estudiando la ecuación de dispersión del LPS bajo la condición de onda larga. Al hacerlo, la ecuación de dispersión [Ec. (B.7)] colapsa en las ecuaciones de una elipse y un círculo para las polarizaciones TE y TM respectivamente [182]:

$$\text{TE waves}: \frac{k_x^2}{n_\perp^2} + \frac{k_z^2}{n_\parallel^2} = k_0^2, \tag{B.9}$$

$$\text{TM waves}: \frac{k_x^2}{n_\parallel^2} + \frac{k_z^2}{n_\parallel^2} = k_0^2. \tag{B.10}$$

Estas dos ecuaciones son entonces las ecuaciones de dispersión de las ondas planas TE y TM que se propagan a lo largo del plano x-z de un LPS en el régimen de sub-longitud de onda profunda. Curiosamente, también son las ecuaciones de dispersión de las ondas planas TE y TM que se propagan a lo largo del plano x-z de un cristal uniaxial homogéneo, siendo $n_\parallel$ y $n_\perp$ los índices de refracción ordinario y extraordinario respectivamente [93]. Por lo tanto, desde el punto de vista electromagnético, la estructura periódica imita el comportamiento de un cristal uniaxial. En otras palabras, el metamaterial homogéneo equivalente a un LPS que trabaja en régimen de sub-longitud de onda profunda es un cristal uniaxial: un medio anisótropo donde la onda se propaga a la misma velocidad en dos de los tres ejes, pero diferente en el tercero. La propagación de la onda a lo largo de un cristal uniaxial se caracteriza por su tensor de permitividad:

$$\boldsymbol{\varepsilon}_{\text{LPS}} = \begin{bmatrix} n_\parallel^2 & 0 & 0 \\ 0 & n_\parallel^2 & 0 \\ 0 & 0 & n_\perp^2 \end{bmatrix}. \tag{B.11}$$

Este tensor impone una velocidad de fase $k_0 n_\parallel$ para las ondas polarizadas a lo largo de los ejes x e y y una velocidad de fase $k_0 n_\perp$ para las ondas polarizadas a lo largo del eje z. Como los LPS y los cristales uniaxiales tienen las mismas ecuaciones de dispersión en el régimen profundo de sub-longitud de onda, el tensor de permitividad dado por la Ec. (B.11) puede ser utilizado para modelar el comportamiento del LPS. Este tipo de homogeneización anisotrópica del LPS se ha utilizado en el campo de la óptica del espacio libre y de las metasuperficies [169–172], pero normalmente se sustituye por la homogeneización isotrópica más simple debido a la pequeña diferencia entre las aproximaciones isotrópicas y anisotrópicas en el

problema del espacio libre. Esta Tesis revisa esta homogeneización en estructuras periódicas integradas, demostrando cómo en ciertos casos la anisotropía es esencial para modelar adecuadamente el comportamiento real de los dispositivos basados en SWG. Pero antes, se estudia la homogeneización de los LPS que funcionan como cristales uniaxiales, comparando las ecuaciones de dispersión de las ondas planas que se propagan a lo largo de los LPS y su metamaterial homogéneo anisótropo equivalente. El primero se calcula con la Ec. (B.7) mientras que el segundo utiliza la Ecs. (B.9) y (B.10). Para ese cálculo, el primer paso es definir cómo se obtienen los componentes del índice tensorial:

$$n_{\parallel} = \frac{k_z}{k_0} \text{ (when } k_x = 0), \tag{B.12}$$

$$n_{\perp} = \frac{k_x}{k_0} \text{ (when } k_z = 0). \tag{B.13}$$

Nótese que estas ecuaciones son los índices efectivos de una onda plana que se propaga a lo largo del eje z y del eje x del LPS respectivamente, obtenidos con la Ec. B.7. La onda que se propaga a lo largo del eje z puede calcularse asumiendo la polarización TE o TM, ya que tanto las ondas planas polarizadas x como las polarizadas y proporcionan el mismo resultado. La onda que se propaga a lo largo del eje x tiene que ser calculada asumiendo la polarización TE para asegurar que la dirección de la polarización es a lo largo del eje z.

Para estudiar la precisión de la homogeneización de estructuras laminares periódicas como cristales uniaxiales, se compara el vector de onda, k de una onda plana que se propaga a lo largo de una LPS, calculada con la Ec. (B.7), y su metamaterial homogéneo anisótropo equivalente, calculado con las Ecs. (B.9) y (B.10). La homogeneización utiliza el modelo propuesto para calcular las componentes del tensor de permitividad, basándose en la resolución de la Ec. (B.7). A modo de ilustración, se han realizado dos comparaciones entre un LPS y su metamaterial equivalente: 1) Un LPS con un período mucho más corto en longitud de onda, $\Lambda = 50$ nm, y 2) Un LPS con un período cercano al régimen de Bragg, $\Lambda = 220$ nm. Como era de esperar, en el régimen de sub-longitud de onda profunda, ambas estructuras presentan exactamente el mismo comportamiento para cualquier ángulo de propagación, ya que ambas estructuras son totalmente equivalentes desde el punto de vista electromagnético en este régimen. Por otro lado, cuando la estructura deja de funcionar en el régimen de sub-longitud de onda profunda, ambas soluciones no son exactamente iguales, sin embargo, sigue arrojando un resultado notablemente similar. Nótese que la homogeneización propuesta no proporciona ningún error en los ejes principales, ya que el modelo se construye utilizando la propagación en el LPS en estos ejes. Tras este estudiar la homogeneización de LPS, se pasa al estudio de guías SWG integradas.

B.2.3. Guías de onda SWG

No existe una definición única de lo que es una guía de onda SWG de fotónica de silicio. Son posibles muchas guías de onda SWG diferentes, pero los dos tipos más comunes son las topologías longitudinales (Fig. B.4a) y transversales (Fig. B.4b). Las guías de onda SWG se han utilizado ampliamente en la fotónica de silicio para optimizar el rendimiento de múltiples dispositivos diferentes, pero apenas se han realizado análisis sobre la homogeneización de este tipo de estructuras en plataformas integradas de fotónica de silicio. Una de las aportaciones de esta Tesis ha sido estudiar la homogeneización de estas guías de onda SWG como

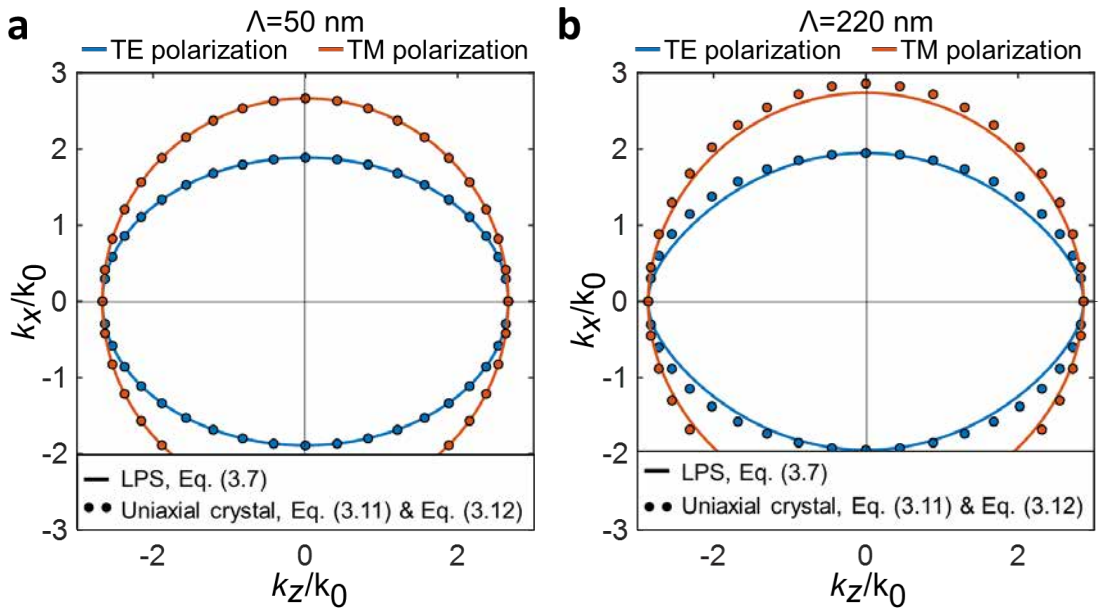

Figure B.3: a) Componentes del vector de onda normalizada, (k_x y k_z), de una onda plana que se propaga a lo largo de cualquier ángulo de la estructura periódica laminar (DC = 0,5) y de su material homogéneo anisótropo equivalente para la estructura.

estructuras homogéneas, proponiendo y validando novedosos modelos de homogeneización para calcular el tensor de permitividad $\varepsilon_{\mathrm{w}} = \mathrm{diag}[n_{xx}^2, n_{yy}^2, n_{zz}^2]$ del material homogéneo equivalente a las estructuras SWG.

Modelo básico de homogeneización de las guías de onda SWG: El modelo LPS

Del estudio de LPS se deriva un modelo de homogeneización simple de la guía de onda SWG. Consiste en los tres pasos siguientes, resumidos esquemáticamente en la Fig B.5:

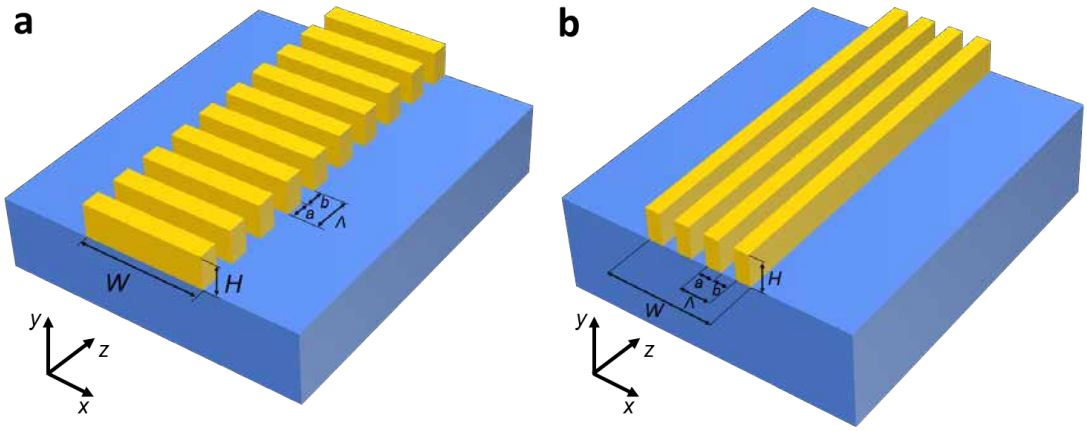

Figure B.4: Representación esquemática de una guía de onda SWG integrada con los segmentos periódicos dispuestos a lo largo de a) la dirección longitudinal y b) la dirección transversal.

1. Extraiga el LPS correspondiente de la guía de ondas SWG. Es decir, el LPS con los mismos materiales, ciclo de trabajo y período que la guía de onda SWG. El eje periódico de la guía de onda SWG y del LPS tiene que ser el mismo.
2. Calcular el metamaterial homogéneo anisótropo equivalente del LPS. Es decir, los componentes del tensor de permitividad, $n_{\parallel}$ y $n_{\perp}$, del tensor de permitividad ε_{LPS} como se muestra en la sección 3.2.2.
3. Utilizar los componentes del tensor de permitividad calculados del LPS como núcleo anisótropo homogéneo. That is, $\varepsilon_{\text{w}} = \text{diag}[n_{xx}^2, n_{yy}^2, n_{zz}^2] = \varepsilon_{\text{LPS}} = \text{diag}[n_{\parallel}^2, n_{\parallel}^2, n_{\perp}^2]$.

Para estudiar la precisión del modelo propuesto, se modela y analiza una guía de onda multimodo con una anchura, $W = 3$ µm, una altura, $H = 220$ nm, y un ciclo de trabajo, DC=0.5. La figura B.6a muestra el índice efectivo de los modos fundamentales TE y TM de la guía de onda SWG (líneas sólidas) y su correspondiente guía de onda homogénea equivalente para diferentes períodos (círculos). El análisis de la estructura periódica requiere complejas simulaciones 3D-FDTD mientras que la simulación de la guía de onda homogénea anisotrópica equivalente sólo requiere un resolutor 2D mucho más sencillo. De esta figura se desprende que la homogeneización predice con precisión el comportamiento de la guía de ondas para un período de hasta $\Lambda = 200$ nm. Más allá de este periodo, la precisión de

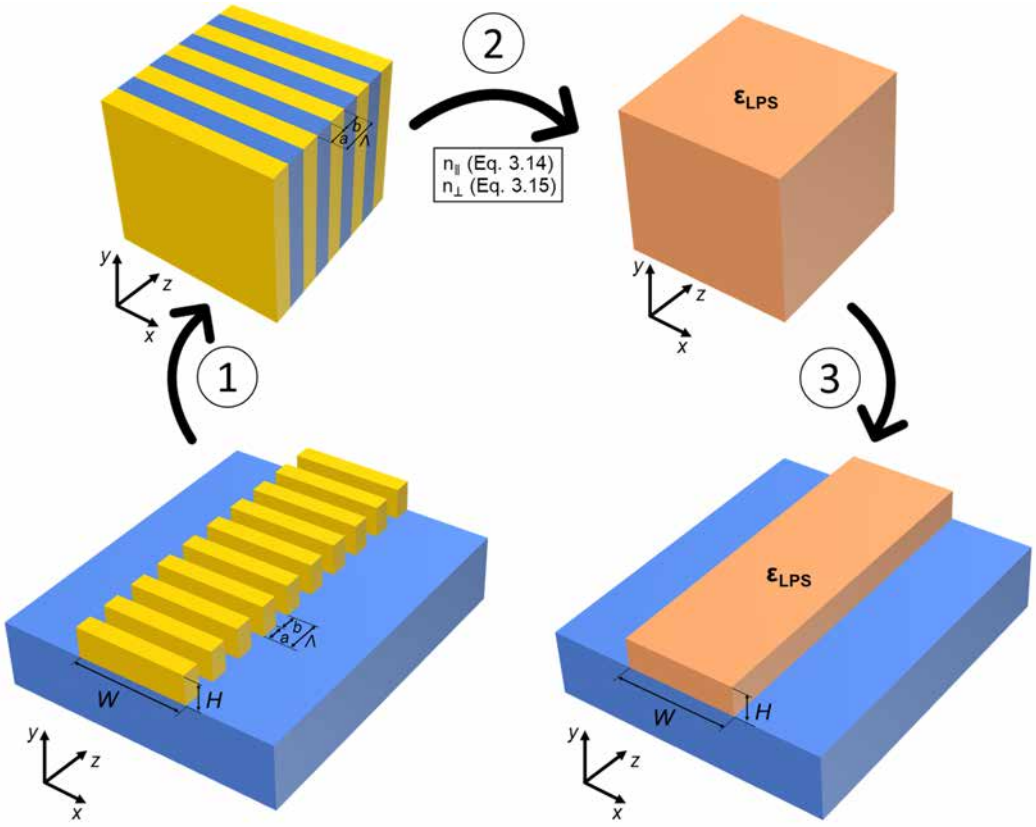

Figure B.5: Algoritmo para calcular el material homogéneo equivalente de una guía de onda SWG dada. Los pasos del algoritmo son 1) Extraer el LPS correspondiente de una guía de onda SWG dada. Es decir, el LPS con los mismos materiales, ciclo de trabajo y periodo. 2) Calcular los componentes del tensor de permitividad, $n_{\parallel}$ y $n_{\perp}$. 3) Imponer los componentes del tensor de permitividad calculados del LPS al núcleo anisótropo homogéneo.

la homogeneización disminuye porque el LPS utilizado para modelar la estructura SWG se aproxima al régimen de Bragg mientras que la guía de onda SWG está todavía lejos del régimen de Bragg debido a su menor confinamiento modal. Más allá del período en el que el LPS entra en el régimen de Bragg, $\Lambda = 240$ nm, la homogeneización del LPS ya no es posible. Las figuras B.6b y B.6c muestran no sólo los modos fundamentales sino también los de alto orden de ambas estructuras para dos períodos diferentes. El primero en el régimen SWG profundo, $\Lambda = 50$ nm y el segundo cerca del régimen de Bragg del LPS, $\Lambda = 220$ nm. Una vez más, en el régimen deep-SWG ambas estructuras ofrecen resultados similares y la precisión disminuye cuando el período se acerca al régimen de Bragg del LPS.

La misma homogeneización puede utilizarse para las guías de onda SWG transversales. Esta rotación se tiene en cuenta en el primer paso del algoritmo, ya que el LPS tiene la misma periodicidad de la guía de onda SWG. Por lo tanto, el LPS se analiza con una rotación de 90º en el plano x-z, siendo el eje x la dimensión periódica. Por lo tanto, el tensor de permitividad de las guías de onda homogéneas equivalentes en este caso viene dado por $\varepsilon_w = \text{diag}[n_{xx}^2, n_{yy}^2, n_{zz}^2] = \text{diag}[n_\perp^2, n_\parallel^2, n_\parallel^2]$. La figura B.6d-f muestra el estudio de homogeneización para las guías de onda SWG transversales, obteniendo conclusiones similares a las realizadas para la guía de onda SWG longitudinal.

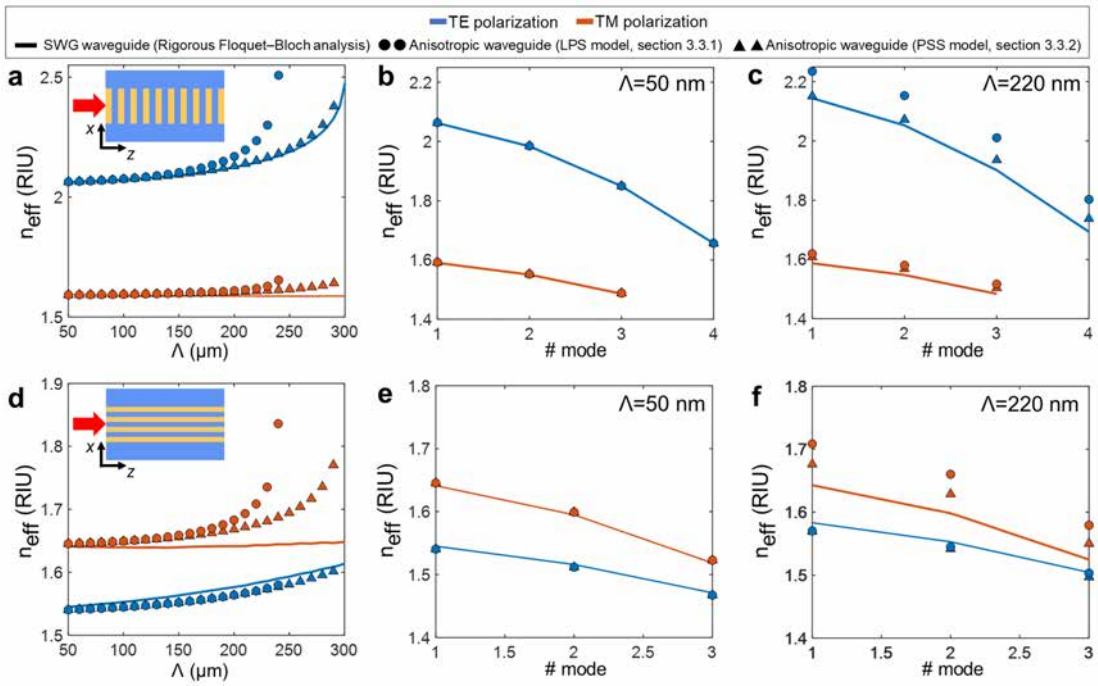

Figure B.6: a-c) Índices efectivos de (a) el modo fundamental de Floquet-Bloch y (b), (c) los modos de Floquet-Bloch de orden superior de una guía de ondas SWG longitudinal calculados mediante simulaciones rigurosas en 3D de vector completo (TE: líneas sólidas azules, TM: líneas sólidas anaranjadas) comparados con los de las correspondientes guías de ondas de núcleo homogéneo anisótropo obtenidas mediante los modelos LPS (círculos) y PSS (triángulos). d-f) Índices efectivos de (d) el modo fundamental de Floquet-Bloch y (e), (f) los modos de Floquet-Bloch de orden superior de una guía de onda SWG transversal calculados mediante rigurosas simulaciones vectoriales completas en 3D (TE: líneas sólidas azules, TM: líneas sólidas naranjas) comparados con los de las correspondientes guías de onda de núcleo homogéneo anisotrópico obtenidas utilizando el modelo laminar (círculos) y el modelo de *slab* (triángulos).

Por lo tanto, tanto en guías de onda SWG longitudinales como transversales, el modelo de homogeneización LPS funciona con precisión para períodos de hasta $\Lambda = 200$ nm asumiendo valores típicos de SOI. A partir de ese punto, la precisión disminuye hasta el período de Bragg, $\Lambda = 240$ nm a partir del cual la homogeneización ya no es posible. Esta indisponibilidad proviene de una cuestión sencilla: La estructura periódica laminar entra en el régimen de Bragg, por lo que no hay solución disponible. Sin embargo, la luz en las guías de onda SWG integradas sigue propagándose durante períodos superiores a 240 nm porque los índices efectivos de las ondas en las guías de onda SWG son menores que en las LPS, por lo que el régimen de Bragg para la guía de onda SWG se alcanza durante un período más largo. Para superar este problema, en la siguiente sección se propone un modelo de homogeneización avanzado.

Modelo avanzado de homogeneización de guías de onda SWG: El modelo PSS

El modelo anterior está limitado porque los LPS entran en el régimen de Bragg para un período más corto que las guías de onda SWG que se están modelando. Esta diferencia en el período del régimen de Bragg se debe a los bajos índices de refracción de los materiales del revestimiento y del sustrato de las guías de onda SWG, que reducen el índice efectivo del modo en comparación con el índice efectivo de una onda plana que se propaga a lo largo de la LPS. Para paliar este problema, se puede tener en cuenta el espesor finito de la guía de onda como una propiedad del material. Para ello, se introduce la estructura *slab* periódica (PSS) (véase la Fig. 3.10a). Esta nueva estructura puede entenderse como un LPS con un espesor finito, H, incrustado entre un sustrato y un revestimiento. Siguiendo un argumento similar al del LPS, el núcleo periódico del PSS puede homogeneizarse como un cristal uniaxial definido por su tensor de permitividad ε_{PSS}. Análogamente, las componentes del tensor de este nuevo metamaterial se calculan a partir de la propagación de ondas TE a lo largo de los ejes x- y z- de esta estructura. Las ondas planas que se propagan a lo largo de estos dos ejes tienen índices de refracción efectivos $n_{\text{eff}x}$ y $n_{\text{eff}z}$ (Véase Fig. B.7b). Para convertir estos índices efectivos en índices de refracción, hay que calcular el indice de refracción del núcleo del *slab* homogéneo que da lugar a estos modos. Para ello se resuelve un *slab* isotrópica con la misma altura, revestimiento y sustrato con diferentes materiales del núcleo n_{eq} (Fig. B.7c), calculando la función de mapeo que relaciona las componentes tensoriales $n_{\text{eq}x}$ y $n_{\text{eq}z}$ de $n_{\text{eff}x}$ y $n_{\text{eff}z}$. Es importante señalar que la resolución de los índices efectivos de PSS requiere resolver un problema periódico 2D, que en esta Tesis se realiza fácilmente con FEXEN en pocos segundos.

A partir de este procedimiento, el modelo de homogeneización del PSS se realiza siguiendo los tres pasos siguientes, resumidos esquemáticamente en la Fig B.8:

1. Extraer el PSS correspondiente de una determinada guía de ondas SWG. Es decir, el PSS con los mismos materiales, ciclo de trabajo, período y espesor. El eje periódico de la guía de onda SWG y del PSS tiene que ser el mismo.
2. Calcular los componentes del tensor de permitividad, $n_{\text{eq}x}$ y $n_{\text{eq}z}$, de la PSS extraída resolviendo la PSS y mapeando los índices efectivos resultantes como se muestra en la Fig. B.7.

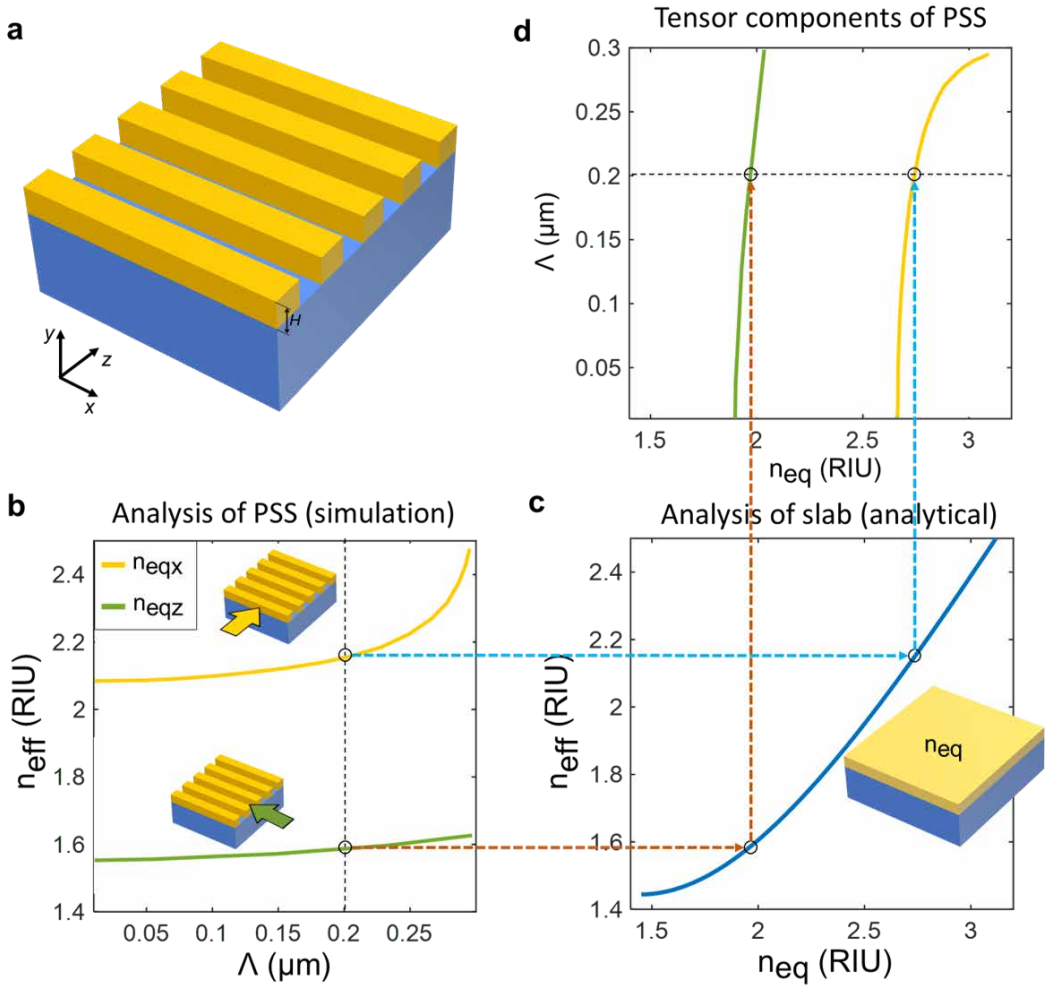

Figure B.7: a) Representación esquemática de una estructura *slab* periódica. b) Índice efectivo del modo TE fundamental que se propaga a lo largo del eje z (n_{effx}) y del eje x (n_{effz}) del slab periódico. (c) Función de mapeo entre el índice efectivo del modo TE fundamental de un *slab* isotrópica y el correspondiente índice de refracción del material del núcleo. (d) Componentes del tensor del índice de refracción sintetizados para un *slab* de núcleo periódico con período Λ.

3. Utilizar los componentes del tensor de permitividad calculados del PSS como núcleo anisótropo homogéneo, es decir, $\varepsilon_{\text{w}} = \text{diag}[n_{xx}^2, n_{yy}^2, n_{zz}^2] = \varepsilon_{\text{PSS}} = \text{diag}[n_{\text{eq}x}^2, n_{\text{eq}x}^2, n_{\text{eq}z}^2]$.

Para estudiar la precisión del modelo PSS, se resuelve la misma guía de onda SWG estudiada en el modelo LPS. En la figura B.6a se comparan los índices efectivos de los modos fundamentales TE y TM de la guía de onda resuelta mediante simulaciones 3D-FDTD Floquet (líneas sólidas), el modelo LPS (círculos) y el modelo PSS (triángulos). Se muestra claramente que el modelo PSS es efectivamente más preciso que el modelo laminar en las proximidades del umbral de Bragg, aunque a costa de una mayor complejidad en la etapa de modelado. Esta mejora también se observa para los modos de orden superior: mientras que para el paso de 50 nm tanto el modelo laminar como el de *slab* dan resultados prácticamente exactos [véase la Fig. B.6b], para el paso de 220 nm el error en los índices efectivos es inferior al 3% para el modelo PSS, frente al 6% para la aproximación laminar [véase la Fig. B.6c]. El mismo estudio se ha realizado para la guía de onda transversal de sub-longitud de onda,

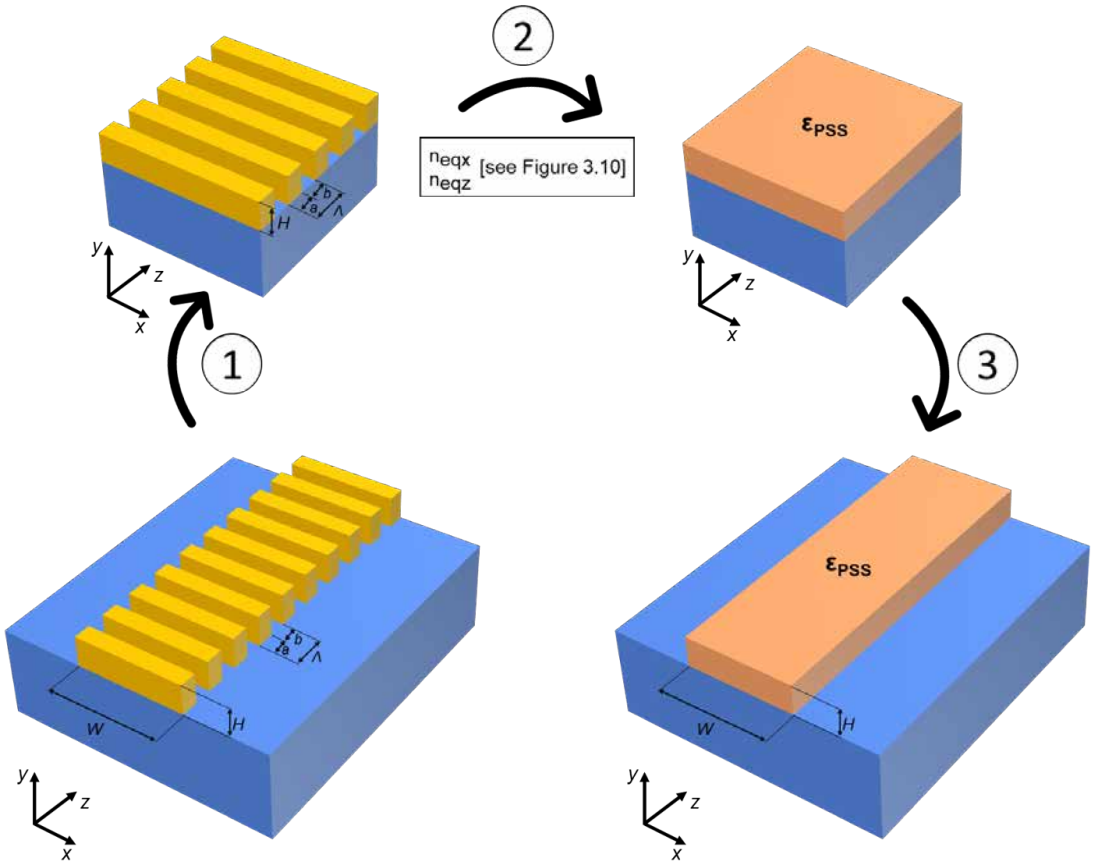

Figure B.8: Algoritmo para calcular el material homogéneo equivalente de una guía de onda SWG dada con el modelo PSS. Los pasos del algoritmo son 1) Extraer el PSS correspondiente de una guía de onda SWG dada. Es decir, el PSS con los mismos materiales, ciclo de trabajo, período, altura y orientación. 2) Calcular los componentes del tensor de permitividad, n_{eqx} y n_{eqz}. 3) Imponer los componentes del tensor de permitividad calculados del PSS al núcleo anisótropo homogéneo.

el modelo PSS también proporciona beneficios en comparación con el modelo laminar en este caso [Véase Fig. B.6d-f]. Sin embargo, la homogeneización de las estructuras SWG transversales es menos frecuente, ya que se resuelven fácilmente con los solucionadores de modos convencionales. En cualquier caso, ambos modelos de homogeneización propuestos proporcionan resultados rápidos pero precisos, ayudando en el análisis de las guías de onda SWG.

B.3. Topologías SWG avanzadas

Las guías de onda SWG longitudinales y transversales son las dos topologías SWG más comunes. Se han utilizado ampliamente en la última década para optimizar el rendimiento de una miríada de dispositivos fotónicos de silicio. Sin embargo, el conjunto limitado de grados de libertad de estas SWG convencionales dificulta la síntesis de metamateriales complejos que requieren un ajuste fino de los componentes del tensor. Para superar este problema, en esta Tesis se han propuesto dos topologías avanzadas de SWG: las topologías de metamateriales SWG inclinados.

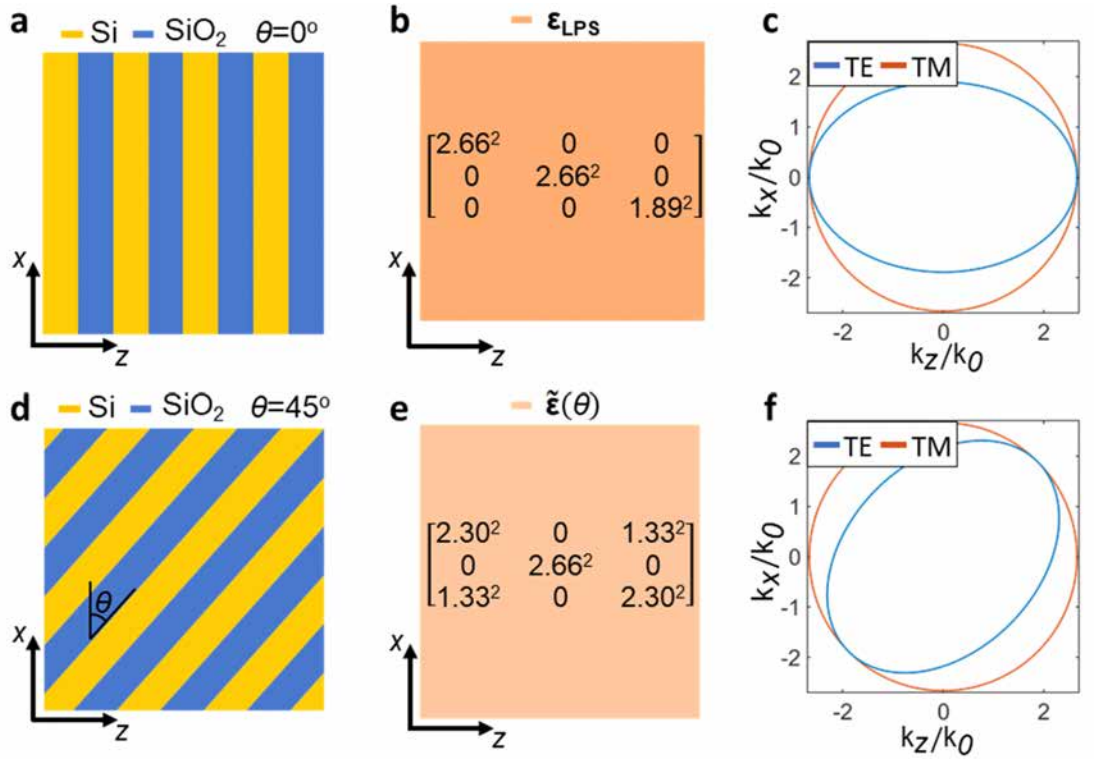

Figure B.9: a,d) Representación esquemática de a) un LPS no inclinado y d) un LPS inclinado 45°. b,e) Representación esquemática y tensor de permitividad del metamaterial equivalente al LPS mostrado en a) y d) respectivamente suponiendo un régimen de sub-longitud de onda profunda e índices de refracción $n_1 = 3.476$ y $n_2 = 1.444$. c,f) Diagramas de dispersión para la onda plana TE (azul) y TM (rojo) que se propaga a lo largo del medio anisótropo mostrado en b) y e) respectivamente.

B.3.1. Topología SWG inclinada

En los materiales anisótropos, el comportamiento de las ondas de luz depende de la orientación de los componentes del campo eléctrico con respecto al eje óptico del material. Por tanto, surge de forma natural la idea de inclinar la estructura de sub-longitud de onda para controlar la propagación de la luz. El estudio de esta estructura, conocida como metamaterial SWG inclinado, ha sido una de las principales líneas de investigación de esta Tesis, dando lugar a varias publicaciones en revistas [132, 154, 156–158]. Las propiedades ópticas únicas de los metamateriales SWG inclinados se discuten a lo largo de esta sección.

B.3.2. Modelo de homogeneización de metamateriales SWG inclinados

El desarrollo de un modelo analítico para homogeneizar los metamateriales SWG inclinados comienza considerando un simple LPS en plataforma SOI (Fig. B.9a). En aras de la simplicidad, se asume el régimen SWG profundo y un ciclo de trabajo del 50%, por lo que el comportamiento de la estructura viene dado únicamente por los índices de refracción del material, $n_{\mathrm{Si}} = 3{,}476$ y $n_{\mathrm{SiO_2}} = 1{,}444$. Dicha estructura se homogeniza como un cristal uniaxial anisotrópico con el tensor de permitividad calculado con el conocido uso de la teoría de Rytov como $\varepsilon_{\mathrm{LPS}} = \mathrm{diag}[n_{\parallel}^2, n_{\parallel}^2, n_{\perp}^2] = [2.66^2, 2{,}66^2, 1{,}89^2]$. Cualquier onda plana TE/TM que

se propague a lo largo de este medio anisótropo homogéneo tiene un vector de onda $\vec{k}$ siguiendo la relación de dispersión mostrada en la Fig. B.9c. Para analizar el LPS inclinado, se inclina la estructura un ángulo θ con respecto al eje z como se muestra en la Fig. B.9d, manteniendo el sistema de coordenadas inalterado. El tensor de permitividad del LPS inclinado se calcula rotando adecuadamente el tensor de la estructura no inclinada como [183]:

$$\tilde{\varepsilon}(\theta) = \mathbf{T^{-1}}(\theta)\varepsilon_{\mathrm{LPS}}\mathbf{T}(\theta) = \begin{bmatrix} \tilde{n}^2_{xx}(\theta) & 0 & \tilde{n}^2_{xz}(\theta) \\ 0 & \tilde{n}^2_{yy} & 0 \\ \tilde{n}^2_{xz}(\theta) & 0 & \tilde{n}^2_{zz}(\theta) \end{bmatrix}, \tag{B.14}$$

donde $\mathbf{T}$ es la matriz de rotación alrededor del eje y. Los elementos del tensor $\tilde{\varepsilon}(\theta)$ se calculan a partir de los componentes del tensor del SWG no inclinado como:

$$\begin{aligned} &\tilde{n}^2_{xx}(\theta) = n^2_{\parallel}\cos^2(\theta) + n^2_{\perp}\sin^2(\theta), \\ &\tilde{n}^2_{yy} = n^2_{\parallel}, \\ &\tilde{n}^2_{zz}(\theta) = n^2_{\parallel}\sin^2(\theta) + n^2_{\perp}\cos^2(\theta), \\ &\tilde{n}^2_{xz}(\theta) = (n^2_{\perp} - n^2_{\parallel})\cos(\theta)\sin(\theta). \end{aligned} \tag{B.15}$$

Este conjunto de ecuaciones se utiliza para calcular las componentes del tensor de permitividad del metamaterial equivalente a un LPS inclinado a partir de las componentes del tensor del LPS no inclinado. La figura 4.3e muestra los componentes del tensor de permitividad resultantes, suponiendo una rotación de $\theta = 45°$.

B.3.3. Propiedades de guía de ondas de los metamateriales SWG inclinados

Para estudiar las propiedades de guiado de onda de los metamateriales SWG inclinados, se estudia la propagación de ondas a lo largo de una guía de onda SWG multimodo inclinada ($W = 3{,}25$ µm, $\Lambda_0 = 0{,}25$ µm y DC = 0,5) en una plataforma de silicio estándar de 220 nm de espesor. El análisis comienza calculando los modos fundamentales TE y TM soportados por la guía de onda SWG inclinada en estudio y su guía de onda homogénea anisotrópica equivalente para diferentes ángulos de inclinación. Mientras que los modos en la guía de onda periódica se calculan con simulaciones modales 3D-FDTD (FullWAVE), que consumen mucho tiempo, las soluciones en la guía de onda homogénea se calculan con simulaciones anisotrópicas FEM rápidas (FIMMWAVE). En este caso, se ha utilizado la homogeneización PSS ya que el período es mayor que $\Lambda_0 = 0{,}24$ µm. En la figura B.10a se comparan los índices efectivos de los modos TE y TM para ambas guías de onda, proporcionando resultados similares y validando así el modelo de homogeneización propuesto para los metamateriales SWG inclinados. Además, también se muestra que el índice efectivo de los modos polarizados TE se ve fuertemente afectado por el ángulo de inclinación, mientras que el índice efectivo del modo TM apenas cambia. Este comportamiento es esperado ya que los modos TE dependen principalmente de la componente n_{xx} del tensor mientras que los modos TM dependen de la componente n_{yy}. A continuación, se analiza la dispersión en longitud de onda de los modos fundamentales TE y TM en el SWG inclinado [Véase Fig. B.10b], mostrando de nuevo cómo los modos TE se ven mucho más afectados por el ángulo de inclinación que los modos TM. Además, también se muestra cómo la dispersión del índice efectivo de los modos polarizados TE también se reduce notablemente al inclinar los segmentos de silicio. Por lo tanto, los

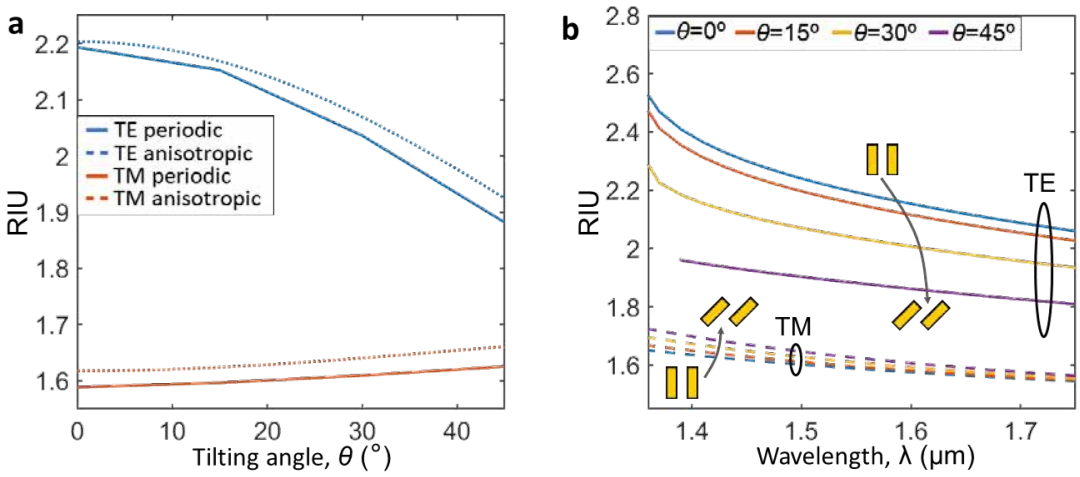

Figure B.10: a) Índices efectivos de los modos fundamentales TE y TM de una guía de onda SWG inclinada y su guía de onda anisotrópica homogénea equivalente con un espesor de silicio $H = 220$ nm, una anchura $W = 3{,}25$ µm, un período no inclinado $\Lambda_0 = 0{,}25$ µm y ciclo de trabajo DC = 0.5 para diferentes ángulos de inclinación que van desde $\theta = 0°$ hasta $\theta = 45°$ a $\lambda = 1{,}55$ µm. b) Dependencia de la longitud de onda del índice efectivo para los modos fundamentales TE y TM de las guías de onda SWG inclinadas descritas en (a) calculadas utilizando el enfoque periódico.

metamateriales SWG inclinados son estructuras ideales para la gestión de la polarización mediante el control de la birrefrigencia y la dispersión de los dispositivos.

B.3.4. Topología SWG enladrillada

La estructura SWG Bricked es la segunda topología de metamaterial SWG propuesta en este capítulo. Esta topología es también una importante contribución de esta Tesis que está siendo explotada en artículos recientes [155, 162]. En esta sección se discuten las propiedades ópticas únicas derivadas de la topología SWG enladrillada.

B.3.5. Modelo de homogeneización del metamaterial SWG enladrillado

Para obtener un modelo analítico del metamaterial SWG enladrillado, se estudia de nuevo un LPS simple en plataforma SOI [Fig. B.11a]. En aras de la simplicidad, el régimen SWG profundo y un ciclo de trabajo del 50% es también en este caso, por lo que el comportamiento de la estructura viene dado únicamente por los índices de refracción del material. El tensor de permitividad del metamaterial homogéneo anisotrópico equivalente se calcula entonces con las conocidas ecuaciones de Rytov $\varepsilon_{\mathrm{LPS}} = \mathrm{diag}[n_{\parallel}^2, n_{\parallel}^2, n_{\perp}^2] = [266^2{,}2{,}66^2{,}1{,}89^2]$ [Fig. B.11b]. Cualquier onda plana que se propague a lo largo de este medio anisótropo homogéneo tiene un vector de onda $\vec{k}$ que sigue la relación de dispersión mostrada en la Fig. B.11c. A continuación, el LPS se transforma en un LPS enladrillado mediante la partición periódica de la estructura a lo largo de la dirección transversal y el desplazamiento de los bloques resultantes como se muestra en la Fig. B.11d para el caso ejemplar en el que los bloques se desplazan la mitad del período. Para obtener el tensor de permitividad del metamaterial equivalente al LPS enladrillado, $\varepsilon(\Delta z)$, se analizan primero los casos límite $\Delta z = 0$ y $\Delta z =$

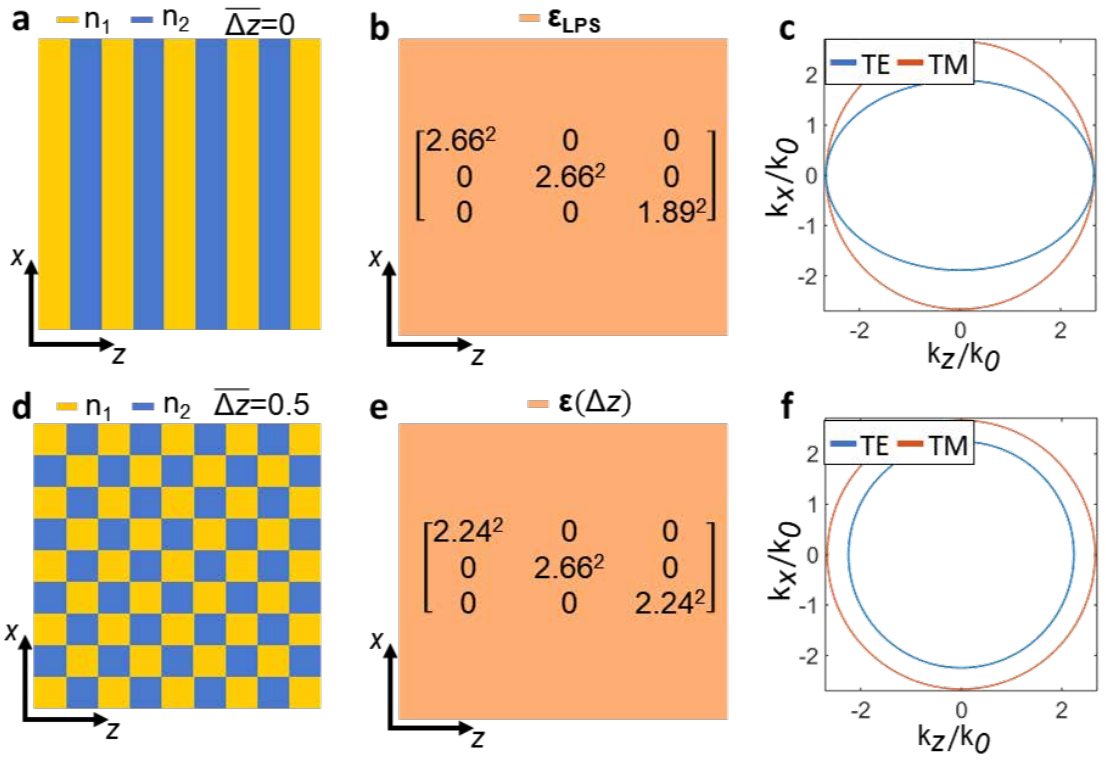

Figure B.11: a,d) Representación esquemática de a) un LPS sin enladrillar y d) un LPS enladrillado $\Delta z = 0{,}5$. b,e) Representación esquemática y tensor de permitividad del metamaterial equivalente al LPS mostrado en a) y d) respectivamente suponiendo un régimen de sub-longitud de onda profunda e índices de refracción $n_1 = 3.476$ y $n_2 = 1.444$. c,f) Diagrama de dispersión para la onda plana TE (azul) y TM (rojo) que se propaga a lo largo del medio anisótropo mostrado en b) y e) respectivamente.

$\Lambda_z/2$. A partir de aquí, el desplazamiento se dará siempre normalizado al período en el eje z: $\overline{\Delta z} = \Delta z/\Lambda_z$, por lo que los casos a estudiar son $\overline{\Delta z} = 0$ y $\overline{\Delta z} = 0{,}5$. Cuando no hay desplazamiento, la estructura se convierte en la LPS convencional mostrada en la Fig. B.11a, por lo que este caso es sencillo y ya está resuelto. Para el cálculo del segundo caso límite, $\overline{\Delta z} = 0{,}5$, se hacen cuatro consideraciones:

1. El tensor de permitividad del LPS enladrillado es un tensor de permitividad diagonal:

$$\varepsilon(\overline{\Delta z}) = \begin{bmatrix} \hat{n}_{xx}^2(\overline{\Delta z}) & 0 & 0 \\ 0 & \hat{n}_{yy}^2 & 0 \\ 0 & 0 & \hat{n}_{zz}^2(\overline{\Delta z}) \end{bmatrix}, \tag{B.16}$$

   por lo que su determinante viene dado por el producto: $|\varepsilon(\overline{\Delta z})| = \hat{n}_{xx}\,\hat{n}_{yy}\,\hat{n}_{zz}$.

2. El determinante del tensor de permitividad es invariante con el desplazamiento (ley de conservación del índice [184]), por lo que se puede calcular a partir del estructurado no desplazado como $|\varepsilon(\overline{\Delta z})| = |\varepsilon(0)| = n_\parallel^4 n_\perp^2$,

3. El desplazamiento no afecta a las ondas polarizadas en y (ondas TM): $\hat{n}_{yy}(\Delta z) = n_\parallel$.

4. La propagación de la luz a lo largo de los ejes x y z es idéntica cuando el desplazamiento es la mitad del período.

Combinando las tres primeras suposiciones se obtiene la siguiente condición para las componentes del tensor de permitividad del LPS de ladrillo: $\hat{n}_{xx}(0{,}5) \cdot \hat{n}_{zz}(0{,}5) = n_{\parallel}^2 n_{\perp}^2$. Por otra parte, la última suposición produce la siguiente condición para las componentes del tensor de permitividad: $\hat{n}_{xx}(0.5) = \hat{n}_{zz}(0.5)$. Combinando estas dos ecuaciones, el tensor de permitividad para $\overline{\Delta z} = 0.5$ se obtiene como $\varepsilon(0.5) = \mathrm{diag}[n_{\parallel} n_{\perp}, n_{\parallel}^2, n_{\parallel} n_{\perp}]$. La figura B.11e muestra el tensor de permitividad calculado para el LPS ejemplar en estudio. Estos dos casos límite, $\overline{\Delta z} = 0$ y $\overline{\Delta z} = 0{,}5$ se han calculado directamente a partir de las consideraciones de simetría y la ley de conservación del índice. Para los valores intermedios se supone una solución periódica y suave:

$$\hat{n}_{xx}(\overline{\Delta z}) = A + B\cos(2\pi\overline{\Delta z}) \tag{B.17}$$

Entonces, el componente n_{zz} se puede calcular como:

$$\hat{n}_{zz}(\overline{\Delta z}) = n_{\parallel} n_{\perp} / \hat{n}_{xx}(\overline{\Delta z}) \tag{B.18}$$

con $A = 0.5(n_{\parallel} + \sqrt{(}n_{\parallel} n_{\perp}))$ y $B = 0.5(n_{\parallel} - \sqrt{(}n_{\parallel} n_{\perp}))$ obtenidos a partir de los casos límite $\overline{\Delta z} = 0$ y $\overline{\Delta z} = 0{,}5$. Es importante señalar que estos componentes del tensor del metamaterial SWG enladrillado se calculan a partir de los componentes del tensor de permitividad del LPS convencional, $n_{\parallel}$ y $n_{\perp}$. Al igual que ocurre en los metamateriales SWG inclinados, se consigue una amplia gama de birrefrigencias para un período y ciclo de trabajo fijos desplazando adecuadamente la estructura. La principal diferencia en este caso es que los metamateriales SWG inclinados mantienen una geometría rectangular, tipo Manhattan.

B.3.6. Propiedades de guía de ondas de los metamateriales SWG enladrilladas

Las propiedades de guía de onda de los metamateriales SWG enladrillados se examinan analizando el mismo escenario que los metamateriales SWG inclinados. Es decir, una guía de onda SWG multimodo ($W = 3{,}25\,\mu$m, $\Lambda = 0{,}25\,\mu$m y DC = 0,5) en una plataforma de silicio estándar de 220 nm de espesor. El estudio parte de la validación del modelo anisotrópico de las guías de onda SWG enladrilladas. Para ello, se calculan los modos fundamentales TE y TM de las guías de ondas SWG enladrillada y su correspondiente guía de ondas anisotrópica homogénea para diferentes desplazamientos Δz utilizando FullWAVE y FIMMWAVE respectivamente. Los índices efectivos de estos modos fundamentales se muestran en la Fig. B.12a, proporcionando resultados similares. Como se esperaba, la polarización TE se ve fuertemente afectada por el desplazamiento, mientras que la TM apenas cambia. A continuación, se revisa la dispersión de longitudes de onda de los índices efectivos de los modos que se propagan a lo largo de la guía de onda SWG enladrillada. La figura B.12b muestra la dispersión del índice efectivo de los modos fundamentales TE y TM que se propagan a lo largo del eje z, para diferentes desplazamientos. Estas simulaciones muestran claramente que las guías de ondas SWG enladrilladas proporcionan un control preciso sobre el índice efectivo y la dispersión de los modos TE, mientras que el modo fundamental TM casi no se ve afectado. Además, como el índice efectivo de los modos TE se reduce mientras el período de la estructura periódica se mantiene constante, la condición de Bragg se satisface para un período más corto. Para mostrar claramente este efecto, se repite el estudio de la dispersión del índice efectivo de la estructura SWG enladrillada para un período de 300 nm [Véase Fig. B.12c]. Sin desplazamiento, la guía de onda SWG con el período de 300 nm, no puede guiar eficazmente las longitudes de onda cercanas a 1,55 µm porque opera en el bandgap.

A medida que aumenta el desplazamiento, la longitud de onda de Bragg se acorta, lo que permite trabajar y aumentar las dimensiones de las características. Las propiedades de guía de ondas de los metamateriales SWG enladrillados son interesantes para la ingeniería de los modos TE en óptica integrada y la birrefrigencia modal, al tiempo que permiten períodos más grandes.

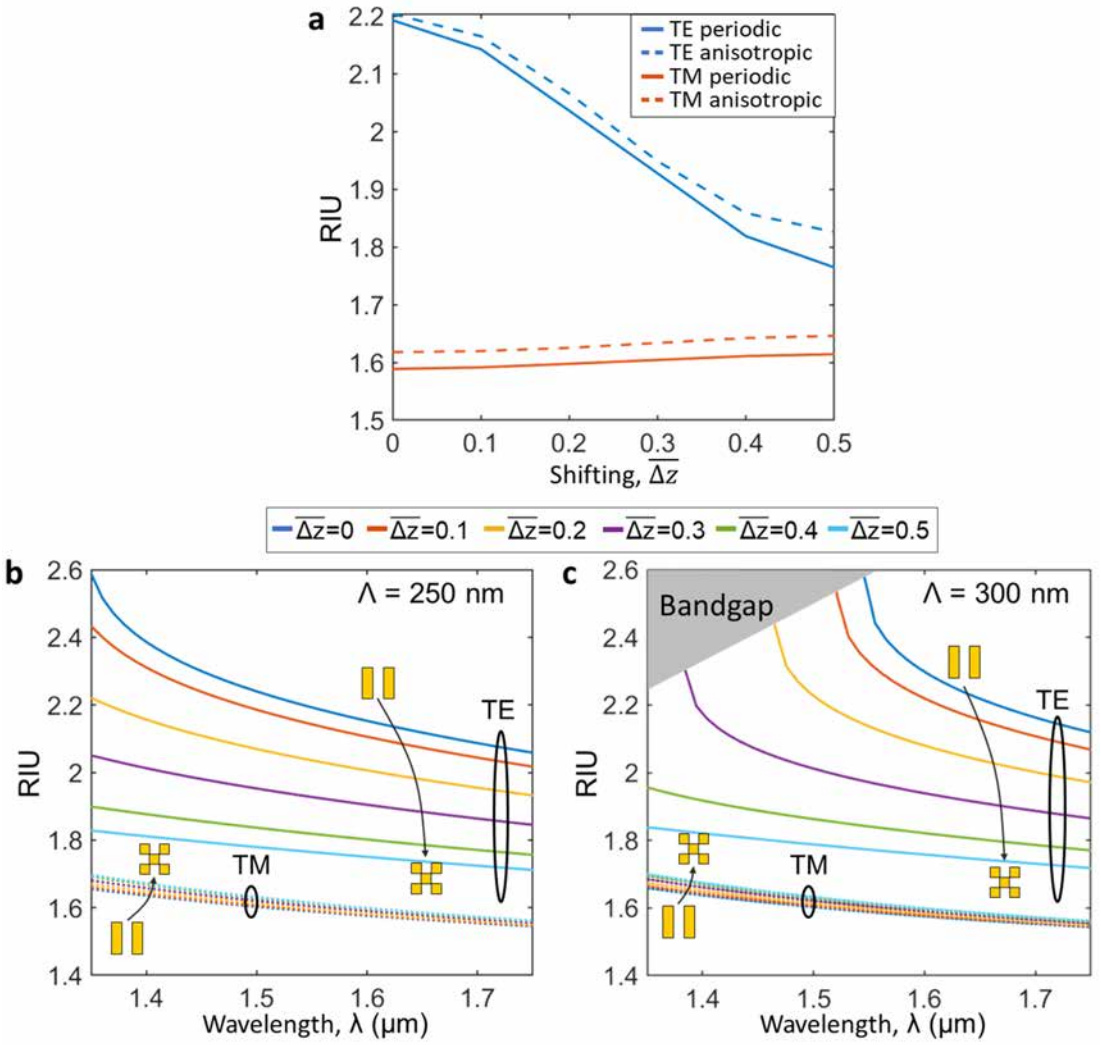

Figure B.12: a) Índices efectivos de los modos fundamentales TE y TM de una guía de onda SWG inclinada y de su guía de onda anisotrópica homogénea equivalente con un espesor de silicio H = 220 µm, una anchura W = 3,25 µm, un periodo Λ = 0,25 µm y un ciclo de trabajo DC = 0,5 para diferentes desplazamientos que van desde $\overline{\Delta z} = 0$ hasta $\overline{\Delta z} = 0.5$ a λ = 1,55 µm. b) Dispersión del índice efectivo de los modos fundamentales TE y TM de la guía de onda SWG inclinada descrita en (a). c) Dispersión del índice efectivo de los modos fundamentales TE y TM de la guía de onda SWG inclinada descrita en (a) con un periodo aumentado a Λ = 300 µm.

B.4. Metamateriales SWG graduales

En esta sección se discute cómo modificando gradualmente el ciclo de trabajo de la estructura SWG se sintetizan metamateriales anisótropos con un índice de refracción gradual. En concreto, en esta sección se propone la topología SWG modulada por ciclo de trabajo, se proporciona un algoritmo de implementación para utilizarla y se valida mediante simulación electromagnética.

B.4.1. Propuesta de topología, algoritmo de diseño y homogeneización

La estructura propuesta es una guía de onda SWG periódica con una anchura w_G, una altura h y un período Λ (Véase Fig. B.13a). El ciclo de trabajo de la estructura periódica, $DC_G(x) = a(x)/\Lambda$, se modula transversalmente para conseguir el perfil deseado. La separación mínima entre segmentos, MFS_G, y la punta de silicio mínima, MFS_T, dan lugar al ciclo de trabajo máximo y mínimo. Los dos principales supuestos que se hacen para analizar esta estructura son:

(i) La estructura modulada por ciclo de trabajo se comporta como un metamaterial GRIN definido por un tensor de permitividad gradual $\varepsilon(x) = \text{diag}[n_{xx}^2(x), n_{yy}^2(x), n_{zz}^2(x)]$ (Véase la Fig. B.13b). Por lo tanto, perfiles isotrópicos graduales no se obtienen mediante esta topología.

(ii) Las componentes del tensor de permitividad en puntos específicos, $n_{xx}^2(x_0)$, $n_{yy}^2(x_0)$, y $n_{zz}^2(x_0)$, son iguales a las componentes del tensor de una estructura SWG no gradual con el ciclo de trabajo en ese punto, $DC(x_0)$. Por lo tanto, la teoría sobre las estructuras SWG no graduales puede aplicarse localmente en esta estructura.

Con estos supuestos, se propone el siguiente algoritmo para implementar los perfiles GRIN, $n_{GRIN}(x)$.

1. Calcular la dependencia del componente del tensor de permitividad con el ciclo de trabajo $n_{xx}(DC)$, $n_{yy}(DC)$, y $n_{zz}(DC)$ para una guía de onda SWG no gradual [Véase la

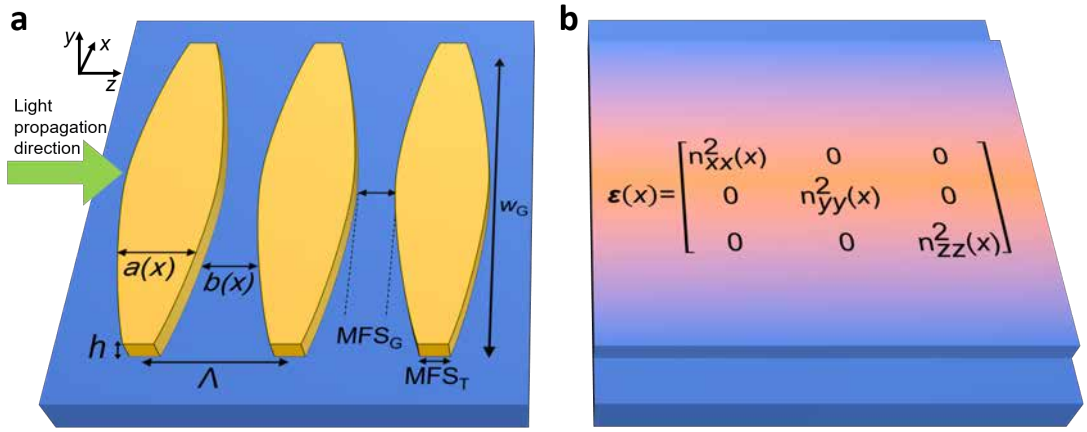

Figure B.13: a) Representación esquemática de la estructura SWG modulada por ciclo de trabajo propuesta y b) su correspondiente modelo homogéneo anisótropo gradual.

Fig. B.14b].

2. Invertir la función $n_{xx}(\mathrm{DC}) \rightarrow \mathrm{DC}(n_{xx})$. La función invertida da el ciclo de trabajo requerido para un índice deseado.
3. Imponer la función objetivo del perfil GRIN deseado a la componente x del tensor, $n_{xx}(x) = n_{\mathrm{GRIN}}(x)$.
4. Utilizar la función invertida, $\mathrm{DC}(n_{xx})$, para calcular el ciclo de trabajo, $\mathrm{DC_G}(x)$, tal que logre la imposición realizada. Es decir $\mathrm{DC_G}(x) = \mathrm{DC}(n_{\mathrm{GRIN}}(x))$ [Véase Fig. B.14c].
5. Completar el modelo de metamaterial anisotrópico calculando la implementación $n_{zz}(x)$ dada por el ciclo de trabajo $\mathrm{DC_G}(x)$ utilizando la función de mapeo $n_{zz}(\mathrm{DC})$, es decir: $n_{zz}(x) = n_{zz}(\mathrm{DC_G}(x))$ [Véase Fig. B.14a, línea roja].

Nótese que, con este algoritmo, el índice gradual deseado se implementa en dos de los tres componentes del tensor como $n_{\mathrm{GRIN}}(x) = n_{xx}(x) = n_{yy}(x)$. En la Fig. B.14 se han considerado valores típicos de silicio sobre aislante. Esto es: $n_1 = 3{,}476$, $n_2 = 1{,}444$, $\lambda_0 =$

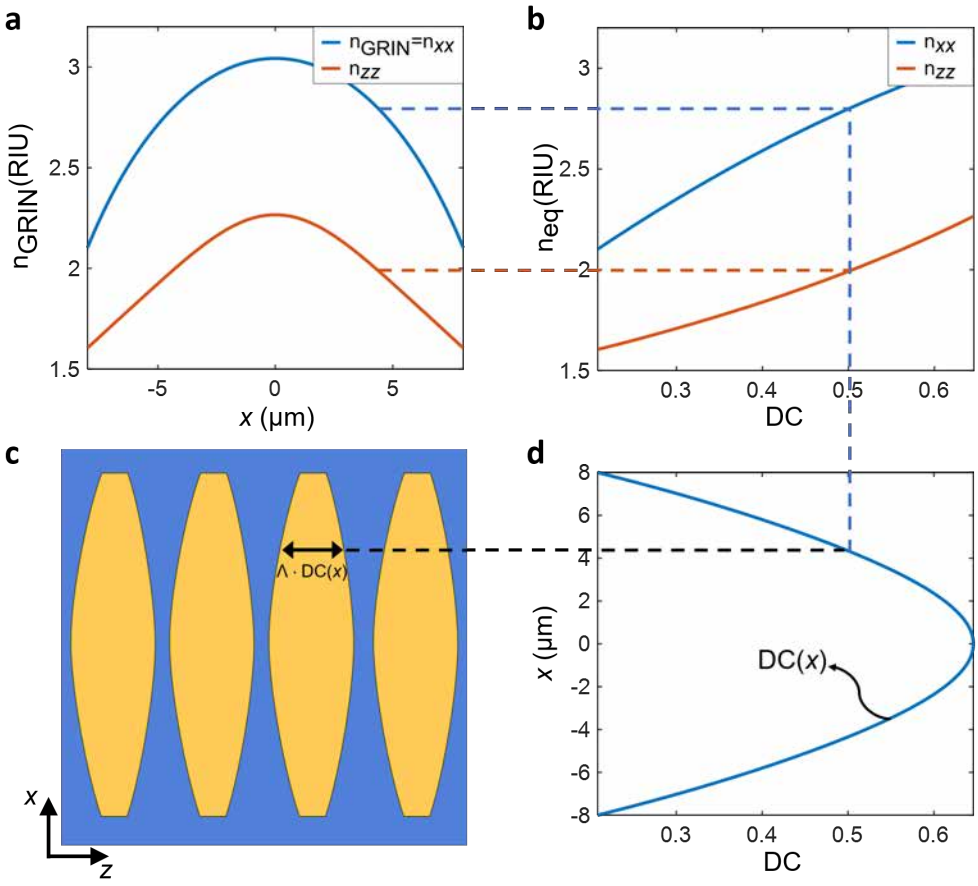

Figure B.14: (a) Índice de refracción equivalente GRIN deseado, $n_{\mathrm{GRIN}}(x)$ (línea azul) y componente $n_{zz}(x)$ implementado (línea roja). (b) Dependencia de los componentes del tensor de permitividad implementados con el ciclo de trabajo, $n_{xx}(\mathrm{DC})$ y $n_{zz}(\mathrm{DC})$. (c) Representación esquemática de la modulación de la forma del segmento de silicio. d) Ciclo de trabajo a lo largo del período transversal requerido para implementar el perfil deseado.

1,55 µm, $h = 220$ nm y $\Lambda = 200$ nm. La anchura del metamaterial se ha elegido para que sea $w_G = 16$ µm y los índices de refracción máximo y mínimo, n_{max} y n_{min}, se calculan asumiendo tamaños de punta mínimos $MFS_T = MFS_G = 50$ nm.

B.5. Conclusiones y líneas futuras

El diseño de metamateriales con propiedades ópticas optimizadas mediante el uso de estructuras de sub-longitud de onda (SWG) se ha convertido en una herramienta esencial en la fotónica de silicio, y más concretamente en la plataforma de silicio sobre aislante (SOI). Los metamateriales SWG permiten mejorar el rendimiento de los dispositivos ópticos integrados, así como nuevas funcionalidades, sin aumentar la complejidad de los procesos de fabricación. Por esta razón, hoy en día es muy común encontrar metamateriales SWG en dispositivos ópticos integrados de altas prestaciones implementados sobre plataforma SOI.

En esta Tesis se han propuesto varios avances en aspectos fundamentales relacionados con el diseño de metamateriales SWG, como el desarrollo de herramientas de modelado y simulación, nuevas topologías para implementar metamateriales SWG y el diseño de dispositivos fotónicos integrados de altas prestaciones. En todos los casos, se han realizado rigurosas simulaciones electromagnéticas de las estructuras propuestas y se han desarrollado prototipos que han sido caracterizados experimentalmente. Los dispositivos se han fabricado en obleas multiproyecto de una fábricas comercial y no han requerido ningún proceso adicional al estándar ofrecido por la fábrica. Las contribuciones más relevantes se han publicado en revistas de alto impacto revisadas por pares y en conferencias internacionales.

Como resultado del trabajo de investigación sobre metamateriales SWG desarrollado en esta Tesis, se han alcanzado las siguientes conclusiones:

1. **Es fundamental disponer de herramientas de modelado y simulación que proporcionen una visión física y reduzcan los tiempos de diseño.** La simulación de estructuras periódicas SWG requiere frecuentemente un alto coste computacional. Las herramientas de modelado desarrolladas para las estructuras periódicas SWG como metamateriales anisotrópicos homogéneos equivalentes nos permiten realizar simulaciones preliminares rápidas pero precisas, ahorrando mucho tiempo en el proceso de diseño de dispositivos fotónicos. Además, la homogeneización de las estructuras de SWG como metamateriales anisótropos facilita la comprensión de la física subyacente promoviendo la propuesta de nuevos dispositivos basados en SWG. Se han demostrado dos modelos de homogeneización para calcular la estructura anisotrópica equivalente de un determinado SWG: El modelo de estructura periódica laminar (LPS) y los modelos de estructura *slab* periódica (PSS). El LPS es un modelo muy sencillo, que sólo requiere la resolución de una ecuación semianalítica, pero está muy limitado por el régimen de Bragg. Suponiendo una plataforma SOI típica, este modelo está limitado a SWG con períodos superiores a ~ 240 nm a una longitud de onda de $\lambda = 1{,}55$ µm y un ciclo de trabajo del 50%. Por otro lado, el modelo PSS es un poco más complejo, ya que requiere la simulación de un *slab* periódico 2D, pero puede utilizarse para estructuras SWG con un período de hasta ~ 300 nm.

2. **La estructuras SWG canónicas tiene un número reducido de grados de libertad, lo que limita las posibilidades de diseño.** El control de las propiedades ópticas de los

metamateriales SWG abre múltiples vías para el diseño de dispositivos fotónicos de altas prestaciones. En esta Tesis se han propuesto dos novedosas topologías de SWG para mejorar el control sobre el metamaterial sintetizado: Los metamateriales SWG inclinados y los metamateriales SWG enladrillados. Estas topologías SWG amplían el espacio de diseño de los metamateriales implementados ofreciendo nuevos grados de libertad para controlar la propagación de la luz en el chip. En concreto, permiten controlar el índice efectivo y la dispersión de los modos polarizados TE sin afectar a los polarizados TM ni añadir dificultades adicionales al proceso de fabricación. Por lo tanto, están bien preparados para el diseño de dispositivos de gestión de la polarización.

3. **Los metamateriales de índice gradual pueden sintetizarse con un proceso de fabricación CMOS estándar.** Los materiales de índice gradual (GRIN) ofrecen un control prácticamente total de la propagación de la luz. En esta Tesis se ha propuesto una metodología para implementar metamateriales GRIN en chips integrados utilizando metamateriales SWG. Se basa en modificar gradualmente el ciclo de trabajo a lo largo de la dirección transversal. La propuesta incluye un modelo matemático para incorporar la gradualidad en la componente del tensor de permitividad de la estructura sintetizada. La síntesis de metamateriales GRIN en chips SOI abre múltiples enfoques de diseño como los basados en el diseño inverso o la óptica de transformación.

4. **Las topologías propuestas anteriormente pueden ser incorporadas en dispositivos con aplicaciones prácticas, mejorando sus prestaciones o implementando nuevas funcionalidades.** El objetivo final de los metamateriales SWG es el diseño de dispositivos de altas prestaciones. A lo largo de esta Tesis se ha demostrado un conjunto de dispositivos que utilizan los modelos y topologías SWG desarrollados.

Bibliography

[1] D. J. Richardson, J. M. Fini, and L. E. Nelson, "Space-division multiplexing in optical fibres," *Nature Photonics*, vol. 7, no. 5, pp. 354–362, May 2013.

[2] P. J. Winzer, "Making spatial multiplexing a reality," *Nature Photonics*, vol. 8, no. 5, pp. 345–348, May 2014.

[3] A. E. Willner, H. Huang, Y. Yan, Y. Ren, N. Ahmed, G. Xie, C. Bao, L. Li, Y. Cao, Z. Zhao, J. Wang, M. P. J. Lavery, M. Tur, S. Ramachandran, A. F. Molisch, N. Ashrafi, and S. Ashrafi, "Optical communications using orbital angular momentum beams," *Advances in Optics and Photonics*, vol. 7, no. 1, pp. 66–101, Mar. 2015.

[4] J. M. Kahn and D. A. B. Miller, "Communications expands its space," *Nature Photonics*, vol. 11, no. 1, pp. 5–8, Jan. 2017.

[5] M. A. Green, A. Ho-Baillie, and H. J. Snaith, "The emergence of perovskite solar cells," *Nature Photonics*, vol. 8, no. 7, pp. 506–514, Jul. 2014.

[6] G. Lanzani, A. Petrozza, and M. Caironi, "Organics go hybrid," *Nature Photonics*, vol. 11, no. 1, pp. 20–22, Jan. 2017.

[7] P. Cheng, G. Li, X. Zhan, and Y. Yang, "Next-generation organic photovoltaics based on non-fullerene acceptors," *Nature Photonics*, vol. 12, no. 3, pp. 131–142, Mar. 2018.

[8] Y. Zhao, M. Boccard, S. Liu, J. Becker, X.-H. Zhao, C. M. Campbell, E. Suarez, M. B. Lassise, Z. Holman, and Y.-H. Zhang, "Monocrystalline CdTe solar cells with open-circuit voltage over 1 V and efficiency of 17%," *Nature Energy*, vol. 1, no. 6, p. 16 067, Jun. 2016.

[9] S. Kurtz, N. Haegel, R. Sinton, and R. Margolis, "A new era for solar," *Nature Photonics*, vol. 11, no. 1, pp. 3–5, Jan. 2017.

[10] M. Yabashi and H. Tanaka, "The next ten years of X-ray science," *Nature Photonics*, vol. 11, no. 1, pp. 12–14, Jan. 2017.

[11] N. Huang, H. Deng, B. Liu, D. Wang, and Z. Zhao, "Features and futures of X-ray free-electron lasers," *The Innovation*, vol. 2, no. 2, p. 100 097, May 2021.

[12] L. V. Wang and S. Hu, "Photoacoustic tomography: In vivo imaging from organelles to organs," *Science*, vol. 335, no. 6075, pp. 1458–1462, 2012.

[13] F. Pisanello, G. Mandelbaum, M. Pisanello, I. A. Oldenburg, L. Sileo, J. E. Markowitz, R. E. Peterson, A. Della Patria, T. M. Haynes, M. S. Emara, B. Spagnolo, S. R. Datta, M. De Vittorio, and B. L. Sabatini, "Dynamic illumination of spatially restricted or large brain volumes via a single tapered optical fiber," *Nature Neuroscience*, vol. 20, no. 8, pp. 1180–1188, 2017.

[14] S. Gigan, "Optical microscopy aims deep," *Nature Photonics*, vol. 11, no. 1, pp. 14–16, 2017.

[15] E. F. Williams, M. R. Fernández-Ruiz, R. Magalhaes, R. Vanthillo, Z. Zhan, M. González-Herráez, and H. F. Martins, "Distributed sensing of microseisms and teleseisms with submarine dark fibers," *Nature Communications*, vol. 10, no. 1, p. 5778, Dec. 2019.

[16] A. Sladen, D. Rivet, J. P. Ampuero, L. De Barros, Y. Hello, G. Calbris, and P. Lamare, "Distributed sensing of earthquakes and ocean-solid Earth interactions on seafloor telecom cables," *Nature Communications*, vol. 10, no. 1, p. 5777, Dec. 2019.

[17] P. Lu, N. Lalam, M. Badar, B. Liu, B. T. Chorpening, M. P. Buric, and P. R. Ohodnicki, "Distributed optical fiber sensing: Review and perspective," *Applied Physics Reviews*, vol. 6, no. 4, p. 041 302, Sep. 2019.

[18] T. Wilken, G. L. Curto, R. A. Probst, T. Steinmetz, A. Manescau, L. Pasquini, J. I. González Hernández, R. Rebolo, T. W. Hänsch, T. Udem, and R. Holzwarth, "A spectrograph for exoplanet observations calibrated at the centimetre-per-second level," *Nature*, vol. 485, no. 7400, pp. 611–614, May 2012.

[19] N. Picqué and T. W. Hänsch, "Frequency comb spectroscopy," *Nature Photonics*, vol. 13, no. 3, pp. 146–157, Mar. 2019.

[20] A. Politi, J. C. Matthews, M. G. Thompson, and J. L. O'Brien, "Integrated quantum photonics," *IEEE Journal of Selected Topics in Quantum Electronics*, vol. 15, no. 6, pp. 1673–1684, 2009.

[21] G. Moody, V. J. Sorger, D. J. Blumenthal, P. W. Juodawlkis, W. Loh, C. Sorace-Agaskar, A. E. Jones, K. C. Balram, J. C. F. Matthews, A. Laing, M. Davanco, L. Chang, J. E. Bowers, N. Quack, C. Galland, I. Aharonovich, M. A. Wolff, C. Schuck, N. Sinclair, M. Lončar, T. Komljenovic, D. Weld, S. Mookherjea, S. Buckley, M. Radulaski, S. Reitzenstein, B. Pingault, B. Machielse, D. Mukhopadhyay, A. Akimov, A. Zheltikov, G. S. Agarwal, K. Srinivasan, J. Lu, H. X. Tang, W. Jiang, T. P. McKenna, A. H. Safavi-Naeini, S. Steinhauer, A. W. Elshaari, V. Zwiller, P. S. Davids, N. Martinez, M. Gehl, J. Chiaverini, K. K. Mehta, J. Romero, N. B. Lingaraju, A. M. Weiner, D. Peace, R. Cernansky, M. Lobino, E. Diamanti, L. T. Vidarte, and R. M. Camacho, "2022 roadmap on integrated quantum photonics," *Journal of Physics: Photonics*, vol. 4, no. 1, p. 012 501, Jan. 2022.

[22] *IPSR-I 2020 overview*, 2020.

[23] S. E. Miller, "Integrated Optics: An Introduction," *Bell System Technical Journal*, vol. 48, no. 7, pp. 2059–2069, Sep. 1969.

[24] R. V. Schmidt and I. P. Kaminow, "Metal-diffused optical waveguides in LiNbO3," *Applied Physics Letters*, vol. 25, no. 8, pp. 458–460, Oct. 1974.

[25] G. Reed and B. Weiss, "Electro-optic effect in He+-implanted optical waveguides in LiNbO3," *Electronics Letters*, vol. 23, no. 8, pp. 424–425, 1987.

[26] D. Nikogosyan, *Nonlinear Optical Crystals: A Complete Survey*. Springer-Science, New York, 2005.

[27] C. Wang, M. Zhang, B. Stern, M. Lipson, and M. Lončar, "Nanophotonic lithium niobate electro-optic modulators," *Optics Express*, vol. 26, no. 2, pp. 1547–1555, Jan. 2018.

[28] D. Zhu, L. Shao, M. Yu, R. Cheng, B. Desiatov, C. J. Xin, Y. Hu, J. Holzgrafe, S. Ghosh, A. Shams-Ansari, E. Puma, N. Sinclair, C. Reimer, M. Zhang, and M. Lončar, "Integrated photonics on thin-film lithium niobate," *Advances in Optics and Photonics*, vol. 13, no. 2, pp. 242–352, Jun. 2021.

[29] R. N. Hall, G. E. Fenner, J. D. Kingsley, T. J. Soltys, and R. O. Carlson, "Coherent Light Emission From GaAs Junctions," *Physical Review Letters*, vol. 9, no. 9, pp. 366–368, Nov. 1962.

[30] Y. Kawamura, K. Wakita, Y. Yoshikuni, Y. Itaya, and H. Asahi, "Monolithic integration of a DFB laser and an MQW optical modulator in the 1.5 μm wavelength range," *IEEE Journal of Quantum Electronics*, vol. 23, no. 6, pp. 915–918, Jun. 1987.

[31] L. Han, S. Liang, H. Wang, L. Qiao, J. Xu, L. Zhao, H. Zhu, B. Wang, and W. Wang, "Electroabsorption-modulated widely tunable DBR laser transmitter for WDM-PONs," *Optics Express*, vol. 22, no. 24, pp. 30 368–30 376, Dec. 2014.

[32] R. Deri and E. Kapon, "Low-loss III-V semiconductor optical waveguides," *IEEE Journal of Quantum Electronics*, vol. 27, no. 3, pp. 626–640, Mar. 1991.

[33] C. Ciminelli, F. Dell'Olio, M. N. Armenise, F. M. Soares, and W. Passenberg, "High performance InP ring resonator for new generation monolithically integrated optical gyroscopes," *Optics Express*, vol. 21, no. 1, pp. 556–564, Jan. 2013.

[34] R. Walker, "High-speed III-V semiconductor intensity modulators," *IEEE Journal of Quantum Electronics*, vol. 27, no. 3, pp. 654–667, Mar. 1991.

[35] Y. Ogiso, Y. Hashizume, H. Tanobe, N. Nunoya, M. Ida, Y. Miyamoto, M. Ishikawa, J. Ozaki, Y. Ueda, H. Wakita, M. Nagatani, H. Yamazaki, M. Nakamura, T. Kobayashi, and S. Kanazawa, "80-GHz Bandwidth and 1.5-V V_π InP-Based IQ Modulator," *Journal of Lightwave Technology*, vol. 38, no. 2, pp. 249–255, Jan. 2020.

[36] J. C. Campbell, "Recent advances in avalanche photodiodes," in *LEOS 2008 - 21st Annual Meeting of the IEEE Lasers and Electro-Optics Society*, vol. 25, IEEE, Nov. 2007, pp. 109–121.

[37] S. Arafin and L. A. Coldren, "Advanced InP Photonic Integrated Circuits for Communication and Sensing," *IEEE Journal of Selected Topics in Quantum Electronics*, vol. 24, no. 1, p. 6 100 612, Jan. 2018.

[38] D. Welch, F. Kish, S. Melle, R. Nagarajan, M. Kato, C. Joyner, J. Pleumeekers, R. Schneider, J. Back, A. Dentai, V. Dominic, P. Evans, M. Kauffman, D. Lambert, S. Hurtt, A. Mathur, M. Mitchell, M. Missey, S. Murthy, A. Nilsson, R. Salvatore, M. Van Leeuwen, J. Webjorn, M. Ziari, S. Grubb, D. Perkins, M. Reffle, and D. Mehuys, "Large-Scale InP Photonic Integrated Circuits: Enabling Efficient Scaling of Optical Transport Networks," *IEEE Journal of Selected Topics in Quantum Electronics*, vol. 13, no. 1, pp. 22–31, 2007.

[39] R. Nagarajan, M. Kato, J. Pleumeekers, P. Evans, S. Hurtt, A. Dentai, M. Missey, A. Chen, A. Mathur, D. Lambert, P. Chavarkar, J. Back, R. Muthiah, S. Murthy, R. Salvatore, C. Joyner, J. Rossi, R. Schneider, and M. Ziari, "Large-Scale Photonic Integrated Circuits," in *2007 IEEE 19th International Conference on Indium Phosphide & Related Materials*, vol. 11, IEEE, May 2007, pp. 32–34.

[40] I. Radu, E. Desbonnets, M. Sellier, and C. Didier, "Enabling 5G — A substrate material perspective: AEM, ET/ID," in *2018 29th Annual SEMI Advanced Semiconductor Manufacturing Conference (ASMC)*, IEEE, Apr. 2018, pp. 143–147.

[41] G. Roelkens, D. Van Thourhout, and R. Baets, "Coupling schemes for heterogeneous integration of III-V membrane devices and silicon-on-insulator waveguides," *Journal of Lightwave Technology*, vol. 23, no. 11, pp. 3827–3831, Nov. 2005.

[42] C. R. Doerr, "Silicon photonic integration in telecommunications," *Frontiers in Physics*, vol. 3, no. August, p. 37, Aug. 2015.

[43] R. Soref and J. Lorenzo, "Single-crystal silicon: a new material for 1.3 and 1.6 μm integrated-optical components," *Electronics Letters*, vol. 21, no. 21, pp. 953–954, 1985.

[44] R. Soref and B. Bennett, "Electrooptical effects in silicon," *IEEE Journal of Quantum Electronics*, vol. 23, no. 1, pp. 123–129, Jan. 1987.

[45] R. Soref and J. Lorenzo, "All-silicon active and passive guided-wave components for λ = 1.3 and 1.6 μm," *IEEE Journal of Quantum Electronics*, vol. 22, no. 6, pp. 873–879, Jun. 1986.

[46] J. P. Lorenzo and R. A. Soref, "1.3 μm electro-optic silicon switch," *Applied Physics Letters*, vol. 51, no. 1, pp. 6–8, Jul. 1987.

[47] R. Soref, J. Schmidtchen, and K. Petermann, "Large single-mode rib waveguides in GeSi-Si and Si-on-SiO_2," *IEEE Journal of Quantum Electronics*, vol. 27, no. 8, pp. 1971–1974, 1991.

[48] R. Soref, "Silicon-based optoelectronics," *Proceedings of the IEEE*, vol. 81, no. 12, pp. 1687–1706, 1993.

[49] A. Rahim, T. Spuesens, R. Baets, and W. Bogaerts, "Open-Access Silicon Photonics: Current Status and Emerging Initiatives," *Proceedings of the IEEE*, vol. 106, no. 12, pp. 2313–2330, Dec. 2018.

[50] S. Y. Siew, B. Li, F. Gao, H. Y. Zheng, W. Zhang, P. Guo, S. W. Xie, A. Song, B. Dong, L. W. Luo, C. Li, X. Luo, and G.-Q. Lo, "Review of Silicon Photonics Technology and Platform Development," *Journal of Lightwave Technology*, vol. 39, no. 13, pp. 4374–4389, Jul. 2021.

[51] T. Baehr-Jones, T. Pinguet, P. Lo Guo-Qiang, S. Danziger, D. Prather, and M. Hochberg, "Myths and rumours of silicon photonics," *Nature Photonics*, vol. 6, no. 4, pp. 206–208, 2012.

[52] P. Muñoz, P. W. L. van Dijk, D. Geuzebroek, M. Geiselmann, C. Dominguez, A. Stassen, J. D. Domenech, M. Zervas, A. Leinse, C. G. H. Roeloffzen, B. Gargallo, R. Banos, J. Fernandez, G. M. Cabanes, L. A. Bru, and D. Pastor, "Foundry Developments Toward Silicon Nitride Photonics From Visible to the Mid-Infrared," *IEEE Journal of Selected Topics in Quantum Electronics*, vol. 25, no. 5, p. 8 200 513, Sep. 2019.

[53] D. J. Blumenthal, R. Heideman, D. Geuzebroek, A. Leinse, and C. Roeloffzen, "Silicon Nitride in Silicon Photonics," *Proceedings of the IEEE*, vol. 106, no. 12, pp. 2209–2231, Dec. 2018.

[54] www.medicaldevice-network.com/analysis/apple-watch-photonics/, *Photonics could reinvent the Apple watch as we know it.*

[55] www.lightwaveonline.com/optical-tech/transmission/article/16664362/silicon-photonics-now-part-of-huawei-imec-partnership, *Silicon photonics now part of Huawei, imec partnership.*

[56] www.servethehome.com/nvidia-gtc-china-2020-co-packaged-photonics-and-inference/, *NVIDIA GTC China 2020 Co-Packaged Photonics and Inference.*

[57] www.intel.com/content/www/us/en/architecture-and-technology/silicon-photonics/silicon-photonics-overview, *Intel Silicon Photonics: How does it work?*

[58] www.cisco.com/c/en/us/products/collateral/interfaces-modules/transceiver-modules/at-a-glance-c45-2411856.html, *Cisco Transceiver Modules - High-Speed Pluggable Optics with Silicon Photonics At-a-Glance*.

[59] www.intel.com/content/www/us/en/architecture-and-technology/silicon-photonics/400g-dr4-qsfp-dd-optical-transceiver.html, *Silicon Photonics 400G DR4 QSFP-DD Optical Transceiver*.

[60] N. Margalit, C. Xiang, S. M. Bowers, A. Bjorlin, R. Blum, and J. E. Bowers, "Perspective on the future of silicon photonics and electronics," *Applied Physics Letters*, vol. 118, no. 22, p. 220 501, May 2021.

[61] G. Poberaj, H. Hu, W. Sohler, and P. Günter, "Lithium niobate on insulator (LNOI) for micro-photonic devices," *Laser & Photonics Reviews*, vol. 6, no. 4, pp. 488–503, Jul. 2012.

[62] Y. S. Lee, G.-D. Kim, W.-J. Kim, S.-S. Lee, W.-G. Lee, and W. H. Steier, "Hybrid Si-LiNbO_3 microring electro-optically tunable resonators for active photonic devices," *Optics Letters*, vol. 36, no. 7, pp. 1119–1121, Apr. 2011.

[63] M. Zhang, C. Wang, R. Cheng, A. Shams-Ansari, and M. Lončar, "Monolithic ultra-high-Q lithium niobate microring resonator," *Optica*, vol. 4, no. 12, pp. 1536–1537, Dec. 2017.

[64] C. Wang, M. Zhang, X. Chen, M. Bertrand, A. Shams-Ansari, S. Chandrasekhar, P. Winzer, and M. Lončar, "Integrated lithium niobate electro-optic modulators operating at CMOS-compatible voltages," *Nature*, vol. 562, no. 7725, pp. 101–104, Oct. 2018.

[65] M. He, M. Xu, Y. Ren, J. Jian, Z. Ruan, Y. Xu, S. Gao, S. Sun, X. Wen, L. Zhou, L. Liu, C. Guo, H. Chen, S. Yu, L. Liu, and X. Cai, "High-performance hybrid silicon and lithium niobate Mach–Zehnder modulators for 100 Gbit/s and beyond," *Nature Photonics*, vol. 13, no. 5, pp. 359–364, May 2019.

[66] M. L. Davenport, S. Skendzic, N. Volet, J. C. Hulme, M. J. R. Heck, and J. E. Bowers, "Heterogeneous Silicon/III–V Semiconductor Optical Amplifiers," *IEEE Journal of Selected Topics in Quantum Electronics*, vol. 22, no. 6, pp. 78–88, Nov. 2016.

[67] S. Keyvaninia, G. Roelkens, D. Van Thourhout, C. Jany, M. Lamponi, A. Le Liepvre, F. Lelarge, D. Make, G.-H. Duan, D. Bordel, and J.-M. Fedeli, "Demonstration of a heterogeneously integrated III-V/SOI single wavelength tunable laser," *Optics Express*, vol. 21, no. 3, pp. 3784–3792, Feb. 2013.

[68] S. Matsuo, T. Fujii, K. Hasebe, K. Takeda, T. Sato, and T. Kakitsuka, "Directly modulated buried heterostructure DFB laser on SiO_2/Si substrate fabricated by regrowth of InP using bonded active layer," *Optics Express*, vol. 22, no. 10, pp. 12 139–12 147, May 2014.

[69] T. Aihara, T. Hiraki, T. Fujii, K. Takeda, T. Kakitsuka, T. Tsuchizawa, and S. Matsuo, "Membrane III-V/Si DFB Laser Using Uniform Grating and Width-Modulated Si Waveguide," *Journal of Lightwave Technology*, vol. 38, no. 11, pp. 2961–2967, Jun. 2020.

[70] T. Fujii, K. Takeda, H. Nishi, N.-P. Diamantopoulos, T. Sato, T. Kakitsuka, T. Tsuchizawa, and S. Matsuo, "Multiwavelength membrane laser array using selective area growth on directly bonded InP on SiO 2 /Si," *Optica*, vol. 7, no. 7, p. 838, Jul. 2020.

[71] T. Hiraki, T. Aihara, Y. Maeda, T. Fujii, T. Tsuchizawa, K. Takahata, T. Kakitsuka, and S. Matsuo, "50-GHz-Bandwidth Membrane InGaAsP Electro-Absorption Modulator on Si Platform," *Journal of Lightwave Technology*, vol. 39, no. 16, pp. 5300–5306, 2021.

[72] Y. Han, X. Zhang, F. Huang, X. Liu, M. Xu, Z. Lin, M. He, S. Yu, R. Wang, and X. Cai, "Electrically pumped widely tunable O-band hybrid lithium niobite/III-V laser," *Optics Letters*, vol. 46, no. 21, pp. 5413–5416, Nov. 2021.

[73] T. Rudenko, A. Nazarov, and V. Lysenko, "The advancement of silicon-on-insulator (SOI) devices and their basic properties," *Semiconductor Physics, Quantum Electronics and Optoelectronics*, vol. 23, no. 3, pp. 227–252, Sep. 2020.

[74] Z. Sheng, Z. Wang, C. Qiu, L. Li, A. Pang, A. Wu, X. Wang, S. Zou, and F. Gan, "A compact and low-loss MMI coupler fabricated with CMOS technology," *IEEE Photonics Journal*, vol. 4, no. 6, pp. 2272–2277, 2012.

[75] Q. Deng, L. Liu, X. Li, and Z. Zhou, "Arbitrary-ratio 1 × 2 power splitter based on asymmetric multimode interference," *Optics Letters*, vol. 39, no. 19, pp. 5590–5593, 2014.

[76] G. F. R. Chen, J. R. Ong, T. Y. L. Ang, S. T. Lim, C. E. Png, and D. T. H. Tan, "Broadband Silicon-On-Insulator directional couplers using a combination of straight and curved waveguide sections," *Scientific Reports*, vol. 7, no. 1, p. 7246, Dec. 2017.

[77] D. Taillaert, Harold Chong, P. Borel, L. Frandsen, R. De La Rue, and R. Baets, "A compact two-dimensional grating coupler used as a polarization splitter," *IEEE Photonics Technology Letters*, vol. 15, no. 9, pp. 1249–1251, Sep. 2003.

[78] M. Aamer, A. M. Gutierrez, A. Brimont, D. Vermeulen, G. Roelkens, J.-M. Fedeli, A. Hakansson, and P. Sanchis, "CMOS Compatible Silicon-on-Insulator Polarization Rotator Based on Symmetry Breaking of the Waveguide Cross Section," *IEEE Photonics Technology Letters*, vol. 24, no. 22, pp. 2031–2034, Nov. 2012.

[79] D. Dai and H. Wu, "Realization of a compact polarization splitter-rotator on silicon," *Optics Letters*, vol. 41, no. 10, pp. 2346–2349, May 2016.

[80] J. R. Ong, T. Y. L. Ang, E. Sahin, B. Pawlina, G. F. R. Chen, D. T. H. Tan, S. T. Lim, and C. E. Png, "Broadband silicon polarization beam splitter with a high extinction ratio using a triple-bent-waveguide directional coupler," *Optics Letters*, vol. 42, no. 21, pp. 4450–4453, Nov. 2017.

[81] T. Tsuchizawa, K. Yamada, H. Fukuda, T. Watanabe, Jun-ichi Takahashi, M. Takahashi, T. Shoji, E. Tamechika, S. Itabashi, and H. Morita, "Microphotonics devices based on silicon microfabrication technology," *IEEE Journal of Selected Topics in Quantum Electronics*, vol. 11, no. 1, pp. 232–240, Jan. 2005.

[82] M. Antelius, K. B. Gylfason, and H. Sohlström, "An apodized SOI waveguide-to-fiber surface grating coupler for single lithography silicon photonics," *Optics Express*, vol. 19, no. 4, pp. 3592–3598, Feb. 2011.

[83] J. Brouckaert, W. Bogaerts, P. Dumon, D. Van Thourhout, and R. Baets, "Planar Concave Grating Demultiplexer Fabricated on a Nanophotonic Silicon-on-Insulator Platform," *Journal of Lightwave Technology*, vol. 25, no. 5, pp. 1269–1275, May 2007.

[84] H. Yan, X. Feng, D. Zhang, K. Cui, F. Liu, and Y. Huang, "Compact Optical Add-Drop Multiplexers With Parent-Sub Ring Resonators on SOI Substrates," *IEEE Photonics Technology Letters*, vol. 25, no. 15, pp. 1462–1465, Aug. 2013.

[85] E. J. Stanton, N. Volet, and J. E. Bowers, "Low-loss demonstration and refined characterization of silicon arrayed waveguide gratings in the near-infrared," *Optics Express*, vol. 25, no. 24, pp. 30 651–30 663, Nov. 2017.

[86] V. G. Veselago, "The electrodynamics of substrances with simultaneously negative values of E and μ," *Soviet Physics Uspekhi*, vol. 10, no. 4, pp. 509–514, Apr. 1968.

[87] J. B. Pendry, A. J. Holden, W. J. Stewart, and I. Youngs, "Extremely Low Frequency Plasmons in Metallic Mesostructures," *Physical Review Letters*, vol. 76, no. 25, pp. 4773–4776, Jun. 1996.

[88] D. R. Smith, J. B. Pendry, and M. C. K. Wiltshire, "Metamaterials and Negative Refractive Index," *Science*, vol. 305, no. 5685, pp. 788–792, Aug. 2004.

[89] B. Zhang, Y. Luo, X. Liu, and G. Barbastathis, "Macroscopic Invisibility Cloak for Visible Light," *Physical Review Letters*, vol. 106, no. 3, p. 033 901, Jan. 2011.

[90] S. M. Rytov, "Electromagnetic properties of a finely stratified medium," *Soviet Physics JETP*, vol. 2, pp. 466–475, 1956.

[91] P. Cheben, D.-X. Xu, S. Janz, and A. Densmore, "Subwavelength waveguide grating for mode conversion and light coupling in integrated optics," *Optics Express*, vol. 14, no. 11, pp. 4695–4702, 2006.

[92] R. Halir, P. Cheben, J. M. Luque-González, J. D. Sarmiento-Merenguel, J. H. Schmid, G. Wangüemert-Pérez, D.-X. Xu, S. Wang, A. Ortega-Moñux, and Í. Molina-Fernández, "Ultra-broadband nanophotonic beamsplitter using an anisotropic sub-wavelength metamaterial," *Laser & Photonics Reviews*, vol. 10, no. 6, pp. 1039–1046, Nov. 2016.

[93] M. Born, E. Wolf, A. B. Bhatia, P. C. Clemmow, D. Gabor, A. R. Stokes, A. M. Taylor, P. A. Wayman, and W. L. Wilcock, *Principles of Optics*. Cambridge: Cambridge University Press, 1999.

[94] B. Naghdi and L. R. Chen, "Silicon Photonic Four-Channel Optical Add-Drop Multiplexer Enabled by Subwavelength Grating Waveguides," *IEEE Photonics Journal*, vol. 10, no. 4, pp. 1–10, 2018.

[95] H. Yun, L. Chrostowski, and N. A. F. Jaeger, "Ultra-broadband 2 × 2 adiabatic 3 dB coupler using subwavelength-grating-assisted silicon-on-insulator strip waveguides," *Optics Letters*, vol. 43, no. 8, pp. 1935–1938, Apr. 2018.

[96] L. Xu, Y. Wang, A. Kumar, E. El-Fiky, D. Mao, H. Tamazin, M. Jacques, Z. Xing, M. G. Saber, and D. V. Plant, "Compact high-performance adiabatic 3-dB coupler enabled by subwavelength grating slot in the silicon-on-insulator platform," *Optics Express*, vol. 26, no. 23, pp. 29 873–29 885, Nov. 2018.

[97] Y. He, Y. Zhang, Q. Zhu, S. An, R. Cao, X. Guo, C. Qiu, and Y. Su, "Silicon high-order mode (De)multiplexer on single polarization," *Journal of Lightwave Technology*, vol. 36, no. 24, pp. 5746–5753, 2018.

[98] W. Jiang, J. Miao, T. Li, and L. Ma, "On-chip silicon dual-mode multiplexer via a subwavelength grating-based directional coupler and a mode blocker," *Applied Optics*, vol. 58, no. 33, pp. 9290–9296, Nov. 2019.

[99] J. Chen and Y. Shi, "Flat-Top CWDM (De)Multiplexers Based on Contra-Directional Couplers with Subwavelength Gratings," *IEEE Photonics Technology Letters*, vol. 31, no. 24, pp. 2003–2006, 2019.

[100] H. Yun, M. Hammood, S. Lin, L. Chrostowski, and N. A. F. Jaeger, "Broadband flat-top SOI add–drop filters using apodized sub-wavelength grating contradirectional couplers," *Optics Letters*, vol. 44, no. 20, pp. 4929–4932, 2019.

[101] W. Jiang, J. Miao, T. Li, and L. Ma, "Ultrabroadband and fabrication-tolerant mode (de)multiplexer using subwavelength structure," *Journal of the Optical Society of America B*, vol. 36, no. 11, pp. 3125–3132, Nov. 2019.

[102] J. Chen, "A broadband wavelength demultiplexer assisted by SWG-based directional couplers," *Optik*, vol. 202, no. July 2019, p. 163 602, Feb. 2020.

[103] R. Halir, P. Cheben, S. Janz, D.-X. Xu, Í. Molina-Fernández, and J. G. Wangüemert-Pérez, "Waveguide grating coupler with subwavelength microstructures," *Optics Letters*, vol. 34, no. 9, pp. 1408–1410, May 2009.

[104] D. Benedikovic, P. Cheben, J. H. Schmid, D.-X. Xu, B. Lamontagne, S. Wang, J. Lapointe, R. Halir, A. Ortega-Moñux, S. Janz, and M. Dado, "Subwavelength index engineered surface grating coupler with sub-decibel efficiency for 220-nm silicon-on-insulator waveguides," *Optics Express*, vol. 23, no. 17, pp. 22 628–22 635, Aug. 2015.

[105] A. Sánchez-Postigo, J. Gonzalo Wangüemert-Pérez, J. M. Luque-González, Í. Molina-Fernández, P. Cheben, C. A. Alonso-Ramos, R. Halir, J. H. Schmid, and A. Ortega-Moñux, "Broadband fiber-chip zero-order surface grating coupler with 0.4 dB efficiency," *Optics Letters*, vol. 41, no. 13, pp. 3013–3016, Jul. 2016.

[106] W. Zhou, Z. Cheng, X. Sun, and H. K. Tsang, "Tailorable dual-wavelength-band coupling in a transverse-electric-mode focusing subwavelength grating coupler," *Optics Letters*, vol. 43, no. 12, pp. 2985–2988, Jun. 2018.

[107] S. Li, L. Cai, D. Gao, J. Dong, J. Hou, C. Yang, S. Chen, and X. Zhang, "Deterministic design of focusing apodized subwavelength grating coupler based on weak form and transformation optics," *Optics Express*, vol. 28, no. 23, pp. 35 395–35 412, Nov. 2020.

[108] A. Hadij-ElHouati, P. Cheben, A. Ortega-Moñux, J. G. Wangüemert-Pérez, R. Halir, J. De-Oliva-Rubio, J. H. Schmid, and Í. Molina-Fernández, "High-efficiency conversion from waveguide mode to an on-chip beam using a metamaterial engineered Bragg deflector," *Optics Letters*, vol. 46, no. 10, pp. 2409–2412, May 2021.

[109] U. Levy, M. Abashin, K. Ikeda, A. Krishnamoorthy, J. Cunningham, and Y. Fainman, "Inhomogenous Dielectric Metamaterials with Space-Variant Polarizability," *Physical Review Letters*, vol. 98, no. 24, p. 243 901, Jun. 2007.

[110] L. Lu, D. Liu, M. Yan, and M. Zhang, "Subwavelength adiabatic multimode Y-junctions," *Optics Letters*, vol. 44, no. 19, pp. 4729–4732, 2019.

[111] Z. Wang, T. Li, A. Soman, D. Mao, T. Kananen, and T. Gu, "On-chip wavefront shaping with dielectric metasurface," *Nature Communications*, vol. 10, no. 1, p. 3547, Dec. 2019.

[112] M. Papes, P. Cheben, D. Benedikovic, J. H. Schmid, J. Pond, R. Halir, A. Ortega-Moñux, G. Wangüemert-Pérez, W. N. Ye, D.-X. Xu, S. Janz, M. Dado, and V. Vašinek, "Fiber-chip edge coupler with large mode size for silicon photonic wire waveguides," *Optics Express*, vol. 24, no. 5, pp. 5026–5038, Mar. 2016.

[113] T. Barwicz, Y. Taira, T. W. Lichoulas, N. Boyer, Y. Martin, H. Numata, J. W. Nah, S. Takenobu, A. Janta-Polczynski, E. L. Kimbrell, R. Leidy, M. H. Khater, S. Kamlapurkar, S. Engelmann, Y. A. Vlasov, and P. Fortier, "A novel approach to photonic packaging leveraging existing high-throughput microelectronic facilities," *IEEE Journal on Selected Topics in Quantum Electronics*, vol. 22, no. 6, pp. 455–466, 2016.

[114] P. J. Bock, P. Cheben, J. H. Schmid, J. Lapointe, A. Delâge, D.-X. Xu, S. Janz, A. Densmore, and T. J. Hall, "Subwavelength grating crossings for silicon wire waveguides," *Optics Express*, vol. 18, no. 15, pp. 16 146–16 155, Jul. 2010.

[115] Y. Zhang, A. Hosseini, X. Xu, D. Kwong, and R. T. Chen, "Ultralow-loss silicon waveguide crossing using Bloch modes in index engineered cascaded multimode interference couplers," *Optics Letters*, vol. 38, no. 18, pp. 3608–3611, 2013.

[116] H. Xu and Y. Shi, "Metamaterial-Based Maxwell's Fisheye Lens for Multimode Waveguide Crossing," *Laser & Photonics Reviews*, vol. 12, no. 10, p. 1 800 094, Oct. 2018.

[117] H. Wu, C. Li, L. Song, H.-K. Tsang, J. E. Bowers, and D. Dai, "Ultra-Sharp Multimode Waveguide Bends with Subwavelength Gratings," *Laser & Photonics Reviews*, vol. 13, no. 2, p. 1 800 119, Feb. 2019.

[118] J. M. Luque-González, R. Halir, J. G. Wangüemert-Pérez, J. De-Oliva-Rubio, J. H. Schmid, P. Cheben, Í. Molina-Fernández, and A. Ortega-Moñux, "An Ultracompact GRIN-Lens-Based Spot Size Converter using Subwavelength Grating Metamaterials," *Laser & Photonics Reviews*, vol. 13, no. 11, p. 1 900 172, Nov. 2019.

[119] D. Pereira-Martín, J. M. Luque-González, J. Gonzalo Wangüemert-Pérez, A. Hadij-ElHouati, Í. Molina-Fernández, P. Cheben, J. H. Schmid, S. Wang, W. N. Ye, J. Čtyroký, and A. Ortega-Moñux, "Complex spectral filters in silicon waveguides based on cladding-modulated Bragg gratings," *Optics Express*, vol. 29, no. 11, pp. 15 867–15 881, May 2021.

[120] P. Ginel-Moreno, A. Sánchez-Postigo, J. De-Oliva-Rubio, A. Hadij-ElHouati, W. N. Ye, J. G. Wangüemert-Pérez, Í. Molina-Fernández, J. H. Schmid, P. Cheben, and A. Ortega-Moñux, "Millimeter-long metamaterial surface-emitting antenna in silicon photonics platform," *Optics Letters*, vol. Accepted, 2021.

[121] J. Gonzalo Wangüemert-Pérez, P. Cheben, A. Ortega-Moñux, C. Alonso-Ramos, D. Pérez-Galacho, R. Halir, Í. Molina-Fernández, D.-x. Xu, and J. H. Schmid, "Evanescent field waveguide sensing with subwavelength grating structures in silicon-on-insulator," *Optics Letters*, vol. 39, no. 15, pp. 4442–4445, Aug. 2014.

[122] V. Donzella, A. Sherwali, J. Flueckiger, S. M. Grist, S. T. Fard, and L. Chrostowski, "Design and fabrication of SOI micro-ring resonators based on sub-wavelength grating waveguides," *Optics Express*, vol. 23, no. 4, pp. 4791–4803, Feb. 2015.

[123] M. Odeh, K. Twayana, K. Sloyan, J. E. Villegas, S. Chandran, and M. S. Dahlem, "Mode Sensitivity Analysis of Subwavelength Grating Slot Waveguides," *IEEE Photonics Journal*, vol. 11, no. 5, p. 2 700 210, Oct. 2019.

[124] C. W. Chang, X. Xu, S. Chakravarty, H. C. Huang, L. W. Tu, Q. Y. Chen, H. Dalir, M. A. Krainak, and R. T. Chen, "Pedestal subwavelength grating metamaterial waveguide ring resonator for ultra-sensitive label-free biosensing," *Biosensors and Bioelectronics*, vol. 141, no. May, p. 111 396, Sep. 2019.

[125] L. Torrijos-Morán, A. Griol, and J. García-Rupérez, "Experimental study of subwavelength grating bimodal waveguides as ultrasensitive interferometric sensors," *Optics Letters*, vol. 44, no. 19, pp. 4702–4705, Oct. 2019.

[126] P. Xu, J. Zheng, J. Zhou, Y. Chen, C. Zou, and A. Majumdar, "Multi-slot photonic crystal cavities for high-sensitivity refractive index sensing," *Optics Express*, vol. 27, no. 3, pp. 3609–3616, Feb. 2019.

[127] C. Ye and D. Dai, "Ultra-Compact Broadband 2 × 2 3 dB Power Splitter Using a Subwavelength-Grating-Assisted Asymmetric Directional Coupler," *Journal of Lightwave Technology*, vol. 38, no. 8, pp. 2370–2375, Apr. 2020.

[128] E. Luan, H. Yun, L. Laplatine, Y. Dattner, D. M. Ratner, K. C. Cheung, and L. Chrostowski, "Enhanced Sensitivity of Subwavelength Multibox Waveguide Microring Resonator Label-Free Biosensors," *IEEE Journal of Selected Topics in Quantum Electronics*, vol. 25, no. 3, p. 7 300 211, May 2019.

[129] P. Cheben, J. H. Schmid, S. Wang, D.-X. Xu, M. Vachon, S. Janz, J. Lapointe, Y. Painchaud, and M.-J. Picard, "Broadband polarization independent nanophotonic coupler for silicon waveguides with ultra-high efficiency," *Optics Express*, vol. 23, no. 17, pp. 22 553–22 563, Aug. 2015.

[130] Y. Wang, M. Ma, H. Yun, Z. Lu, X. Wang, N. A. F. Jaeger, and L. Chrostowski, "Ultra-Compact Sub-Wavelength Grating Polarization Splitter-Rotator for Silicon-on-Insulator Platform," *IEEE Photonics Journal*, vol. 8, no. 6, pp. 1–9, Dec. 2016.

[131] H. Xu, D. Dai, and Y. Shi, "Anisotropic metamaterial-assisted all-silicon polarizer with 415-nm bandwidth," *Photonics Research*, vol. 7, no. 12, pp. 1432–1439, Dec. 2019.

[132] J. M. Luque-González, A. Herrero-Bermello, A. Ortega-Moñux, M. Sánchez-Rodríguez, A. V. Velasco, J. H. Schmid, P. Cheben, Í. Molina-Fernández, and R. Halir, "Polarization splitting directional coupler using tilted subwavelength gratings," *Optics Letters*, vol. 45, no. 13, pp. 3398–3401, Jul. 2020.

[133] H. Xu, D. Dai, and Y. Shi, "Ultra-Broadband and Ultra-Compact On-Chip Silicon Polarization Beam Splitter by Using Hetero-Anisotropic Metamaterials," *Laser and Photonics Reviews*, vol. 13, no. 4, pp. 1–7, 2019.

[134] A. Hadij-ElHouati, P. Cheben, A. Ortega-Moñux, J. G. Wangüemert-Pérez, R. Halir, J. H. Schmid, and Í. Molina-Fernández, "Distributed Bragg deflector coupler for on-chip shaping of optical beams," *Optics Express*, vol. 27, no. 23, pp. 33 180–33 193, Nov. 2019.

[135] D. Oser, D. Pérez-Galacho, X. Le Roux, S. Tanzilli, L. Vivien, L. Labonté, É. Cassan, and C. Alonso-Ramos, "Silicon subwavelength modal Bragg grating filters with narrow bandwidth and high optical rejection," *Optics Letters*, vol. 45, no. 20, pp. 5784–5787, Oct. 2020.

[136] L. Liu, Q. Deng, and Z. Zhou, "Manipulation of beat length and wavelength dependence of a polarization beam splitter using a subwavelength grating," *Optics Letters*, vol. 41, no. 21, pp. 5126–5129, Nov. 2016.

[137] Y. Xu and J. Xiao, "Compact and high extinction ratio polarization beam splitter using subwavelength grating couplers," *Optics Letters*, vol. 41, no. 4, pp. 773–776, Feb. 2016.

[138] L. Xu, Y. Wang, A. Kumar, D. Patel, E. El-Fiky, Z. Xing, R. Li, and D. V. Plant, "Polarization beam splitter based on MMI coupler with SWG birefringence engineering on SOI," *IEEE Photonics Technology Letters*, vol. 30, no. 4, pp. 403–406, Feb. 2018.

[139] Y. Xu and J. Xiao, "Ultracompact and high efficient silicon-based polarization splitter-rotator using a partially-etched subwavelength grating coupler," *Scientific Reports*, vol. 6, no. June, pp. 1–11, 2016.

[140] H. Xu and Y. Shi, "Subwavelength-grating-assisted silicon polarization rotator covering all optical communication bands," *Optics Express*, vol. 27, no. 4, pp. 5588–5597, Feb. 2019.

[141] Y. Xiong, D.-X. Xu, J. H. Schmid, P. Cheben, S. Janz, and W. N. Ye, "Fabrication tolerant and broadband polarization splitter and rotator based on a taper-etched directional coupler," *Optics Express*, vol. 22, no. 14, p. 17 458, Jul. 2014.

[142] M. Ma, A. H. K. Park, Y. Wang, H. Shoman, F. Zhang, N. A. F. Jaeger, and L. Chrostowski, "Sub-wavelength grating-assisted polarization splitter-rotators for silicon-on-insulator platforms," *Optics Express*, vol. 27, no. 13, pp. 17 581–17 591, Jun. 2019.

[143] Y. Xiong, D.-X. Xu, J. H. Schmid, P. Cheben, and W. N. Ye, "High Extinction Ratio and Broadband Silicon TE-Pass Polarizer Using Subwavelength Grating Index Engineering," *IEEE Photonics Journal*, vol. 7, no. 5, p. 7 802 107, Oct. 2015.

[144] B. Ni and J. Xiao, "Subwavelength-grating-based compact and broadband TE-pass polarizer for slot waveguides on a SOI platform," *Journal of the Optical Society of America B*, vol. 36, no. 8, pp. 2126–2133, Aug. 2019.

[145] S. Jahani, S. Kim, J. Atkinson, J. C. Wirth, F. Kalhor, A. A. Noman, W. D. Newman, P. Shekhar, K. Han, V. Van, R. G. DeCorby, L. Chrostowski, M. Qi, and Z. Jacob, "Controlling evanescent waves using silicon photonic all-dielectric metamaterials for dense integration," *Nature Communications*, vol. 9, no. 1, p. 1893, Dec. 2018.

[146] M. van Niekerk, S. Jahani, J. Bickford, P. Cho, S. Anderson, G. Leake, D. Coleman, M. L. Fanto, C. C. Tison, G. A. Howland, Z. Jacob, and S. F. Preble, "Two-dimensional extreme skin depth engineering for CMOS photonics," *Journal of the Optical Society of America B*, vol. 38, no. 4, pp. 1307–1316, Apr. 2021.

[147] R. Halir, A. Maese-Novo, A. Ortega-Moñux, Í. Molina-Fernández, J. G. Wangüemert-Pérez, P. Cheben, D.-X. Xu, J. H. Schmid, and S. Janz, "Colorless directional coupler with dispersion engineered sub-wavelength structure," *Optics Express*, vol. 20, no. 12, pp. 13 470–13 477, Jun. 2012.

[148] D. González-Andrade, J. M. Luque-González, J. Gonzalo Wangüemert-Pérez, A. Ortega-Moñux, P. Cheben, Í. Molina-Fernández, and A. V. Velasco, "Ultra-broadband nanophotonic phase shifter based on subwavelength metamaterial waveguides," *Photonics Research*, vol. 8, no. 3, pp. 359–367, Mar. 2020.

[149] R. Halir, P. J. Bock, P. Cheben, A. Ortega-Moñux, C. Alonso-Ramos, J. H. Schmid, J. Lapointe, D.-x. Xu, J. G. Wangüemert-Pérez, and S. Janz, "Waveguide sub-wavelength structures : a review of principles," *Laser & Photonics Reviews*, vol. 49, no. 1, pp. 25–49, 2015.

[150] R. Halir, A. Ortega-Moñux, D. Benedikovic, G. Z. Mashanovich, J. G. Wangüemert-Pérez, J. H. Schmid, Í. Molina-Fernández, and P. Cheben, "Subwavelength-Grating Metamaterial Structures for Silicon Photonic Devices," *Proceedings of the IEEE*, vol. 106, no. 12, pp. 2144–2157, Dec. 2018.

[151] P. Cheben, R. Halir, J. H. Schmid, H. A. Atwater, and D. R. Smith, "Subwavelength integrated photonics," *Nature*, vol. 560, no. 7720, pp. 565–572, Aug. 2018.

[152] C. Li, M. Zhang, H. Xu, Y. Tan, Y. Shi, and D. Dai, "Subwavelength silicon photonics for on-chip mode-manipulation," *PhotoniX*, vol. 2, no. 1, p. 11, Dec. 2021.

[153] J. M. Luque-González, A. Sánchez-Postigo, A. Hadij-ElHouati, A. Ortega-Moñux, J. G. Wangüemert-Pérez, J. H. Schmid, P. Cheben, Í. Molina-Fernández, and R. Halir, "A review of silicon subwavelength gratings: building break-through devices with anisotropic metamaterials," *Nanophotonics*, vol. 10, no. 11, pp. 2765–2797, Aug. 2021.

[154] J. M. Luque-González, A. Herrero-Bermello, A. Ortega-Moñux, Í. Molina-Fernández, A. V. Velasco, P. Cheben, J. H. Schmid, S. Wang, and R. Halir, "Tilted subwavelength gratings: controlling anisotropy in metamaterial nanophotonic waveguides," *Optics Letters*, vol. 43, no. 19, pp. 4691–4694, Oct. 2018.

[155] J. M. Luque-González, A. Ortega-Moñux, R. Halir, J. H. Schmid, P. Cheben, Í. Molina-Fernández, and J. G. Wangüemert-Pérez, "Bricked Subwavelength Gratings: A Tailorable On-Chip Metamaterial Topology," *Laser & Photonics Reviews*, vol. 15, no. 6, p. 2 000 478, Jun. 2021.

[156] A. Herrero-Bermello, J. M. Luque-González, A. V. Velasco, A. Ortega-Moñux, P. Cheben, and R. Halir, "Design of a Broadband Polarization Splitter Based on Anisotropy-Engineered Tilted Subwavelength Gratings," *IEEE Photonics Journal*, vol. 11, no. 3, p. 6 601 508, Jun. 2019.

[157] A. Herrero-Bermello, J. M. Luque-González, R. Halir, P. Cheben, A. Ortega-Moñux, I. Molina-Fernandez, and A. V. Velasco, "Zero-Birefringence Silicon Waveguides Based on Tilted Subwavelength Metamaterials," *IEEE Photonics Journal*, vol. 11, no. 5, p. 2 700 308, Oct. 2019.

[158] A. Herrero-Bermello, A. Dias-Ponte, J. M. Luque-González, A. Ortega-Moñux, A. V. Velasco, P. Cheben, and R. Halir, "Experimental demonstration of metamaterial anisotropy engineering for broadband on-chip polarization beam splitting," *Optics Express*, vol. 28, no. 11, pp. 16 385–16 393, May 2020.

[159] J. Yang, Y. Dong, Y. Xu, B. Zhang, and Y. Ni, "Broadband and high-extinction-ratio polarization beam splitter on tilted subwavelength gratings waveguides," *Applied Optics*, vol. 59, no. 25, pp. 7705–7711, 2020.

[160] H. Sun and L. R. Chen, "Polarization-dependent tuning of Bragg reflection enabled through tilted subwavelength grating waveguide Bragg gratings," *Optics Letters*, vol. 46, no. 6, pp. 1450–1453, Mar. 2021.

[161] H. Liu, J. Feng, J. Ge, S. Zhuang, S. Yuan, Y. Chen, X. Li, Q. Tan, Q. Yu, and H. Zeng, "Tilted Nano-Grating Based Ultra-Compact Broadband Polarizing Beam Splitter for Silicon Photonics," *Nanomaterials*, vol. 11, no. 10, p. 2645, Oct. 2021.

[162] C. Pérez-Armenta, A. Ortega-Moñux, J. Manuel Luque-González, R. Halir, P. J. Reyes-Iglesias, J. Schmid, P. Cheben, Í. Molina-Fernández, and J. G. Wangüemert-Pérez, "Polarization-independent multimode interference coupler with anisotropy engineered bricked metamaterial," *Photonics Research*, vol. 10, no. 4, A57, Apr. 2022.

[163] M. Lu, C. Deng, Y. Sun, D. Wang, L. Huang, P. Liu, D. Lin, W. Cheng, T. Lin, G. Hu, B. Yun, and Y. Cui, "High extinction ratio and broadband polarization beam splitter based on bricked subwavelength gratings on SOI platform," *Optics Communications*, p. 128 288, Apr. 2022.

[164] S. H. Badri and M. M. Gilarlue, "Silicon nitride waveguide devices based on gradient-index lenses implemented by subwavelength silicon grating metamaterials," *Applied Optics*, vol. 59, no. 17, pp. 5269–5275, Jun. 2020.

[165] Z. Zhang, Y. Tong, Y. Wang, and H. K. Tsang, "Nonparaxial Mode-Size Converter Using an Ultracompact Metamaterial Mikaelian Lens," *Journal of Lightwave Technology*, vol. 39, no. 7, pp. 2077–2083, Apr. 2021.

[166] L. Zavargo-Peche, A. Ortega-Moñux, J. G. Wangüemert-Pérez, and Í. Molina-Fernandez, "Fourier based combined techniques to design novel sub-wavelength optical integrated devices," *Progress In Electromagnetics Research*, vol. 123, no. July 2011, pp. 447–465, 2012.

[167] C.-L. Chen, *Foundations for Guided-Wave Optics*. Hoboken, NJ, USA: John Wiley & Sons, Inc., Aug. 2006.

[168] P. Yeh, A. Yariv, and C.-S. Hong, "Electromagnetic propagation in periodic stratified media I General theory*," *Journal of the Optical Society of America*, vol. 67, no. 4, pp. 423–438, Apr. 1977.

[169] H. Kikuta, H. Yoshida, and K. Iwata, "Ability and Limitation of Effective Medium Theory for Subwavelength Gratings," *Optical Review*, vol. 2, no. 2, pp. 92–99, May 1995.

[170] P. Lalanne and D. Lemercier-lalanne, "On the effective medium theory of subwavelength periodic structures," *Journal of Modern Optics*, vol. 43, no. 10, pp. 2063–2085, Oct. 1996.

[171] C. Gu and P. Yeh, "Form birefringence dispersion in periodic layered media," *Optics Letters*, vol. 21, no. 7, pp. 504–506, Apr. 1996.

[172] H. Kikuta, Y. Ohira, H. Kubo, and K. Iwata, "Effective medium theory of two dimensional subwavelength gratings in the non-quasi-static limit," *Journal of the Optical Society of America A*, vol. 15, no. 6, pp. 1577–1585, Jun. 1998.

[173] https://www.appliednt.com/nanosoi/, *Applied Nanotools Inc. Canada*.

[174] R. Halir, Í. Molina-Fernández, J. G. Wangüemert-Pérez, A. Ortega-Moñux, J. De-Oliva-Rubio, and P. Cheben, "Characterization of integrated photonic devices with minimum phase technique," *Optics Express*, vol. 17, no. 10, pp. 8349–8361, May 2009.

[175] D. Rittenhouse, "Explanation of an Optical Deception," *Transactions of the American Philosophical Society*, vol. 2, no. 1786, pp. 37–42, 1786.

[176] G. Floquet, "Sur les équations différentielles linéaires à coefficients périodiques," *Annales scientifiques de l'École normale supérieure*, vol. 12, pp. 47–88, 1883.

[177] L. Rayleigh, "XVII. On the maintenance of vibrations by forces of double frequency, and on the propagation of waves through a medium endowed with a periodic structure," *The London, Edinburgh, and Dublin Philosophical Magazine and Journal of Science*, vol. 24, no. 147, pp. 145–159, Aug. 1887.

[178] F. Bloch, "Über die Quantenmechanik der Elektronen in Kristallgittern," *Zeitschrift for Physik*, vol. 52, no. 7-8, pp. 555–600, Jul. 1929.

[179] J. D. Joannopoulos, S. G. Johnson, J. N. Winn, and R. Meade D., *Photonic crystals: molding the flow of light*, 2nd ed. Princeton University, 2008.

[180] T. Tamir and S. T. Peng, "Analysis and design of grating couplers," *Applied Physics*, vol. 14, no. 3, pp. 235–254, Nov. 1977.

[181] P. Yeh and H. F. Taylor, "Contradirectional frequency-selective couplers for guided-wave optics," *Applied Optics*, vol. 19, no. 16, pp. 2848–2855, Aug. 1980.

[182] A. Yariv and P. Yeh, "Electromagnetic propagation in periodic stratified media II Birefringence, phase matching, and x-ray lasers *," *Journal of the Optical Society of America*, vol. 67, no. 4, pp. 438–448, Apr. 1977.

[183] D. Marcuse, "Modes of a symmetric slab optical waveguide in birefringent media - Part I: Optical axis not in plane of slab," *IEEE Journal of Quantum Electronics*, vol. 14, no. 10, pp. 736–741, Oct. 1978.

[184] J. Li, F. Miao, Z. Liang, and S. Guenneau, "Constructing metamaterials from subwavelength pixels with constant indices product," *Optics Express*, vol. 23, no. 6, pp. 7140–7151, Mar. 2015.

[185] A. Ortega-Moñux, J. Čtyroký, P. Cheben, J. H. Schmid, S. Wang, Í. Molina-Fernández, and R. Halir, "Disorder effects in subwavelength grating metamaterial waveguides," *Optics Express*, vol. 25, no. 11, p. 12 222, May 2017.

[186] J. Wang, D. Liang, Y. Tang, D. Dai, and J. E. Bowers, "Realization of an ultra-short silicon polarization beam splitter with an asymmetrical bent directional coupler," *Optics Letters*, vol. 38, no. 1, p. 4, Jan. 2013.

[187] T. Zhang, X. Yin, L. Chen, and X. Li, "Ultra-compact polarization beam splitter utilizing a graphene-based asymmetrical directional coupler," *Optics Letters*, vol. 41, no. 2, p. 356, Jan. 2016.

[188] B. Ni and J. Xiao, "Ultracompact and Broadband Silicon-Based Polarization Beam Splitter Using an Asymmetrical Directional Coupler," *IEEE Journal of Quantum Electronics*, vol. 53, no. 4, pp. 1–8, Aug. 2017.

[189] Y. Tian, J. Qiu, C. Liu, S. Tian, Z. Huang, and J. Wu, "Compact polarization beam splitter with a high extinction ratio over S + C + L band," *Optics Express*, vol. 27, no. 2, p. 999, Jan. 2019.

[190] J. D. Sarmiento-Merenguel, A. Ortega-Moñux, J.-M. Fédéli, J. G. Wangüemert-Pérez, C. Alonso-Ramos, E. Durán-Valdeiglesias, P. Cheben, Í. Molina-Fernández, and R. Halir, "Controlling leakage losses in subwavelength grating silicon metamaterial waveguides," *Optics Letters*, vol. 41, no. 15, pp. 3443–3446, Aug. 2016.

[191] F. Zhang, J. Zheng, Y. Song, W. Liu, P. Xu, and A. Majumdar, "Ultra-broadband and compact polarizing beam splitter in silicon photonics," *OSA Continuum*, vol. 3, no. 3, pp. 560–567, 2020.

[192] K. Chen, K. Yu, and S. He, "High Performance Polarization Beam Splitter Based on Cascaded Directional Couplers Assisted by Effectively Anisotropic Structures," *IEEE Photonics Journal*, vol. 11, no. 6, pp. 1–9, Dec. 2019.

[193] A. Ortega-Moñux, C. Alonso-Ramos, A. Maese-Novo, R. Halir, L. Zavargo-Peche, D. Pérez-Galacho, Í. Molina-Fernández, J. G. Wangüemert-Pérez, P. Cheben, J. H. Schmid, J. Lapointe, D. Xu, and S. Janz, "An ultra-compact multimode interference coupler with a subwavelength grating slot," *Laser and Photonics Reviews*, vol. 7, no. 2, pp. 12–15, 2013.

[194] D. J. Thomson, Y. Hu, G. T. Reed, and J.-M. Fedeli, "Low Loss MMI Couplers for High Performance MZI Modulators," *IEEE Photonics Technology Letters*, vol. 22, no. 20, pp. 1485–1487, Oct. 2010.

[195] R. Halir, G. Roelkens, A. Ortega-Moñux, and J. G. Wangüemert-Pérez, "High performance 90° hybrid based on a silicon-on-insulator multimode interference coupler," *Optics Letters*, vol. 36, no. 2, pp. 178–180, Jan. 2011.

[196] W. Yang, M. Yin, Y. Li, X. Wang, and Z. Wang, "Ultra-compact optical 90° hybrid based on a wedge-shaped 2 × 4 MMI coupler and a 2 × 2 MMI coupler in silicon-on-insulator," *Optics Express*, vol. 21, no. 23, p. 28 423, Nov. 2013.

[197] L. Soldano and E. Pennings, "Optical multi-mode interference devices based on self-imaging: principles and applications," *Journal of Lightwave Technology*, vol. 13, no. 4, pp. 615–627, Apr. 1995.

[198] J. C. Maxwell, "Solutions of Problems, problem no. 2," *Cambridge and Dublin Mathematical Journal*, vol. 8, p. 188, 1854.

[199] R. Wood, "Physical Optics," *Macmillan, New York*, pp. 86–91, 1905.

[200] R. K. Luneburg, *Mathematical theory of optics*. University of California press, 1944.

[201] A. Fletcher, T. Murphy, and A. Young, "Solutions of two optical problems," *Proceedings of the Royal Society of London. Series A. Mathematical and Physical Sciences*, vol. 223, no. 1153, pp. 216–225, 1954.

[202] P. Sinai, "Correction of Optical Aberrations by Neutron Irradiation," *Applied Optics*, vol. 10, no. 1, p. 99, Jan. 1971.

[203] R. S. Moore, *Plastic optical element having refractive index gradient*, 1973.

[204] D. B. Keck and R. Olshansky, *Optical Waveguide Having Optimal Index Gradient*, 1975.

[205] C. P. Gomez-Reino, M. Victoria, and C. Bao, *Gradient-index optics: fundamentals and applications*. Springer Science \& Business Media, 2002.

[206] D. M. Cleomedes, *Circularis Inspectionis Meteororum*, See ref (History). 1585.

[207] Alhazen, *Opticae Thesaurus, Book VII*. (Translated into Latin by Vitello and published by F. Risner), 1572, p. 251.

[208] S. Molesky, Z. Lin, A. Y. Piggott, W. Jin, J. Vucković, and A. W. Rodriguez, "Inverse design in nanophotonics," *Nature Photonics*, vol. 12, no. 11, pp. 659–670, 2018.

[209] J. B. Pendry, D. Schurig, and D. R. Smith, "Controlling electromagnetic fields (Supporting Online Material)," *Science (New York, N.Y.)*, vol. 312, no. 5781, pp. 1780–2, 2006.

[210] U. Leonhardt and T. G. Philbin, *Chapter 2 Transformation Optics and the Geometry of Light*, 08. Elsevier B.V., 2009, vol. 53, pp. 69–152.

[211] L. Xu and H. Chen, "Conformal transformation optics," *Nature Photonics*, vol. 9, no. 1, pp. 15–23, Jan. 2015.

[212] L. H. Gabrielli, D. Liu, S. G. Johnson, and M. Lipson, "On-chip transformation optics for multimode waveguide bends," *Nature Communications*, vol. 3, pp. 1216–1217, 2012.

[213] I. Staude and J. Schilling, "Metamaterial-inspired silicon nanophotonics," *Nature Photonics*, vol. 11, no. 5, pp. 274–284, May 2017.

[214] D. McGrath, "ASML claims major EUV milestone," *EETimes*, 2017.